Structural Investigation of the Interaction between Glypican-3 and Uncoordinated-5



Onno Akkermans

Wolfson College

University of Oxford

A thesis Submitted in fulfilment of the requirements for the degree of Doctor of Philosophy

DPhil of Biochemistry

Trinity 2019

University of Oxford

Department of Biochemistry

Structural Investigation of the Interaction between Glypican-3 and Uncoordinated-5

by Onno Akkermans
Wolfson College
Trinity 2019

Supervisors
Prof. Elena Seiradake
Dr. Metin Aksu

Abstract

Uncoordinated-5 (Unc5) receptors are known for their function to induce repulsion in axonal and cell migration. Another proposed function is as dependency receptors where withdrawal of their ligands results in apoptosis. Unc5's interactions with its ligands Netrin and fibronectin leucine-rich transmembrane (FLRT) have been extensively investigated; however, the molecular mechanisms of Unc5 as a switch for repulsive signalling and as a dependency receptor remain elusive. Recent work identified a novel interaction between Unc5 and Glypican-3 (GPC3), for which there are no known biological functions. GPC3 is a GPI-anchored heperan sulfate proteoglycan that has been studied in its role of modulating several morphogen signalling pathways. Using X-ray crystallography, this thesis reveals the structure of the core protein of human and mouse GPC3 at 2.6 and 2.9 Å resolution respectively. From this, the crystal structure of the GPC3/Unc5 complex was solved in two different crystal forms, at 4.0 to 4.6 Å. The crystal structure revealed an octameric assembly, showing that GPC3 clusters several Unc5 receptors. Biophysical studies attempted to validate the identified stiochiometry to further understand the molecular mechanisms of this interaction. The work presented provides the foundations for further functional studies for the GPC3/Unc5 interaction.

Acknowledgements

Throughout my D.Phil I had support from numerous colleagues, collaborators and friends, whom have been integral to this thesis. I am also grateful to Clarendon and Wolfson College for generously funding my work.

First I would like to thank my supervisor, Elena Seiradake, who welcomed me into her lab. Her willingness to let me develop the project independently is something I greatly appreciate. Throughout, she provided the support and guidance to improve my personal development as a scientist. She also actively created a pleasant working environment, which made the past few years an enjoyable experience.

I must also thank my co-supervisor, Metin Aksu, who welcomed a barrage of questions and was always happy share all of his expertise. His contributions were invaluable in solving the crystal structures presented in this thesis. Besides this, his love for good coffee was a welcome excuse for an occasional break from the lab.

Many of the skills used in this thesis were honed through the patient training by Maria Carrasquero, whose technical expertise paved much of the path through my D.Phil. I also want to thank all members of the lab who I had the pleasure to work alongside.

Others I would like to thank include Ed Lowe (Department of Biochemistry), for all his knowledge of useful techniques of X-ray crystallography; Kamel el-omari (Diamond Light Source) for his help in collection and analysing SAD datasets; David Staunton (Department of Biochemistry) for his help in SPR and SEC-MALS; Svenja Hester and Shabaz Mohammed for their collaboration with XL-MS; Ritu Raj (Carol Robinsons lab, Chemistry Department) for their collaboration in native MS.

The never-ending support offered by friends and family, even from locations across the globe, constantly reminded me to not give up. Their willingness to listen to me describe the problems of low-resolution crystals, even when they had no clue what I was talking about, helped me keep my sanity intact. In particular, I would like to thank Todd Nordgren, Tom Ormsby and Owen Crowther for reading through my thesis to provide focused edits, without hesitation. Their corrections and suggestions have made this thesis more than I could have ever done on my own.

Contents

List of Figures **viii**

List of Tables **x**

List of Abbreviations **xi**

1 Introduction **1**

1.1 Introduction 2

1.1.1 The migrating cell 3

1.1.2 Newly discovered ligand 5

1.2 The Receptor Family Unc5 6

1.2.1 Developmental expression of Unc5 6

1.2.2 The architecture of Unc5 7

1.2.3 Unc5 signalling 9

1.2.4 Unc5s role in disease 15

1.3 The Glypican Family 16

1.3.1 Structure of glypican 17

1.3.2 S-/N- glycosylation of GPC3 19

1.3.3 Molecular mechanisms of signal modulation 20

1.3.4 GPC3 role in cancer 25

1.4 Project Aims 27

2 Materials and Methods **28**

2.1 Molecular Biology and Cloning 29

2.1.1 Genes and constructs 29

2.1.2 Molecular cloning 30

2.2 Protein Expression and Purification 31

2.2.1 Cell lines 31

2.2.2 Mammalian cell culture maintenance 32

2.2.3 Small-scale transient transfection 33

2.2.4 Protein biotinylation 33

2.2.5 Large-scale protein expression 34

2.2.6 Protein purification 34

2.2.7 SDS-PAGE and western blotting 35

2.3 Cell Biology 37

2.3.1 Cell-binding assay 37

2.4 Biophysical Methods 38

2.4.1 Surface plasmon resonance 38

2.4.2 Size-exclusion chromatography multi-angle light scatter . . . 40

2.4.3 Cross-linking mass spectrometry 41

2.4.4 Native mass spectrometry 42

2.5 X-ray Crystallography 43

2.5.1 crystallization and crystal optimization 44

2.5.2 Data collection 47

2.5.3 Data processing 47
2.5.4 Molecular replacement 49
2.5.5 Experimental phasing 50
2.5.6 Model building and refinement 51
2.5.7 Validation 53

3 Solving the Crystal Structure of GPC3 55

3.1 Summary 56
3.2 Results 57
3.2.1 Crystallization and optimization of GPC3 57
3.2.2 Data collection and processing 65
3.2.3 Phasing and model building 67
3.2.4 The crystal structure of GPC3 72
3.2.5 Conformational change of GPC3 75

4 Solving the Crystal Structure of the GPC3/Unc5D Complex 77

4.1 Summary 78
4.2 Results 79
4.2.1 Crystallization of GPC3 and Unc5D 79
4.2.2 Data collection and processing 82
4.2.3 Phasing of the crystal complex data 84
4.2.4 Structure solutions and refinement 87
4.2.5 The crystal structure of GPC3 and Unc5D 92
4.2.6 Conservation of the binding interfaces 96
4.2.7 Isoform specific binding 99

5 Characterization of the GPC3/Unc5 Complex 101

5.1 Summary 102

5.2 Results 103

5.2.1 Mutational disruption of the protein complex 103

5.2.2 XL-MS identifies the topology of interface 3 108

5.2.3 SEC-MALS suggests a one-to-one protein complex 110

5.2.4 Native MS of the protein complex 111

6 Discussion and Future Work 115

6.1 Organization of the GPC3/Unc5 Signalling Complex 116

6.2 Biological Significance of the GPC3/Unc5 Interaction 118

6.2.1 GPC3 extends the neuronal context 118

6.2.2 Modulating migration 122

6.3 GPC3s Role in Cancer 124

6.4 One Receptor and its Several Functions 125

Appendices

A Appendix: Previous Constructs and Primers 128

B Appendix: Anisotropy Data Statistics 131

C Appendix: Conservational Analysis 135

D Appendix: Native MS of GPC3 139

References 141

List of Figures

1.1 Process of angiogenesis. 4
1.2 Short- and long- range attraction and repulsion in neuronal guidance. 5
1.3 Domain architecture of Unc5. 8
1.4 Proposed Unc5's dependency receptor mechanism of action. 10
1.5 Netrin1 oligomerizes DCC and neogenin. 12
1.6 Unc5s interaction with FLRT and Lphn. 14
1.7 Schematic of GPC3 and the crystal structure of GPC1. 18

2.1 Inhibiting N-glycosylation maturation. 32
2.2 Surface plasmon resonance setup. 38
2.3 Phase diagram of a vapour diffusion experiment. 44

3.1 Design and purification of *hs*GPC3$^{\Delta C}$ 58
3.2 Initial crystal hits for *hs*GPC3$^{\Delta C}$ 59
3.3 Anistropy analysis of *hs*GPC3$^{\Delta C}$ (#3). 60
3.4 Design of the non-cleavable mutant and deletion constructs. 61
3.5 Best crystals for *hs*GPC3$^{\Delta C}$ and *mm*GPC3$^{\Delta C}$ 63
3.6 Data collection of *hs*GPC3$^{\Delta C}$ (#5). 66
3.7 Molecular replacement model design. 68
3.8 Electron density map of *hs*GPC3$^{\Delta C}$ (#3). 70
3.9 The crystal structure of *hs*GPC3$^{\Delta C}$. 72
3.10 The electron density map of *hs*GPC3$^{\Delta C}$ (#5). 73
3.11 The electron density map at N-glycosylation site N418 for *hs*GPC3$^{\Delta C}$ (#5). 74
3.12 Unresolved N-terminus of GPC3$^{\Delta C}$ in both human (#5) and mouse (#6). . 75
3.13 Structural comparison of GPC1 and GPC3. 76
4.1 Minimal binding construct of Unc5 for GPC3 interaction. 79
4.2 Crystals of the GPC3/Unc5D protein complex (#7, #8, and #9). 80
4.3 Data collection diffraction image of *mm*GPC3$^{\Delta C}$ and *rn*Unc5D$^{\text{Ig1-Ig2-TSP1}}$. . . 82
4.4 Experimental phasing of *mm*GPC3$^{\Delta C}$/*rn*Unc5D$^{\text{Ig1-Ig2-TSP1}}$ (#7). 84
4.5 Fluorescence scan of Ta_6Br_{12} derivative *mm*GPC3$^{\Delta C}$/*rn*Unc5D$^{\text{Ig1-Ig2-TSP1}}$ (#7).85

4.6 Density modification reveals the small globular Ig domain of Unc5. 88
4.7 Electron density maps of the GPC3/Unc5 complex. 89
4.8 GPC3 in the octameric assembly of *hs*GPC3$^{\Delta C}$/*rn*Unc5D$^{Ig1\text{-}Ig2\text{-}TSP1}$ complex. 92
4.9 Unc5D In the octameric assembly of *hs*GPC3$^{\Delta C}$/*rn*Unc5D$^{Ig1\text{-}Ig2\text{-}TSP1}$ complex. 93
5.1 Mutagenesis of Unc5 disrupts the formation of the complex. 104
5.2 SPR analysis of the GPC3 and its mutants binding to Unc5. 106
5.3 SPR binding curves of GPC3 and its mutants binding to Unc5. 107
5.4 XL-MS analysis of the GPC3/Unc5 complex. 109
5.5 SEC-MALS analysis of *mm*GPC3$^{\Delta C}$ in complex with *rn*Unc5D$^{Ig1\text{-}Ig2\text{-}TSP1}$. . . 111
5.6 Native MS of GPC3/Unc5D complex and MS/MS of the 1:1 peak. 113
5.6 MS/MS analysis of the larger oligomer of GPC3/Unc5D complexes. 114

6.1 The three possible higher order complexes derived from the crystal structure. 117
6.2 Possible orientations of the GPC3/Unc5D interactions. 119
6.3 RNAseq profile of different populations of hippocampal/subiculum neurons. . 120
6.4 Superposed FLRT^{LRR} domain on the GPC3/Unc5D 2:2 stoichiometries. . . . 122
6.5 The known extracellular interactions of Unc5s. 126

C.4 Sequence alignment of TSP1 and TSP2. 138
D.4 Native MS of *mm*GPC3$^{\Delta C}$. 140

List of Tables

1.1 Summary of human glypican family adapted from Filmus et al. 16
1.2 Percent sequence identity matrix of the human glypican family. 17
1.3 Examples of the developmental function of the glypican family. 21

2.1 Summary of cDNAs used for sub-cloning. 29

3.1 Summary of crystallization conditions for the GPC3 constructs. 65
3.2 Data collection parameters for *hs*GPC3$^{\Delta C}$ (#3 & #5) and *mm*GPC3$^{\Delta C}$ (#6). 66
3.3 Anisotropically processed data statistics for *hs*GPC3$^{\Delta C}$ (#3). 67
3.4 Processed data statistics for the best crystal datasets (#5 and #6). 69
3.5 Processed data statistics for *hs*GPC3$^{\Delta C}$ (#5) in spacegroup P3 2 1 and P3. . 69
3.6 Refinement statistics for *hs*GPC3$^{\Delta C}$(#3 and #5), and *mm*GPC3$^{\Delta C}$ (#6). . . 71

4.1 Crystallization conditions for the GPC3/Unc5D complex. 81
4.2 Data collection parameters and data statistics for the GPC3/Unc5 complex. . 83
4.3 Data collection parameters for TaBr derivative crystals (#7). 86
4.4 Processed data statistics for native and TaBr derivative crystals (#7). 87
4.5 Refinement and model geometry statistics for the GPC3/Unc5 complex. . . . 91

5.1 Calculated dissociation coefficient (K_D) and B_{max}. 106
5.2 Apparent Mass of *m*GPC3$^{\Delta C}$ and *mm*GPC3$^{\Delta C}$/*rn*Unc5D$^{\text{Ig1-Ig2-TSP1}}$ 111
5.3 Assigned molecular masses determined by Native MS. 112

A.1 Previously cloned constructs used in this thesis. 129
A.2 Primers of the constructs used in this thesis. 130
B.1 Anisotropy correction for *hs*GPC3$^{\Delta C}$ (#3). 132
B.2 Anisotropy correction for *mm*GPC3$^{\Delta}$/*rn*Unc5D$^{\text{Ig1-Ig2-TSP1}}$ (#7). 133
B.3 Anisotropy correction for *hs*GPC3$^{\Delta}$/*rn*Unc5D$^{\text{Ig1-Ig2-TSP1}}$ (#9). 134
C.1 Conservational analysis of GPC3. 136
C.2 Conservational analysis of GPC1. 137
C.3 Conservational analysis of Unc5. 137

List of Abbreviations

AFP . . . . . α-fetoprotein.
MI . . . . . α-mannosidase I.
β**ME** . . . . . β-mercaptoethanol.
BirA . . . . . Biotin ligase.
BS3 . . . . . Bis(sulfosuccinimidyl)suberate.
BMP . . . . . Bone-morphogenetic protein.
BSA . . . . . Bovine serum albumin.
CS . . . . . Chondroitin sulphate.
CRD . . . . . Cysteine rich domain.
DLP . . . . . Dally-Like-Protein.
ES . . . . . Electrospray.
DAPK . . . . . Death-associated protein kinase.
DCC . . . . . Deleted in colorectal cancer.
DD . . . . . Death domain.
DSCAM . . . . Down syndrome cell adhesion molecule.
DMEM . . . . . Dulbecco's modified eagle's medium.
ELISA . . . . . Enzyme-linked immunosorbent assay.
EMT . . . . . Epithelial-mesenchymal transition.
FGF . . . . . Fibroblast growth factor.
FLRT . . . . . Fibronectin leucine rich transmembrane protein.
FBS . . . . . Foetal bovine serum.
GAG . . . . . Glycosaminoglycans.
GlcNAc . . . . . acetyl-D-glucosamine.
GPI . . . . . Glycosylphosphatidylinositol.
GPC . . . . . Glypican.
Hh, Ssh . . . . . Hedgehodge, Sonic hedgehodge.
HCC . . . . . Hepatocellular carcinoma.
HSPG . . . . . Heparan sulfate proteoglycan.
HS . . . . . Heparan sulfate.

HRP . . . . . Horse radish peroxidase.
Ig . . . . . Immunoglobin-like domain.
IHC . . . . . Immunohistochemistry.
Lphn . . . . . Latrophillin.
LLG . . . . . Log-likelihood gain.
LRR . . . . . Leucine-rich repeat domain.
LRP1/5/6 . . . Low-density lipoprotein receptor-related protein 1/5/6.
MS . . . . . Mass spectrometry.
MR . . . . . Molecular replacement.
GnTI . . . . . N-acetylglucosaminyltransferase I.
NCS . . . . . Non-crystallographic symmetry.
NDSB256 . . . Nondetergent sulfobetaine-256
Ptch1/2 . . . . . Patched receptor.
PBS . . . . . Phosphate buffer saline.
PEG . . . . . Polyethylene glycol.
PEI . . . . . Polyethylenimine.
RU . . . . . Response units.
PIDD . . . . . P53-induced protein with a death domain.
RMSD . . . . . Root-mean-square deviation.
SAD . . . . . Single anomalous dispersion.
SEC-MALS . . Size-exclusion chromatography-multi-angle light scatter.
SGBS . . . . . Simpson-Golabi-Behmel syndrome.
SMO . . . . . Smoothened transmembrane protein.
SDS-PAGE . . Sodium dodecyl sulfate polyacrylamide gel electrophoresis.
SPR . . . . . Surface plasmon resonance.
TSP . . . . . Thrombospondin type-1 domain.
TSR . . . . . Thrombospondin type-1 repeats.
TFZ . . . . . Translation function Z-score.
Unc5 . . . . . Uncoordinated-5.
VEGF . . . . . Vascular endothelial growth factor.
VIP . . . . . Vasoactive intestinal peptide.
XL-MS . . . . . Cross-linking mass spectrometry.
YAP . . . . . Yes-associated protein.

1

Introduction

1.1 Introduction

During embryonic development, a single fertilized oocyte gives rise to specialised cells, organs and eventually an organism. To develop the organism, cells can perform a number of actions, which include proliferation [1], programmed cell death [2, 3], cell shape/polarity [4] and migration [5, 6]. These cell behaviours are regulated by sequential activation of key developmental genes, but also by chemical cues in their environment. The intercommunication between cells and tissue is established by diffusible chemical or contact-dependent cues that provide spatiotemporal information [7]. This collaboration ensures that the correct cellular behaviour is performed in the context of the body plan of the organism.

Over the past decade, many conserved signalling pathways have been deciphered, such as morphogens [8] and guidance cues [9]. To sense these cues, transmembrane receptors transduce the information to the cell to produce a specific cellular behaviour. There are numerous of specialized cells, all with unique behaviours. To respond in such a precise and discrete manner cells would require a large subset of receptors and ligands. Instead cells respond to ligands in a context dependent manner, in which the presence or absence of downstream signalling components, external co-factors and/or crosstalk between multiple signal pathways modulates their response. The context in which the cell receives the chemical cue is therefore pivotal to how it is interpreted. In recent years, a growing body of evidence supports the idea of an increasingly integrated signalling mechanism [10–16]. Therefore, understanding how cell decision making is influenced by the modulation and interplay of these pathways is essential to deciphering the complexity of development.

1.1.1 The migrating cell

Functional structures are formed, in part, by the movement of individual or groups of cells through a process known as cell migration. Migration typically occurs in four steps: actin-driven formation of cellular protrusions at the leading edge, adherence of the protrusion to the extracellular matrix or tissue, loss of adhesion at the cell rear, and a pulling motion to move the cell forward [17–19]. Migration is directed by external cues that induce cell polarity and allow the cell to move and guide itself towards (attraction) or away (repulsion) from the guidance source [20, 21]. The induction of migration results in the cell to lose epithelial properties and to acquire a more fibroblast-like phenotype, known as the epithelial-mesenchymal transition (EMT) [22–24].

The extent of the transition to a mesenchymal phenotype depends on the cell type. Some cells undergo a partial mesenchymal transition that occurs when some, but not all, the mesenchymal phenotypes are presented, which allows cells to migrate as a collective [24]. Examples of collective migration include the development of limb buds and mammary tissue, or during angiogenesis. Angiogenesis is the process by which endothelial cells form new blood vessels from pre-existing vessels. Like epithelial cells, endothelial cells are oriented by an apical-basal polarity and possess intercellular junctions. Proangiogenic growth factors, such as vascular endothelial growth factor, transforming growth factor-β, Wnt and bone morphogenetic protein (BMP) are secreted during morphogenesis or in hypoxic tissue, controlling vascularization (figure 1.1) [25]. These growth factors promote the formation of a tip cell, which reorganizes the cytoskeletal to form cytoplasmic extrusions, called filopodia. Filopodia sense the environment for guidance cues and migrate towards or away from it [26–29]. The tip cell is followed by a group of cells, known as stalk cells, which assist migration through proliferation, which induces forward motion [30].

A special case of migration is observed in nerve cells, of which a neurite is projected from the cell body to innervate distant targets. Neuronal cells are guided

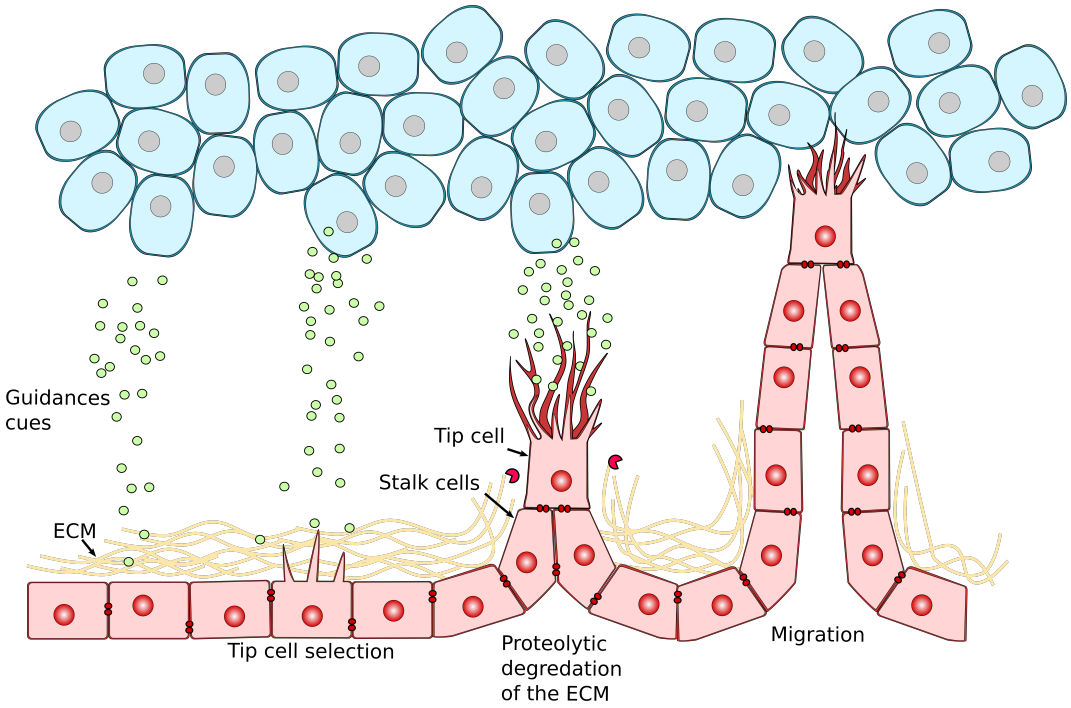


Figure 1.1: Process of angiogenesis. Collective migration by angiogenesis occurs when an endothelial cell is exposed to guidance cues which form the tip cell, such as VEGF. The extracellular matrix (ECM) is degraded by proteases, such as matrix metalloproteases, allowing the endothelial cells to migrate towards the source of the guidance cues. All diagram and figures in this thesis were prepared in Inkscape.

by long- and short-range chemical cues (figure 1.2). These guidance cues consist of four main families which are the semaphorins, ephrins, netrins, slits, and fibronectin leucine rich transmembrane protein (FLRTs). In addition, while initially considered distinct groups of signalling, morphogens such as Wnt, BMPs and Sonic hedgehog (Shh) have also been reported to play a role in neuronal guidance [31–34].

During neuronal migration, a specialized structure called the growth cone forms at the tip of the axons. Similar to the tip cell, the growth cone presents filopodia that are enriched with receptors. These receptors sense the environment for long- and short-range guidance cues to direct the growth cone [35, 36]. When a filopodia senses an attractive signal, reorganization of the microtubules and the formation of adhesive contacts occurs, promoting motility and forward motion [37, 38]. Sensing a repulsive signal leads to rearrangement of local actin and results in a growth cone

collapse [39]. The responses are not binary, however, and the integration of both attractive and repulsive guidance cues graduate the navigation of neurons [40].

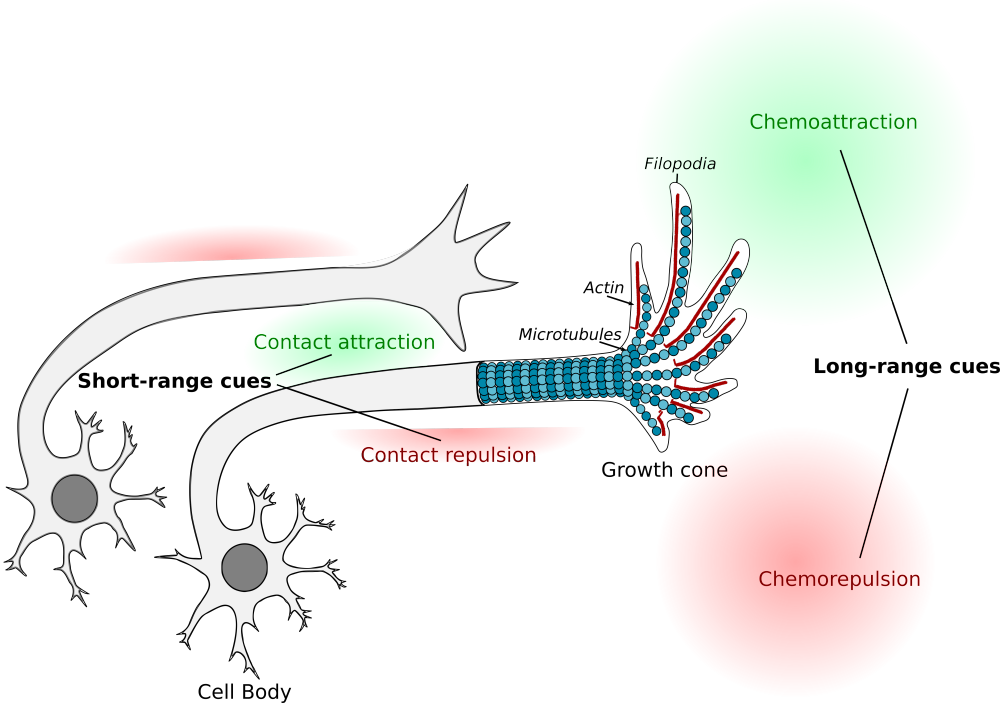


Figure 1.2: Short- and long- range attraction and repulsion in neuronal guidance. Short-range repulsion and attraction ensures self-avoidance. Long-range guidance cues direct the neuron toward their destination.

1.1.2 Newly discovered ligand

Cell-surface proteins often present multiple individually folded extracellular domains, which can interact with different proteins and ligands independently. Elucidating the multiple interactions that these cell-surface proteins can form is essential to understanding the complex biological processes. Recent work by the Comoletti lab aimed to decipher such unknown protein-protein interactions involved in neurodevelopment. They utilized a high-throughput enzyme-linked immunosorbent assay (ELISA)-based ligand-receptor screen, with proteins implicated in neurodevelopment [41]. The proteomic screen identified over eighty new interaction pairs, of which they recently characterized the neuronal growth regulator-1 with IgLON5 [42].

Of interest to this thesis is the newly identified interaction between glypican-3 (GPC3), a modulator of many different morphogens, and the Uncoordinated-5 (Unc5) receptor, which is involved in migration and apoptosis. The glypican family are heparan sulfate proteoglycans (HSPG), which have several chains of highly charged heparan sulfate glycosaminoglycans (HS-GAGs) [43]. The Comoletti lab identified that GPC3, and not its homologues, interact with Unc5. Furthermore, this interaction was shown to be independent of the HS-GAGs. Taken together, these findings suggest a biologically relevant interaction between Unc5 and GPC3, of which there is no known function.

1.2 The Receptor Family Unc5

1.2.1 Developmental expression of Unc5

Unc5 was initially identified in C. *elegans* [44], while in vertebrates the family contains four homologues (Unc5A-Unc5D) [45–47]. Loss of the Unc5 receptors results in migration defects, while ectopic expression switches a chemoattractive to a chemorepulsive response [44, 48]. Chemorepulsion through Unc5 is known to occur with two ligands, netrin1 [44, 49–51] and fibronectin leucine rich transmembrane protein (FLRT) [52–54].

In *situ* hybridization experiments revealed distinct, but partially overlapping, expression patterns in the nervous system (E9.5-E19.5) [47, 55, 56]. Unc5A is detected in differentiating motoneurons in the ventral spinal cord (embryonic day E11), and several brain structures, such as the developing hypothalamus, thalamus, and pallidum (E13) [44]. Unc5B is expressed in thalamic neurons, which are repelled by FLRT3 [54]. Unc5C expression is found in Purkinje cells of the cerebellum (E11-E13), where disruption results in a malformed cerebellum with fewer leaf-like structures (folia) [56]. At postnatal day P0, high levels of Unc5C is identified in all layers of the cerebellum [55, 57, 58]. The expression peaks at

P7, and is downregulated when granule cell migration is completed at P21 [55]. Nonetheless, expression of Unc5C persists in Purkinje cells through adulthood [45]. Lastly, Unc5D is expressed in multipolar neurons to slow down migration in the cortical plate by FLRT2 [53].

Unc5 is also found outside the nervous system, in which expression of Unc5B-D has been identified in the developing limbs (E9.5) and mammary glands (E12.5) [47]. Furthermore, Unc5B is prominently expressed in the developing vascular system at all stages [47, 59]. Knockout of Unc5B results in embryo lethality due to vascular defects, such as increased capillary branching and tip-cell filipodia extension [59]. These findings suggest that Unc5B has an anti-angiogenic role [54, 59–61]; however, some findings have demonstrated that Unc5 can also have a pro-angiogenic role [62–65]. The contradictory findings can be attributed to the later identified ligand FLRT [54, 61], and/or to a biphasic response to netrin1 [64, 66, 67].

1.2.2 The architecture of Unc5

The Unc5 receptor is a single pass transmembrane receptor. The extracellular domains, from the N- to C- terminus, consists of two immunoglobin-like domains (Ig1 & Ig2) and two thrombospondin type 1 domains (TSP1 & TSP2). The intracellular domains consist of a supramodule of ZU5, deleted in colorectal cancer (DCC) receptor binding motif-containing domain (UPA) and the death domain (DD) (figure 1.3A).

The ectodomains of Unc5 have been solved by X-ray crystallography, of which the human Unc5A$^{\text{Ig1-Ig2-TSP}}$ (PDB 4V2A; figure 1.3B), rat Unc5D$^{\text{Ig1}}$ in complex with mouse FLRT2$^{\text{LRR}}$ (PDB 4V2C) and rat Unc5D$^{\text{Ig1}}$ & rat Unc5D$^{\text{Ig1-Ig2-TSP1}}$ in complex with FLRT2$^{\text{LRR}}$ and Latrophilin3$^{\text{Lec-Olf}}$ (Lphn; PDB 5FTU & 5FTT) are available [54, 69]. Ig-like domains are approximately 15 kDa in size and have a compact globular fold that contains two layers of antiparallel β-strands. The fold is held together by an intradomain disulfide bond. TSP domains are approximately 8 kDa in size and is structurally similar to the type 1 repeats (TSR) of the

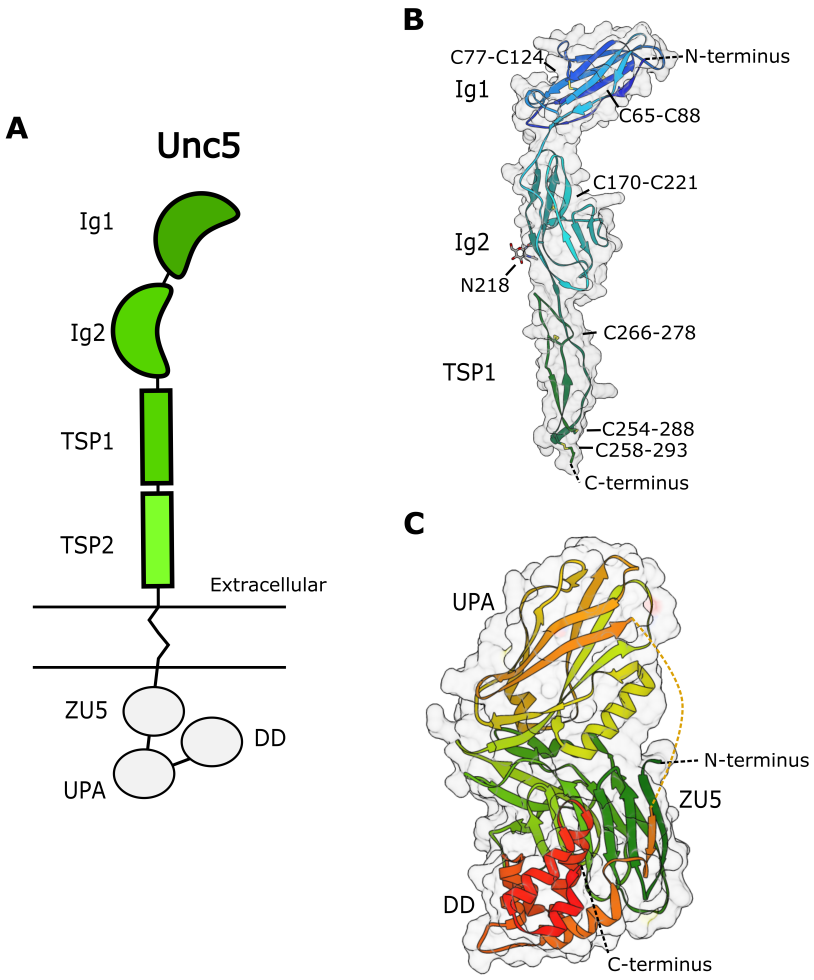


Figure 1.3: Domain architecture of Unc5. A) Schematic of the Unc5 domains. **B)** Crystal structure of ectodomains (Ig1-Ig2-TSP) of Unc5A (PDB 4V2A) **C)** The cytoplasmic domains (ZU5-UPA-DD) of Unc5B (PDB 3G5B). The structures are shown with a transparent surface representation and with a cartoon depiction. The colour scheme is according to the rainbow from the N-terminus in blue to the C-terminus in red. The structures were prepared in Chimera [68].

Thrombospondins, a family of matricellular glycoproteins involved in regulating cell proliferation, migration and apoptosis (PDB 1LSL & 3R6B) [70, 71]. TSP1 contains three antiparallel strands with stacking tryptophan and arginine residues, resulting in a grooved surface that could be involved in binding GAGs [70, 71].

From the N-terminal ectodomains of the receptor, a single transmembrane-helix crosses the cell membrane to the intracellular domains. The cytoplasmic domains

ZU5-UPA-DD of Unc5B has been solved by X-ray crystallography (PDB 3G5B; figure 1.3C), which revealed a compact association between ZU5-DD, which is considered the closed, autoinhibitory, configuration of the supramodule [72]. This supramodule (ZU5-UPA-DD) has also been identified in scaffold protein families, such as ankyrins [73], and P53-inducible protein with a DD (PIDD).

1.2.3 Unc5 signalling

Unc5 as a dependency receptor

Dependency receptors induce proapoptotic signalling when a ligand is withdrawn from the cell. Therefore, presentation of one of these receptors makes the cell dependent on the ligand to survive [75, 76]. The first discovered dependency receptor was $p75^{NTR}$ [77], and also contains a DD [78, 79]. The DD superfamily contains the DD, the death effector domain, the caspase recruitment domain and the pyrin domain subfamilies [79]. The mechanism by which these domains induce apoptosis is through oligomerization, which forms a platform to assemble the apoptosome [80]. This oligomerization was demonstrated in the crystal structure of the PIDD (PDB 2OF5) [81, 82]. Indeed, the crystal structure of the DD domain of Unc5 (PDB 1WMG) reveals a dimer that also forms in solution [83]. The dimer's interface is inaccessible in the closed conformation of the ZU5-UPA-DD supramodule [72].

The mechanism by which Unc5 induces apoptosis is not yet fully understood. Current literature suggests that upon withdrawal of Unc5s ligand, netrin1, the cytoplasmic supramodule adopts an open conformation [72], and undergoes cleavage by Caspase-3 at its caspase cleavage motif ($DXXD^{412}$ in *hs*Unc5B) [84, 85] (figure 1.4); however, the timing of these events remain unclear. After ligand withdrawal the cytoplasmic domains of Unc5 recruit the death-associated protein kinase (DAPK), PR65β and PP2A, which results in the dephosphorylation of DAPK by PP2A [86]. The activated DAPK proceeds to initiate downstream apoptotic signalling. In the presence of netrin1, the cytoplasmic domains are in the closed

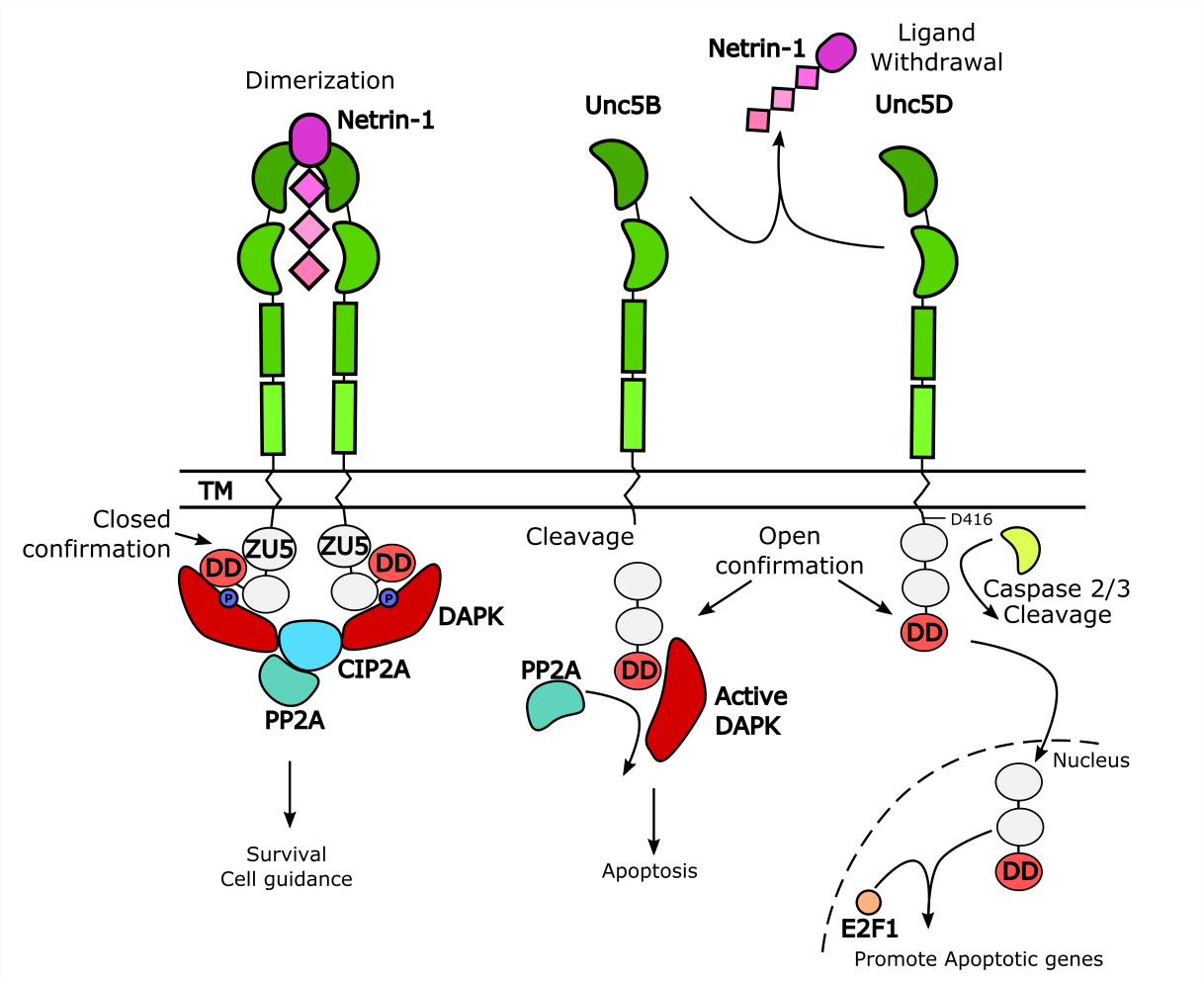


Figure 1.4: Proposed Unc5's dependency receptor mechanism of action. Upon ligand induced dimerization the cytoplasmic domain of Unc5 adopts an autoinhibitory closed state, which associates with DAPK and CIP2A. Upon ligand withdrawal, cleavage occurs, and the cytoplasmic domains adopt an open conformation. Either, activation of DAPK by dephosphorylation through PP2a activates downstream apoptotic signalling, or the cytoplasmic domain translocate to the nucleus where it promotes apoptotic signalling with E2F1. The figure was adapted from Mehlen and Tauszig-Delamasure (2014) [74].

conformation which associates with DAPK, in its phosphorylated state, and CIP2A [86]. Furthermore, the dephosphorylation of DAPK is inhibited by CIP2A [87]. Another mechanism was demonstrated by Zhu and colleagues, where the cleaved cytoplasmic fragment of Unc5D translocate to the nucleus in which it activates apoptotic genes with E2F1 [88].

Unc5 and its interaction with netrin1/DCC

Besides acting as a ligand for Unc5 in dependency, netrin1 is a well-established chemoattractive cue in axon guidance, such as in the migration of commissural spinal cord axons [48, 89]. Commissural neurons cross the midline of the body through a highly orchestrated signalling [90]. Netrin1 induced chemoattraction is through neurons expressing DCC or its paralog neogenin [91, 92]. It had been long believed that netrin1 from the floor plate acted as a long-range guidance cue, however recent findings demonstrated that netrin1 from the floor plate is not necessary [93, 94]; instead neural progenitor cells secrete netrin1 as short-range cues along the migratory path of neurons expressing DCC and its paralog neogenin [95]. When cells express Unc5, the attractive signal is switched to repulsion. The switch can occur by the heterodimerization of Unc5 to DCC, neogenin, down syndrome cell adhesion molecule (DSCAM) [57, 96, 97], or through homodimerization [96]. Indeed, the misexpression of Unc5 in commissural axons was shown to prevent midline crossing by repulsing axons away from the netrin1 source [48].

Crystal structures have revealed how DCC/neogenin may dimerize/cluster upon netrin1 binding. Currently, two models have been proposed by which netrin1 may oligomerize these receptors (figure 1.5). Xu and colleagues solved $DCC^{FN4\text{-}FN5}$ (4PLO) and $neogenin^{FN4\text{-}FN5}$ (PDB 4PLN) in complex with netrin $^{VI\text{-}EGF3}$ (figure 1.5C; model 1)([92]. Finci and colleagues solved $DCC^{FN5\text{-}FN6}$ (PDB 4URT) in complex with $netrin^{VI\text{-}EGF3}$ (figure 1.5D; model 2) [98]. The interaction between EGF3 and FN5 were similar in all structures. Indeed, the crystal structure of draxin, a competitive antagonist for netrin1, with DCC used the same interface (PDB 5Z5K) [99]. The models diverge at their second binding interface. In model 1, netrin's V1 domain interacts with FN4, whilst in model 2 netrin's EGF1 domain interacts with FN5/6. The interaction between the EGF1 and FN5/6 domains are held by hydrophobic interaction and coordinated ions, including chlorine and sulfate. Finci and colleagues suggested that sulfated sugars, such as HS, could facilitate this interaction, as suggested by previous immuno-precipitation experiments [50, 100].

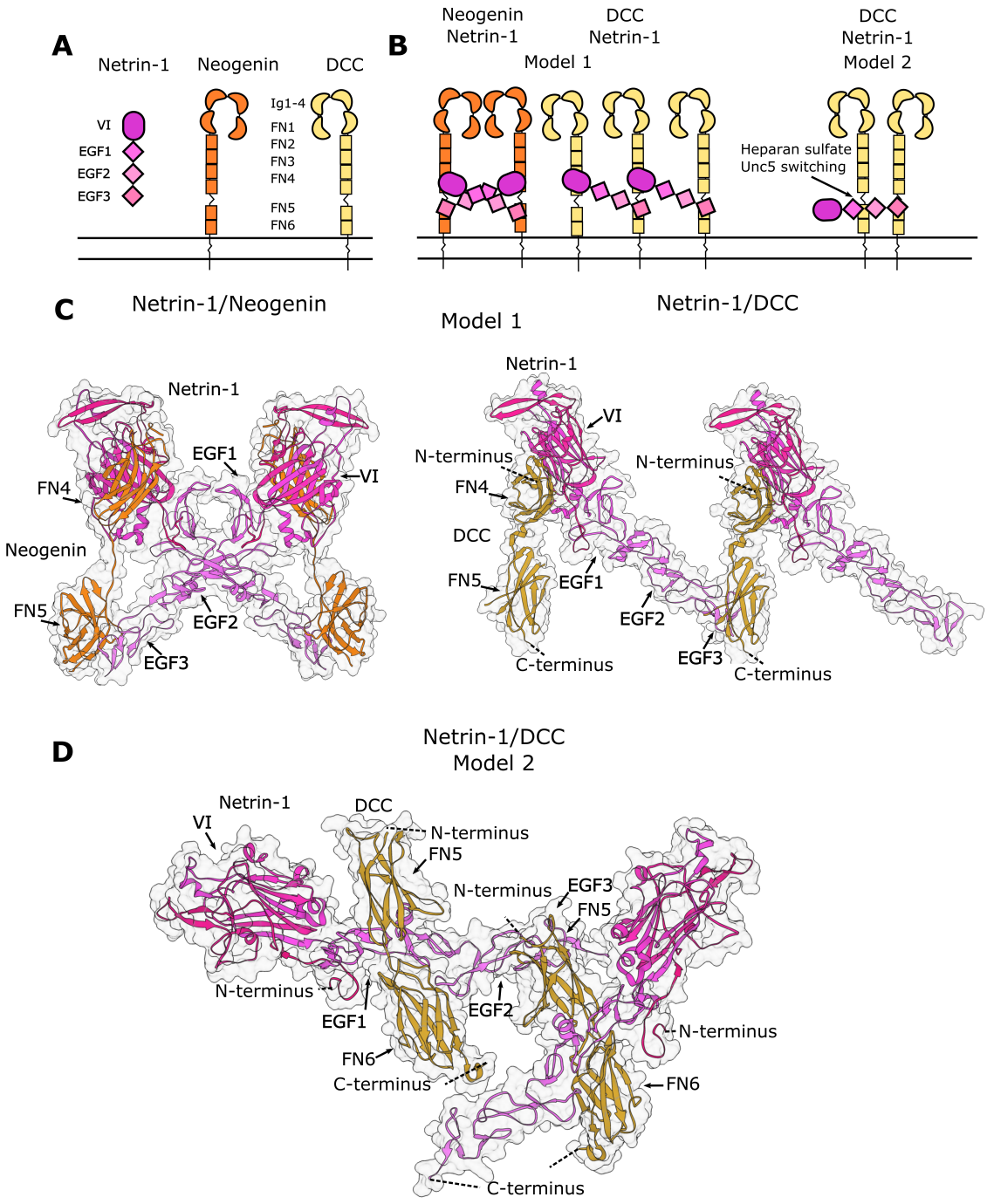


Figure 1.5: Netrin1 oligomerizes DCC and neogenin. A) Schematic representation of netrin1 (pink), neogenin (orange) and DCC (yellow). **B)** Schematic representation of model 1, proposed by Xu and colleagues, and model 2, proposed by Finci and colleagues. **C)** Crystal structure of neogenin$^{FN4/FN5}$ (left) and DCC$^{FN4/FN5}$ (right) in complex with netrin1 (PDB 4PLO and 4PLN). **D)** Crystal structure of DCC$^{FN5/FN6}$ in complex with netrin1 (PDB 4URT). Crystal structures are shown with transparent surfaces and cartoon representation. Colouring of each protein is as follows netrin1 (pink), neogenin (orange) and DCC (yellow). The structures were prepared in Chimera [68].

They proposed that in the presence of a specific HS may switch the homodimerization of DCC to incorporate Unc5 instead.

Unlike netrin1/DCC, there is little structural characterization of the netrin1/Unc5 interaction and how this may be incorporated into the DCC signalling complex. Early research demonstrated that the Ig1 and Ig2 domain of Unc5C were essential for binding with netrin1 [50, 101]. Subsequent research revealed that the netrin1^{EGF2} motif ($R^{348}RCR^{351}$) interacts with the Ig1 domain of Unc5B, which would be the same interface identified in model 2 of netrin1/DCC binding [51]. however, Grandin and colleagues noted that this anti-netrin1 antibody does not disrupt DCC signalling, suggesting that netrin1/Unc5 is spatially unique from the netrin1/DCC binding interface [51].

Unc5 and its interaction with FLRT/Lphn

Mouse genetic analysis of Unc5 family members resulted in several phenotypes that were not observed in netrin1$^{-/-}$ mice, such as retinal vascularization [54] and trochlear and phrenic nerve guidance [102]. These findings suggested to presence of other ligands independent of netrin1 signalling [55]. Indeed, FLRTs were subsequently demonstrated to interact with Unc5 [52, 103]. FLRTs are a single pass transmembrane protein that can act as homophilic adhesion molecule or interact with Unc5 to induce repulsion [104]. FLRTs ectodomain can be cleaved by metalloprotease, which have been shown to be important in the developing brain by inducing growth cone collapse and repulsion [104]. Both hippocampal and cortical neurons were shown to be repelled by FLRT through Unc5 [104]. Structural investigation revealed that both the FLRT/FLRT and FLRT/Unc5 interaction occurs through the FLRT^{LRR} and Unc5D^{Ig1} domains (figure 1.6B; PDB 4V2C). Additionally, this interaction is also important in regulating vascular patterning. Conditional knockout of FLRT results in increased vascular branching, by loss of repulsive guidance cues [54, 61]. Live retinal explants (P5) were incubated with FLRT3 and non-binding Unc5 mutants, in which the wild type significantly

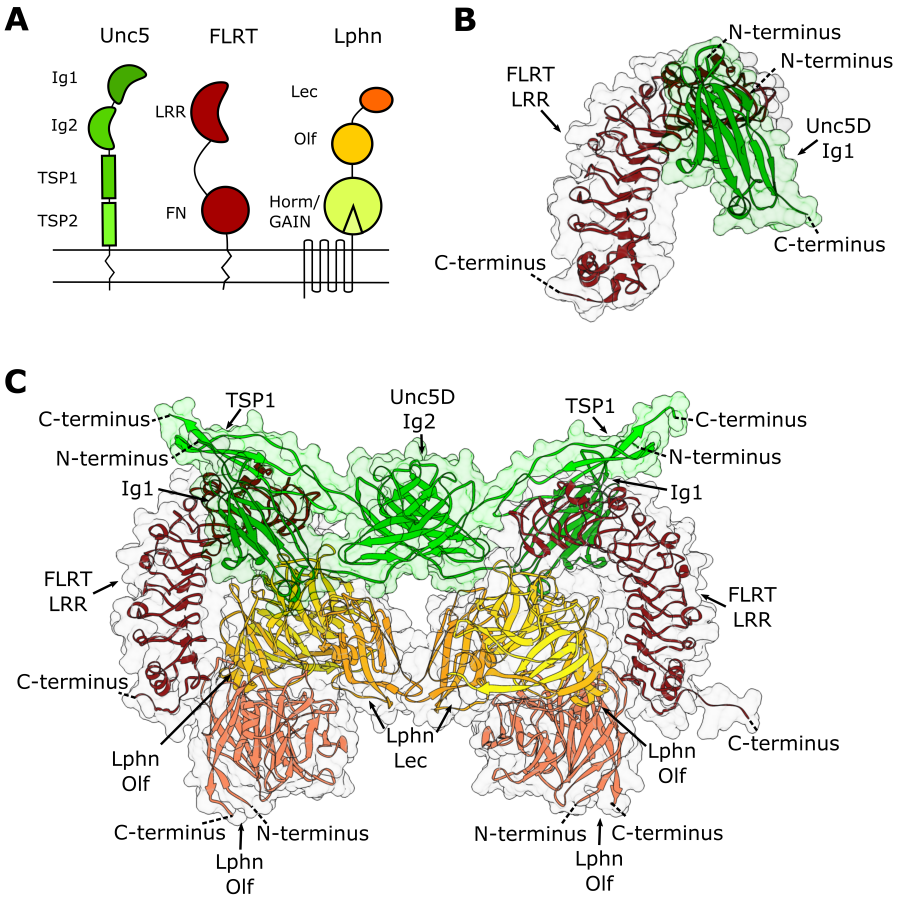


Figure 1.6: Unc5s interaction with FLRT and Lphn. A) Schematic representation of the ectodomains of Unc5 (green), FLRT (red) and Lphn (orange/yelow). **B)** Crystal structure of Unc5D$^{\text{Ig1}}$ in complex with FLRT$^{\text{LRR}}$ (PDB 4V2). **C)** Octameric crystal structure of two copies of Unc5D$^{\text{Ig1-Ig2-TSP1}}$, two copies of FLRT$^{\text{LRR}}$ and four copies of Lphn$^{\text{Lec-Olf}}$. Two copies of Lphn$^{\text{Lec-Olf}}$ did not have an ordered lec domain (copy 2). Crystal structures are shown with transparent surfaces and cartoon representation. Each chain is coloured, Unc5 (green), FLRT (red), Lphn copy 1 (yellow to orange) and Lphn copy 2 (coral). The structures were prepared in Chimera [68].

reduced the presence of filopodia on tip cells compared to the Unc5 mutants, thus inhibiting angiogenesis [54].

FLRTs were also shown to be able to interact with an adhesion G-coupled receptor Lphn. Structural and biological work revealed that FLRT/Unc5/Lphn formed different heteromeric complexes, including a large complex consisting of two Unc5s, two FLRTs and four Lphns (figure 1.6C; PDB 5FTU & 5FTT) [69]. The octameric complex is formed by Unc5's TSP1, which acts as a scaffold between

two tetrameric halves. The stoichiometry of the complex is dependent on the Unc5 homologue, in which Unc5D can form an octamer, while Unc5B only forms a tetramer [69]. It has been suggested that these multiple oligomeric states could expend the signalling capacity of a few receptors, graduating the cellular response [69].

1.2.4 Unc5s role in disease

Unc5 has been associated with neurodegenerative disease and cancer, through the misregulation of apoptosis and migration. A rare Unc5C variant (T835M), near the ZU5-DD interface, predisposes individuals to late-onset Alzheimer's disease [105]. Replication studies in Chinese population identified four SNP of which three were found damaging near the T835M variant (S843G, Q860H and T837K) [106]. In *vitro* experiments found that the Unc5C variant T835M expressing neurons have a significantly shorter survival time, through the activation of DAPK [105]. Alzheimer's disease is the most common chronic neurodegenerative disorder, characterized primarily by memory loss, of which there are limited treatment options[107–109]. Therefore, the identification of therapeutic targets for the treatment of Alzheimer's disease will expand the ability to curb the disease's effects.

Unc5's role in cancer, as both a dependency receptor and a repulsive guidance receptor in migration, correlates with the down regulation of this receptor in most cancers [110]. Conversely, its ligand netrin1 has been shown to be upregulated in several cancer types, such as breast, lung, and liver cancer [111–115]. The role of netrin1 in cancer seems to both inhibit apoptosis but also confer a metastatic phenotype [116–118]. Silencing netrin1 in liver cancer, HepaRG, induces apoptosis, which could be rescued by silencing Unc5 [119]. Therefore, investigators have developed an antibody that inhibits netrin1/Unc5 binding, which results in the induction of apoptosis in several cancer cell lines [51]. Clinical trials are currently ongoing for antibodies against netrin1 [120], further exploration on the role of Unc5 as both a regulator of cell survival and migration may open the field to new therapeutics for cancer treatment.

1.3 The Glypican Family

HSPGs are glycoproteins that contain a variable number of covalently linked HS-GAG chains. There are several families of HSPG, which are secreted into the extracellular matrix, such as perlecan or agrin [121, 122], or are cell surface attached. The two families of cell-surface attached HSPG include the transmembrane syndecans [123], and glycosylphosphatidylinositol- (GPI) anchored glypicans [43].

The glypican family is found throughout the Eumetazoa, a basal animal clade [43]. Vertebrates generally contain six glypicans (GPC1 to GPC6, see table 1). In model organisms, two glypican homologues are found in *Drosophila* (dally and dally-like protein (DLP)) [124, 125], two in C. *elegans* (GPN1 and LON-2) and ten in zebrafish (GPC1-GPC6(a-c)) [126]. The sequence similarity between the glypican family has prompted the suggestion of two broad subfamilies, which consist of GPC 1/2/4/6 and GPC 3/5 [43]. As shown in table 1.2, GPC 1/2/4/6 and GPC 3/5 share a sequence identity of ∼38-64% within the subfamilies, and ∼30% between subfamilies. Interestingly, the *Drosophila* genome consists of a single representative of each subfamily, where dally is an ortholog to glypican 3/5, and DLP is an ortholog to glypican 1/2/4/6.

Table 1.1: Summary of the human glypican family adapted from Filmus et al. [43].

Gene	Protein Name	Locus	Accession	Protein Length (a.a)	Reference
GPC1	glypican-1	2q37.3	NM002081	558	[127]
GPC2	glypican-2	7q22.1	NM152742	579	[128]
GPC3	glypican-3	Xq26	NM004484	580	[129]
GPC4	glypican-4	Xq26.1	NM001448	556	[130]
GPC5	glypican-5	13q32	NM004466.3	572	[131]
GPC6	glypican-6	13q32	NM005708.2	555	[132]

Table 1.2: Percent sequence identity matrix of the human glypican family, Dally and DLP.

	GPC1	GPC2	GPC3	GPC4	GPC5	GPC6	Dally	DLP
GPC1	100	39.3	22.1	43.7	25.6	45.6	23.5	30.7
GPC2		100	19.5	38.5	24.0	41.4	22.0	25.5
GPC3			100	22.3	42.5	24.7	20.5	19.4
GPC4				100	25.7	64.0	22.8	35.7
GPC5					100	27.8	26.	23.5
GPC6						100	23.1	36.4
Dally							100	19.5
DLP								100

1.3.1 Structure of glypican

The glypican protein chain can be divided into a predominantly α-helical core, at the N-terminus, and a predicted disordered stalk region at the C-terminus (figure 1.3) [133]. To date, the crystal structure of human GPC1 (PDB 4YWT & 4ACR; figure 1.3B) and DLP core (PDB 3ODN) have been solved by X-ray crystallography [134–136]. It was hypothesized that the 14 conserved cysteines across the family maintain a three-dimensional structure of the core protein [43]. Superimposing the GPC1 and DLP core structures reveals a similar overall fold with a root-mean-square deviation (RMSD) of 2.7 Å across all atom pairs, even though they only share a sequence identity of 32.97%.

The GPC1 core contains an extended α- helical fold, with an overall cylindrical shape (figure 1.7B; 120 x 30 x 30 Å). The core protein can be subdivided into three components, termed the cys-rich lobe/N-lobe, central lobe/M-lobe, and protease site lobe/C-lobe. The GPC1 structure consist of fourteen α-helices and three major loops. Glypicans contain 14 conserved cysteines, in which 12 are found in the cys-rich lobe. The centre lobe consists of 5 helices, that contain two hydrophobic centres. The protease-lobe, in some glypicans, contains a furin cleavage motif RXXR ($R^{355}QYR^{358}$ in GPC3), on the long disordered loop that spans between helices α11 and α12. Furin processing of the glypican results in the generation of a

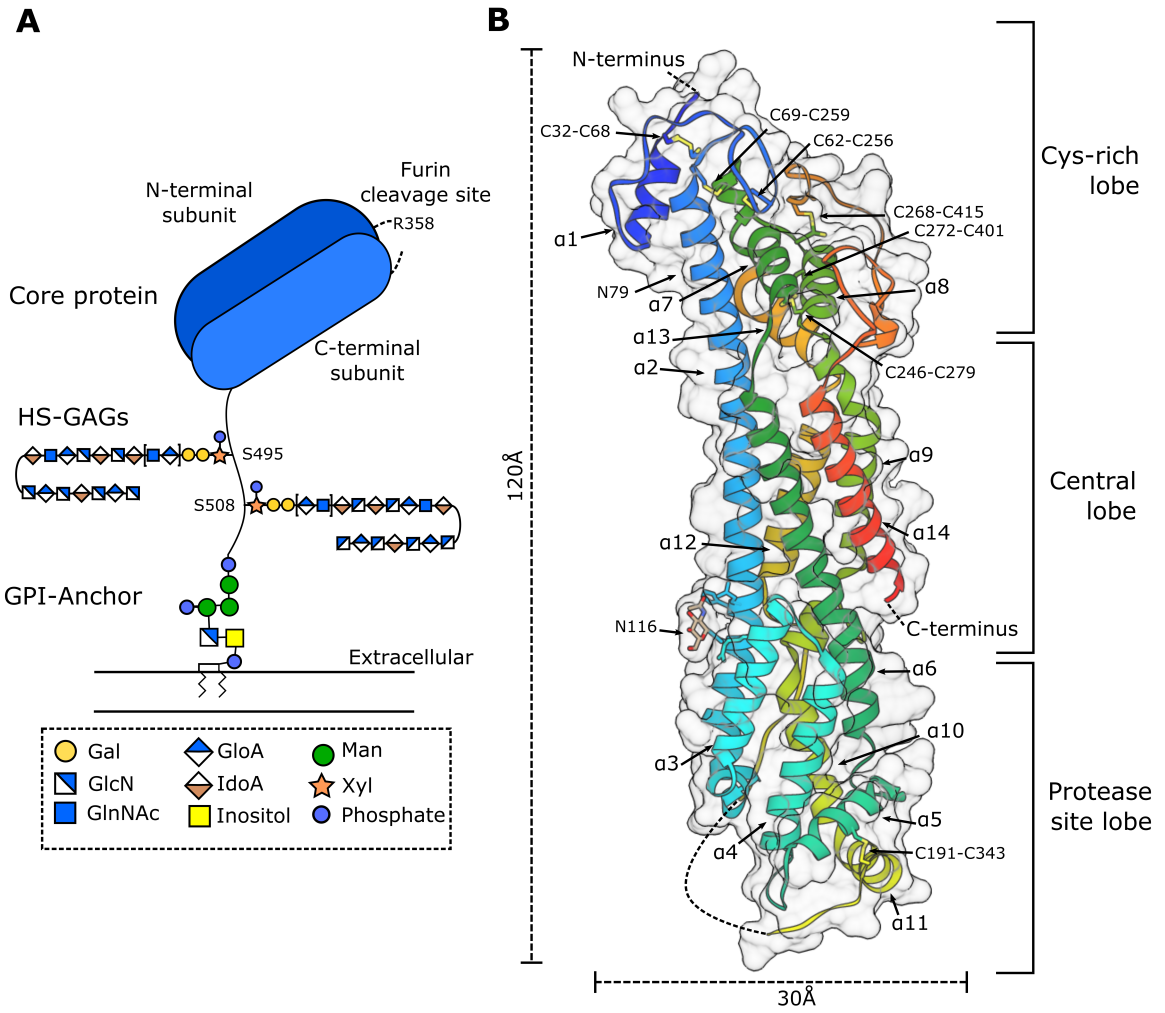


Figure 1.7: Schematic of GPC3 and the crystal structure of GPC1. A) Diagram representation of GPC3, containing a GPI-anchor at the C-terminus, two HS-GAG chains, and a core protein. The core protein is divided in a N-terminal and C-terminal subunit by the furin cleavage at R358. The Glycans are depicted according to privateer glycoblock depiction [137]. The HS-GAGs are according to Weiss et al. (2017) [138]. Abbreviations are Galactose (Gal), Glucosamine (GlcN), N-acetyl glucosamine (GlnNAc), Glucuronic Acid (GloA), Iduronic Acid (IdoA), Manose (Man), and Xylose (Xyl). **B)** Crystal structure of GPC1 (4YWT) core protein is subdivided in three components, the cys-rich, central and protease site lobe. The structure is shown with a transparent surface and cartoon depiction. The colour scheme is according to the rainbow from the N-terminus in blue to the C-terminus in red. The structures were prepared in Chimera [68].

~40 kDa N-terminal subunit and a ~30 KDa C-terminal subunit [139]. however, these two subunits remain covalently linked by two disulfide bonds (C268-C415 and C272-C401). Studies also suggested that GPC1 undergoes proteolytic cleavage by furin [140]. Investigators that solved the GPC1 structure noted that little cleavage

was observed. This may be caused by the lack of a clear furin cleavage motif in GPC1, as predicted by the ProP server [141].

The stalk region is a ∼100 amino acid predicted disordered region [133]. The disordered C-terminus contains a GPI-anchor recognition motif and a homologue dependent variable number of HS-GAG Ser-Gly repeat motif sites [142]. GPC3 contains two Ser-Gly repeat motifs on its stalk region (figure 1.7A). The GPC1 structure was crystallized with part of the C-terminal stalk region (a.a 24-528), missing the GPI-anchor region (a.a 529-558). no No density was observed for residues 473-528, suggesting it to be disordered [134].

1.3.2 S-/N- glycosylation of GPC3

Since the discovery of HSPGs, it has been suggested that their role is to act as an extracellular storage for ligands. Nonetheless, HSPG has other recognized functions, such as forming signalosomes or establishing ligand gradients [143–146]. HS-GAGs themselves are diverse within their sulfation of the sugar backbone, which is modified by N-deacetylase/N-sulfotransferase enzyme [147, 148]. The presence of different sulfation modification enzymes results in a "sugar code" that interacts and modulates different ligands and receptors [143, 149, 150]. For example, Mii and colleagues recently demonstrated that the Wnt morphogens clustered specifically to one subpopulation of HS-GAGs [143].

Modulation of this "sugar code" is regulated by the core protein of the HSPG. Glypicans are covalently attached to HS or, in some cases, chondroitin sulfate (CS) at their repetitive Ser-Gly motif [151]. It has been demonstrated that the core protein of glypican regulates the enzymes involved in HS-/CS-GAG attachment, in which it promotes the preferential attachment of HS-GAGs [152]. Indeed, mutations in the conserved GPC1 core protein loop 3 (between $\alpha 7$ and $\alpha 8$) results in a predominantly CS-GAG attachment [135]. Processing of the glypican core protein, such as Furin cleavage, has been demonstrated to modulate the sulfation of the

HS-GAGs [153]. Therefore, cells can alter their "sugar code" by altering their expression of essential enzymes involved in HS processing, or by expressing different HSPG homologues. Indeed, this may change the cellular context and adjust how the cell responds to signalling molecules.

Besides the HS-GAG attachment, the core protein contains several N-glycosylation sites, which may have a role in the localization of GPI-anchored protein [154]. The GPC1 crystal structure contains three N- glycosylation sites, Asn^{79},Asn^{116} and Asn^{382}, of which Asn^{79} and Asn^{116} are on the second α-helix (Residue 71-130), which spans the whole protein (figure 1.3B). Svensson and colleagues demonstrated that the N-glycosylation is not required for the folding of GPC1 [155], which is in line with the DLP crystal structure which was obtained after mutational disruption of the N-glycosylation sites [136]. Nonetheless, the N-glycans were shown to extend the protein stability and prevent aggregation [134]. It has been reported that N-glycosylation of GPC1 appears to promote proliferation through increasing the responsiveness to fibroblast growth factor-2 (FGF) in turkey myogenic satellite cells [156]; however, the exact mechanism of action of the N-glycans remain unclear.

1.3.3 Molecular mechanisms of signal modulation

Glypicans play a fundamental role during development due to their interactions with different growth factors and morphogens, including Wnt [143, 157–161], Hhs[162–165], BMPs [166–169], and FGF [170–174]. Modulation of these pathways, either stimulatory or inhibitory, is homologue dependent and can be altered by post-translational modification, such as furin cleavage [139]. The HS-GAGs are involved in many of these signalling pathways, but in some cases, the core protein directly contributes to its modulatory role. This thesis will focus on GPC3's role in modulating these signal pathways; however, examples of the physiological functions of the other glypican family members are shown in table 1.3.

Table 1.3: Examples of the developmental function of the glypican family.

Protein	Expression location	Pathway	Descriped role	Reference
GPC1	Progenitor neuronal and glia cells	FGF	Regulating brain size	[170]
	Osteoblast and smooth muscles	BMP	Osteogenesis	[168]
GPC2	brain, spinal cord, dorsal root ganglia and cranial nerves		Maintains immature neurons & migration	[175]
	Adult Hippocampus	FGF2	Dentate granule cell neorogenesis	[176]
GPC3	cardiomyocytes	Shh & FGF9	Cardiac and coronary vascular development	[177]
	reteric bud and collecting duct cells	BMP & FGF	Renal branching morphogenesis	[178]
	hematopoietic lineage cells	Hh	skeletal development & regulates endochondral ossification	[179, 180]
GPC4	Neural precursor cells	wnt3a;	Cortical neurogenesis	[181]
	Secreted by astrocytes	RPTPδ	Exitatory synapse maturation	[182]
	cardiac progenitor cells	wnt3a & BMP	Cardiac cell proliferation and differentiation	[183]
GPC5	Dorsal root ganglia, limb buds and mesonephros	Wnt3a	Onset of mesenchymal transition	[151]
	Hippocampal neurons	LRR-Trans-membrane Neuronal-4 (LRRTM4)	Mediate synapse formation	[184]
GPC6	bone growth plate	Hh	Bone development	[185]
	Astrocytes	RPTPδ	Exitatory synapse maturation	[182]

The role of glypicans as an organ size regulator was initially pioneered by the findings of Pilia and colleagues who identified that the loss-of-function mutations in the GPC3 gene result in the congenital developmental disorder called Simpson-Golabi-Behmel syndrome (SGBS) [186]. SGBS is characterized by pre- and postnatal overgrowth and a broad spectrum of clinical manifestations, including cardiac defects, skeletal defects, enlarged liver, enlarged tongue, supernumerary nipples and polydactyly [187–189]. A recent meta-analysis of the mutations found in the GPC3 gene shows that many of the mutations result in frameshifts or deletions of large regions of the gene. The few point mutations found often resulted in a premature stop codon, while only several rare missense mutations have been identified [190]. These rare missense mutations were identified to be structurally important and most likely result in improper folding and/or secretion [191]. For example, the missense mutant, W296R, was not cell surface expressed because it could not be processed correctly [191]. Another missense mutant, G556R, was shown to prevent GPI-tethering to the cell surface, consequently affecting GPC3 signal modulation function [192]. Studies in $GPC3^{-/-}$ mice display many of the clinical manifestations observed in SGBS [193, 194].

The expression of the glypican homologues is broad during development, and all except GPC3 have been found expressed and functioning in the developing nervous system. In *situ* hybridization in mouse embryo, age E6.5-18.5, revealed high levels of GPC3 expression, with peak expression at E11.5-14.5 [195]. GPC3 expression was identified in the mesoderm-derived tissue (myocardium, cartilage and bone), endoderm (tongue forming tissue), limb buds, developing liver and lungs; however, no expression was found in the nervous system. A subsequent study that used immunohistochemistry (IHC) on human tissue (foetal periods P1-P4, weeks 5 to 28) had similar findings of GPC3 expression, except that GPC3 was identified in the spinal cord motoneurons and dorsal root ganglia neurons [196]. The presence of GPC3 in the motoneurons and dorsal root ganglia may have clinical significance because SGBS patients present with hypotonia and have an increased risk for developing neuroblastomas [197, 198]. In addition, ISH data from the Allen brain

atlas also indicated to postnatal expression of GPC3 in the developing mouse brain [199]. Specifically, GPC3 can be observed in the ventral CA1 of the hippocampus and the ventral subiculum (postnatal age P4 to 56).

GPC3 in Wnt and Hh signalling

GPC3 has been extensively studied for its role in Wnt and Hh signalling. Wnt and Hh signalling are conserved developmental morphogen pathways [200–203]. Briefly, the activation of Wnt receptor produces a downstream of the canonical Wnt/β-catenin or β-catenin-independent pathways [204]. Canonical Wnt signalling occurs when the Wnt ligand binds to the cysteine-rich domain (CRD) of the frizzled receptor and heterodimerizes it with low-density lipoprotein receptor-related 5 and 6 (LRP5/6) [205]. Hh signalling includes three secreted Hh ligands, of which Sonic Hedgehog (Shh) is widely expressed and the most studied. During signal transduction, the Hh ligand binds to the receptor patched (Ptch1/2), which prevents it from inhibiting the transmembrane protein smoothened (SMO) [206].

In Wnt signalling, GPC3 contributes to the formation of the frizzled/Wnt complex by interacting with the CRD through its HS-GAGs [158], and Wnt through its core protein [207], stabilising the complex. The HS-GAG in GPC6 are unable to interact with the frizzled, resulting in inhibition [158]. It has been proposed that the cys-rich domain shares minimal structural similarity to the frizzled CRD domain [43, 208]. Experiments have demonstrated that the Wnt signalling complex is internalized by clathrin-mediated endocytosis and is essential for signalling [209–212]. Capurro and colleagues demonstrated that GPC3 was endocytosed along with Wnt–frizzled–LRP complex [158]. Another proposed mechanism by which glypican can modulate Wnt signalling is by the recent findings of Kakugawa and colleagues [161]. Inhibition of the Wnt signalling was suggested to occur through the cleavage of the GPI-anchor of GPC3 through notum [213–216]. In *drosophillia*, notum is a negative regulator of Wnt by removing an acyl group through its carboxylesterase activity. This acyl group directly contributes to receptor binding [217]. Kakugawa and

colleagues demonstrated that Dally and DLP are not shedded from cell extracts by notum. Interestingly, notum contains a highly charged surface patch that could bind HS-GAGS, allowing the colocalization of notum to Wnt, through glypican.

GPC3 can negatively modulate Hh signalling through competing with Ptch for Hh binding. Hh is able to bind with a high affinity to the core protein of GPC3, in which the HS chains are not essential but facilitate binding [163]. In contrast, GPC5 has been shown to increase the affinity of Hh to its Ptch receptor through its HS-GAG chains by being able to interact with both Hh and Ptch [153, 218]. One explanation proposed has been the observation that GPC5 display a higher degree of sulfation than that of GPC3 [218]. Further investigation revealed that GPC3 inhibition of Hh is dependent on furin processing and that the GPC3 mutant (R355A R358A) was able to interact with both Hh and Ptch. This was explained by the unprocessed GPC3 having higher sulfation on their HS-GAG chains, compared to the wild-type [153]. Another proposed mechanism in which GPC3 may downregulate Hh signalling occurs after the binding of Hh to GPC3. Investigators have demonstrated that GPC3 is predominately localized outside lipid rafts, and when Ssh binds to GPC3, it results in the recruitment of LRP1 and the subsequent clathrin-mediated endocytosis of the Hh/GPC3/LRP1 complex [219].

Like Wnt, Hh is extensively post-translationally modified, which regulates their spread and function [220–223]. Lipid modification of the Hh ligand has been shown to cause the retention of Hh at the plasma membrane [224, 225], but it also has been shown to be essential in long distance signalling [226]. Release of Hh from the cell membrane is facilitated by dispatched, which allows a secreted glycoprotein to bind and solubilising it as a monomer [227, 228]. Glypicans involvement in Hh secretion has been demonstrated by the colocalization and clustering of Hh at the cell surface and the recruitment of circulating lipoproteins for transport [229, 230]. Hh inability to transverse HSPG depleted cells in *Drosophilia* imaginal discs demonstrates HSPG facilitated planar diffusion of neighbouring cells [231, 232].

1.3.4 GPC3 role in cancer

The diagnostic and therapeutic potential of glypicans have come to light in recent years. GPC3 is upregulated in several different malignancies, in which its involvement in hepatocellular carcinoma (HCC) has been extensively studied [207, 233–241]. Recent data from GLOBOCAN 2018 predicts liver cancer, of which 75-85% of cases are HCC, to be the sixth most commonly diagnosed cancer and fourth leading cause of cancer death worldwide [242]. Most cases of HCC are identified in developing countries, of which the main risk factor remains chronic infection of hepatitis B or C virus [243]. Nonetheless, the upward trend in liver cancer diagnoses in developed countries has been attributed to the growing rate of obesity [244, 245]. Due to its high mortality rate, biomarkers for early detection or new therapeutic targets are highly sought after.

Meta-analysis of a cohort of studies indicated that surveillance and early detection of HCC had a significant improvement in overall survival [246]. α-fetoprotein (AFP) is a common biomarker for the screening of HCC; however, there remain disputes over its effectiveness due to its high rate of false positives [247–249]. Therefore, the identification of new biomarkers that can be used in combination with AFP may improve the early detection of HCC and lower the false positive rate. GPC3 has been proposed to be an ideal candidate for the detection of HCC, as GPC3 expression has been observed in 70-80% of HCC [250], of which it has been reported that 48.8% of GPC3 were AFP negative, potentially reducing false positives [251].

A recent meta-analysis of the research into GPC3 expression in HCC has shown a poorer prognosis in patients, caused by various features of the tumour cells, such as worse differentiation, later stages, and presence of vascular invasion [233]. As presented above, the developmental role of GPC3 is through its activation or inhibition of several signalling pathways. Extensive studies have shown that GPC3 modulates the Wnt/β-catenin and TFG-β/BMP signal pathways, promoting growth and invasion [207, 234–241]. Therefore, several research groups set out to

develop treatment alternative, such as therapeutic antibodies or antibody fragments that could disrupt the GPC3 modulatory function [252]. The IgG antibodies YP7 (epitope a.a 511-560) and GC33 (epitope a.a 524-563) both target the disordered C-terminal trunk and have shown anti-cancer properties through antibody-dependent cell cytotoxicity [253–257]. In recent years, the development of the antibody fragment (VH-hFc), HN3, which has intrinsic disruptive ability by binding to the core region of GPC3 [258]. Upon binding, HN3 inhibits the GPC3 activation of the Wnt pathway, reducing proliferation and invasiveness of HCC [258, 259]. Knockdown or inhibition of GPC3 is not in itself fatal to the cancer cell; therefore, researchers linked an immunotoxin to the HN3 fragment, providing dual inhibition in liver cancer [259].

Pleiotropic mechanisms in which GPC3 modulates tissue behaviour are observed in breast cancer. GPC3 is normally expressed in adult mammary tissue; however, in breast cancer GPC3 is downregulated [260]. In *vitro* experiments demonstrated that re-expression of GPC3 resulted in a reduction in invasion and proliferation of the cancer cell line [261]. Conversely, GPC3 silencing is correlated to a more aggressive form of breast cancer where it induces EMT [261]. The exact molecular mechanism is still not fully understood, although a study has shown that in breast cancer cell lines, the application of Shh results in a decrease of surface GPC3, suggesting that it is endocytosed with Shh [219].

1.4 Project Aims

Both GPC3 and Unc5 interact through several different pathways to elicit cell context specific responses. The newly discovered interaction between this glycoprotein and cell guidance receptor poses questions regarding its biological significance. To study this interaction, the molecular basis of this interaction needs to be deciphered, so that appropriate non-binding mutants can be designed. Therefore, the aim of my D.Phil. is to understand the molecular mechanisms involved in the GPC3/Unc5 interaction by solving the X-ray crystal structure of this protein complex. The work presented in this thesis would present the first structural insight into the GPC3/Unc5 protein complex. To solve the X-ray crystal structure of the protein complex and understand the molecular basis of the GPC3/Unc5 interaction, this thesis aims to accomplish the following objectives:

- Confirm the interaction between the core protein of GPC3 and ectodomains of Unc5, using biophysical and cellular assays;
- Solve the crystal structure of the core protein of GPC3, in order to use it in solving the crystal structure of the GPC3/Unc5 protein complex;
- Solve the crystal structure of the core protein of GPC3 in complex with the ectodomains of Unc5;
- Biophysically characterize the GPC3/Unc5 interaction and design mutants for further functional studies.

2

Materials and Methods

2.1 Molecular Biology and Cloning

2.1.1 Genes and constructs

All constructs used in this thesis were subcloned from cDNAs obtained from the from the mammalian gene collection [262], and are summarized in table 2.1. For recombinant protein expression, protein constructs were cloned into the high-level mammalian expression vector, pHlSec (Addgene plasmid #99845) [263]. This vector consists of a secretory N-terminal signal peptide derived from receptor-type tyrosine-protein phosphatase S and a C-terminal hexahistidine tag. Constructs were fused to these two features through the AgeI/KpnI restriction sites. In some cases, the original signal peptide of the protein was used, and so constructs were cloned into the vector with the EcoRI/KpnI restriction sites. An Avitag variant of the pHlSec vector was used for in biotinylation (S2.2.4). The Avitag variant, at the C-terminus, contains a flexible GSSGSS linker, a biotin ligase (BirA) recognition site and a hexahistidine tag. The mVenus variant contains a C-terminal yellow fluorescent protein (mVenus) [264], which is predominantly used for the visualization of cells expressing a membrane protein, such as Unc5. All the constructs that were cloned previously and as a result of this thesis are summarized in appendix A.1 and A.2, respectively.

Table 2.1: Summary of cDNAs used for sub-cloning. The accession numbers refers to the protein-product of the cDNA.

Protein	Species	Accession
Unc5A	*Homo sapiens*	BC167811.1
Unc5B	*Homo sapiens*	XR_945617.1
	Mus musculus	NM_029770
Unc5D	*rattus norvegicus*	NM_001107319.2
GPC3	*Homo sapiens*	AAH35972.1
	Mus musculus	NP_057906.2

2.1.2 Molecular cloning

For the purpose of this thesis, subcloning was performed using the In-Fusion™ HD cloning kit (Takara). In-Fusion uses a vaccinia virus DNA polymerase with an intrinsic exonuclease activity [265, 266]. The exonuclease activity exposes single-stranded DNA tails which allows for the recombination of complementary DNA sequences, similar to the Gibson assembly. Primers were designed according to the manufacturer's instruction and are summarized in the appendix A.2. Typically, the 3' end of the primers has a ∼25 bases sequence that anneals to the target gene, and at the 5' end of the primer a 15 bases overlap sequence with the vector. Mutagenesis was performed by inserting the change in bases between the annealing and overlap regions.

To expose the overlap regions for subsequent recombination, pHlSec vectors were linearized by restriction digestion. Restriction digestion was typically performed using 6 μg vector plasmid and 2 units of each restriction enzymes (NEB) in their appropiate NEBuffer (NEB). Reactions were incubated for 3 hours at 37 °C. The gene of interest were amplified using the CloneAmp HiFi PCR Premix (Takara-Bio, Clonetech) according to the manufacturer's instructions. After PCR and restriction digestion, the DNA product were mixed with 6X DNA loading dye (Thermofisher) and loaded into an agarose gel of 0.8% to 1.2% in TAE buffer (40 mM Tris base, 20 mM acetic acid, 1 mM EDTA). The DNA products were electrophoresed at 150 V for 30 to 60 minutes. DNA Bands were visualized using SYBR™ safe DNA gel Stain (Invitrogen) through a Dark Reader blue light transilluminator (ISS). The PCR products and restriction digested plasmids were extracted and purified using the NucleoSpin Gel and PCR Clean-up kit (Machery-Nagel), according to the manufacturer's instructions. In-Fusion™ premix (Takara) was added to 50 ng of PCR insert and 50 ng of vector on ice. The final mix was adjusted to 5 μl with ice cold milliQ water and subsequently incubated at 55 °C for 15 minutes.

The reaction mixtures was transformed into Stellar chemically competent cells (*E. coli* HST08) (Takara) according to the manufacturer's instructions. Transformed cells were plated on Lysogeny broth (LB)-agar plates containing 100 μg/ml ampicillin and grown overnight at 37 °C in a static incubator. Single colonies were picked and grown in 5 *ml* of LB media containing 100 μg/ml ampicillin. Cultures were incubated at 37 °C overnight while shaking. Plasmid DNA was isolated using the miniprep kit (Qiagen), as according to the manufacturer's instructions. The purified DNA plasmids were sequenced and verified by Sanger Sequencing (Source Biosciences, Nottingham, UK). In the case of purified plasmids, sub-cloning-efficiency chemically competent DH5α cells (Life Technologies) were used instead.

2.2 Protein Expression and Purification

2.2.1 Cell lines

All protein expression was performed in adherent HEK293 cell lines. Eukaryotic expression systems utilize protein glycosylation for direct the proper folding of proteins. N-glycosylations, the addition of oligosaccharides to asparagine through the Asn-X-Ser/Thr motif, is extensively diversified in the Golgi apparatus resulting in a heterogenous populations. The heterogenous glycosylation may hinder downstream biophysical characterizations, such as in crystallization [267]. To prevent N-glycosylation diversification, protein was expressed either in HEK293T treated with kifunensine or N-acetylglucosaminiltransferease I (GNTI$^-$) HEK293S cells. Kifunensine is a α-mannosidase I inhibitor, which inhibits the trimming of the oligomannose chain, resulting in oligomannose-type N-glycans ($Man_{5\text{-}9}GlcNAc_2$) [267, 268]. The GNTI$^-$ HEK293S cell lines are unable to process the N-glycosylation lacking GNTI, resulting in a predominantly $Man_5GlcNAc_2$ N-linked glycans (figure 2.1) [267, 269].

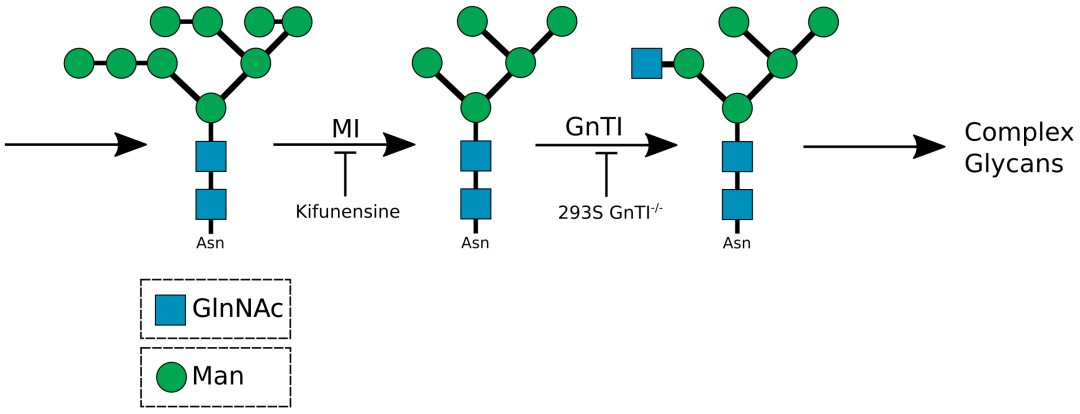


Figure 2.1: Inhibiting N-glycosylation maturation. N-Acetylglucosamine (GlnNAc) is depicted as a blue square and Mannose (Man) is depicted as a green circle. The N-glycosylation maturation involves the trimming of mannose by α-mannosidase I (MI), which is inhibited by kifunensine. N-acetylglucosaminyltransferase I (GnTI) adds a GlnNAc, which allows for further complex glycosylation. In HEK293S cells lack GnTI and thus are unable to produce complex glycans. Image was adapted from Chang et al. (2007) [267].

2.2.2 Mammalian cell culture maintenance

Mammalian cells were maintained in T75 flasks (Greiner-Bio) with 12 *ml* of Dulbecco's modified eagle's medium (Sigma) supplemented with 1% non-essential amino acids (Gibco) and 1% L-glutamine (Gibco) referred to as supplemented DMEM. For cell maintenance, 10% foetal bovine serum (FBS; Gibco) was added to supplemented DMEM. Cells were grown to 90% confluency at 37 °C in a 5% CO_2 atmosphere. Once 90% confluency was reached the cells were subcultured, approximately every 2-3 days. Subculturing of cells were done by aspirating the media of the cells. The cells were gently washed with 10 ml of phosphate buffer saline (PBS; Lonza). Cells were enzymatically detached with 2 *ml* 0.05% trypsin-EDTA (Gibco) for 4 minutes at 37 °C. The detached cells were resuspended in pre-warmed fresh media and seeded into a new flask or plate at the required density.

2.2.3 Small-scale transient transfection

HEK293T cell lines were used in the small-scale expression, for the purpose of biotinylation and cell binding assays. Cells were seeded into a 6-well plate and grown at 37 °C in a 5% CO_2 atmosphere for 24 hours. For transfection, 3 μg plasmid DNA was diluted into 50 μl of OptiMEM (Gibco) and 9 μg of Polyethylenimine (PEI) (Sigma) or Fugene6 (Promega) was diluted in another sterile eppendorf containing 50 μl of OptiMEM. The PEI/Fugene6 solution was mixed with the DNA and incubated for 10 minutes. The transfection cocktail was added to the sides of the well plates and carefully mixed. Cells were then grown at 37 °C in a 5% CO_2 atmosphere for either 3 days, in the case of secreted proteins, or 1 day, in the case of membrane protein expression. In the case of secreted expression, the media was harvested and centrifuged at 15000 g for 5 minutes to remove any cell debris.

2.2.4 Protein biotinylation

Protein biotinylation was carried out using Avitag protein constructs [270]. The Avitag sequence (GLDNIFEAQKIEWHE) is recognized by BirA which covalently links biotin to the lysine in the Avitag sequence. Similar to small-scale expression, cells were seeded into a 6-well plate. After 24 hours, the cells were co-transfected with 3 μg of the protein of interest plasmid DNA and 1 μg of plasmid DNA encoding BirA, allowing for biotinylation to occur in cells. The BirA gene is fused to a endoplasmic reticulum retention signal peptide. 12 μg of PEI (Sigma) or Fugene6 (Promega) was used to prepare the transfection cocktail. Media were supplemented with sterile filtered 100 mM biotin. After expression, the conditioned medium was harvested and dialysed against PBS at 4 °C for immobilization or used for detection by Western blotting.

2.2.5 Large-scale protein expression

HEK293T or HEK293S cells were scaled up to T175 flasks (Greiner-Bio) and allowed to grow to confluency. Grooved roller bottles (CELLMASTER; Greiner-Bio) were prepared with 250 ml of supllemented DMEM with 10% FBS and seeded with cells (one flask per bottle). Roller bottles were incubated at 37 °C in roller bottle incubator (Wheaton) for 3 days, in the case of HEK293T, or 4 days, in the case of HEK293S. Transient transfection was performed using DNA prepared from Gigapreps (Invitrogen), according to the manufacturer's instructions. Purified DNA was sterilized by adding 100 μl of chloroform to 1 ml of DNA and mixed by inverting and briefly vortexing. The DNA was centrifuged at 20,0000 g for 10 minutes. A transfection cocktail was prepared consisting of 0.5 mg DNA with 1 mg of PEI in 50 ml serum-free supplemented DMEM, per bottle. The transfection cocktail was prepared by mixing the appropriate amount of DNA serum-free supplemented DMEM. PEI was added to the mixture and incubated for 10 minutes at room temperature. In the case of HEK293T transfection, 0.38 mg per bottle of kifunensine was added to the transfection cocktail. The medium from the roller bottles was decanted and replaced with 200 ml of supplemented DMEM with 2% FBS and 50 ml of transfection cocktail. After transfection, cells were allowed to grow for 4 days for HEK293T, or 10 days in the case of HEK293S cells. Media from bottles were harvested, centrifuged at 6000 g for 20 minutes, and subsequently filtered using a 0.22 μm sterile filter (Millipore, Merck).

2.2.6 Protein purification

Recombinant protein expression medium was concentrated, and buffer exchanged into diafiltration buffer (20 mM Tris (pH 7.5), 100 mM NaCl, 137 mM Phosphate-buffered Saline) using a tangential flow filtration device (Pall). The medium was loaded onto a 5 ml HisTrap FF column (GE Healthcare). The column was washed with 200 ml wash buffer (20 mM Tris-HCl (pH 7.5), 300 mM NaCl, 40 mM

Imidazole). Protein was eluted as 1 *ml* fractions using elution buffer (20 *mM* Tris-HCl (pH 7.5), 300 *mM* NaCl, 500 *mM* Imidazole). Fractions were selected using Bradford protein assay and subsequently used for size-exclusion chromatography (SEC). Before loading the protein for SEC, a superdex 200 16/60 HiLoad column (GE Healthcare) was equilibriated with SEC buffer (10 *mM* Tris (pH 7.5), 200 *mM* NaCl). Fractions of 1.5 *ml* were collected and the peak fractions were analysed by denaturing polyacrylamide gel electrophoresis (SDS-PAGE).

2.2.7 SDS-PAGE and western blotting

Samples were mixed with either non-reducing 6x SDS-loading dye (375 *mM* Tris-HCL pH 6.8, 6% SDS, 48% glycerol, 0.03% bromophenol blue), or with 6X SDS-loading dye containing 5% β-mercaptoethanol for a reducing SDS-PAGE. The samples were then boiled for 5 minutes at 95 °C. Samples were run on a gradient NuPAGE® 4-12% Bis-Tris Gels with NuPAGE® MES running buffer (Invitrogen), in a XCell *surelock*™ Mini-Cell. The gels were run at 180 V for 5 minutes and subsequently at 150 V for 45 minutes. Gels were stained with InstantBlue™ (Sigma) for visualization of purified protein.

For western blotting, protein from an SDS-PAGE gel were transferred onto a nitrocellulose membrane (GE Healthcare) according to the NuPage® XCellII™ Blot module manufacturer's setup. NuPAGE® Transfer Buffer was prepared with 20% ethanol. The transfer was performed with a constant voltage of 30 V for 70 minutes.

The nitrocellulose membrane was blocked for 1 hour with PBST (PBS and 0.1% Tween-20) with 3% Bovine Serum Albumin (BSA; Sigma) or 5% non-fat milk powder (Oxoid). Primary antibody, 1:1000 anti-His (Mouse; Qiagen) were diluted in PBST (PBS and 0.1% Tween-20) with 3% BSA and incubated with the membrane for 1 hour at room temperature or overnight at 4 °C. The membrane was subsequently washed three times for for 10 minutes with PBST. Then the membrane was incubated with a horse radish peroxidase (HRP) conjugated secondary antibody, anti-mouse (Goat;

Sigma) were diluted in PBST (1:10,000) with 3% BSA and incubated with the membrane for 60 minutes. The membrane was washed three times for 10 minutes with PBST. Excess PBST was removed and the membrane was incubated with Amersham^{TM}ECL^{TM} Western Blotting Detection Kit (GE Healthcare) for 2 minutes. The membrane was visualized with Amersham Hyperfilm ^{TM}.

2.3 Cell Biology

2.3.1 Cell-binding assay

HEK293T cells were seeded into 6-well plates containing coverslips. After 18 hours, cells were transfected with the gene of interest fused to the C-terminal mVenus (S2.2.3). 24 hours after transfection, coverslips were gently moved to an ice-cold surface. Cells were incubated with ice-cold Hank's balanced salt solution supplemented with 1% BSA and 20 *mM* Hepes (pH 7.5) for 30 minutes. A mixture of 200 *nM* or 500 *nM* of *mm*GPC3$^{\Delta C}$, or *mm*FLRT^{LRR} was prepared with mouse primary anti-His antibodies (Qiagen) in a 2:1 molar protein-to-antibody ratio and incubated for 30 minutes. A no protein control was prepared with the same concentration of antibodies as its protein equivalent. The protein-antibody mixture was gently added to the cells and incubated for 60 minutes on ice. The cells were washed twice with ice-cold PBS and subsequently fixed with ice-cold 4% paraformaldehyde for 20 minutes. Paraformaldehyde was quenched with ice-cold PBS containing 20 *mM* ammonia chloride (Acros Organics) and subsequently washed with ice-cold PBS. Cy3-conjugated anti-mouse antibodies (Thermofisher; 1:400) were added to the cells and incubated for 60 minutes at room temperature. The cells were washed twice with PBS, and then incubated with 350 *nM* DAPI solution in PBS for 2 minutes. Then cells were washed with PBS and MiliQ water before mounting the coverslips on glass slides with Immu-mount^{TM} (Invitrogen).

2.4 Biophysical Methods

2.4.1 Surface plasmon resonance

Surface plasmon resonance (SPR) was used to measure the label-free protein-protein interactions in liquids [271]. The SPR experiment involves the characteristics of the plasmon resonance phenomenon, in which the matching of the angle of incidence (θ) above a critical angle results in the total internal reflection which produces an electromagnetic surface plasmon. The electromagnetic surface plasmon has a characteristic drop in light intensity that can be used as a readout for the adjustment of the angle of incidence. Binding of an analyte results in a change in refractive index at the flow cell and so the angle of incidence must be adjusted. The change in angle is measured in an arbitrary response unit (RUs).

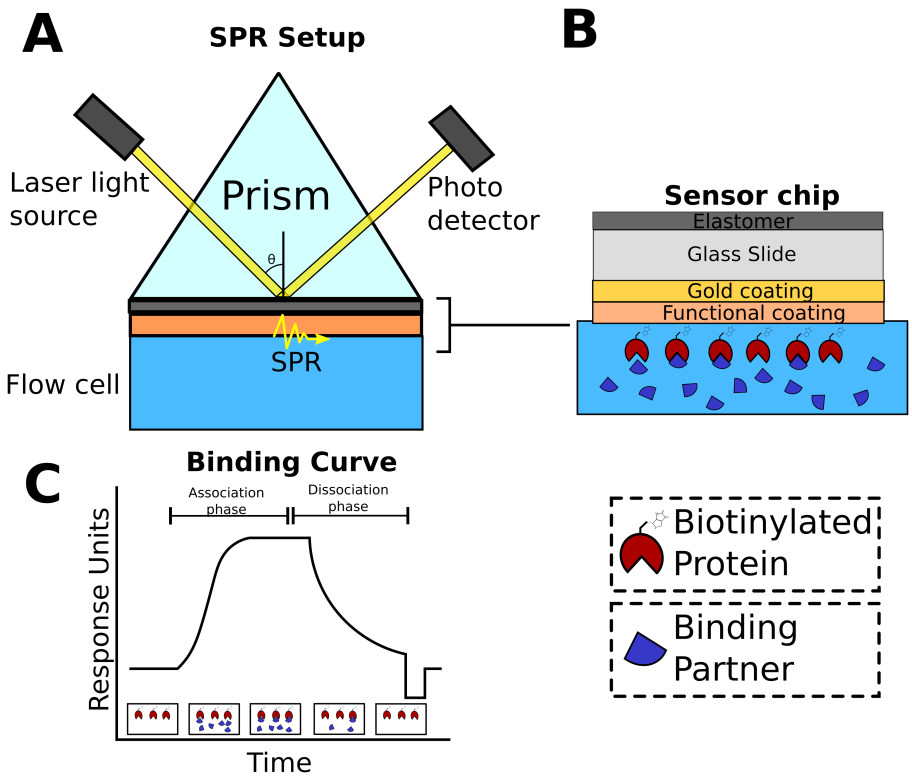


Figure 2.2: Surface plasmon resonance setup. The reflection of a laser light above a critical angle (Θ) results in an SPR **(A)**. Protein that binds to interface bound biotinylated protein results in an increase in refractive index **(B)**. The change in refractive index requires a change in angle (Θ), which is recorded as response units (RU) **(C)**.

During a SPR experiment, at the gold layer-flow cell medium interface, immobilized protein can freely interact with components in the flow cell (figure 2.2B). The SPR experiments in this thesis used biotinylated protein for immobilization, because it controls the directional attachment of the protein to the chip. CM5 chips (GE healthcare) were coated with streptavidin via amine coupling (GE Healthcare Kit). The streptavidin coated chips were flown over with biotinylated protein until a density of 500-1000 RU was achieved. To determine relative binding, a single concentration of analyte is flown over the flowcells with different protein constructs. To determine the equilibrium dissociation constant (K_D), a dilution series was prepared of the analyte and flown over the chip. The analyte was injected for 300-500 seconds, followed by 100 seconds of dissociation time. The chips were fully dissociated of its analyte using 2 M $MgCl_2$ for 30 seconds. The flow rate was set at 5 μl/min with a running buffer of PBST (PBS + 0.005% Tween-20) at 25 °C. SPR experiments were performed by Prof. Elena Seirdake.

The specific binding coefficient was determined by subtracting the control flow cell (streptavidin only flow cell) against the experimental flow cell (biotinylated bound flow cell). The interaction overtime when the analyte (A) is flown over the ligand (B) is described in equation 2.1 and shown in figure 2.2C.

$$\frac{d[AB]}{d_t} = Ka[A]_t[B]_t - Kd[AB]_t \tag{2.1}$$

The response (R_t) is proportional to the formation of complex ($[AB]_t$), and B_{max} is propertional to R_{max}. The one-to-one Langmuir interaction model was used to determine the K_D and B_{max}. Equation 2.2 presents the response over time, in which K_D and R_{max} can be derived. Data was analysed using BIAevaluation software 1.0 (GE Healthcare) and Prism 7 (Graphpad).

$$R_t = \frac{R_{max}[A]}{K_D + [A]}[1 - e^{-(Ka[A]+Kd)t}] \tag{2.2}$$

2.4.2 Size-exclusion chromatography multi-angle light scatter

Size-exclusion chromatography multi-angle light scatter (SEC-MALS) combines the separation of polydisperse samples by a SEC column and a series of detectors to elucidate the molecular weights and root mean square radius of the macromolecule. When a laser beam illuminates a macromolecule, the oscillating electromagnetic wave induces an oscillation of a local dipole moment. As a result, the oscillating electrons of the molecule emit electromagnetic radiation, known as scattering. The intensity of the scattered light is dependent on the magnitude of the dipole induced, which is proportional to the molecular weight of the protein. The formation of dimers or complexes can be observed by the change in scattered intensity. When a macromolecule is present as a monomer in solution, the monomers are subject to random Brownian motion which would result in the scattered light to be incoherent in phase. In the case of an interaction, the two macromolecules will move in relation to each other allowing the scattered light to be coherent, and the resulting intensity would be amplified.

For SEC MALS, *mm*GPC3$^{\Delta C}$ at 1 mg/ml and a one-to-one molar ratio mixture of *mm*GPC3$^{\Delta C}$ with *rn*Unc5D$^{\text{Ig1-Ig2-TSP1}}$ at 5 mg/ml were injected onto a Superose 6 10/30 column (GE Healthcare) by Dr David Staunton (Molecular Biophysics Suite, Biochemistry Department Oxford). The column was initially equilibrated with 10 *mM* Tris-HCl (pH 7.5) and 200 *mM* NaCl. Data was collected using the Heleos 8 instrument (Wyatt Optilab) at 662 *nm* at angles between 20.6° and 149.1°, the rEX refractive index monitor (Wyatt Optilab) and the SPD20A UV/Vis detector. Data was analysed using ASTRA 6.1 software (Wyatt Technology).

2.4.3 Cross-linking mass spectrometry

Chemical crosslinking mass spectrometry (XL-MS) provides structural information which is complimentary to X-ray crystallography [272]. A chemical crosslinker connects two functional groups together, dependent on the type of crosslinker. For example, Nhydroxysuccinimide esters, such as bis(sulfosuccinimidyl)suberate (BS3) and disuccinimidylsuberate, are commonly used to preferentially interact with amine groups. Protein-protein interactions can be probed by crosslinking lysines within a certain distance. Fragments obtained by enzymatic digestion are then analysed by MS and assigned a sequence. Crosslinked sequences are then analysed in respect to the structure of the complex.

Crosslinking was performed on purified mixed mmGPC3$^{\Delta C}$ and rnUnc5D$^{\text{Ig1-Ig2-TSP1}}$ at a concentration of 2 mg/ml. 20 times molar excess of BS3 crosslinker (spacer arm 11.4 Å; Thermofisher) was added to the protein sample, and incubated for 30 minutes at room temperature. The BS3 was quenched with a final concentration of 50 mM Tris HCL. The quenched solution was incubated for 30 minutes at room temperature. The crosslinked sample was separated and visualized by SDS-PAGE. The band corresponding to a GPC3/Unc5 complex was extracted and provided for enzymatic digestion and MS, performed by Dr. Svenja Hester (Advanced Proteomic Facility, Biochemistry Department Oxford). The data was analysed by Prof. Shabaz Mohammed.

2.4.4 Native mass spectrometry

Native MS allows for the investigation of intact protein assemblies [273]. The general principle of native MS is that a protein mixture is ionized by electrospray (ES) ionization. The ES technique is considered soft ionization, because it ionizes the macromolecule into small droplets instead of fragmenting the biological assemblies. The droplets are further desolvated, resulting in macromolecules associated with protons. The charged macromolecules will have different velocities, based on size and charge. These different velocities are recorded by a time-of-flight analyser, which determine the mass-to-charge ratio and the relative intensity ratios.

For the formation of small droplets and the subsequent desolvation, the macromolecule must be in a volatile buffer. The presence of salt and other buffer components will impede the spectra of the protein complex. Sample preparation consist of buffer exchange to a volatile buffer, such as aqueous ammonium acetate. For the individual protein spectra, *mm*GPC3$^{\Delta C}$ and *rn*Unc5D$^{\text{Ig1-Ig2-TSP1}}$ were concentrated to 10 μM and dialysed to 1 M ammonium acetate buffer overnight at 4 °C. For the protein complex, purified GPC3 and Unc5 constructs were mixed in a 1:1 molar ratio and concentrated to 10 to 15 μM (assuming a 4:4 stoichiometry). The complex was dialysed to 200, 500 or 1000 mM ammonium acetate (pH 7.5). Data used for mass determination was obtained by injecting 1.0 mg/ml *mm*GPC3$^{\text{R355R358AA }\Delta C}$ in complex with *rn*Unc5D$^{\text{Ig1-Ig2-TSP1}}$ in 200 mM ammonium acetate.

Data collection and analysis was performed by Dr. Ritu Raj (Robinson lab, University of Oxford). The protein samples were loaded into gold-coated capillary needles and introduced to the mass spectrometer. Experiments were typically done using a capillary voltage of 1.5 kV, cone voltage of 100-200 V and a collision cell energy of 20-50 V.

2.5 X-ray Crystallography

The diffraction of an X-ray beam from a crystal produces characteristic patterns of spots, or reflections, that contain information about the atomic structure. When an incident X-ray beam "hits" the electron cloud around an atom, either the kinetic energy is conserved (elastic scattering) or it is absorbed (inelastic or compton scattering). The elastic scattering of this collision with the electron cloud produces the reflections observed in the unique X-ray scattering pattern. During a typical single-crystal X-ray diffraction experiment, a crystal is mounted between an X-ray beam source (typical wavelength of 1 Å) and a detector. The X-ray is allowed to pass through the crystal and the diffraction data is recorded on a detector. A crystal is a three-dimensional array of objects in which different diffraction patterns are recorded when unrelated cross sections of the crystals lies perpendicular to the X-ray beam. Therefore, for a complete data set, a crystal is rotated by a goniometer to collect all unique cross sections of the three-dimensional array. The recorded position and intensities of the reflections in combination with the phase information of the wave are then used to determine the 3-dimensional electron density map using a Fourier transformation. The electron density map allows for a model to be build that reflects this distribution of electrons.

2.5.1 crystallization and crystal optimization

To obtain well-diffracting crystals, protein must precipitate out of solution in an orderly manner. This is achieved when sufficiently pure protein is mixed with a precipitant, with the right condition parameters (pH, Salt, Temperature, etc.). Several experimental crystallization trials setups can be used, such as vapour diffusion (sitting or hanging drop) and lipidic mesophases. In this thesis, the sitting drop vapour diffusion was used. Vapour diffusion results in a gradual increase in protein and precipitant concentration, which may reach the labile zone that allows for crystal nucleation. crystallization in vapour diffusion can be represented in a 2-dimensional phase diagram (figure 2.3).

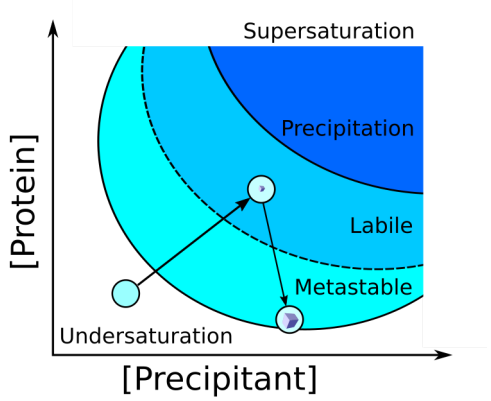


Figure 2.3: Phase diagram of a vapour diffusion experiment. A drop is setup with a concentration of protein and precipitant, by gradual diffusion the concentration increases. In the labile zone, a nucleation event can occur. The crystal grows, which decreases the protein concentration in solution, until it reaches the undersaturation zone.

The protein concentration used for crystallization screening was empirically deduced. This was done by preparing a Morpheus I screen at interval protein concentrations. The screen was checked for signs of precipitation under a microscope and, if 50% of the drops had signs of precipitation, the protein concentration would be used for further crystallization trials. Different crystallization conditions were sampled using the commercial screens Morpheus (I and II) [274, 275], JCSGcore I-IV/JCSG+ [276, 277], PACT premier [277], PGA [278], Proplex[279], Midas [280], and Index.

To elaborate on the strategy for crystallization condition screening, the number of screens was determined based on the protein volume, and the commercial screens were ranked according to previous observations. The Morpheus screen is a three-dimensional grid which samples four different precipitant conditions, three different buffer systems and eight different additives. As discussed above, Morpheus I was invariably used, while Morpheus II was only used when excess protein was available. In the case where experimental phasing was the goal, this screen was prioritized. Morpheus II conditions contain heavy atoms, which may be incorporated into the crystal, foregoing the need to do soaking experiments. Next, the sparse matrix screens JCSGcore I-IV would be set up; however, if only a small amount of sample was available the JCSG+ screen was used instead. JCSG+ combines the four core screens through data mining strategies, minimizing redundancy [277]. Grid screens like PACT premier, a screen that systematically test the effect of pH, anions and cations in combination with a polyethylene glycol (PEG) as precipitant, was setup along with JCSG+, as recommended [277]. In the case of screening for protein complex crystallization conditions, screens like Proplex would be prioritized, since they were specifically designed for protein complex crystallization [279]. The PGA and Midas screens were used to sample different crystallization conditions with unconventional precipitants.

A general setup consisted of using a 96-well 2-drop Swissci plate with 50 μl of reservoir solution of the commercial screen, prepared by Ed Lowe (Crystallography Facility, Biochemistry Department Oxford). Normally, a drop was prepared by mixing 100 nl of protein solution with 100 nl of reservoir solution, using the mosquito crystal nanolitre protein crystallization robot (TTP Labtech). When sufficient protein sample was available, the second drop well was used for a 2:1 protein-to-reservoir ratio drop, of which 133 nl of protein solution and 67 nl of reservoir solution was added. The plates were subsequently sealed and stored in crystal hotel and imager (Rigaku) at either 18 °C or 4 °C. The alternative temperature of 4 °C was done in duplicate to the 18 °C if excess protein was available. Images, including UV, were collected at regular intervals, and were checked for crystal hits.

Crystal hits were harvested using the appropriately sized cryo-loop (Hampton) and plunge-cooled in liguid nitrogen. During crystal harvesting, when the crystallization buffer was not cryo-protected, crystals were briefly soaked in a second drop of the original reservoir containing a cryo-protecting agent. Cryo-protecting agents used included the addition of glycerol, PEG400, or polyethylene glycol to the original reservoir buffer [281]. In some cases, when the original reservoir contained a PEG3350, the buffer was cryo-protected by increasing the concentration of PEG to 40-50%. The most common cryo-protection strategy used in this thesis was the addition of glycerol to a final concentration of 20%. In the case of cryo-protected crystallization conditions, such as the Morpheus screen conditions, the crystal was briefly transferred into the original crystallization buffer before cryo-cooling.

Crystals were tested for diffraction potential at a synchrotron beamline. When the crystal diffracted insufficiently for a structure solution, the crystallization condition was further optimized. Crystal optimization strategies were performed by adjusting several parameters of the initial crystallization condition [282, 283]. 96-well 2-drop Swissci plate were setup with larger drop sizes and two protein-to-reservoir ratios of 150:150 and 200:100 nl [284]. The crystallization buffer was diluted with filtered MilliQ water (100-60%). In some instances, the individual components were available and only the precipitant was diluted. Screens were also prepared with additives, from Hampton and the Silver Bullet screen, in which 5 μl of additive was added to 45 μl of crystallization buffer [285, 286]. Lastly, microseeding was performed in which crystals were collected and vortexed with a "seed-Bead" (Jena Bioscience) [287]. A serial dilution of the seed stock was prepared and drops containing a protein-to-seed-to-reservoir ratio of 100:50:100 and 100:50:50 nl were prepared using the aforementioned gradient screen. Additionally, as shown by Abuhammad and colleagues, cross-seeding with homologues proteins in commercial screens can help identify new crystallization conditions [288]. In this thesis, cross-seeding of poorly diffracting crystals from the same protein construct were prepared, as described above, and used for cross-seeding into commercial screens with a protein-to-seed-to-reservoir ratio of 100:50:100 nl.

2.5.2 Data collection

All crystal data collection, for the purpose of this thesis, was collected at synchrotrons beamlines (Diamond Light Source and ESRF). For Native data collection, a fixed X-ray wavelength of approximately 0.9-1.0 Å was used. To ensure that the crystal was consistently exposed to the beam path, the crystals were manually centered, and three images at 45° intervals were collected. These three images informed data collection strategies and experimental parameters like detector distance, beam size, transmission, exposure time and oscillation angle. Furthermore, these three images provide information on the symmetry of the crystal, such as the total oscillation required for a complete data set. Nonetheless, to record all possible symmetry operators of a crystal and to obtain a high multiplicity, data collection was performed to obtain at least 180° data sets.

Protein crystals are especially sensitive towards ionising X-ray radiation, which causes the crystal to undergo a reduction in diffraction power and loss of high-resolution data. X-ray radiation damage is caused by the absorption of energy from the beam or inelastic scattering (Compton scattering), from which photoelectrons that can have secondary effects can be produced. At 100 K the secondary effect is sufficiently slowed down, causing radiation damage to be proportional to the absorption coefficient [281]. Obtaining a complete and a high multiplicity data set improves the accuracy of the observations; however, incorporating radiation-damaged data has a negative impact on the data quality [289]. Radiation damage was carefully analysed, and exposure time was adjusted to minimize radiation damage.

2.5.3 Data processing

Data processing was done using Xia2 [290], through DIALS [291]. Data processing is normally carried out by indexing, integration, and scaling. X-ray diffraction provides two sets of information, the intensity and its position *hkl*. The intensity of the reflection corresponds to the electron density of the plane in which it diffracted

from. The position of the diffraction spots, *hkl*, gives information about the crystal's symmetry and lattice. The spacing between reflections is related to the reciprocal vector distance. Indexing attempts to identify the approximate unit cell parameters by the geometry of the diffraction pattern. DIALS use 3D fast Fourier transform to index the data in real space. The indexed reflections are further refined to obtain a more accurate description of crystal geometry and may correct for instrument errors.

During integration, the intensity of the observations (I) are determined. In Dials, this process consists of determining the reflection spot profile, estimation of the background under the peak, and then determination and evaluation of the peak intensity [292]. Firstly, the spot profile is described in 3-dimensional space (spanning across multiple images), which enables the determination of which pixels correspond to the observation and the noise. Secondly, the background noise (σI) is modeled around the peak observation. Finally, the observation intensity is calculated by either direct summation, in which the peak pixels have the background value subtracted, or by profile fitting. Dials uses profile fitting to improve the intensity calculation of weak observations. Further refinement protocols can be used after integration to improve the unit-cell refinement and correct for experimental and instrumental errors.

Once the data has been integrated, it will be scaled and merged. Scaling of the integrated reflection is performed because of changes in experimental or crystal parameters that effect the overall recorded intensities. Examples of these parameters are illumination of the crystal, anisotropic absorption, detector sensitivity and radiation damage. Observations are scaled by minimizing the difference of the same reflection. Afterwards, the data is merged according to their symmetry related equivalents, into unique observations, using Aimless [293]. Strong to severe anisotropy was a common characteristic of the crystals obtained in this thesis. During the scaling process, these weak reflections are scaled up, while the strong reflections are scaled down. This has an overall effect on the later refinement process, if anisotropy is severe [294]. To correct for the anisotropy-induced noise incorporation, data that was deemed to have strong to severe anisotropy were corrected by the

Staraniso server [295]. To ensure that strong reflections in the outer shells were still collected, data were processed to a higher resolution shell and the unmerged data was submitted to the server, where the default parameters were chosen.

Data quality indicators, such as $CC_{1/2}$, completeness, $R_{merge/meas}$, and $I/\sigma I$, are calculated after data reduction and inform towards resolution cut-off and potential crystal pathologies. Karplus and Diederichs proposed that $CC_{1/2}$ should be used as a resolution cut-off indicator [296]. $CC_{1/2}$ indicates the correlation between two randomly selected halves of the data sets. For this thesis, $CC_{1/2}$ of 30-50% was used as a primary resolution cut-off point.

R_{merge} were previously used as resolution cut-off indicators; however, it has been shown that the values can be misleading, especially in high multiplicity cases [296]. Therefore, R_{meas} was developed, which is multiplicity independent [297]. Additionally, R_{pim} was developed, which calculates the precision of the merged data. The overall $R_{merge/meas}$ is useful for determining radiation damage throughout batches of crystals. Aimless will produce data an R_{merge} for each batch of images across the entire data set, this R_{merge} value should remain constant throughout and was used to determine the presence of radiation damage in the crystal data set. Additionally, significant high $R_{merge/meas}$ in the low-resolution data shell, can suggest towards crystal pathologies such as wrong spacegroup identification [297].

2.5.4 Molecular replacement

X-ray diffraction can be calculated back into a 3-dimensional electron density map using a Fourier transformation. This requires the structure-factor, which is a mathematical function describing the amplitude, which is Search Results Featured snippet from the web proportional to the intensity of the observation, and the phase of the wave diffracted from the crystal lattice plane. However, the phases are lost during data collection and should be "solved". This is known as the phase problem in X-ray crystallography. The common methodology to determine the phases is

through molecular replacement (MR). MR uses a known homology structure to approximate the phases of the crystal structure. The phasing technique works especially well when a known homology structure shares a high sequence identity and C_α RMSD. In MR, the model's Patterson map is calculated and is then rotated and translated in space to match the observed Patterson map. The Patterson map is derived from the Fourier transformation of the squared structure amplitudes without the phases. In this thesis, Phaser was used for MR, which utilizes a maximum-likelihood probability to determine the most probable solution, while taking into account for any errors in the search model [298]. Phaser reports the log-likelihood gain (LLG) and translation function Z-score (TFZ). A high LLG indicates a correct solution and should increase as the unit cell is filled up. A single solution with a TFZ score above 8 represents an unambiguous solution suggesting that it is a correct solution. Nonetheless, the model and maps were analysed to confirm the solution.

2.5.5 Experimental phasing

Experimental phases were obtained by soaking crystals in its original reservoir buffer containing dissolved heavy atoms. Soaking solutions were prepared, in which pH compatible heavy atom powder from the heavy atom screens (Hampton) and Tantalum Bromide cluster (Ta_6Br_{12}) derivatization kit (Jena Bioscience) were dissolved in the crystallization buffer and directly pipetted onto the drop. The crystal drop was resealed and incubated for 4 to 24 hours. Crystals were transferred to a cryo-protected reservoir solution to remove any unbound heavy atoms.

Crystal structures that require experimental phase information for a structure solution have special considerations during data collection. Experimental phases are deduced when intensity of Friedel reflections are not equivalent. Therefore, the total oscillation should be double for a complete anomalous data set. Additionally, to maximize this anomalous signal, data is collected at an element-specific wavelength, also known as the anomalous peak. The element-specific anomalous peak is experimentally determined with a fluorescence scan, also known as an edge scan.

Fluorescence scans screen around the element's theoretical absorption wavelength to empirically determine the absorption peak.

Heavy atom derivative data was processed using Xia2, with XDS, which uses XScale for scaling and Aimless for data reduction [299]. The log files generated by these programs were used to analyse the anomalous signal data quality indicators, CC_{ano} and SigAno. CC_{ano}, similar to $CC_{1/2}$, indicates the correlation between a randomly selected halves of the anomalous differences in the data set. SigAno corresponds to the ratio of the mean anomalous difference to its standard deviation, in which values above 1.0 are considered significant. These values were used to monitor any radiation induced loss of anomalous signal, and the anomalous signal resolution.

Experimentally phasing was done using single anomalous dispersion (SAD) with the automated structure solution pipeline of Phenix Autosol [300], which combines HYSS/Phaser LLG in order to find heavy-atom sites and Resolve for density modification [301, 302]. For SAD data there remains some phasing ambiguity of the enantiomorphs. However, in the case of this thesis, one map showed a clear α-helical globular protein, indicating a correct solution.

2.5.6 Model building and refinement

Phase determination either through MR or experimental phasing provides with the initial map. From this electron density map, atomic coordinates can be placed that represent the observed electron density. Further model building and refinement is performed to match the models structure factors with the observed structure factors. When appropriate, iterative model building was performed using automatic model building using Phenix Autobuild [303], and manual model building using Coot [304]. Autobuild uses density modified maps to place an initial protein backbone. Subsequent refinement and build cycles attempt to extend the protein backbone, adding side chains that allow the sequence to be docked. In the case of

low-resolution data sets, model building involved the manual placement of higher resolution domains into a density modified map, using Coot. This was predominantly achieved through the use of experimentally phased maps and cross-crystal averaging. Statistical density modification initially determines what regions of the crystal correspond to the solvent and protein. The solvent is then set to a low constant value, flattened, to improve the phases. Cross-crystal averaging is possible when two crystal forms are available of the same protein. This allows for a more accurate protein mask and solvent estimation, further improving the maps [305].

Once the initial model was built, further refinement was done to correct atomic positions in agreement with the data. This refinement attempts to improve the atomic (x,y,z, B-factors and occupancy) and global parameters (Global B-factor and bulk solvent correction) to closer match the observed data. In this thesis, two main methods were performed for high-to-moderate resolution refinement (<3 Å) and low-resolution refinement. The high-to-moderate resolution data was refined using Phenix Refine [301]. Initial refinement involved using reciprocal space refinement and isotropic atomic displacement factors with secondary structure restraints. In addition to stereochemical restrains, which include bond distances and angles, secondary structure restrains add known bond distances and angles for α-helices and β-sheets. During the refinement process, manual intervention by Coot may prevent the model in falling to a local minimum or correct for any serious geometry errors. Once the model was nearly completed, TLS (translation/libration/screw) refinement was added, secondary structure restraints were removed (when appropriate), and geometry/X-ray refinement weights were optimized. TLS refinement defines groups that have related motion to each other, describing it as translation, libration, and screw motion. This improves B-factor refinement, similar to anisotropic B-factor refinement, without the addition of many more parameters that would be required in anisotropic refinement [306]. Refinement was allowed to reach convergence. A final round of refinement was added using real space refinement, which corrects for any side chain outliers. Additionally, optimized bulk solvent correction was used for the final macrocycle.

In macromolecular crystallography, the data-to-parameter ratio is especially poor, and the degrees of freedom should be limited by restraints. However, in low-resolution data, this is especially difficult and may still result in overfitting even with geometry restraints. In addition, the electron density maps often do not have any side chain features to guide model building. In this thesis, high-resolution structures were available for the components of the low-resolution crystal content. All components were placed in the electron density map, as described above. Initial refinement used Autobuster, in which only rigid body refinement was performed. Each domain was described as an individual rigid body. *xyz* coordinates were refined by reciprocal space refinement. Importantly, refinement was highly restrained with local non-crystallographic symmetry (NCS), secondary structure and reference model restraints. Reference model restraints use high resolution structures to restraint the torsion angles of the model in the lower resolution data. In this thesis, the higher resolution GPC3 and Unc5D (PDB 5FTT) structures were used as reference models. Reference restraints introduce prior knowledge to effectively minimize the torsion-angle degrees of freedom of a macromolecule in lower resolution refinement [307]. Group B-factor refinement was also performed, in which two groups were assigned to the side chain and main chain, per residue, minimizing the parameters that have to be refined [308]. Refinement was allowed to reach convergence.

2.5.7 Validation

Structure solutions are validated based on the sum of the residuals squared between the model and observed structure factors, represented in the R-factors. Before any refinement of the model is performed, the reflection data is separated into a working (approximately 95%) and test (approximately 5%) set. During refinement the working data set is used, while the test set is kept separate. When the model improves, and corresponds more to the observed data, the R-factors will improve until it reaches 0%. In macromolecular crystallography such low R-factors are unlikely, because of the high solvent content and so R-factors tend to range between 20-25%

(dependent on the resolution). The working data sets calculated R-factors are called R_{work}, while the test set data is called R_{free}. The separation of the test set from refinement ensures that overfitting is prevented. Model geometry was also validated using MolProbity [309, 310]. MolProbity analyses Ramachandran geometry, rotamer geometry, C-β outliers, and protein clashes. Because proteins were crystallized with minimal N-glycosylation, some glycosylation could be observed and modelled into the density maps. Therefore, Privateer was used to validate the glycan geometry [311].

3

Solving the Crystal Structure of GPC3

3.1 Summary

Low-resolution crystals were obtained for the GPC3/Unc5 complex (4.0-5.0 Å). Experimental phasing of the complex crystal structure revealed that the solved homologue structure, GPC1 (PDB 4YWT), deviated from the electron density maps, and therefore could not be placed with confidence. To confidently solve the low-resolution structure GPC3/Unc5 structure, I set out to obtain the structure of GPC3.

The core protein of GPC3 (32-483) produced several initial crystals, however, these crystals diffracted to a low resolution. Optimization trials yielded crystals that diffracted to an anisotropic 3.0 Å resolution, with the lowest diffracting planes diffracting to 4.5 Å. I tried several approaches to obtain better resolution data, which included: redesigning the protein construct, adjusting crystallization parameters and cross-seeding. Eventually, optimized crystals were obtained that diffracted to 2.6 and 2.9 Å, for human and mouse GPC3 respectively. The data obtained was enough to solve the crystal structure of the core region of human and mouse GPC3.

As expected, the structure of GPC3 revealed a conformational difference compared to the model of GPC1. The newly solved crystal structure of GPC3 will act as a better model for the low resolution GPC3/Unc5 protein complex data. This chapter will describe the process of the structure determination of GPC3 and present the resulting models.

3.2 Results

3.2.1 Crystallization and optimization of GPC3

The lab provided a construct of mouse GPC3, which had the residue boundaries of 31-482, termed *mm*GPC3$^{\Delta C}$. These boundaries were based of the published GPC1 crystal structure, and do not include the predicted disordered proline-repeat at the N-terminus and the predicted disordered C-terminus that contains two HS-GAGs attachment sites and the GPI-anchor recognition sequence. In parallel, I cloned a human GPC3 construct with the same boundaries, corresponding to residues 32-483, termed *hs*GPC3$^{\Delta C}$ (Figure 3.1A). The sequence identity between *mm*GPC3$^{\Delta C}$ and *hs*GPC3$^{\Delta C}$ is 98%. Both the mouse and human GPC3$^{\Delta C}$ were used for initial crystallization trials.

GPC3$^{\Delta C}$ has three N-glycosylation sites, which are N124, N240, and N418 (in human), according to N-glycan prediction (NetNGlyc server [312]) and mass spectrometry data by Saad and colleagues [313]. Therefore, both human and mouse GPC3$^{\Delta C}$ were expressed in HEK293S cell lines (S2.2.1) and purified using standard purification protocols (S2.2.6). Sufficiently pure fractions (D10-E2) were used for crystallization trials (figure 3.1D). GPC3 contains a furing cleavage site which results in three bands being identified on a reducing SDS-PAGE [314]. These three band correspond to the unprocessed *hs*GPC3$^{\Delta C}$ (53.3 kDa) and the proteolytically processed N-terminal (/α; 37.7 kDa) and C-terminal (/β; 15.6 kDa) subunits of *hs*GPC3$^{\Delta C}$ (figure 3.1D).

Sitting drop vapour diffusion commercial screens were prepared with both human and mouse GPC3 on different days. *mm*GPC3$^{\Delta C}$ was setup with a concentration of 6 mg/ml, while *hs*GPC3$^{\Delta C}$ was prepared with 4 and 8 mg/ml. Initial trials for *mm*GPC3$^{\Delta C}$ did not yield any crystals. Screens prepared with *hs*GPC3$^{\Delta C}$ had crystal hits in the first 7 days. These hits were identified in the commercial screen conditions Index H4, JCSG+ G6, and Morpheus G1, referred to as conditions #1,

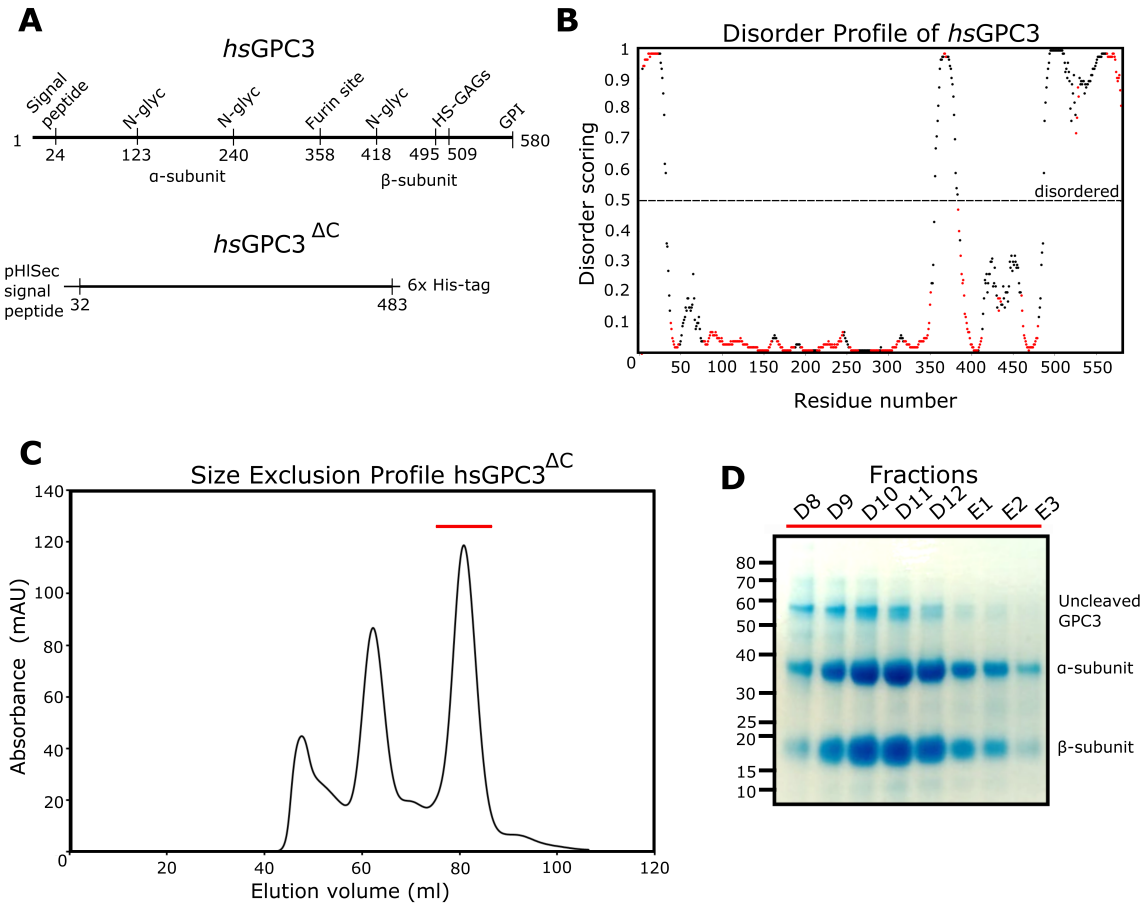


Figure 3.1: Design and purification of *hs*GPC3$^{\Delta C}$. A) *hs*GPC3 is a 580 amino acid protein which is proteolytically cleaved at the furin site, which produces two subunits (α (1-358) and β (359-580). *hs*GPC3 has three predicted N-glycosylation sites at N123, N240, and N418 and two HS-GAG attachment sites at S495 and S509. For crystallization, the core protein was cloned from residue 32-483 into a pHlSec vector with a signal peptide and a C-terminal 6x His-tag, named *hs*GPC3$^{\Delta C}$. **B)** Disorder profile of *hs*GPC3 calculated by DISOPRED [133]. Red dots have a predicted secondary structure according to PSIPRED. **C)** SEC chromatogram graph. The first peak is the void volume and the second peak is a common contaminant of the expression system. The third sharp peak is the *hs*GPC3$^{\Delta C}$.**D)** Reducing SDS-PAGE of the third peak fractions. For *hs*GPC3$^{\Delta C}$, three bands are observed which include unprocessed GPC3, subunit α (32-358), and subunit β (359-483)

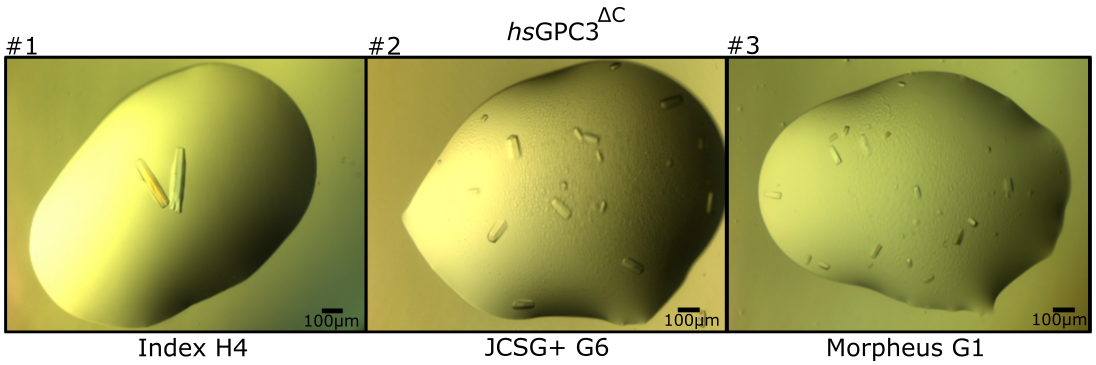


Figure 3.2: Initial crystal hits for *hs*GPC3$^{\Delta C}$. Drops were setup containing 100 *nl* of 4 mg/ml and 8 mg/ml of *hs*GPC3$^{\Delta C}$ and 100 *nl* of crystallization buffer. Three different crystallization conditions were identified from the commercial screens Index, JCSG+ and Morpheus at 18°C. All three conditions formed crystals after 7 days.

#2, and #3 respectively (figure 3.2). Crystals from Condition #1 grew in plates containing both 4 and 8 mg/ml of protein, while conditions #2 and #3 only grew with 4 mg/ml. Optimized crystal conditions for each crystal hit described in this chapter are summarized at the end of this section (table 3.1).

Crystals from condition #1 and #2 were harvested in the crystallization buffer containing a final concentration of 20% glycerol. Addition of another component to the crystallization buffer may have detrimental effects on diffraction quality [289]. Therefore, different cryo-buffers were tested. Examples of other cryoprotection conditions include different glycerol concentrations (15-25%), addition of Polyethylene glycol (25-30%), PEG400 (25%), and increasing the original reservoir conditions (PEG3350 40-50%). The minimal cryoprotectant required was determined by cryo-cooling an empty loop and examining it under the microscope for ice. Crystals from condition #3 were obtained in the Morpheus screen, and so were transferred to a drop containing the original reservoir solution briefly prior to cryo-cooling.

Diffraction data obtained from these crystals were not of sufficient quality, which prevented me from solving the structure. Both condition #1 and #2 crystals diffracted to 5-6 Å. In addition, the data quality indicator R_{meas} was 20-30% in the inner resolution shell, suggesting to crystal pathologies. Condition # 3 crystals

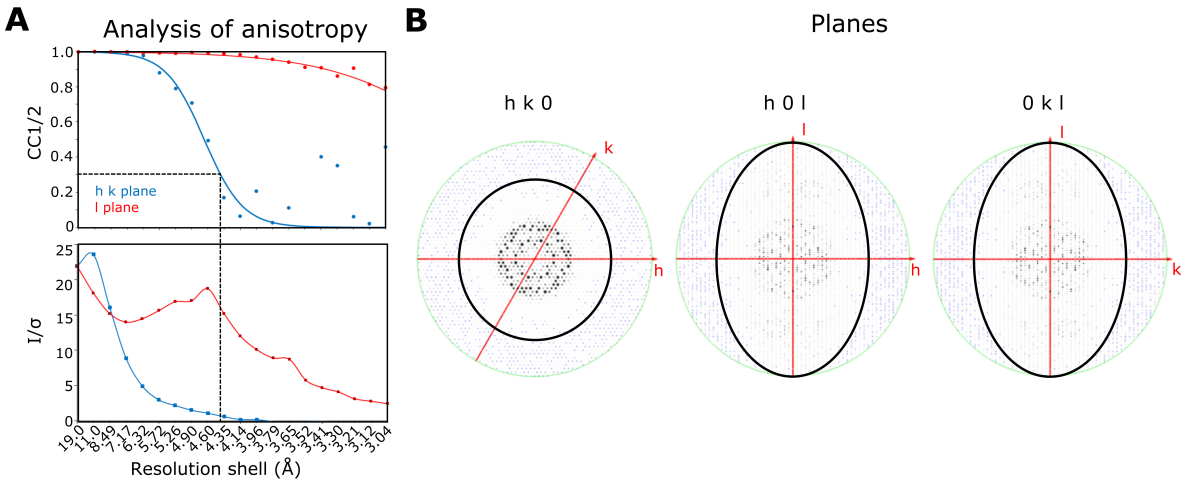


Figure 3.3: Anistropy analysis of *hs*GPC3$^{\Delta C}$ (#3). A) Plotted $CC_{1/2}$ and I/*sigma*I for each resolution shell for the h k plane (blue) and l plane (red) obtained from Aimless. The h k plane signal quality indicators drop significantly between 5.0-4.0Å, while the l plane signal quality indicators remain significantly higher until 3.0 Å. **B)** Graphical representation of the h k l planes.

diffracted to approximately 4 Å but also suffered from high R_{merge} in the inner resolution shell. Optimization was performed by increasing the drop size and by preparing dilution and additive screens (S2.5.1) [283, 284]. Crystals of condition #1 and #2 obtained through these optimization screens did not improve in diffraction resolution and maintained their high R_{merge}. Crystals from condition #3 improved in diffraction resolution, to 3.0 Å . The best diffracting crystals were obtained by the addition of the silver bullet additive (C8), which corresponds to a final concentration of 0.005% of amino acids (see table 3.1). Unfortunately, these crystals suffered from severe anisotropy, shown in figure 3.3. Anisotropy is the result of a crystal being differently ordered in its planes of diffraction. After extensive optimization trials, the crystallization condition trialled did not favour high quality diffracting crystals.

The poorly diffracting crystals prompted me to redesign the protein construct to minimize heterogeneity. Observed in the wild type protein, two species are present, uncleaved and cleaved, which may complicate crystallization. I cloned the mutations, R355A R358A, into *hs*GPC3$^{\Delta C}$, referred to as *hs*GPC3$^{R355R358AA\ \Delta C}$ (figure 3.4A), which prevents furin cleavage [153]. The mutant resulted in a predominantly

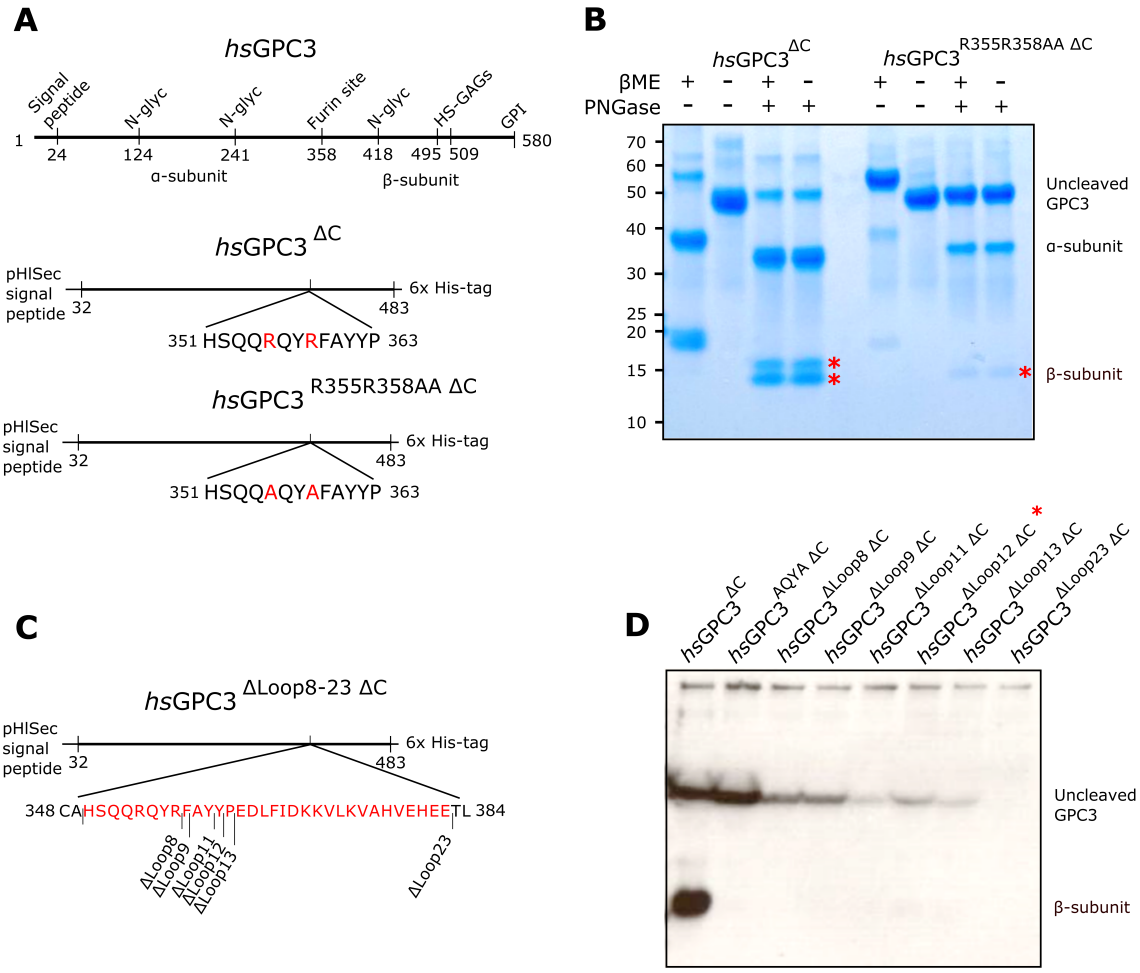


Figure 3.4: Design of the non-cleavable mutant and deletion constructs. A) Construct design of *hs*GPC3$^{\mathrm{R355R358AA\ \Delta C}}$.**B)** 10 µg of GPC3 variants were incubated with and without PNGase F (NEB) in denaturing conditions for 1 hour at 37 °C. Samples were visualized by SDS-PAGE under reducing (βME) and non-reducing conditions. In reducing conditions *hs*GPC3$^{\Delta C}$ runs as three bands. In non-reducing conditions the two lower bands are not present. Construct *hs*GPC3$^{\mathrm{R355R358AA\ \Delta C}}$ predominately runs as an uncleaved product, in both reducing and non-reducing conditions. Of note, annotated by a red asterix, is that in reducing condition the wild type *hs*GPC3$^{\Delta C}$ has a faint double band at the β-subunit, which can be appreciated after deglycosylation with PNGase F. On the contrary, *hs*GPC3$^{\mathrm{R355R358AA\ \Delta C}}$ β-subunit only contains one band. **C)** Construct design of *hs*GPC3$^{\Delta\mathrm{loop\ \Delta C}}$, in which 8,9,11,12,13 or 23 amino acids were deleted from the disordered loop, starting from residue H351. **D)** Western blot of expression tested constructs, *hs*GPC3$^{\Delta C}$, *hs*GPC3$^{\mathrm{R355R358AA\ \Delta C}}$, and *hs*GPC3$^{\Delta\mathrm{loop8\text{-}23\ \Delta C}}$. Membranes were blocked with 3% BSA and then constructs were decorated with anti-HisTag primary mouse antibodies in 3% BSA in PBST (1:1000; Qiagen cat. 34660) and visualized by secondary anti-mouse antibodies conjugated with HRP (1:10,000; Sigma cat. AO168). Membranes were washed in between each step with PBST. Expression was observed for all deletion constructs, except for the negative control deletion construct Δloop23. Construct *hs*GPC3$^{\Delta\mathrm{loop12\ \Delta C}}$ was subsequently used for large-scale expression, indicated by a red asterisk.

uncleaved form of GPC3 (figure 3.4B). Nonetheless, some cleavage was still observed for the *hs*GPC3$^{\text{R355R358AA }\Delta\text{C}}$ mutant. Interestingly, the β subunit has a double band in the wild-type construct, which is not observed in the *hs*GPC3$^{\text{R355R358AA }\Delta\text{C}}$. PNGase treatment of both wild-type and mutant suggest that this double band is the result of a second cleavage site and not an alternate glycosylation state (Figure 3.4B). Secondly, I designed several constructs that remove a number of residues from the long disorded loop, starting at H352 (figure 3.1B). From the crystal structure of GPC1 we can determine that the loop must span at least 60 Å. Therefore, I designed deletion constructs that removed eight to thirteen residues and a negative control construct lacking twenty-three residues (*hs*GPC3$^{\Delta\text{loop8-23 }\Delta\text{C}}$). Additionally, the deletion constructs lack the Furin cleavage motif. The constructs were expression tested and visualized using western blotting. All deletion constructs, except for the negative control GPC3$^{\Delta\text{loop23 }\Delta\text{C}}$ expressed and ran at the size of the uncleaved *hs*GPC3$^{\Delta\text{C}}$. I used construct *hs*GPC3$^{\Delta\text{loop12 }\Delta\text{C}}$ for further expression and crystallization trials, as it removes the most residues while the western blot suggest a slightly better expression then *hs*GPC3$^{\Delta\text{loop13 }\Delta\text{C}}$.

*hs*GPC3$^{\text{R355R358AA }\Delta\text{C}}$ and *hs*GPC3$^{\Delta\text{loop12 }\Delta\text{C}}$ were purified and concentrated to 5 mg/ml for crystallization trials. For construct *hs*GPC3$^{\text{R355R358AA }\Delta\text{C}}$, crystals were obtained in commercial screen PGA, well B2, (#4). For construct *hs*GPC3$^{\Delta\text{loop12 }\Delta\text{C}}$, crystal hits were obtained in the previously obtained commercial screen Index, well H4 (#1). The crystals were screened on a beamline for diffraction; however, no diffraction was identified.

None of the methods attempted obtained high-resolution diffraction data; therefore, I trialled cross-seeding crystals from condition #3 into new commercial screens. Sitting drops were setup with 5 mg/ml of *hs*GPC3$^{\Delta\text{C}}$ with the seed stock and the commercial screen crystallization buffer (100:50:100 *nl* respectively). Cross-seeding resulted in crystals growing in Morpheus, well H10 (#5). Unlike the rod-shaped crystals of condition #3, these crystals had a prism-like morphology (figure 3.5). Similar crystals were obtained after 3 months for *mm*GPC3$^{\Delta\text{C}}$. These

crystals were obtained by the addition of 100 *mM* nondetergent sulfobetaine-256 (NDSB-256) before concentrating the protein to 10 mg/ml, in the commercial screen JCSGcore I, well E1, (#6; figure 3.5). Addition of NDSB-256 is helpful when working with aggregation prone proteins, as it solubilizes and stabilizes the protein [315, 316]; however, this may require higher concentrations of protein for crystallization trials. Crystals obtained from both homologs were harvested and the resulting data collections yielded isotropic diffraction beyond 3 Å, presented in the following section.

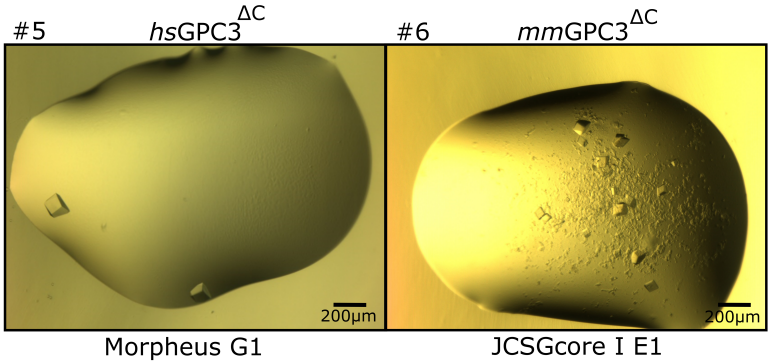


Figure 3.5: Best crystals for *hs*GPC3$^{\Delta C}$ and *mm*GPC3$^{\Delta C}$. Best crystal hit for *hs*GPC3$^{\Delta C}$ was obtained by mixing 50 *nl* of crystal seeds of condition #1 with 100 *nl* of 5 mg/ml of protein and 100 nl of commercial Morpheus screen, well H10 (#5) at 18°C (left). Crystals for *mm*GPC3$^{\Delta C}$ were obtained by mixing 100 *nl* of 10 mg/ml of *mm*GPC3$^{\Delta C}$ with 100 *mM* NDSB-256 with 100 *nl* of commercial screen JCSGcore I, well E1 (#6) at 18°C (right). Crystals were obtained after 21 days.

Table 3.1: Summary of crystallization conditions for the GPC3 constructs.

#	Construct	Condition	Res. (Å)
1	*hs*GPC3$^{\Delta C}$	0.2 M Ammonium citrate tribasic (pH 7.0); 20% PEG w/v 3350	N.A
	*hs*GPC3$^{\Delta loop12\ \Delta C}$	0.2 M Ammonium citrate tribasic (pH 7.0); 20% PEG w/v 3350	N.A
2	*hs*GPC3$^{\Delta C}$	0.2 M Sodium malonate dibasic monohydrate; 20% w/v PEG 3350	N.A
3	*hs*GPC3$^{\Delta C}$	0.1 M Imidazole MES (pH 6.5); 18% v/v PEG 500 MME; 9% w/v PEG 20,000; 0.018 M (Sodium formate; Ammonium acetate; Sodium citrate tribasic dehydrate; Sodium potassium tartrate tetrahydrate; Sodium oxamate); 0.005% w/v (Glycine; L -(-)-Threonine; L-(+)-Lysine; L-Alanine; L-Arginine; L-Asparagine; L-Aspartic acid; L-Glutamic acid; L-Glutamine; L-Histidine; L-Isoleucine; L-Leucine; L-Methonine; L-Phenylalanine; L-Proline; L-Serine; L-Tryptophan; L-Tyrosine; L-Valine)	3.1
4	*hs*GPC3$^{R355R358AA\ \Delta C}$	0.1 M Sodium acetate (pH 5.0) 5 % w/v -PGA (Na+ form, LM); 15 % w/v PEG 4000	N.A
5	*hs*GPC3$^{\Delta C}$	0.1M Tris/BICINE (8.5); 20% Ethylene glycol; 10% w/v PEG 8000 0.02M (L-Na-Glutamate; Alanine; Glycine; Lysine HCL; Serine)	2.6
6	*mm*GPC3$^{\Delta C}$	0.2 M Ammonium nitrate 20% PEG w/v 3350	2.9

Table 3.2: Data collection parameters for datasets *hs*GPC3$^{\Delta C}$ (#3 & #5) and *mm*GPC3$^{\Delta C}$ (#6).

	*hs*GPC3$^{\Delta C}$	*hs*GPC3$^{\Delta C}$	*mm*GPC3$^{\Delta C}$
Condition	#3	#5	#6
Beamline	i04-1	i03	i24
Wavelength (Å)	0.9159	0.9201	0.9686
Beam size (μm)	30x30	50x20	50x50
Oscillation (°)	0.2	0.1	0.2
Exposure (s)	0.2	0.1	0.1
Transmission (%)	100	50	48
Number of Images	900	1800x2	900

3.2.2 Data collection and processing

All GPC3 crystals were screened at the Diamond Light Source synchrotron. The datasets used for structure solutions were collected at beamlines i04-1, i03 and i24 for #3, #5, and #6, respectively (figure 3.6). The data collection parameters are summarized in table 3.2. Several parameters like exposure, transmission and detector distance, were determined based on test "shots" and previous crystal collections to determine radiation damage sensitivity of the crystals.

The data was subsequently processed using the automated pipeline Xia2 [290], which uses Dials to integrate the reflections [291, 318], Pointless and Aimless to merge the data sets [319]. The resolution cut-off was assessed using predominantly $CC_{1/2}$ between 30-50%. Radiation damage was determined by observing the increase in R_{meas} in batches of images across the entire dataset, in which batches with a significant increase in R_{meas} were excluded. Many refinement programs can handle moderate cases of anisotropy; however, in severe cases it may halt refinement and result in poor map quality and high R-factors [294]. In the case of #3, scaled unmerged data was applied with an anisotropic mask by the Staraniso server [295]. The resulting processed data is shown in table 3.3. The reduction in completeness is the result of applying an ellipsoidal cut-off. The resolution shell with full completeness was 4.6 Å, of which the statistics per resolution shell are shown in appendix B.1.

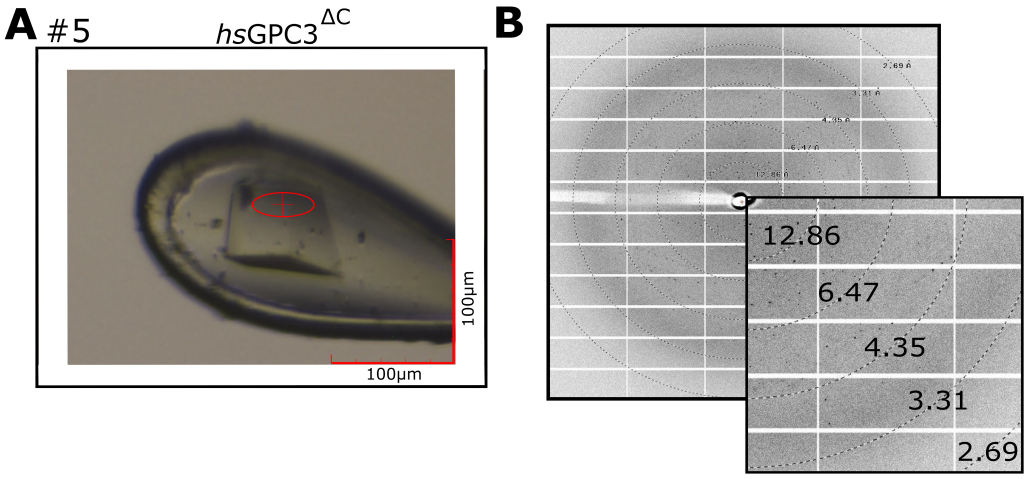


Figure 3.6: Data collection of *hs*GPC3$^{\Delta C}$ (#5). A) *hs*GPC3$^{\Delta C}$ (#5) crystal in a cryoloop mounted on the goniometer for data collection. **B)** A single diffraction image from #5, obtained using the ADXV viewer [317]. The image inside the box is a zoomed in version of the original image.

Table 3.3: Processed data statistics for *hs*GPC3$^{\Delta C}$ (#3), before and after an anisotropic cut-off. Data was processed using Xia2 with Dials and merged using Aimless. Anisotropic cut-off was performed on unmerged data using the Staraniso server [295].

Construct	*hs*GPC3$^{\Delta C}$	
Condition	#3	
Space group	P3	
Cell dimensions		
a, *b*, *c* (Å)	96.6, 96.6, 163	
α, β, γ (°)	90.0, 90.0, 120	
	Isotropic	Anisotropic
Resolution (Å)	83.7-3.01 (3.42-3.01)	83.6-3.01 (3.42-3.01)
Completeness (spherical) (%)	94.8 (98.9)	38.0 (5.90)
Completeness (ellipsoidal) (%)	94.8 (98.9)	85.5 (64.0)
Rmerge (%)	15.3 (432)	7.60 (74.8)
$CC_{1/2}$ (%)	99.9 (30.0)	99.9 (59.1)
I/σI	3.5(0.1)	10.5 (1.8)
Multiplicity	5.2(5.0)	5.3 (5.0)

Table 3.4: Processed data statistics for the best crystal datasets (#5 and #6). Data was processed using Xia2 with Dials and merged using Aimless. The dataset for #5 is the result of merging two crystal data sets.

Construct	*hs*GPC3$^{\Delta C}$	*mm*GPC3$^{\Delta C}$
Condtion	#5	#6
Space group	P321	P321
Cell dimensions		
a, *b*, *c* (Å)	100.1, 100.1, 90.14	100.5, 100.5, 90.62
α, β, γ ()	90.0, 90.0, 120	90.0, 90.0, 120
Resolution (Å)	43.8-2.55 (2.64-2.55)	43.9-2.90 (3.00-2.90)
Completeness (%)	99.6 (96.3)	99.7 (97.6)
Rmerge (%)	5.78 (162.4)	13.5 (197.7)
$CC_{1/2}$ (%)	99.9 (53.6)	99.7 (53.7)
I/σI	18.8 (1.24)	9.23 (1.24)
Multiplicity	11.9 (8.1)	9.5 (9.6)

The high-resolution datasets statistics for *hs*GPC3$^{\Delta C}$ (#5) and *mm*GPC3$^{\Delta C}$ (#6) are shown in table 3.4. Both data sets, were indexed into the same space group with similar unit cells of which *mm*GPC3$^{\Delta C}$ (#6) has a slightly bigger unit cell volume. In the case of *hs*GPC3$^{\Delta C}$ (#5), full data sets were collected from two crystals and were subsequently merged after radiation damage correction. The statistics were analysed and showed an improvement in data quality.

3.2.3 Phasing and model building

The crystallized constructs of GPC1 and *hs*GPC3$^{\Delta C}$ share only 25.3% sequence identity, which is considered low for molecular replacement. Nonetheless, the glypican family shares 14 conserved cysteines suggesting that the overall structure may be similar. Accordingly, molecular replacement was used to phase and solve the structure of dataset *hs*GPC3$^{\Delta C}$ #5. Xtriage was used to analyse the data for pathologies and its solvent content [320]. According to the Matthew coefficient, there was likely one copy in the asymmetric unit, which corresponds to a solvent content of 50.8% [321].

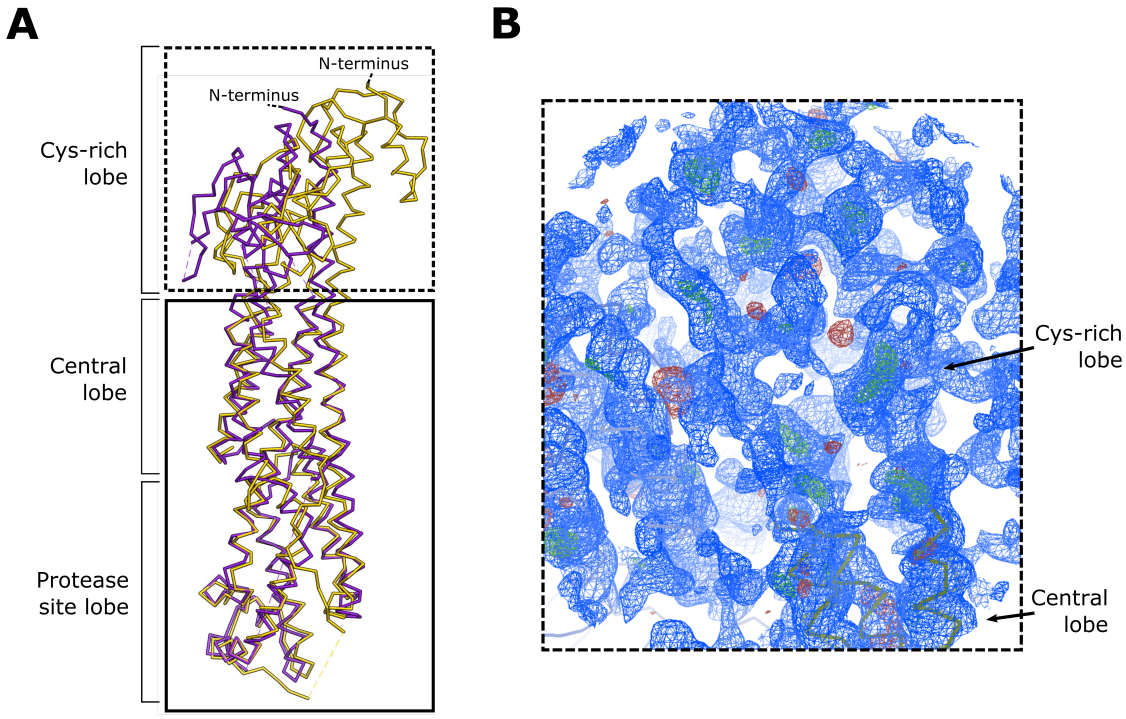


Figure 3.7: Molecular replacement model design. A) Overlay of GPC1 (PDB 4YWT) in yellow and DLP (PDB 3ODN) in purple superposed using the central lobe. Both structures are similar at their central and proteolytic site lobe and were used for molecular replacement as a poly-alanine model. **B)** Density map of expected location of the cys-rich lobe (portrayed by the dashed line box) after molecular replacement and refinement of the top solution obtained when using the poly-alanine model of the central and protease site lobe. The electron density map is shown in blue (2Fo-Fc, contour level σ 1.0). Structures were prepared in Chimera [68] and the image was obtained in Coot [304].

Molecular replacement was performed using a homologue model based on GPC1 (PDB 4YWT), generated by the SWISS server [322]. The homology model was truncated to a poly-alanine containing the central lobe and protease site lobe (figure 3.7A). Using the modified model for molecular replacement resulted in thirteen solutions, with the top solution having a TFZ score of 6.5 and LLG of 34.5 in space group $P3_121$. After a round of rigid body and all atom refinement, the resulting Rwork/Rfree was 51.9%/55.9%. The R-factors are considered poor for an initial solution, but the resulting map showed clear extensions in density where the cys-rich lobe was expected to be (figure 3.7B), indicating a possible correct solution. Using this as a guide, the homology model was adjusted to account for the movement of the cys-rich lobe. After several rounds of auto-building using Phenix Autobuild and

Table 3.5: Processed data statistics for *hs*GPC3$^{\Delta C}$ (#5) in spacegroup P321 and P3. Data was processed using Xia2 with Dials and merged using Aimless.

Construct		*hs*GPC3$^{\Delta C}$
Condition		#5
Space group	$P3_121$	$P3_1$
Resolution (Å)	43.8-2.55 (2.64-2.55)	43.4-2.64 (2.73-2.64)
Completeness (%)	99.6 (96.3)	99.0 (91.2)
Rmerge (%)	5.78 (162.4)	5.42 (87.3)
$CC_{1/2}$ (%)	99.9 (53.6)	99.9 (63.2)
I/σI	18.8 (1.24)	13.9 (1.43)
Multiplicity	11.9 (8.1)	6.4 (4.2)

iterative manual building, a finalized model for both human and mouse GPC3$^{\Delta C}$ were obtained. Phasing was performed with the help of Dr. Metin Aksu.

Refinement was done using Phenix Refine [323]. Initial refinement was done on the XYZ coordinates and isotropic atomic displacement parameters with secondary structure restraints, described in the PDB file [324]. During the final stages of refinement, the secondary structure restraints were removed, X-ray weights were optimized, and TLS parameters were added per chain [306]. TLS refinement aims to model the vibrational displacement of atoms/molecules similar to anisotropic refinement; however, TLS refinement requires less parameters, allowing it to be used at lower resolutions compared to anisotropic refinement. The *mm*GPC3$^{\Delta C}$ was refined in the space group $P3_121$, in which the map quality and model geometry are of high quality (table 3.5). However, *hs*GPC3$^{\Delta C}$ refinement stalled was Rwork/Rfree of 24.4%/29.3%, which is relatively high for the working resolution. I decided to reindex the spacegroup from $P3_121$ to $P3_1$, assuming that the data may suffer from pseudosymmetry. I used the Phenix shake dynamics to reset the model and prevent Rfree bias; then two GPC3 were placed and refined to an improved Rwork/Rfree of 22.3%/26.5% (table 3.5). The change in spacegroup improved the refinement statistics, but this may be a consequence of several factors, including the use of NCS restraints in refinement.

The anisotropic dataset of *hs*GPC3$^{\Delta C}$ (#3) was solved using the high-resolution crystal structure. Three copies were identified in the asymmetric unit cell corresponding to a solvent content of 56.3%. Before refinement, as according to Staraniso recommendations, a unique Rfree of 5% was created using the CCP4 Uniqueify script and missing reflections were removed using the CCP4 SFTOOL [325]. This was done to prevent refinement programs from introducing unobserved reflections into the anisotropic data which can lead to excessive model bias. To account for the low-resolution data, the model was highly restrained to ensure correct geometry. The restraints used include *mm*GPC3$^{\Delta C}$ as a reference model restraint [307], secondary structure restraints, and NCS restraints. Refinement included XYZ refinement and isotropic atomic displacement parameters and TLS refinement (1 group per chain), which resulted in a noisy but clear map, with some sidechains resolved (figure 3.8). The finalized model refinement statistics and model geometry for #3, #5 and #6 are summarized in table 3.6. The high resolution *hs*GPC3$^{\Delta C}$ (#5) was used for further scientific interpretation.

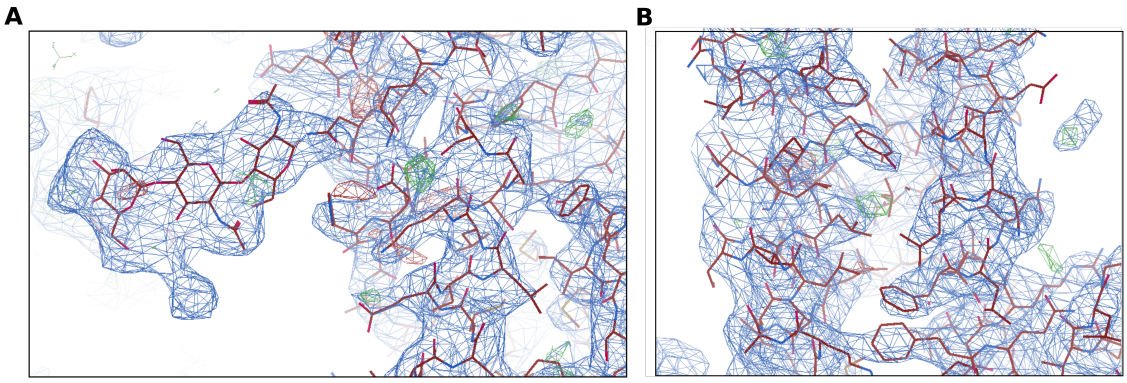


Figure 3.8: Electron density map of *hs*GPC3$^{\Delta C}$ (#3). A) Electron density map around N124 in which two N-acetyl-D-glucosamine (glcNAc) and a Mannose were modelled **B)** The electron density map around of the central lobe, in which some bulky side chains can be seen. The density map is shown in blue (2Fo-Fc, contour level σ 1.0) and difference map shown in green and red (Fo-Fc,contour level $\pm$ σ 3.0). Atoms are coloured in red. The image was prepared using Coot [304].

Table 3.6: Refinement and model geometry statistics for *hs*GPC3$^{\Delta C}$(#3 and #5), and *mm*GPC3$^{\Delta C}$ (#6).

construct	*hs*GPC3$^{\Delta C}$	*hs*GPC3$^{\Delta C}$	*mm*GPC3$^{\Delta C}$
Condition	#3	#5	#6
Resolution range	75-3.00 (3.11-3.00)	43-2.64 (2.73-2.64)	44-2.90 (3.00-2.90)
spacegroup	$P3_2$	$P3_1$	$P3_121$
Reflections			
Refinement	15118 (328)	29400 (2668)	12069 (1155)
Rfree	778 (4)	1381 (143)	569 (60)
Rwork (%)	25.32 (33.30)	22.26 (34.76)	22.67 (30.03)
Rfree (%)	29.22 (31.94)	26.45 (42.33)	25.20 (36.41)
CCwork (%)	70.1 (50.0)	95.6 (67.3)	95.4 (76.5)
CCfree (%)	57.0 (16.1)	87.5 (50.2)	93.8 (56.5)
Protein residues	1037	715	355
Number of atoms			
Protein	8038	5527	2758
Glycans	81	56	28
Solvent	0	12	0
RMS(bonds)	0.005	0.007	0.004
RMS(angles)	0.970	1.050	0.673
Ramachandran			
Favoured (%)	97.58	97.26	98.25
Allowed (%)	2.22	2.74	1.75
Outliers (%)	0.2	0.00	0.00
Rotamer outliers (%)	0.00	0.00	1.97
Clashscore	8.62	10.26	5.08
Average B-factor	62.77	91.08	88.48
Macromolecules	62.76	91.10	88.39
Ligands	62.83	93.90	97.34
Solvent	-	71.01	-

3.2.4 The crystal structure of GPC3

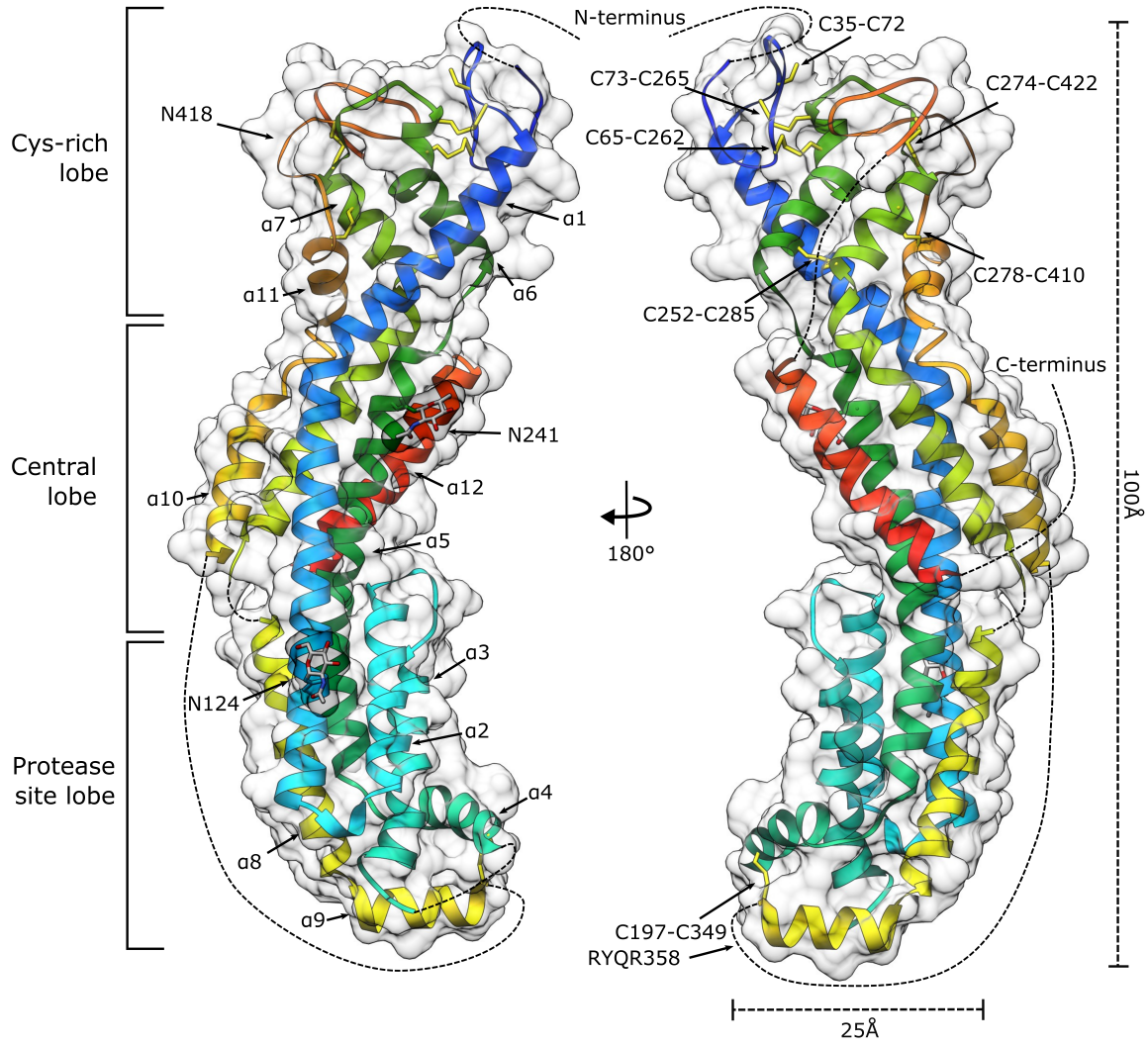


Figure 3.9: The crystal structure of *hs*GPC3$^{\Delta C}$. *hs*GPC3$^{\Delta C}$ (#5) is shown in cartoon and transparent surface repsresentation. The protein chain is coloured in rainbow from blue to red, from N-terminus to C-terminus. The structure is annotated for the observed helices (α1-12), the expected N-glycans (N124,N241 N418), and the disulfide bridges. Image was prepared in Chimera [68].

The crystal structure of *hs*GPC3$^{\Delta C}$ (chain A) reveals a similar fold to GPC1 (figure 3.9). The structure has a cylindrical shape (20 x 20 x 120 Å), in which the first resolved helix (α1) spans the entire protein. The cys-rich lobe is composed of helices, α1, α6, α7 and α11. The cys-rich lobe contains the N-glycosylation site N418, which was not sufficiently resolved in the crystal structure. The central lobe consists of a five-helix bundle, α1, α5, α7, α10, and α12. In addition, the central

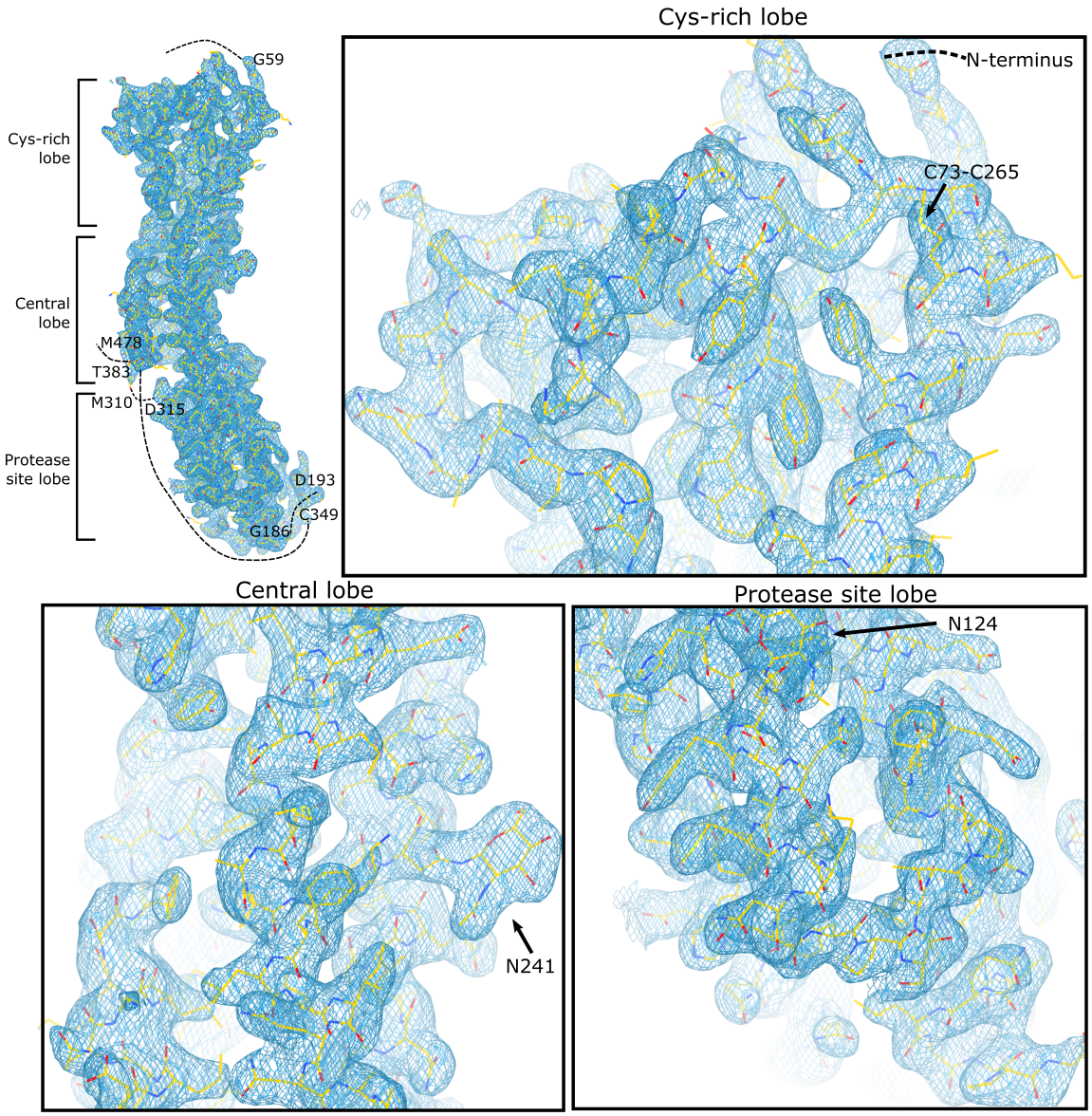


Figure 3.10: The electron density map of *hs*GPC3$^{\Delta C}$. The electron density map shown for three lobes of *hs*GPC3$^{\Delta C}$ (#5). The electron density map is in blue (2Fo-Fc, contour 1.0 σ), and the protein chain is shown as sticks, in which the carbons are coloured yellow, nitrogen as blue and oxygen as red. The map was calculated by the CCP4 programme FFT and the images were prepared in Chimera [68].

lobe contains the N-glycosylation site N241. The protease site lobe contains the helices, α2, α3, α4, α8, and α9, and contains the N-glycosylation site, N124. The large disordered loop, containing the furin cleavage site, from helix α9 to helix α10 was not resolved (C349-383). Several other regions were not resolved in the electron density which include the N-terminus, up to residue G59 and the C-terminus (P479-V483 and His-tag). Additionally, several loops were not resolved in the electron density which include residues between, G186-D193, M310-D315, and Q434-P455. A total of 78.5% of the residues were resolved for the human core protein GPC3$^{32\text{-}483}$.

The highest resolution data set electron density map is of high quality in which most side chains could be observed (figure 3.10). Two N-linked glycans were resolved, N124 and N241, in which there was enough density to confidently place one GlcNAc. The third N-linked glycan predicted site, N418, does present positive density in the Fo-Fc map, shown in figure 1.11. The residual density suggest that it requires the modelling of a glycan; however, it was not sufficiently resolved to confidently place a GlcNAc.

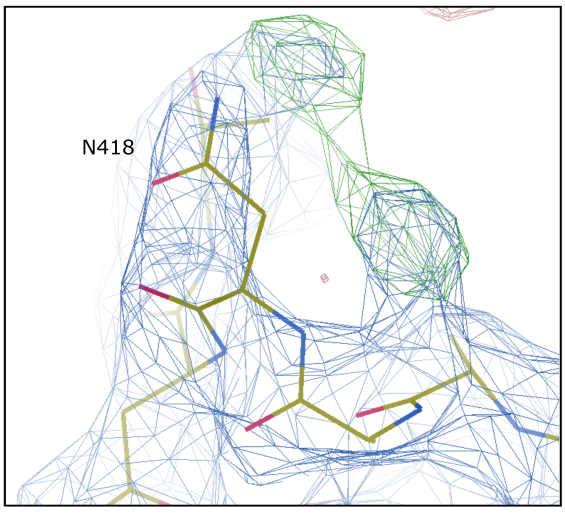


Figure 3.11: The electron density map at N-glycosylation site N418 for *hs*GPC3$^{\Delta C}$ (#5). Electron density map shown in blue (2Fo-Fc, contour 1.0 σ) and difference map shown in green (Fo-Fc,contour 3.0 σ). The protein chain is shown as atoms in which the carbon is coloured yellow, nitrogen as blue and oxygen in red. The difference map suggests the presence of an unmodelled atom but was not sufficiently resolved to place a glycan with confidence. The figure was prepared using Coot [304].

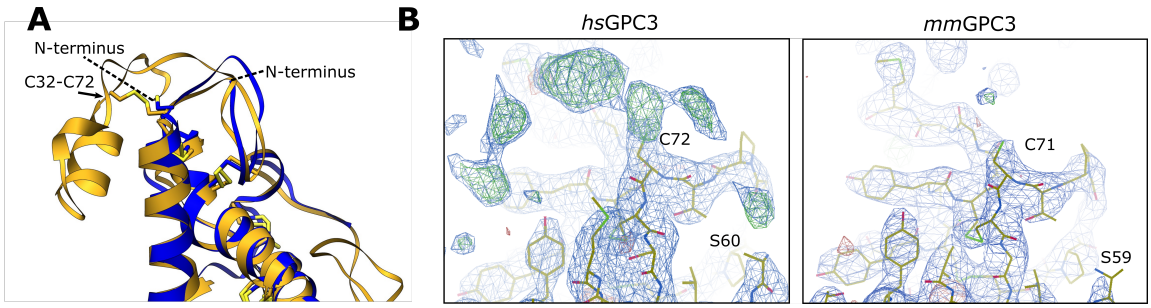


Figure 3.12: Unresolved N-terminus of GPC3$^{\Delta C}$ in both human (#5) and mouse (#6). A) Cartoon representation of *hs*GPC1 (yellow) and *hs*GPC3$^{\Delta C}$ (blue) reveals the unbuild N-terminus of GPC3.**B)** Electron density at the N-terminus for the crystal structure of *hs*GPC3$^{\Delta C}$ suggest the presence of parts of the N-terminus. **C)** Electron density at the N-terminus for the crystal structure of *hs*GPC3$^{\Delta C}$, which suggest that the N-terminus is not ordered in the crystal. The electron density map shown in blue (2Fo-Fc, contour 1.0 σ) and difference map shown in green (Fo-Fc, contour 3.0 σ). The protein chain is shown as atoms in which the carbon is coloured yellow, nitrogen as blue and oxygen in red. The structures were prepared using Chimera [68] and the electron density map was prepared in Coot [304].

The N-terminal region (32-44) was not sufficiently resolved to confidently build the N-terminus of GPC3. Residual density was observed for *hs*GPC3$^{\Delta C}$ but not for *mm*GPC3$^{\Delta C}$ (figure 1.12B). The density was especially visible near C72, which forms a disulfide bridge with C35 in the disordered N-terminus. I attempted to build the N-terminus from C35, however placement of the residues could not be done with confidence. Similar to DLP (PDB 3ODN) the N-terminus is disordered, while in the GPC1 (PDB 4YWT) structure, the missing N-terminus is structured and forms an alpha helix which is held by a disulfide bond (figure 3.12A).

3.2.5 Conformational change of GPC3

The SAD phased data suggested that GPC1 and GPC3 were conformationally different and when superimposing the crystal structure of GPC1 and GPC3 there is a clear conformational shift (figure 3.13). Superposing the central lobe of both glypican structures, the cys-rich and protease site lobe are rotated inwards, forming a concave surface in GPC3 (figure 3.13A). The Cα atom root mean square deviation (RMSD) was calculated for each atom pair using Chimera [68]. The crystal structure

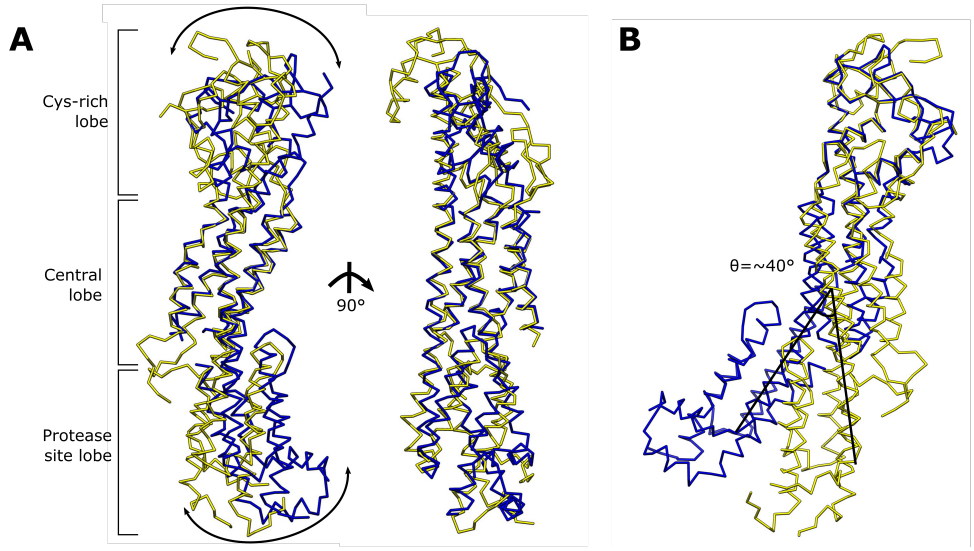


Figure 3.13: Structural comparison of GPC1 and GPC3. A) Aligned with respect to the central lobe of structure of GPC1 (PDB 4YWT) (yellow) and *hs*GPC3$^{\Delta C}$ (blue). **B)** Aligned with respect to the cys-rich. The GPC3 structures are depicted by their carbon backbone chain only. The structures were prepared using Chimera [68].

of GPC3 has a total RMSD of 6.03 Å across all 345 atom pairs compared to GPC1 (PDB 4YWT). Aligning GPC1 and GPC3 with respect to the cys-rich lobe further demonstrates the extend of the conformational rotation of 40° (figure 3.13B). Unlike DLP and GPC1, which also share only 25% sequence identity, their RMSD was calculated to be 2.6 Å [135]. This may present the structural variation between the two subfamilies within the glypican family.

4

Solving the Crystal Structure of the GPC3/Unc5D Complex

4.1 Summary

Deciphering the function of the GPC3 and Unc5 interaction is complicated by their interactions with different ligands and receptors. Structural tools can be used to obtain insight into the molecular mechanics involved in the protein-protein interactions. I used X-ray crystallography to solve the structure of the GPC3/Unc5 complex.

Using the models of GPC3 and the previously solved Unc5 (PDB 5FTT & 4V2A), and with the use of experimental phases, I solved the crystal structure of the GPC3/Unc5D complex. The crystal structure revealed a tightly packed octameric assembly, with a stoichiometry of four GPC3 and four Unc5D molecules. This octameric assembly was identified in two distinct crystal forms. The GPC3/Unc5 complex contains three distinct interfaces, which are highly conserved. The conservation of these interfaces is not present in GPC1, which support the data indicating that only GPC3 interacts with Unc5. This chapter will describe the process of the structure determination of the GPC3/Unc5D complex and present the resulting models.

4.2 Results

4.2.1 Crystallization of GPC3 and Unc5D

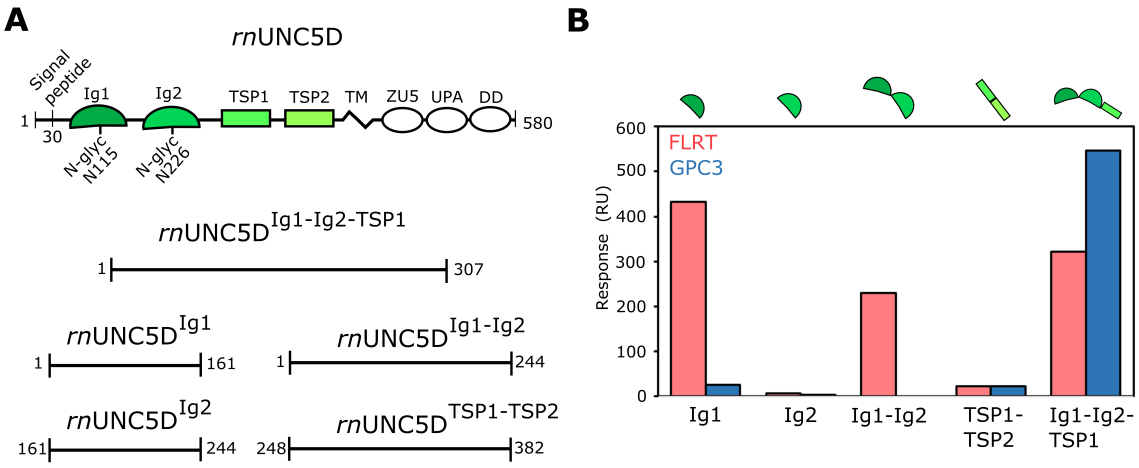


Figure 4.1: Minimal binding construct of Unc5 for GPC3 interaction. A) Previously cloned construct boundaries of *rn*Unc5D. **B)** SPR response of *mm*FLRT2^{LRR} (red) and *mm*GPC3$^{\Delta C}$ (blue) as ligands with different domains of *rn*Unc5D as analyte.

Like many cell surface receptors, Unc5 contains several ectodomains that are connected by a flexible linker. To identify the minimal domains required to interact with GPC3, preliminary SPR experiments were performed. Previously designed and expressed domains of *rn*Unc5D (provided by the lab) were injected as analyte over chips containing either *mm*FLRT2^{LRR} and *mm*GPC3$^{\Delta C}$ as ligands (figure 4.1). For FLRT2^{LRR}, any construct which contained the Ig1 domain of Unc5 resulted in an increase in response, as previously published [54]. Contrary to this, GPC3 was unable to bind to either individual Ig domains, the combined domains of *rn*Unc5D$^{Ig1\text{-}Ig2}$ and *rn*Unc5D$^{TSP1\text{-}TSP2}$. Binding was only observed with the construct containing all three domains *rn*Unc5D$^{Ig1\text{-}Ig2\text{-}Tsp1}$, where it had a binding affinity of 260 *nM* (previously determined by the lab). Prior to starting, first hit crystals of construct *rn*Unc5D$^{Ig1\text{-}Ig2\text{-}Tsp1}$ with *mm*GPC3$^{\Delta C}$ (7.5 mg/ml) and 200 *mM* NDSB-256 were identified by the lab in the commercial screen PGA, well G5 (#7). These crystals only diffracted to ~6 Å. The crystallization conditions are summarized at the end of this section.

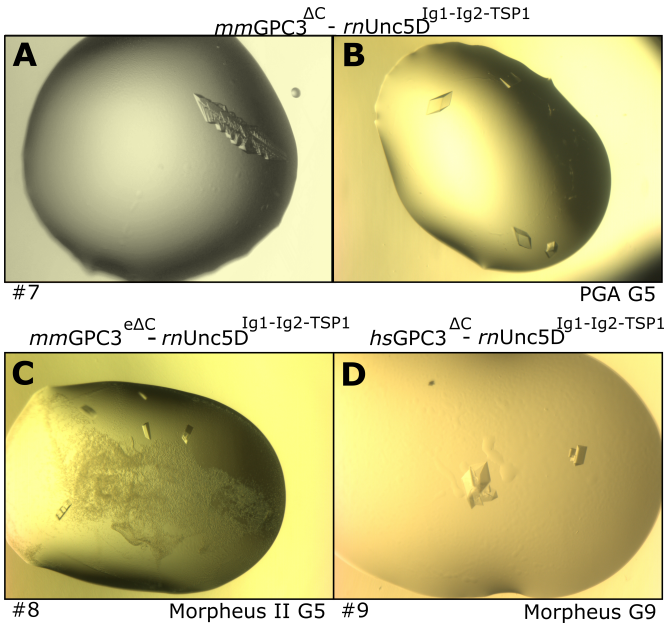


Figure 4.2: Crystals of the GPC3/Unc5D protein complex (#7, #8, and #9). **A)** Starting crystals of condition #7. **B)** Optimized crystals of condition #7 after seeding. **C)** Crystals of condition #8 which were obtained in Morpheus II, well G5. **D** Crystals of condition #9 which were obtained in Morpheus, well H10.

To optimice the crystallization condition #7, I expressed both constructs in HEK293S cells, and subsequently mixed them in a one-to-one ratio. A final concentration of 200 *mM* NDSB-256 was added to the mixture and concentrated to 7.8 mg/ml. Dilution screens of # 7 (100%-60%) were prepared with 150:150 and 200:100 *nl* protein to crystallization buffer. The reproduced crystals presented a crystal morphology of stacked sheets in a needle-like shape (figure 4.2A). Using standard optimization methods of gradient and additive screens did not yield single crystals (S2.5.1). Therefore, I used repeated seeding into gradient screen to improve the quality of the seeds and promote single and higher quality crystals [326, 327]. After several cycles of repeated seeding, I was able to obtain crystals that appeared singular (figure 4.2B). After several attempts of optimization, the best diffracting crystals diffracted to approximately 3.8 Å.

Different protein constructs were trialled for crystal hits. The C-terminus extended *mm*GPC3 (residue 31 to 488), termed *mm*GPC3$^{e\Delta C}$ with *rn*Unc5D$^{Ig1\text{-}Ig2\text{-}Tsp1}$ were expressed in HEK293S cells, mixed in a one-to-one molar ratio and concentrated

Table 4.1: Crystallization conditions for the GPC3/Unc5D complex.

#	Construct	Condition	Res. (Å)
7	*mm*GPC3$^{\Delta C}$ *rn*Unc5D$^{\Delta Ig1\text{-}Ig2\text{-}TSP1}$	0.1M Tris (pH 7.8); 5% w/v γ-PGA; 20% w/v PEG 3350	3.8
8	*mm*GPC3$^{e\Delta C}$ *rn*Unc5D$^{\Delta Ig1\text{-}Ig2\text{-}TSP1}$	0.1M Gly-Gly/AMPD (pH 8.5); 15% w/v PEG3000; 20% v/v 1,2,4-butanetrol, 1% w/v NDSB256; 0.02M (DL-Arginine HCL; DL-Threonine; DL-Histidine HCL; DL-5-hydroxylysine HCL; trans-4-hydroxyl-L-proline)	4.5
9	*hs*GPC3$^{\Delta C}$ *rn*Unc5D$^{\Delta Ig1\text{-}Ig2\text{-}TSP1}$	0.1M Tris/BICINE (pH 8.5); 20% Ethylene glycol; 10% w/v PEG 8000; 0.02M (L-Na-Glutamate; Alanine; Glycine; Lysine HCL; Serine)	4.1

to 5.0 mg/ml. Crystallization screens were set up as described above and crystals were obtained using the commercial Morpheus II screen, in condition G5 (Figure 4.2C; #8). The crystals diffracted to 4.5 Å. The human construct *hs*GPC3$^{\Delta C}$ with *rn*Unc5D$^{Ig1\text{-}Ig2\text{-}Tsp1}$ were prepared as discussed above, and concentrated to 6 mg/ml. Crystals were obtained using the commercial screen Morpheus, condition H10 (figure 4.2D; # 9). The crystal diffracted anisotropically to 4.1 Å. Importantly, the crystals obtained indexed into a different spacegroup and unit cell, compared to #7. With the three data sets of #7, #8 and #9, I aimed to solve the crystal structures of GPC3/Unc5D.

4.2.2 Data collection and processing

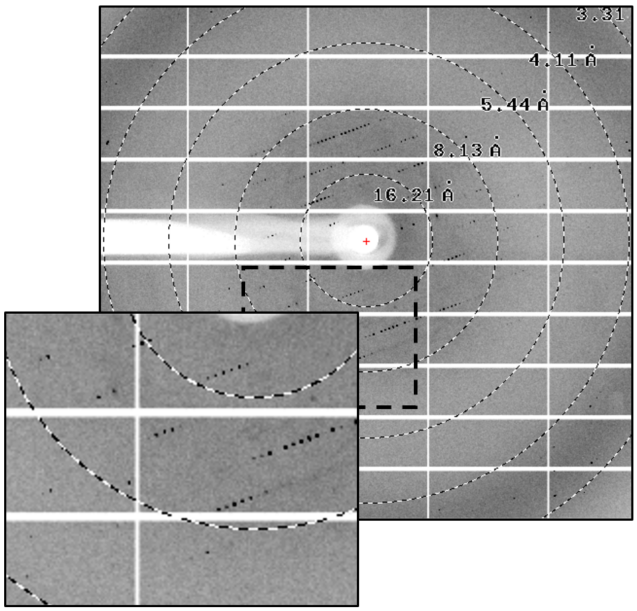


Figure 4.3: Data collection diffraction image of *mm*GPC3$^{\Delta C}$ and *rn*Unc5D$^{\text{Ig1-Ig2-TSP1}}$. An example diffraction image of data collected for crystals of #7. A magnified region (dashed line box) shows clear and well-separated reflections. The image was obtained from the ADXV viewer [317].

All crystals were screened at the Diamond Lightsource synchrotrons and at the European Synchrotron Radiation Facility (ESRF). The best crystal datasets, which were used for the structure solution, were collected at the Diamond light source beamlines i03, i04, and i04-1, for #7, #8, and #9 respectively. The data collection parameters are summarized in table 4.2. Data collection for crystals from #8 was performed at the Diamond-CCP4 data collection and structure solution workshop course in December 2018. To ensure that there was minimal spot overlap, the detectors were placed as far as possible from the crystal (figure 4.3).

Data was processed using the automated pipeline of Xia2, which uses Dials for integration and Aimless for merging the data set in the appropriate spacegroup. As discussed before, the crystals were analysed for radiation damage by observing the R_{merge} across image batches, and radiation damaged images were excluded (S2.5.3). The best data set of *mm*GPC3$^{\Delta C}$ and *rn*Unc5D$^{\text{Ig1-Ig2-TSP1}}$ (#7) was obtained by

Table 4.2: Data collection parameters and data statistics for the GPC3/Unc5 Complex. Data collection parameters and data statistics for #7 (*mm*GPC3$^{\Delta C}$/*rn*Unc5D$^{\text{Ig1-Ig2-TSP1}}$), #8 (*mm*GPC3$^{e\Delta C}$/*rn*Unc5D$^{\text{Ig1-Ig2-TSP1}}$) and #9 (*hs*GPC3$^{\Delta C}$/*rn*Unc5D$^{\text{Ig1-Ig2-TSP1}}$).

Construct	*mm*GPC3$^{\Delta C}$ *rn*Unc5D	*mm*GPC3$^{e\Delta C}$ *rn*Unc5D	*hs*GPC3$^{\Delta C}$ *rn*Unc5D
Condition	#7	#8	#9
Beamline	i03	i04	i04-1
Wavelength (Å)	0.800	0.980	0.992
Beam size (μm)	50x20	32X20	50X50
Oscillation (°)	0.2	0.1	0.2
Exposure (s)	0.2	0.119	0.2
Transmission (%)	100	100	100
Number of Images	2X900	3600	900
Space group	$P3_121$	$P2_1$	$P2_1$
Cell dimensions			
a, *b*, *c* (Å)	119.6,119.6,257.9	102.2,157.8,126.6	102.6,157.6,126.6
α, β, γ (°)	90.0, 90.0, 120	90, 103.0, 90	90.0, 103.0, 90.0
Resolution (Å)	80.8-3.80 (4.02-3.80)	61.88-4.60 (4.76-4.60)	123-4.1 (4.55-4.10)
Completeness (spherical)(%)	72.6 (24.0)	99.70 (100)	58.4 (11.0)
Completeness (ellipsoidal) (%)	92.9 (99.6)		89.2 (72.1)
Rmerge (%)	7.4 (256.1)	9.28 (82.8)	10.9 (73.0)
$CC_{1/2}$ (%)	99.8 (63.1)	99.7 (48.5)	99.4 (73.8)
I/σI	13.3 (1.4)	7.77 (1.81)	3.3 (1.6)
Multiplicity	15.5 (14.5)	6.6 (6.4)	3.3 (3.5)

merging two isomorphous datasets. Data sets #7 and #9 had particular strong anisotropy and were processed using the Staraniso server, the data statistics per resolution shell are summarized in appendix B.2 & B.3. Crystals from #7 diffracted in the best plane to 3.8 Å and in the other two planes to 4.7 Å. Condition #9 diffracted in the best plane to 4.1 Å, in which the other two planes diffract to 4.6 Å and 4.3 Å. The final processed data of condition #7, #8 and #9 are summarized in table 4.2.

4.2.3 Phasing of the crystal complex data

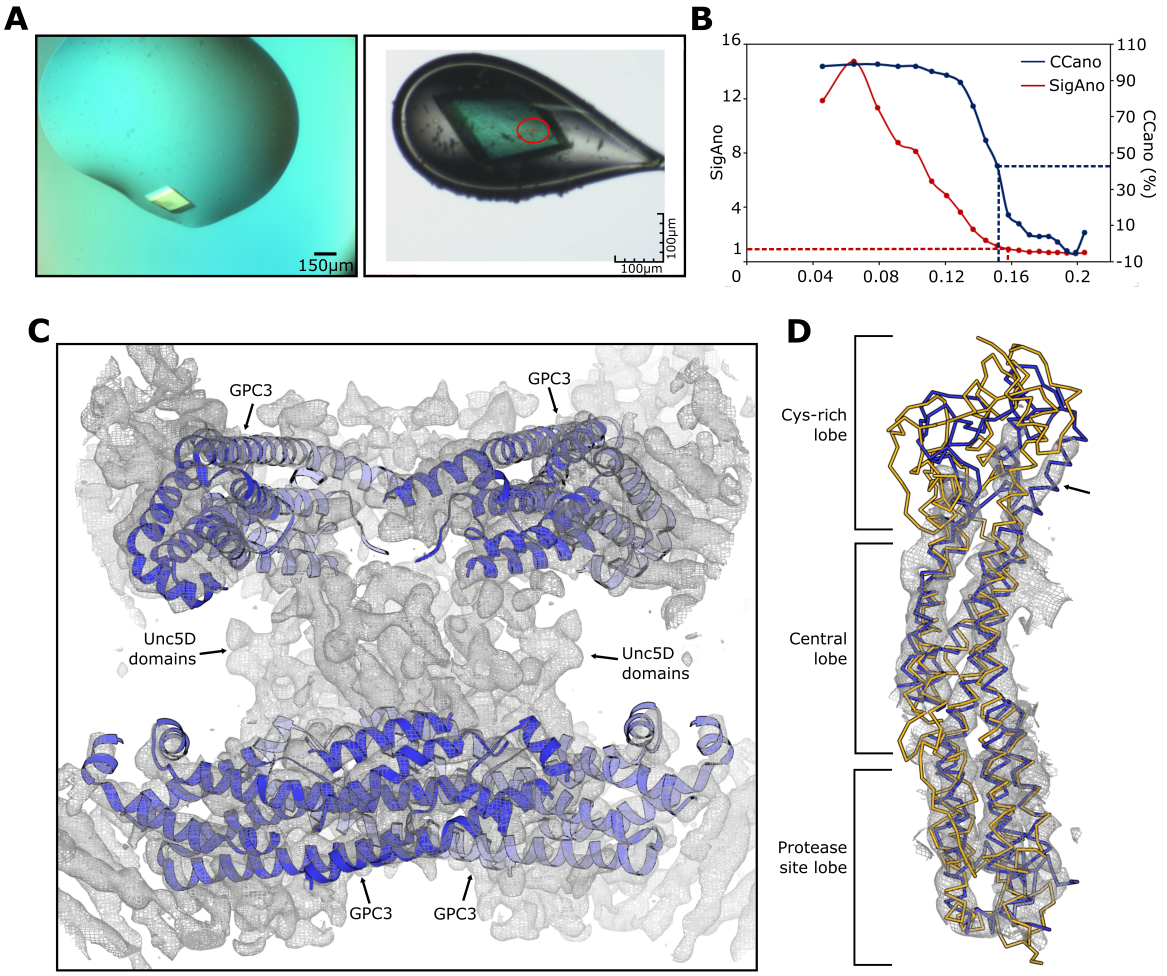


Figure 4.4: Experimental phasing of crystal (#7) containing *mm*GPC3$^{\Delta C}$ and *rn*Unc5D$^{Ig1\text{-}Ig2\text{-}TSP1}$. A) Condition #7 crystal before soaking and after 24-hour soak with TaBr and mounted on the goniometer. **B)** Anomalous correlation (blue) and SigAno (red) plotted against the reciprocal of the resolution. Significant anomalous signal went to a resolution of 6.6 Å, shown with the dashed line. **C)** Experimentally phased map after density modification using Phenix Autosol, shown in grey for clarity (2Fo-Fc, contour level σ 1.0). The map shows density for α-helices, which was sufficient to place GPC3 in, shown as a cartoon (blue). Residual density corresponds to the small Ig domain of Unc5D. **D)** Placed GPC1 (yellow) and GPC3 (blue) carbon backbone models in the experimental electron density map. Part of GPC1 deviates from the electron density, which is indicated by the arrow. Images were prepared in Excel and Chimera [68].

Experimental phases were obtained for crystal *mm*GPC3$^{\Delta C}$/*rn*Unc5D$^{Ig1\text{-}Ig2\text{-}TSP1}$ (#7). The experimental electron density map demonstrated that GPC1 was not a suitable as a homology model, which directed me to solve the structure of GPC3.

Crystal soaking was performed as described in the material and methods section (S2.5.1). Before data collection, for each heavy atom soak, a fluorescence scan of the crystal was performed to determine the presence of the heavy metal, and empirically determined the atom specific absorption peak and inflection point. In the case of this project, the crystals soaked with the Ta_6Br_{12} had a strong anomalous signal and was still able to diffract to a reasonable resolution of 4.9 Å . In the literature, Ta_6Br_{12} clusters have been successfully employed in solving several low resolution structures owning to their ability to act as super scatters at a low resolution [328, 329].

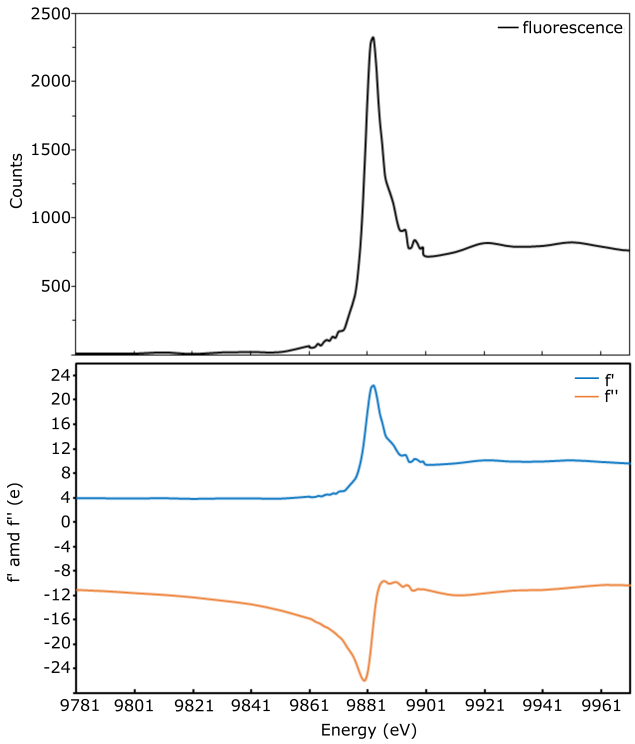


Figure 4.5: Fluorescence scan of Ta_6Br_{12} derivative *mm*GPC3$^{\Delta C}$ and *rn*Unc5D$^{Ig1\text{-}Ig2\text{-}TSP1}$ (#7). Scan around of the L-III edge of tantalum. The scan shows an emission peak at 9.8811 keV. Image was prepared in Excel.

Ta_6Br_{12} derivative data was collected at Diamonds tuneable beamline i04. The wavelength was set to the peak of the L-III edge of the tantalum atom, which was determined to be 1.2545 Å (9.8811 keV; figure 4.5). The anomalous dispersion coefficients, f' and f", were calculated to be -15.86 and 22.35, respectively. The data collection parameter used for the best anomalous data set is summarized in table 4.3.

Table 4.3: Data collection parameters for TaBr derivative *mm*GPC3$^{\Delta C}$/*rn*Unc5D$^{Ig1\text{-}Ig2\text{-}TSP1}$ (#7) crystals (#7).

Construct	*mm*GPC3$^{\Delta C}$ *rn*Unc5D$^{Ig1\text{-}Ig2\text{-}TSP1}$
Condition	#7
	TaBr Derivative
Beamline	i04
Wavelength (Å)	1.2545
Beam size (μm)	65X50
Oscillation (°)	0.2
Exposure (s)	0.2
Transmission (%)	100
Number of Images	2X900

The Ta_6Br_{12} derivative crystals were processed using the automated pipeline Xia2, using XDS and Xscale. Both the R_{merge} data statistics of the merged (I+ & I-) and unmerged (I+/I-) intensities are shown (table 4.5). Data was collected on two regions of the best crystal. These two datasets were subsequently merged after images with radiation damaged were removed. Significant anomalous signal was obtained to 6.6 Å (figure 4.4B). The data was processed using the Staraniso server. The final native and derivative data statistics are summarized in table 4.4. Soaking with TaBr resulted in a 5 Å shrinkage in the c direction.

Ta_6Br_{12} derivative crystals were experimentally phased using the automated structure solution pipeline of Phenix Autosol, which combines HYSS/Phaser LLG, to find heavy-atom sites and Resolve for density modification. Twelve refined heavy atom sites were found. Density modification, with NCS, was performed assuming two copies of both *mm*GPC3$^{\Delta C}$ and *rn*Unc5D$^{Ig1\text{-}Ig2\text{-}Tsp1}$, with a solvent content of 59.6%. The resulting electron density map reveals an α-helical bundle, corresponding to GPC3, and residual density for several Ig domains (figure 4.5C). Using these maps, Two GPC3 were manually placed, in which the central and protease site lobe fit density satisfactorily (figure 4.4D). Approximately 60% of the asymmetric unit was thereby modelled.

Table 4.4: Processed data statistics for the native and TaBr derivative crystals of *mm*GPC3$^{\Delta C}$/*rn*Unc5D$^{Ig1\text{-}Ig2\text{-}TSP1}$ (#7).

Construct		*mm*GPC3$^{\Delta C}$ *rn*Unc5D$^{Ig1\text{-}Ig2\text{-}TSP1}$
Condtion		#7
	Native	TaBr derivative
Space group	$P3_121$	$P3_121$
Cell dimensions		
a, *b*, *c* (Å)	119.6,119.6,257.9	118.7, 118.7, 252.9
α, β, γ (°)	90.0, 90.0, 120	90.0, 90.0, 120
Resolution (Å)	80.8-3.80 (4.02-3.80)	95.2-4.90 (5.17-4.90)
Completeness (spherical)(%)	72.6 (24.0)	79.6 (29.5)
Completeness (ellipsoidal) (%)	92.9 (99.6)	89.9 (75.0)
Rmerge (I+ & I-) (%)	7.4 (256.1)	12.0 (147.6)
Rmerge (I+/I-) (%)		6.1 (1.47.7)
$CC_{1/2}$ (%)	99.8 (63.1)	99.7 (78.0)
I/σI	13.3 (1.4)	20.2 (2.4)
Multiplicity	15.5 (14.5)	18.6 (17.2)

4.2.4 Structure solutions and refinement

GPC3$^{\Delta C}$ was superposed on the Ta_6Br_{12} derivative map and this partial model was used for MR in the native data set. A clear solution was identified (TFZ>8.0) in all three data sets. Identifying Unc5 in the low-resolution data, through manual placement or MR was especially difficult. This was because of the inherent flexibility between the small domains of Unc5, corresponding to ∼13, ∼10 and ∼8 kDa for Ig1, Ig2 and TSP1 respectively. Placement was further complicated by the fact that each domain is composed of β-sheets and loops. Using the fixed solutions of GPC3 and subsequent density modification of the individual crystal data sets, and cross-crystal averaging density modification using data from #7 and #8, resulted in sufficient density to place one Ig2 domain with confidence (figure 4.6A). Density at the N-glycosylation site (N226) validated the placement (figure 4.6B). Using the non-crystallographic symmetry of the GPC3 chains, the remaining Ig2 domains could be placed. The Ig1 and TSP1 domains were placed, by superposing the previously

solved Unc5D structure on the placed Ig2 domains. Manual rigid body refinement in coot was done to orientate the individual domains correctly, completing the models.

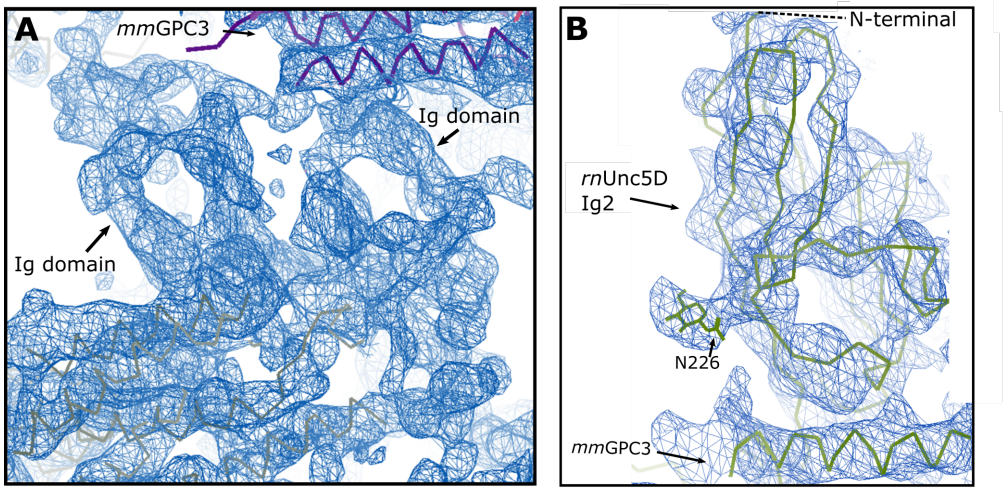


Figure 4.6: Density modification reveals the small globular Ig domain of Unc5. Residual electron density maps after density modification (2Fo-Fc, contour level σ 1.0, blur of 60) near the GPC3 chains (Dark blue and grey) **A)** Density modification using Phenix Resolve with NCS reveals domains corresponding to two Ig2 domains. **B)** Placed Ig2 domains reveals density that corresponds to the N-glycosylation site N226. Image was obtained prepared in Coot.

Initial refinement of all three data sets was done using AutoBuster for Rigid body refinement, in which each domain of Unc5 was defined separately. Afterwards, all atom and group B-factor refinement was performed using Phenix Refine. Two groups per residue were assigned for B factor refinement, these included the side chain and alpha backbone. Refinement was restrained, using NCS, secondary structure and reference structure restraints. The target restraints used the crystal structure of *mm/hs*GPC3$^{\Delta C}$ and *rn*Unc5D$^{\text{Ig1-Ig2-Tsp1}}$ (PDB 5FTT). Manual building of the N-glycans was done using Coot [304]. In the final stages of refinement TLS groups (1 group per chain) were added and refinement was performed until convergence. For the data sets of #7 and #8, relatively clear electron density maps were obtained (figure 4.7), and the final geometry and map statistics are within reasonable range for the working resolution (table 4.5).

Refinement of #7 stalled at a high R_{work}/R_{free}. Considering the alternative crystal form did not have a two-fold axis along the 4:4 stoichiometry, I considered a

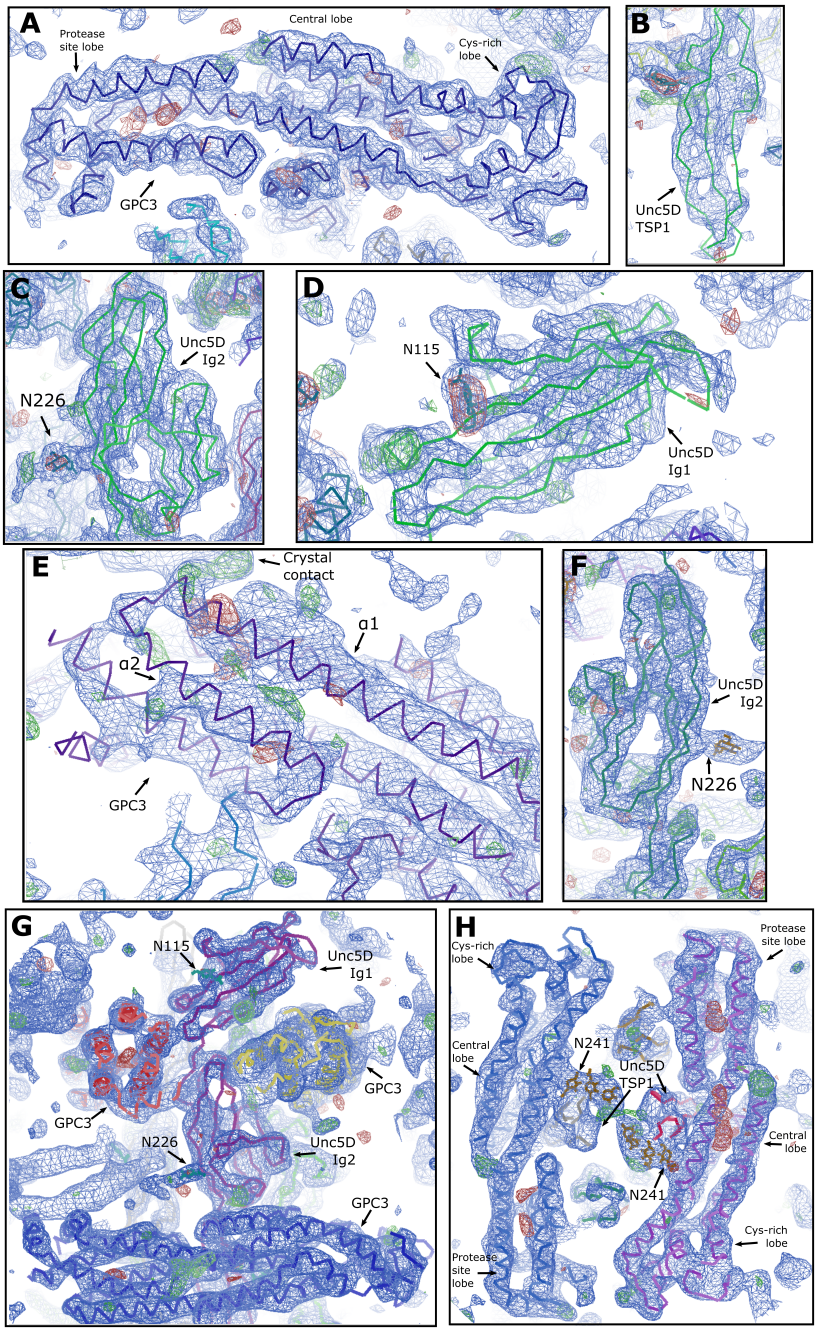


Figure 4.7: Electron density maps of the GPC3/Unc5 complex. In all figures, the protein models are depicted as C-alpha carbons with N-glycosylation sugars. **A-D)** Electron density maps of #9. **A)** Electron density of *hs*GPC3$^{\Delta C}$ **B)** Electron density of the TSP1 domain. **C)** Electron density of the IG2 domain **D)** Electron density of Ig1, only one of the NCS copies had clear density (as shown here) **E-F)** Electron density maps for #7. **E)** The electron density suggesting a conformational change near the protease site lobe of GPC3 **F)** Electron density of Ig2, with clear density of its glycosylation site. **G-H)** Electron density of #8. **G)** Electron density around the Ig1 and Ig2 domains. **H)** Electron density around two copies of GPC3 with clear extension around its N-glycosylation sites. All figures have their electron density map shown in blue (2Fo-Fc, contour level σ 1.0) and difference map shown in green and red (Fo-Fc,contour level $\pm$ σ 3.0). The images were prepared in Coot.

possible pseudosymmetry. The dataset was reindexed into spacegroup $P3_1$. After placing two additional copies of GPC3 and Unc5 (using NCS), the model was refined further. The R_{work}/R_{free} statistics improved from >40% to 32.9/37.2%; however, no further improvement was obtained. Closer inspection of the electron density map revealed a very poor region at the GPC3 protease site lobe. The difference map indicates that the model underwent a slight conformational change, which is only present in two of the four NCS copies. These NCS copies are at a crystal contact which may have resulted in this conformational change. To fit the model to the data better, and so improve R_{work}/R_{free}, extensive manual model building would be required; however, at this low resolution this cannot be done with confidence, and so no further refinement was performed.

The models obtained after restraint refinement are summarized in table 4.5. The models obtained for *mm*GPC3$^{e\Delta C}$ and *rn*Unc5D$^{Ig1\text{-}Ig2\text{-}Tsp1}$ (#8), and *hs*GPC3$^{\Delta C}$ and *rn*Unc5D$^{Ig1\text{-}Ig2\text{-}Tsp1}$ (#9) were of better quality, and so were used for scientific interpretation.

Table 4.5: Refinement and model geometry statistics for the GPC3/Unc5 complex.

Construct	*mm*GPC3$^{\Delta C}$ *rn*Unc5D	*mm*GPC3$^{e\Delta C}$ *rn*Unc5D	*hs*GPC3$^{\Delta C}$ *rn*Unc5D
Condition	#7	#8	#9
Resolution range	40.4-4.0 (4.1-4.0)	61.9-4.60 (4.76-4.60)	84.5-4.10 (4.25-4.10)
Spacegroup	$P3_1$	$P2_1$	$P2_1$
Reflections			
Refinement	25960 (970)	21813 (2165)	18398 (284)
Rfree	1328 (50)	1867 (185)	899 (20)
Rwork (%)	32.87 (41.08)	28.97 (40.01)	28.47 (36.92)
Rfree (%)	37.22 (42.30)	31.62 (41.31)	30.38 (44.30)
CCwork (%)	87.4 (34.5)	87.9 (55.7)	84.3 (53.3)
CCfree (%)	81.3 (33.2)	85.5 (60.8)	87.1 (69.4)
Protein residues	2408	2416	2412
Number of atoms			
Protein	18955	19216	19184
Glycans	315	293	282
RMS(bonds)	0.005	0.004	0.005
RMS(angles)	1.16	0.91	1.02
Ramachandran			
Favoured(%)	96.86	96.95	96.69
Allowed (%)	2.92	2.75	3.14
Outliers (%)	0.21	0.30	0.17
Rotamer outliers (%)	3.64	0.00	0.09
Clashscore	8.69	9.98	12.02
Average B-factor	301.39	359.52	201.05
Macromolecules	303.85	361.36	203.14
Ligands	153.51	239.12	58.57

4.2.5 The crystal structure of GPC3 and Unc5D

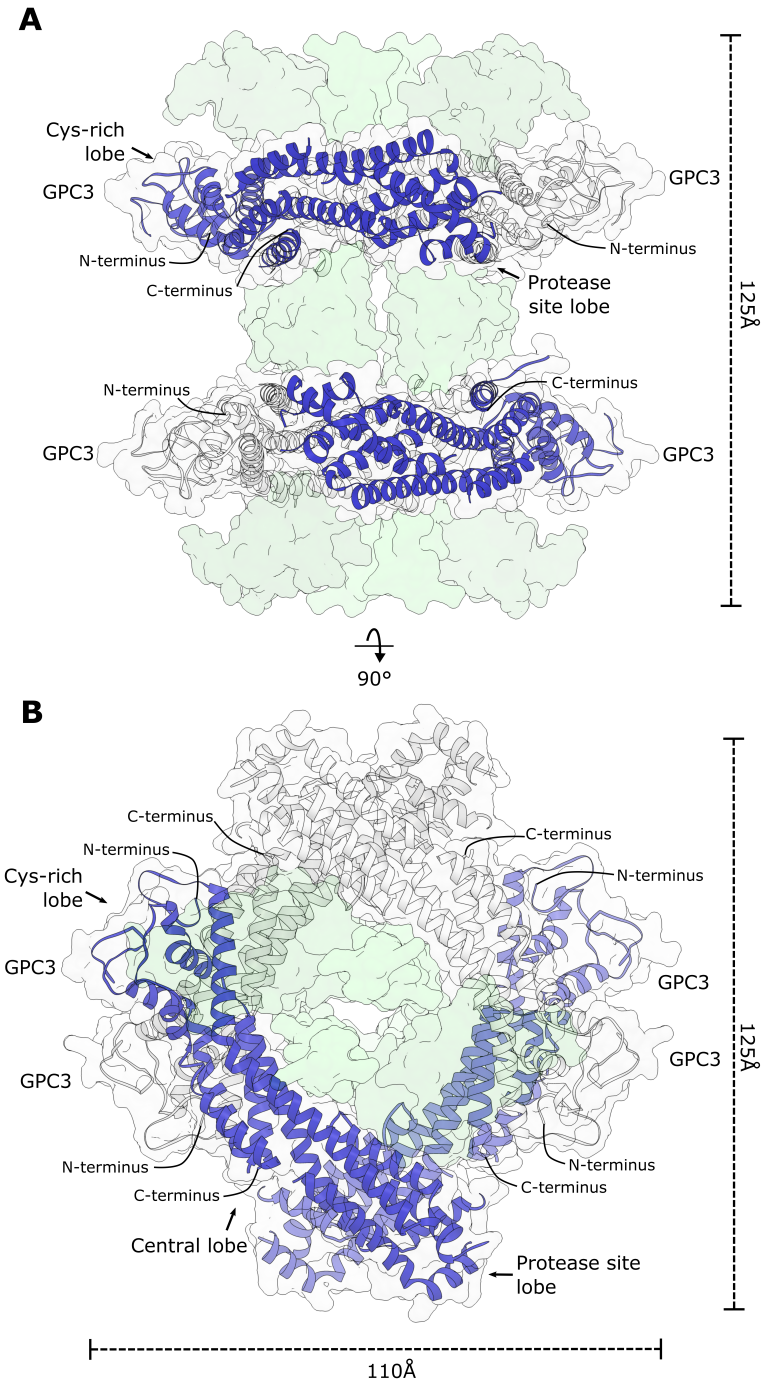


Figure 4.8: GPC3 inside the octameric assembly of the *hs*GPC3$^{\Delta C}$/*rn*Unc5D$^{Ig1\text{-}Ig2\text{-}TSP1}$ complex. GPC3 is depicted as cartoon ribbons with transparent white surfaces. For clarity, two GPC3 chains are shown in blue and two in white. Unc5 is shown as transparent green surfaces. The side view of the octameric assembly **(A)**, and the top view of the octameric assembly **(B)** are shown.

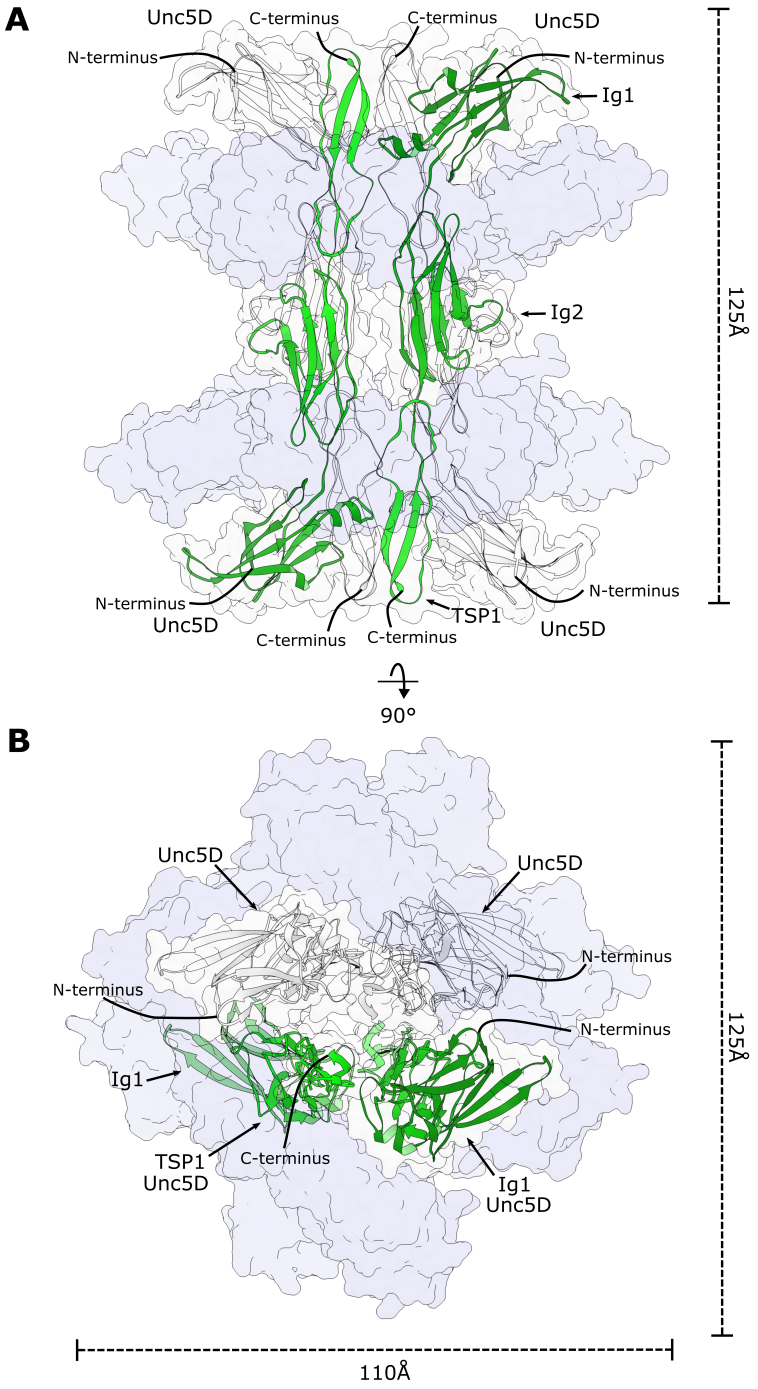


Figure 4.9: Unc5D inside the octameric assembly of the *hs*GPC3$^{\Delta C}$/*rn*Unc5D$^{Ig1\text{-}Ig2\text{-}TSP1}$ complex. Unc5D is depicted as cartoon ribbons with transparent white surfaces. For clarity, two Unc5D chains are shown in shaded in green, from the N-terminus (dark green) to the C-terminus (light green), and two chains in white. GPC3 is shown as blue transparent surfaces. The side view of the octameric assembly **(A)**, and the top view of the octameric assembly **(B)** are shown.

The crystal structure of the complex reveals a tightly packed octameric assembly, containing four GPC3 and four Unc5D chains. In this octameric assembly, GPC3 resembles a scaffold protein which encloses the four copies of Unc5D (figure 4.8). In the middle of the assembly are the four Unc5D molecules, in which four Ig2 domains are brought into proximity. Furthermore, the Unc5D molecule is arranged in an alternating antiparallel configuration (figure 4.9). The octameric arrangement is present in both crystal forms, of which both crystal forms contain different crystal contacts (figure 4.10). The obtained crystal structure is consistent with the binding study, in which GPC3 requires both the Ig and TSP1 domains to interact.

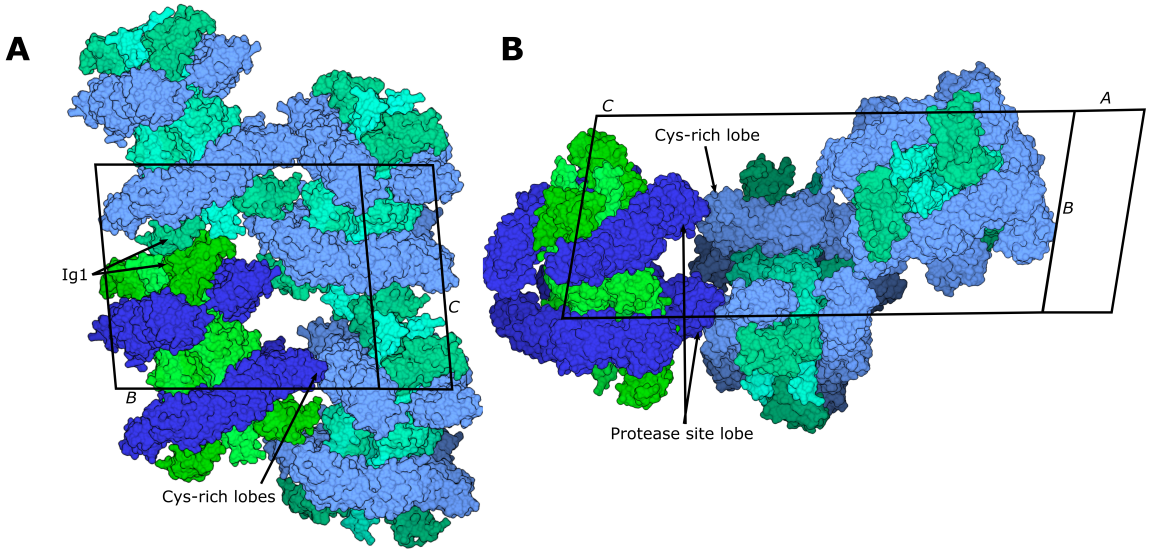


Figure 4.10: The GPC3/Unc5 complex in two crystal forms. Crystal packing of the GPC3/Unc5D complex, in which the 4:4 assembly of GPC3 (dark blue) and Unc5D (green) shown with a surface representation. The unit cells is depicted as a black box.**A)** Crystal packing of crystals from *hs*GPC3$^{\Delta C}$/*rn*Unc5D$^{\text{Ig1-Ig2-TSP1}}$ (#7) and *mm*GPC3$^{\text{e}\Delta C}$/*rn*Unc5D$^{\text{Ig1-Ig2-TSP1}}$ (#8). **B)** Crystal packing of crystals from *mm*GPC3$^{\Delta C}$/*rn*Unc5D$^{\text{Ig1-Ig2-TSP1}}$ (#6). Structures were prepared in Chimera [68].

Within this assembly, three surfaces can be identified between GPC3 and Unc5D. Interestingly, one GPC3 forms contacts with three different Unc5 molecules, and vice versa. The following surface area of the interfaces were calculated using the PISA server [330]. Interface 1 consist of a small contact between the linker region of the Ig1-Ig2 domain with the protease site lobe of GPC3 (figure 4.11A). The surface area could not be determined for this interface. This may a consequence of the

linker region not being well resolved; also, it is near the large unresolved loop of GPC3. Interface 2 is the largest interface between GPC3 and Unc5D (598.0 Å^2; figure 4.11B), in which several hydrophobic residues are buried by the interactions (solvation free energy of -5.5 ΔG determined by PISA [330]). This interaction may be further mediated by the N-glycosylation of GPC3 (N241), which contains ordered glycans. These glycans form close interactions with residues of the TSP1 domain, especially S255 and N279. The similar fold of thrombospodin-1 type 1 repeats have been suggested to interact with glycans, suggesting that this function could be maintained in the TSP domains of Unc5 [331]. Interface 3 also involves the Ig1-Ig2 domains; however, the contact is made with the anterior side of the Ig1-Ig2 domains, to the cys-rich lobe (278.2 Å^2; figure 4.11C). Importantly, the contact surface area could be larger as this interface is near the unresolved N-terminal region of GPC3.

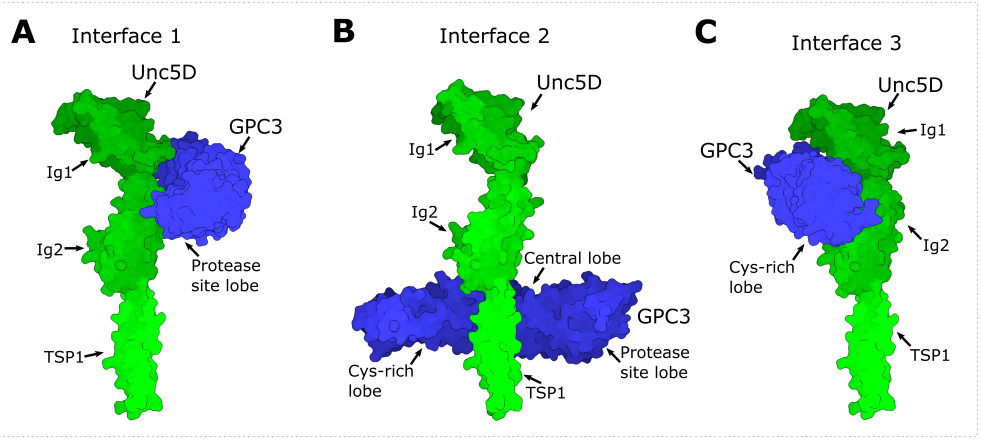


Figure 4.11: The three interfaces of GPC3/Unc5D. *hs*GPC3$^{\Delta C}$ (dark blue) and *rn*Unc5D$^{\text{Ig1-Ig2-TSP1}}$ (Green) are shown with a surface representation. Interface 1 consist of Unc5Ds Ig1-Ig2 linker with the protease site of GPC3. Interface 2 consist of the interface between Unc5Ds TSP1 domain and central lobe of GPC3 (598.0Å^2). Interface 3 consist of the interface between Unc5Ds anterior side of the Ig1-Ig2 domains and the cys-rich lobe of GPC3 (278.2Å^2). Structures were prepared in Chimera [68] and the surface area were calculated using the PISA server [330].

4.2.6 Conservation of the binding interfaces

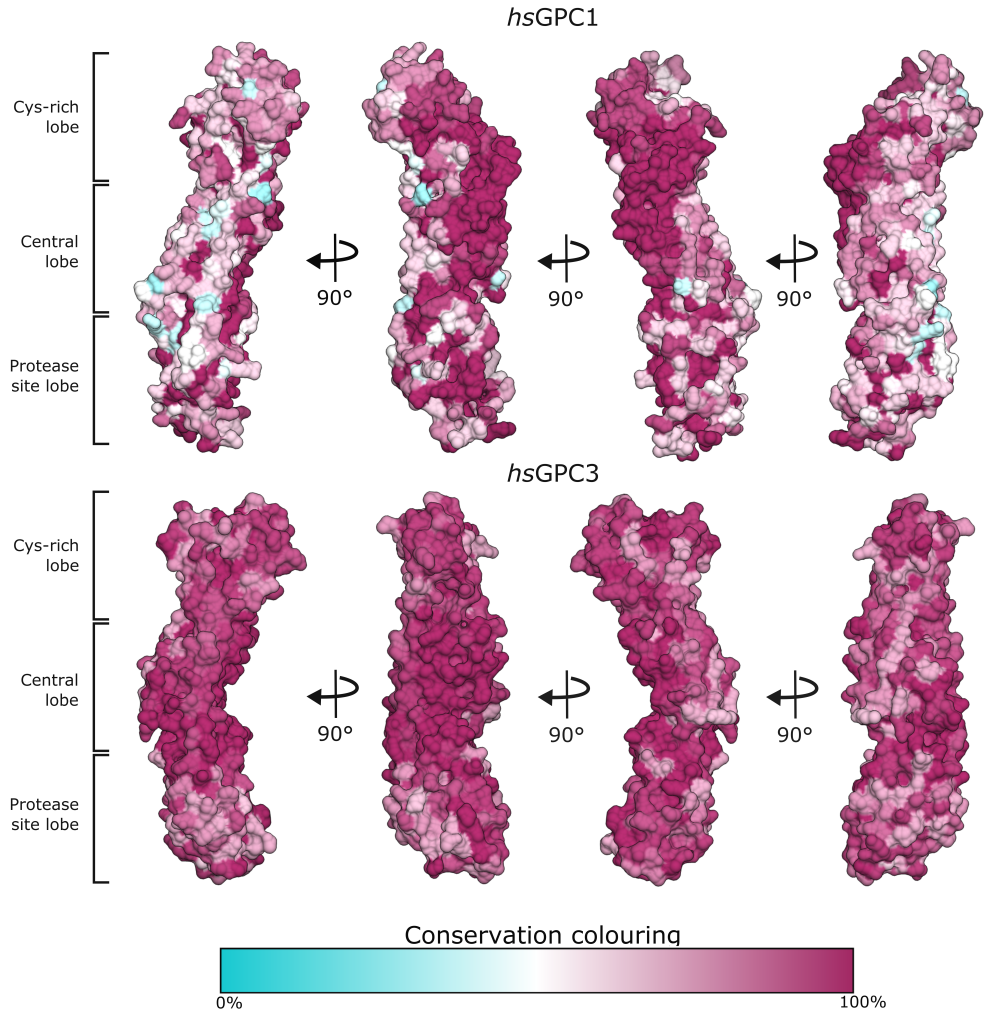


Figure 4.12: Surface conservation of *hs*GPC3$^{\Delta C}$ and GPC1. GPC1 and GPC3 are represented as surfaces with the same orientation. **A)** Surface conservation of GPC1 (PDB 4YWT). Sequences of human, chimpanzee, marmoset, mouse, rat, dog, mallard, bovine, horse, platypus, chicken, turkey, and frog were used. **B)** Surface conservation of *hs*GPC3$^{\Delta C}$. Sequences of human, chimpanzee, orangutan, gibbon, macaque, mouse, rat, rabbit, squirrel, dog, cat, ferret, opossum, mallard, bovine, horse, pig, giant panda, platypus, chicken, and finch were used (appendix C.1 and C2). Conservation of both GPC1 and GPC3 was coloured and shaded according to the same percentage boundaries. The degree of conservation is depicted from 0% (cyan) to 50% (white) to 100% (maroon). Conservation scores were obtained by the Consurf server [332], and prepared in Chimera [68].

Conservation of surface residues is often linked to functionally conserved protein-binding surface. Work done by collaborators revealed that GPC3 is the only Glypican that interacts with Unc5, suggesting that conservation of its binding

interface for Unc5 should only be conserved within the GPC3 family and not its other homologues. Conservation of the two solved crystal structures of GPC1 and GPC3 were calculated using the Consurf server [332]. Orthologue sequences for both GPC1 and GPC3 were collected from mammals, amphibians and birds, which are summarized in Appendix C.1 & C.2. As shown in figure 4.11 and in agreement with previous published findings [135], GPC1 is highly conserved in a localized region along the cys-rich lobe and the most C-terminal alpha-helix (equivalent to GPC3 α12). This conserved area is important in the preferential attachment of HS-GAGs [135]. GPC3 contains conserved surface across the protein, predominantly localized along the concave face of GPC3. To date, only the cys-rich lobe has been proposed to have a function in Wnt binding [208].

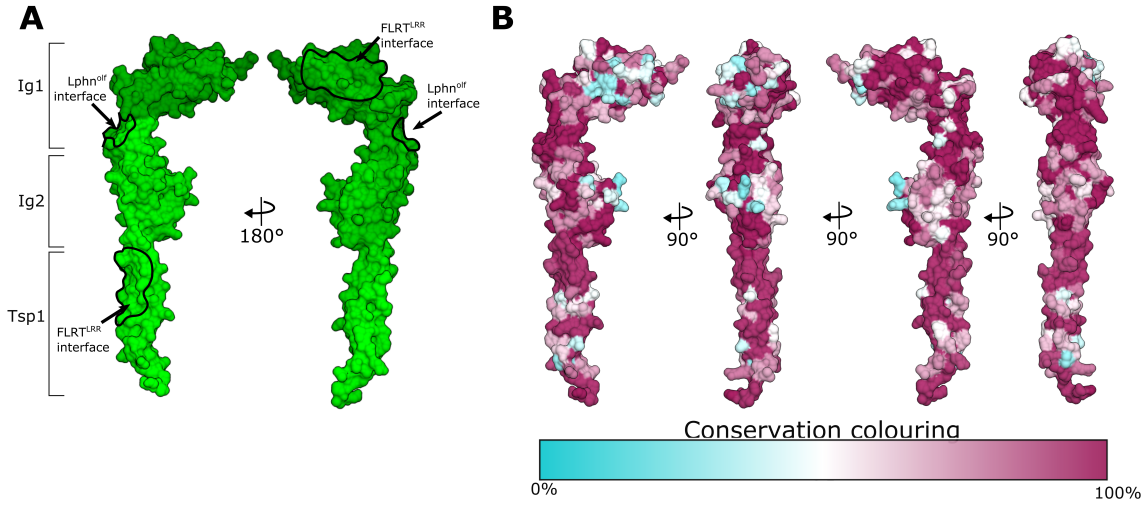


Figure 4.13: Surface conservation of *rn*Unc5D$^{\text{Ig1-Ig2-TSP1}}$. Unc5 orthologue sequences (Human, Chimpanzee, Mouse, Rat, Chicken, and Frog) were aligned and used for conservation analysis by the Consurf server [332]. The degree of conservation is depicted from 0% (cyan) to 50% (white) to 100% (maroon). The structures were prepared using Chimera [68].

All four homologues of Unc5 have been shown to interact with GPC3, therefore surface conservation was performed using sequences from all four members of the Unc5 family. All family members of the Unc5 family (Unc5A,Unc5B, Unc5C, and Unc5D) and their orthologues from different species (Human, Chimpanzee, Mouse, Rat, Chicken, and Frog) were aligned and used for conservation analysis using the Consurf server (C.3). Isoforms lacking TSP1, such as human Unc5A

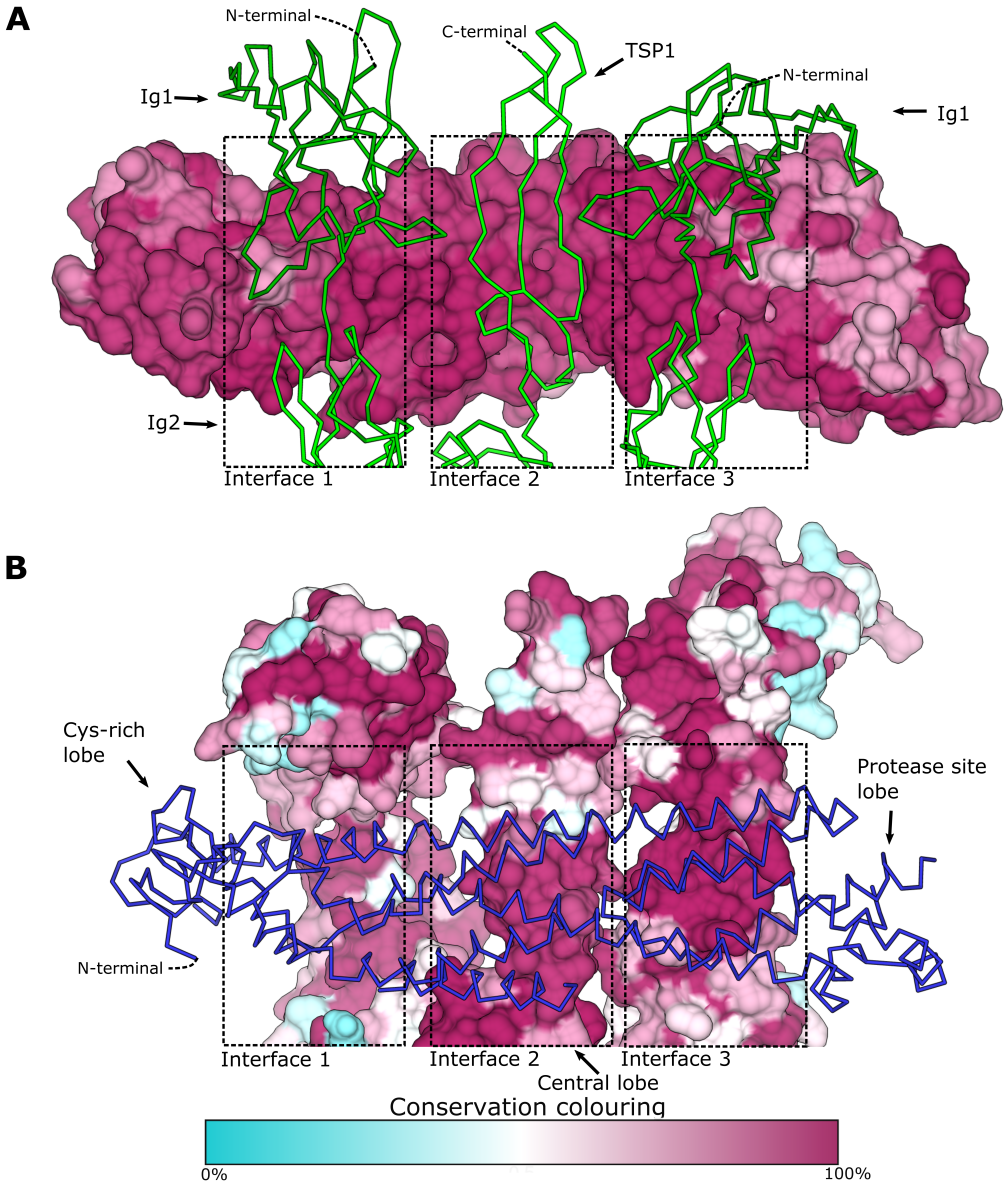


Figure 4.14: Conservation of the GPC3/Unc5 interfaces. The conservation of both GPC3 and Unc5D, shown above are depicted with their corresponding interface to Unc5 and GPC3 respectively. Highly conserved surfaces are coloured according to low conservation (cyan) to highly conserved (maroon). **A)** Conservation of the concave face of GPC3 with all three Unc5 (depicted as carbon backbone in green). **B)** Conservation of the Unc5 surfaces with GPC3 (depicted as carbon backbone in blue). Structures were prepared with Chimera [68].

(uniprot Q6ZN44) were not included in the conservational analysis; this will be discussed in the following section.

The three Unc5 chains that interact with GPC3 at interface 1, 2 and 3 are all at the highly conserved concave face (figure 4.14B). Considering this interface is not conserved in GPC1, it supports the findings that GPC3 interacts with Unc5 in a homologue specific manner (data provided by Comoletti's lab). Conversely, Unc5D molecule interacts with GPC3 with three highly conserved interfaces (figure 4.14B). Interface 1 has no known interaction partners, while interface 2 and 3 have been shown to interact with the Lphn$^{\mathrm{Lec}}$ and FLRT$^{\mathrm{LRR}}$ domain in the octameric FLRT/Unc5/Lphn supercomplex [69].

4.2.7 Isoform specific binding

The vertebrate genome expresses an Unc5A isoform which lacks the TSP1 domain [333], of which the human Unc5A, lacking the TSP1 domain, was previously determined by the lab to not bind to GPC3. Suggesting that TSP1, but not TSP2, is required for the GPC3/Unc5 interaction. The sequence for TSP1 and TSP2 were prepared for multiple species and aligned (MUSCLE). The Consurf server identified two distinct clades, of predominantly TSP1 and TSP2, respectively (figure 4.15B) [332]. Conservational analysis is depicted on the TSP domain of *hs*Unc5A$^{\mathrm{ecto}}$ (PDB 4V2A) using sequences from the TSP2 clade, and *rn*Unc5D$^{\mathrm{TSP1}}$ (PDB 5FTT) using sequences of the TSP1 clade. Three highly conserved hydrophobic residues can be identified in TSP1 (L283, A287, and F288), which are swapped to charged and bulky residues in *hs*Unc5A$^{\mathrm{TSP1}}$ (R272, E276, and E277) (figure 4.15C; appendix C.4). In the GPC3/Unc5D crystal structure we can observe that residue L283 and F288 are near uncharged and hydrophobic interfaces (figure 4.15D). A bulky charged residue could prevent binding through unfavourable interactions and steric hinderance (Figure 4.15D). These findings suggest towards a possible switch from GPC3-independent signalling to GPC3-dependent signalling pathways.

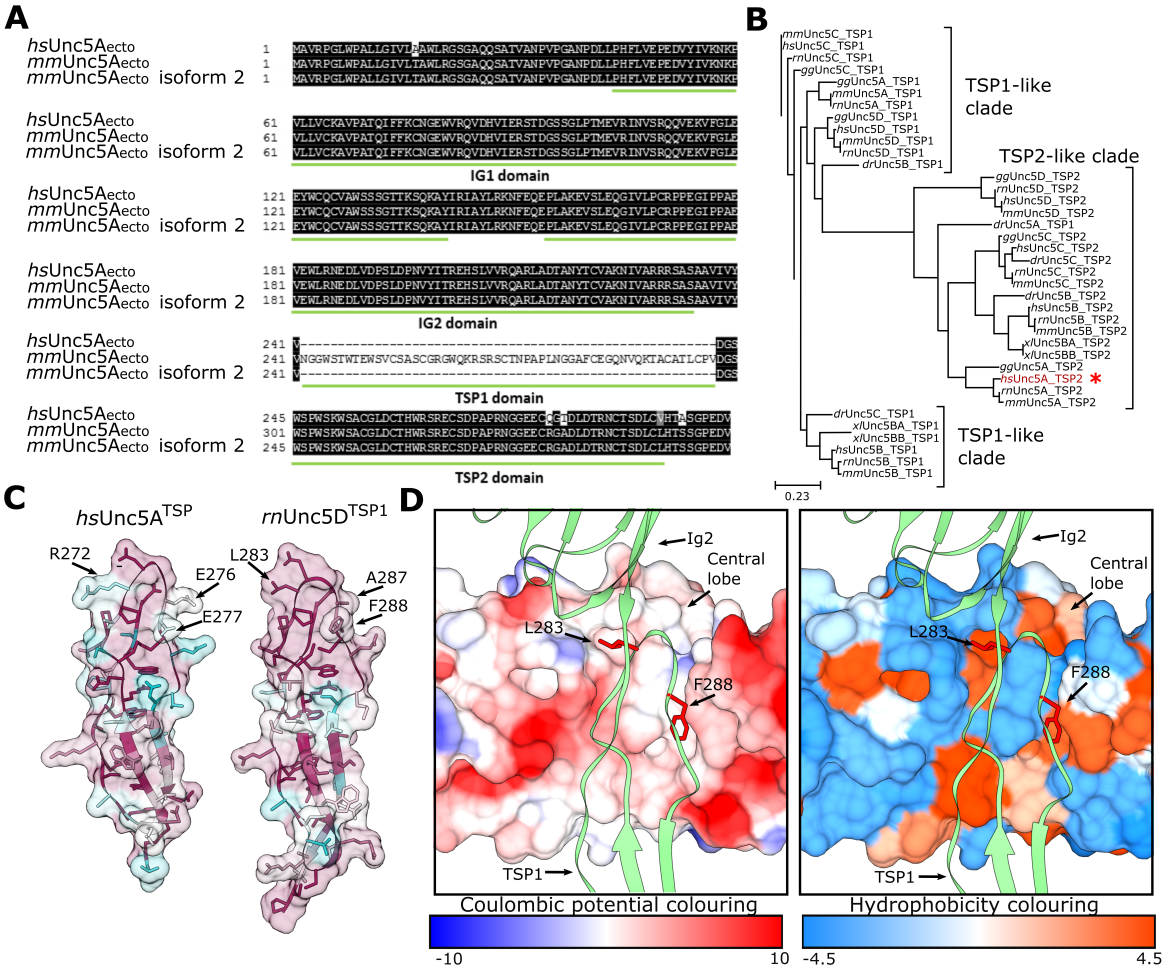


Figure 4.15: The Unc5A isoforms reveals conserved residues in TSP1 and not in in TSP2. A) Sequence alignment of the ectodomains of human and the two mouse isoforms of Unc5A, in which TSP1 is lacking. Black shading indicates a conserved residue. **B)** Tree diagram of sequences for TSP1 and TSP2 across different homologues of Unc5 and different species. The red star indicates that Unc5A TSP1 closely resembles a TSP2-like clade. **C)** Conservation analysis of the *hs*Unc5A$^{\text{TSP1}}$ and *rn*Unc5D$^{\text{TSP1}}$ across the TSP2-like clade and TSP1-like clade, respectively. Transparent surface is shown, in which conservation is coloured in cyan, for not conserved, and maroon, for highly conserved, residues. Residues L283, A287 and F288 conserved in TSP1 are consistently found as charged residues in TSP2 (R272, E276 and E277 in *hs*Unc5A$^{\text{TSP1}}$). *D)* GPC3 surface depiction of Coulomb charge (in kcal/mol $\cdot$ e), and Kyte-Doolittle hydrophobicity scale in which hydrophilic (blue) and hydrophobic (orange) surfaces are depicted. TSP1, shown as carbon backbones in green, binds to the central lobe, in which the residues L283 and residue F288 (in red) are found near hydrophobic pockets. Sequence alignment depicted was performed using TCoffee [334] and prepared using Boxshade [335]. The phylogenetic tree was obtained from the Consurf server [332], and structures were prepared in Chimera [68].

5

Characterization of the GPC3/Unc5 Complex

5.1 Summary

The solved structures of GPC3/Unc5D reveals an octameric assembly, in two different crystal forms. The identified stoichiometry of the complex may be a consequence of crystal packing or could hint to a biologically relevant complex. Indeed, it is conceivable that the crystal structure represents the clustering of Unc5, by binding with GPC3. Such clustering of the receptors in the presence has been demonstrated in pathways related to Unc5, such as the DCC-Netrin1 pathway [336].

To further characterize the GPC3/Unc5 interaction, I aimed to validate the protein-protein interfaces identified in the crystal structure. Mutagenesis experiments reveal that Unc5 requires its Ig domains in combination with TSP1 to bind to GPC3; however, mutations on the GPC3 interface were unable to abolish binding on SPR.

Mutational disruption of each interface was complicated due to the low-resolution data, therefore I performed XL-MS to elucidate the binding topology of the complex in solution. GPC3/Unc5D were crosslinked with BS3 and visualized using SDS-PAGE. A protein band corresponding to a 1:1 complex was isolated and analysed. Two intermolecular crosslinks were identified which correspond to interface 3. This interface was difficult to validate by mutagenesis because of the small contact area identified in the crystal structure.

Furthermore, to determine the true stoichiometry of the interaction, I used SEC-MALS and native MS. SEC-MALS suggested a one-to-one interaction; however, the protein complex was not stabile in SEC. Native MS revealed the presence of several stoichiometries, including a 1:1, 2:2 and 4:4 GPC3/Unc5D complex. The presence of a 4:4 GPC3/Unc5D complex in the gas phase, supports the 4:4 stoichiometry identified in the crystal structure.

5.2 Results

5.2.1 Mutational disruption of the protein complex

To validate the interfaces observed between GPC3 and Unc5, several mutations were designed that introduce an artificial glycosylation motif (N-X-T/S), where X is any amino acid except proline [337, 338]. The introduction of an N-glycosylation site should sterically hinder any nearby interaction. This method of disrupting a complex is especially useful in the case of a low-resolution structures where binding sites are difficult to interpret.

I decided to investigate mutants of the human Unc5B homologue since Unc5B is predominately expressed in the vascular system where GPC3 is also expressed [47, 177]. Mutants were cloned in a construct of *hs*Unc5B^{ecto}, containing all ecto domains, with a C-terminal Avitag used for biotinylating (S2.2.4). The wild type and two mutants, *hs*Unc5B$^{Y150N\ R152T}$ and *hs*Unc5B$^{A279N\ L281T}$, were used as ligands for SPR . *hs*Unc5B$^{Y150N\ R152T}$ affects the linker between Ig1 and Ig2, while *hs*Unc5B$^{A279N\ L281T}$ introduces an N-glycosylation at interface 2. A two-fold serial dilution of the purified *hs*GPC3$^{\Delta C}$ was used as analyte with a maximum concentration of 8.3 μM. The results indicate that the wild type protein can bind to *hs*GPC3$^{\Delta C}$, with a calculated dissociation constant of 1437 nM, calculated assuming a one-to-one binding model. Interestingly, at a maximum concentration of analyte there is a change in response which could be the result of a conformational change. In contrast both the mutants were unable to bind to *hs*GPC3$^{\Delta C}$ (figure 5.1B).

Significantly, the K_D is almost six times higher than what was previously observed between *mm*GPC3$^{\Delta C}$ and *mm*Unc5D$^{Ig1\text{-}Ig2\text{-}TSP1}$ (K_D 260 nM). I performed preliminary cell binding studies, in which wild type *rn*Unc5D^{ecto}-mVenus and *rn*Unc5D$^{Y154N\ R156T}$-mVenus were expressed in HEK293T cells. The *rn*Unc5D$^{Y154N\ R156T}$ mutant is at the same interface as mutant *hs*Unc5B$^{Y150N\ R152T}$. Cell binding was performed as described in section 2.3.1, with soluble *mm*GPC3$^{\Delta C}$ and *rn*FLRT^{LRR},

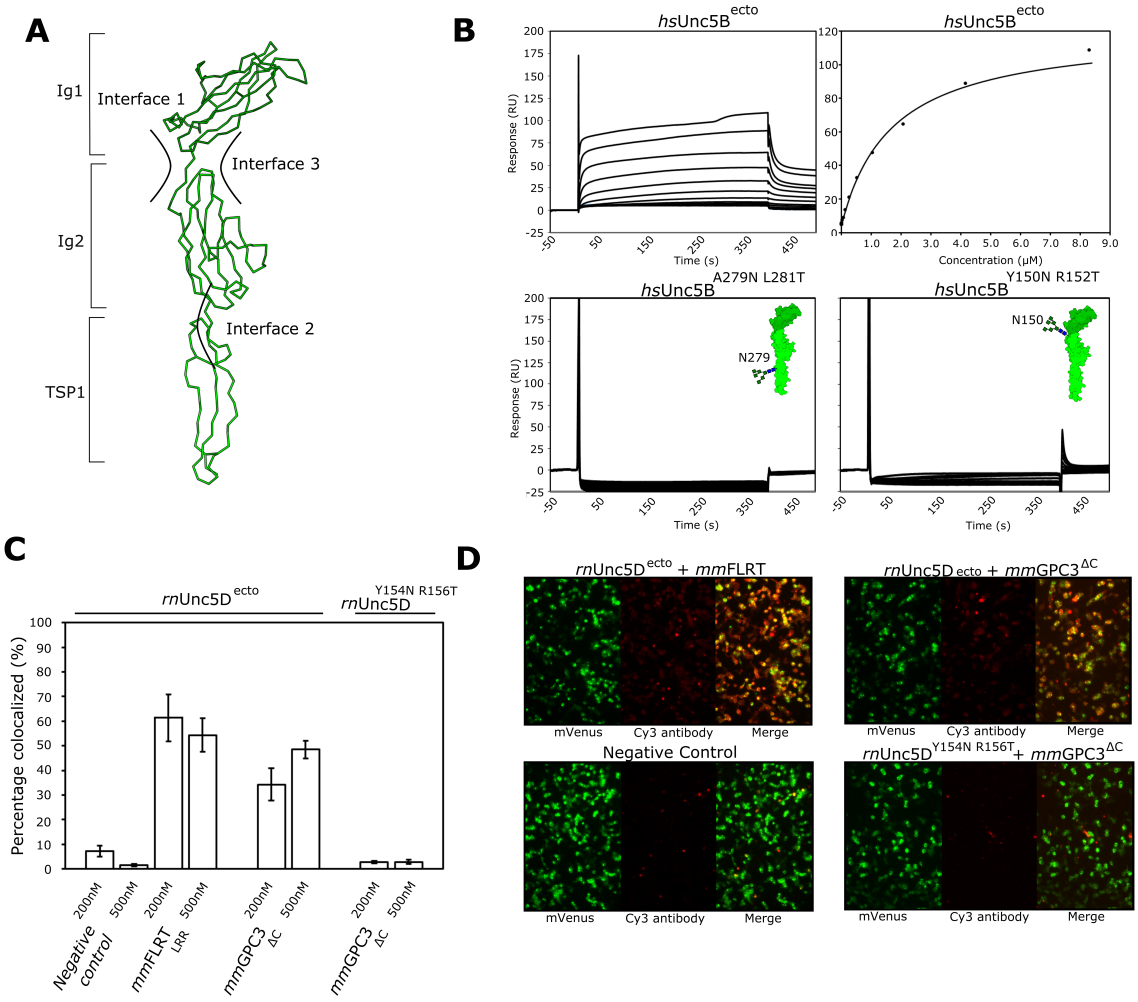


Figure 5.1: Mutagenesis of Unc5 disrupts the formation of the complex. A) Backbone representation of Unc5D (green). The three interfaces are labelled on the structure. **B)** SPR data of sensors coated with *hs*Unc5B^{ecto} and *hs*Unc5B^{N150} and *hs*Unc5B^{N279} as ligand. A dilution series, with a maximum concentration of 8.3 μM, of *hs*GPC3$^{\Delta C}$ was flown over as analyte. The artifical N-glycosylation site mutations *hs*Unc5B^{N150} and *hs*Unc5B^{N279} are depicted on the surface representation model. Both mutants showed no binding on SPR. **C)** Preliminary colocalization experiment shows that 200 and 500 nM of soluble *mm*GPC3$^{\Delta C}$ binds to cells overexpressing *rn*Unc5D^{ecto} with a transmembrane helix and cytoplasmic GFP (mVenus), as does *mm*FLRT2^{LRR}. When cells express the *rn*Unc5D$^{Y154N\ R156T}$, *mm*GPC3$^{\Delta C}$ does not bind to the cells, with either concentration. **D)** The green channel shows the mVenus GFP signal, the red channel shows the Cy3 conjugated secondary antibody signal. The merged channels are also shown. In the merged channel the red signal brightness was increased for visualization purposes. The protein molecules were prepared in Chimera [68], cell binding and colocalization was analysed using ImageJ and graphs were prepared using Excel.

at a concentration of 200 and 500 *nM*. The percentage of the total area of colocalized pixels compared to the total area of green pixels. The preliminary results suggest that both soluble protein, *mm*FLRT$^{\mathrm{LRR}}$ and *hs*GPC3$^{\Delta\mathrm{C}}$, are able to bind to cells overexpressing *rn*Unc5D$^{\mathrm{ecto}}$. However, and in agreement with the SPR data, cells overexpressing *rn*Unc5D$^{\mathrm{Y154N\ R156T}}$ have a significantly reduced affinity to GPC3 that results in no cell binding (figure 5.1C).

Next, N-glycosylation mutants for GPC3's respective interfaces were designed. Designing N-glycosylation mutants for GPC3 was difficult because of the α-helical nature of GPC3. The residue that would be mutated to a threonine to target an exposed site was often a structurally important hydrophobic residue pointing into the protein core. Nonetheless, two potential glycosylation mutants were designed on a loop near interface 2. These mutations were *hs*GPC3$^{\mathrm{L156N}}$ and *hs*GPC3$^{\mathrm{S158N\ I160T}}$ (figure 5.2B). Biotinylated wild type and mutants GPC3 were bound onto the SPR chip as ligands. *rn*Unc5D$^{\mathrm{Ig1\text{-}Ig2\text{-}TSP1}}$ and *hs*Unc5B$^{\mathrm{ecto}}$ were flown over the chip to observe relative binding. These preliminary results suggest that, although there is a decrease in measured binding, these mutants can still bind Unc5. It is possible that the N-glycosylation site is located on a flexible loop not essential for the interaction and/or can adjust its conformation and still allow binding. As there was no complete disruption in binding, other mutants were investigated.

Mutants of Unc5 suggest that interface 1 is essential for binding, I cloned an artificial glycosylation mutant at position D151N, termed *hs*GPC3$^{\mathrm{D151N}}$, in which there is a Serine at position 153. Further analysis of this interface revealed that the surface has a negatively charged patch (figure 5.2C), which is not found in GPC1. Therefore, I designed a charge swap mutant, *hs*GPC3$^{\mathrm{E147R\ D151R\ E169R}}$. The wild type and both mutants were immobilized as ligands on an SPR chips and analysed by flowing a dilution series of purified constructs of *rn*Unc5D$^{\mathrm{Ig1\text{-}Ig2\text{-}TSP1}}$ and *hs*Unc5B$^{\mathrm{ecto}}$, with a maximum concentration of 30 and 25 μM respectively, over the chip. The SPR response curves for the dilution series are shown in figure 5.1D.

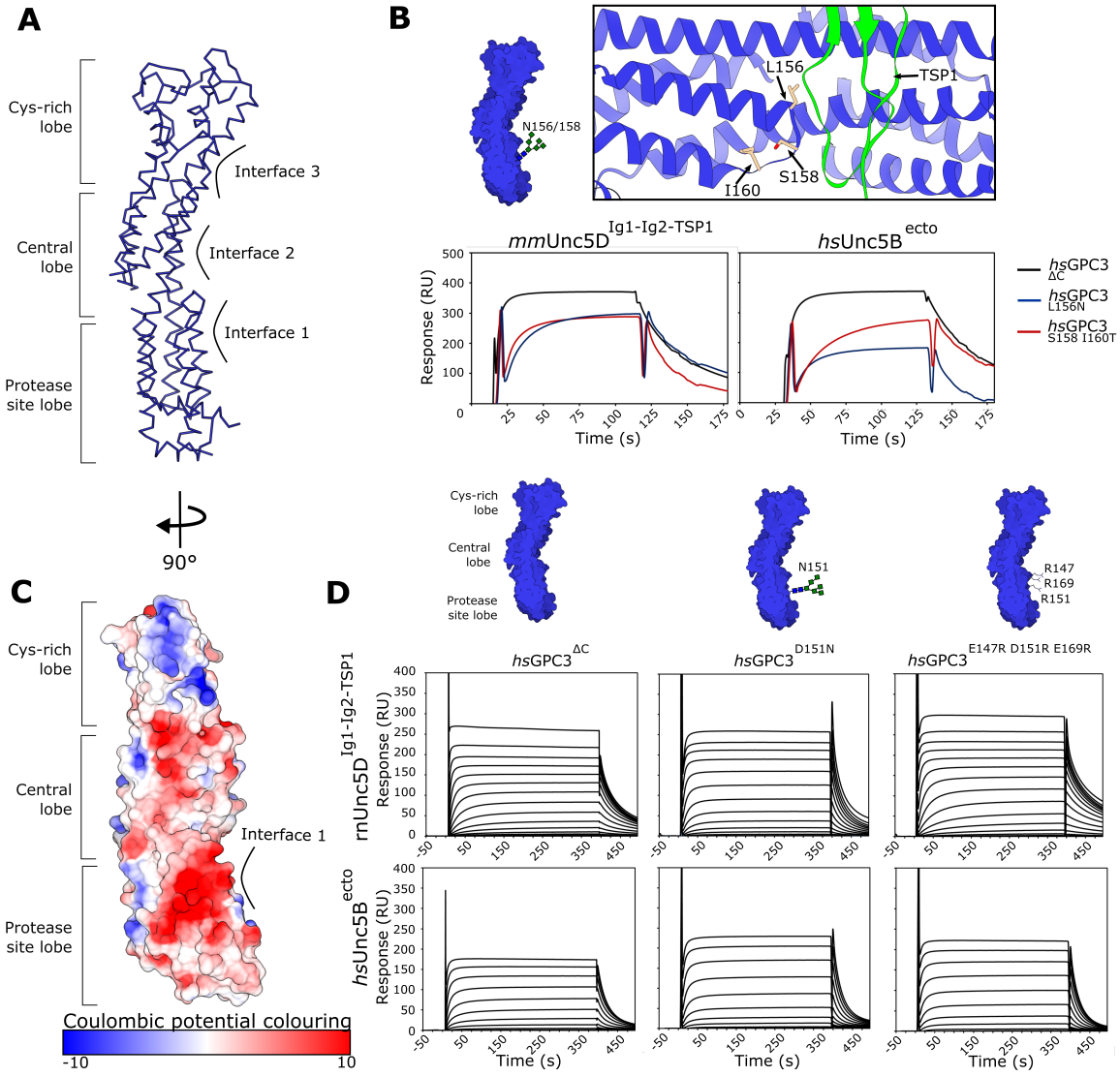


Figure 5.2: SPR analysis of the GPC3 and its mutants binding to Unc5 A) Backbone representation of GPC3 (Blue). The three interfaces observed in the structure are labelled. **B)** N-glycosylation mutations *hs*GPC3$^{\text{L156N}}$ and *hs*GPC3$^{\text{S158N I160T}}$, found near interface 2, show slight disruption in binding affinity on SPR, when flowing over the analyte *rn*Unc5D$^{\text{Ig1-Ig2-TSP1}}$ and *hs*Unc5B$^{\text{ecto}}$, with a maximum concentrations of 30 and 25 μM respectively. **C)** Surface representation of GPC3, coloured by Coulomb charge, from negative (Red) to positive (Blue). Interface 1 consist of a highly conserved negative charge. **D)** SPR experiments of N-glycosylation mutant, *hs*GPC3$^{\text{D151N}}$ and a charge swap mutant *hs*GPC3$^{\text{E147R D151R E169R}}$ were bound to the SPR chip and different concentrations of analyte of *rn*Unc5DIg1-Ig2-TSP1 and *hs*Unc5B$^{\text{ecto}}$ was flown over. The SPR graphs indicate similar binding responses to both analytes across the wild type and mutants. Figure was prepared in Chimera [68], and graphs were prepared in Excel.

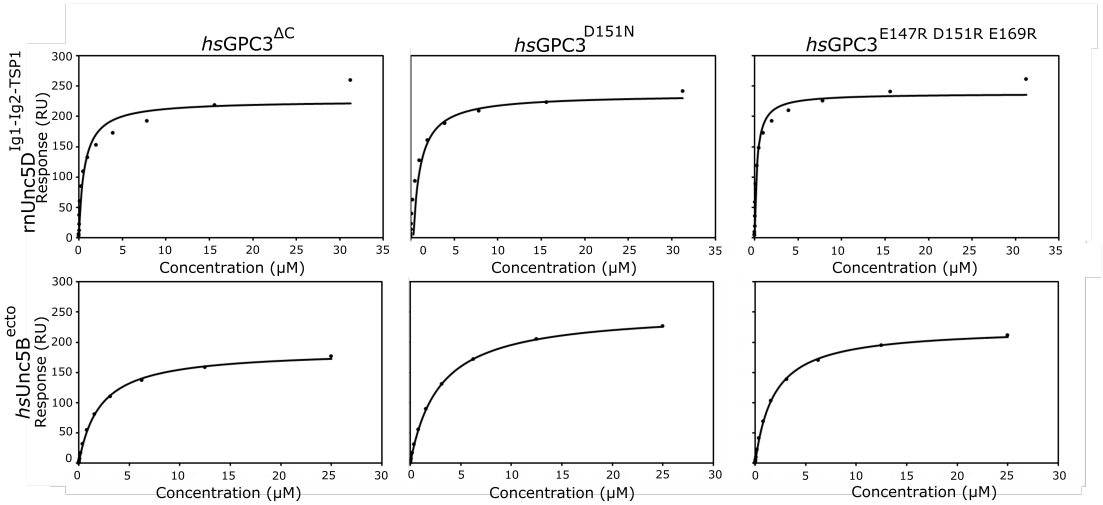


Figure 5.3: SPR binding curves of GPC3 and its mutants binding to Unc5. Binding curves for *hs*GPC3$^{\Delta C}$ and its mutants *hs*GPC3^{D151N} and *hs*GPC3$^{D147R\ D151R\ D159R}$ with the analytes *hs*Unc5B^{ecto} and *rn*Unc5D$^{Ig1\text{-}Ig2\text{-}TSP1}$. Graphs were prepared in Excel and Graphpad Prism.

The K_D and B_{max} were calculated by plotting the RU for each concentration (figure 5.3), and are summarized in table 5.1. As expected, the wild type binds to both *rn*Unc5D$^{Ig1\text{-}Ig2\text{-}TSP1}$ and *hs*Unc5B^{ecto}. The affinity to *rn*Unc5D$^{Ig1\text{-}Ig2\text{-}TSP1}$ was calculated as 500 *nM*, which is a two fold increase compared to the previously obtained data for *mm*GPC3$^{\Delta C}$. The affinity of *hs*Unc5B^{ecto} was calculated to be a K_D of approximately 2000 *nM*, which is similar to the value obtained previously with Unc5B. The glycosylation mutants have an 47% and 36% increase in K_D for *rn*Unc5D$^{Ig1\text{-}Ig2\text{-}TSP1}$ and *hs*Unc5B^{ecto}, respectively. Conversely, the charge swap mutant shows a decrease in K_D.

Table 5.1: Calculated (K_D) and B_{max}. The (K_D) and B_{max} were determined from the SPR data for *hs*GPC3$^{\Delta C}$ and its mutants *hs*GPC3^{D151N}, and *hs*GPC3$^{D147R\ D151R\ D159R}$ with the analytes *hs*Unc5B^{ecto} and *rn*Unc5D$^{Ig1\text{-}Ig2\text{-}TSP1}$. The values were calculated using Graphpad Prism.

Ligand	Analyte	K_D (nM)	B_{max} (RU)
*hs*GPC3$^{\Delta C}$	$_{rn}$Unc5D$^{Ig1\text{-}Ig2\text{-}TSP1}$	523	221
	$_{hs}$Unc5B^{ecto}	2072	187
*hs*GPC3^{D151N}	$_{rn}$Unc5D$^{Ig1\text{-}Ig2\text{-}TSP1}$	774	236
	*hs*Unc5B^{ecto}	2826	224
*hs*GPC3$^{D147R\ D151R\ D159R}$	$_{rn}$Unc5D$^{Ig1\text{-}Ig2\text{-}TSP1}$	247	236
	*hs*Unc5B^{ecto}	1838	252

5.2.2 XL-MS identifies the topology of interface 3

XL-MS is a versatile tool in which residues are covalently crosslinked to each other. Enzymatic digestion of the crosslinked sample produces small peptides that are analysed by MS. The crosslinked peptides represent a topological map of residues that are within proximity of each other. In the case of a complex, crosslinking of residues from one molecule to another can provide insight into which interfaces are formed in solution.

*mm*GPC3$^{\Delta C}$ and *rn*Unc5D$^{\text{Ig1-Ig2-TSP1}}$ were crosslinked using BS3 crosslinker (spacer arm 11.4Å) and visualized on SDS-PAGE (figure 5.4A). The SDS-PAGE revealed that both Unc5D and GPC3 were readily crosslinked into higher order oligomers, making it difficult to select for crosslinked complexes. Nonetheless, one higher order species was observed for the GPC3-Unc5D protein complex, which was not present within the crosslinked samples of the individual proteins. This species runs at an approximate size of 90 kDa, which would be equivalent to an 1:1 Stoichiometry. In collaboration with Prof. Shabaz Mohammed, several crosslinks were identified, in which three links were intermolecular (L1, L2, L3). L1 was identified between GPC3 (residue K49) and Unc5D (residue K157), L2 was identified between two GPC3 (residue K452), and L3 was identified between GPC3 (residue K434) and Unc5D (residue K157) (figure 5.4B).

Each link, in red, is shown on the crystal structure of the GPC3 Unc5 protein complex (figure 5.4C). The crosslinked residues found on GPC3 were identified in regions that were disordered in the high-resolution structure. The model was completed using SWISS modelling [322]; however, this complicates the prediction of distances between crosslinked residues. The distance between the Cα of the crosslinked residue were used so that side chain dynamics are excluded. Links 1, 2, & 3 were calculated to have 28 Å, 26 Å and 48 Å respectively. BS3 with a fully extended lysine residue can extend up to 24 Å, nonetheless molecular dynamics

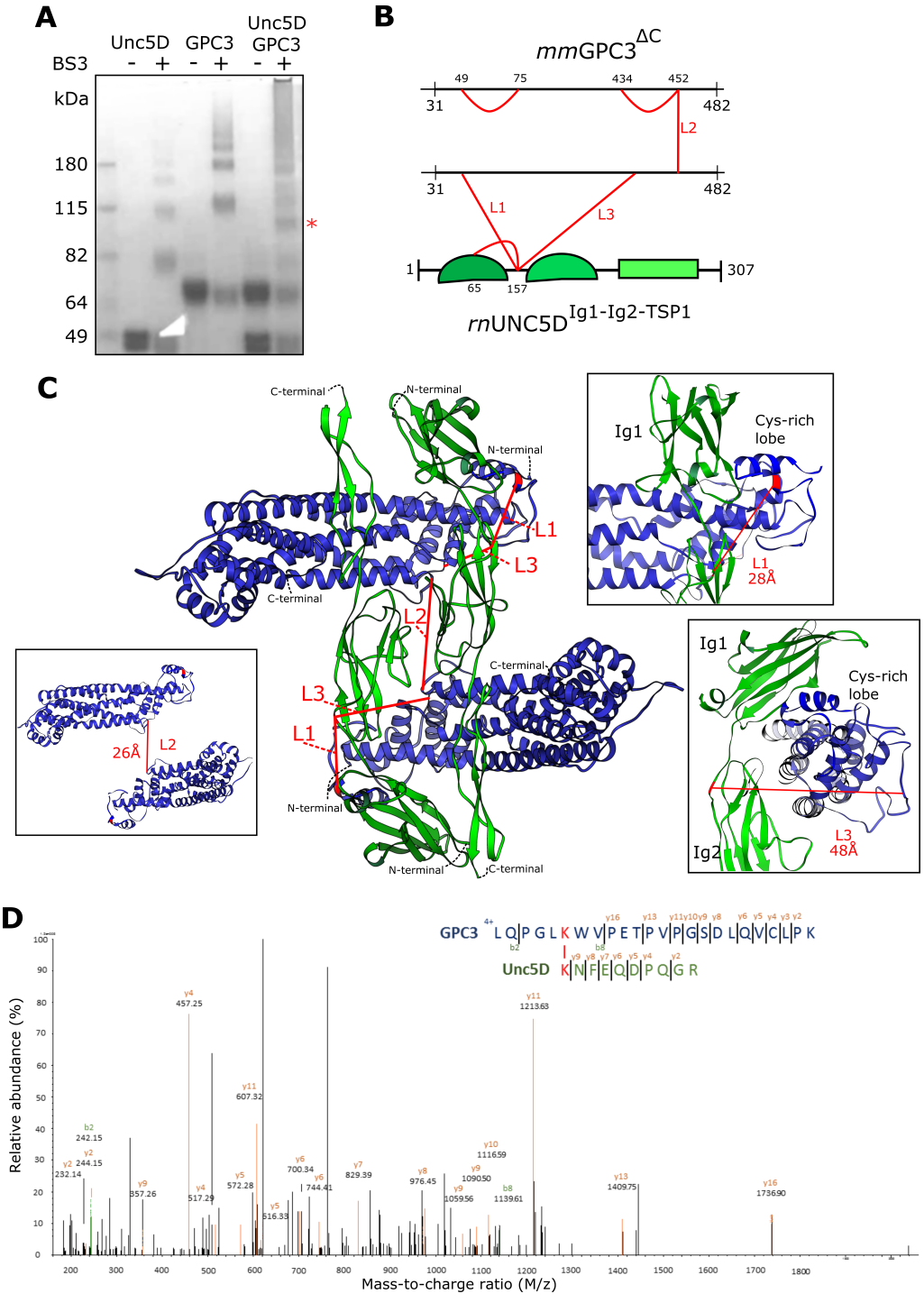


Figure 5.4: XL-MS analysis of the GPC3/Unc5 complex. **A)** SDS-PAGE showing uncrosslined controls and BS3 crosslinked samples of purified rnUnc5D$^{\text{Ig1-Ig2-TSP1}}$,*mm*GPC3$^{\Delta C}$, and mixed *mm*GPC3$^{\Delta C}$ and *rn*Unc5D$^{\text{Ig1-Ig2-TSP1}}$. The red asterisk indicates a crosslinked band that was not present in either individual protein samples. **B)** Diagram representing all intra- and inter- molecular crosslinks. The intermolecular crosslinks are annotated, L1, L2 and L3. **C)** Links L1, L2 and L3 represented on the crystal structure, in red. For purpose of clarity only two chains are presented of GPC3 (blue) and Unc5D (Green). The distances between links were calculated from the alpha carbon of the residue. **D)** Annotated peaks of Link 1.

simulations have shown that an upper bound of 26-30 Å is more consistent with experimental findings, because of global protein flexibility [339].

Link 1 was identified between the Ig1-Ig2 domain to the cys-rich lobe of GPC3. Link 3 connects the same lysine residue on the Unc5 molecule to a flexible loop found near the cys-rich lobe. The distance is far above the expected value but could be accounted for by the flexible nature of the loop. These two links reflect a binding site of the Ig1-Ig2 domains to the cys-rich lobe (interface 3), which has not yet been validated by mutagenesis experiments, providing further support that the Ig domains form an interaction with GPC3 in solution, and that higher oligomers of 2:2 or 4:4 is possible.

5.2.3 SEC-MALS suggests a one-to-one protein complex

SEC-MALS couples size exclusion chromatography with multiple-angle light scattering, which allows for the determination of the mass of a protein in solution. *mm*GPC3$^{\Delta C}$ and *mm*GPC3$^{\Delta C}$ mixed with *rn*Unc5D$^{\text{Ig1-Ig2-TSP1}}$ in a one-to-one molar ratio. *mm*GPC3$^{\Delta C}$ eluted as a single peak with an apparent mass of 54 kDa (figure 5.5). The determined size corresponds roughly to the expected size of a monomer, which is calculated to be 53.0 kDa, or 56.6 kDa when adjusted for HEK293S N-glycosylation. *mm*GPC3$^{\Delta C}$ with *rn*Unc5D$^{\text{Ig1-Ig2-TSP1}}$ was mixed in a one-to-one molar ratio and injected at the concentrations 1 mg/ml and 5 mg/ml. The elution time of the complex was shifted, with an apparent mass of 67.6 kDa. The mass of a one-to-one complex is approximately 89 kDa, which is significantly higher than the apparent mass obtained. The peak obtained had a shoulder indicating to a possible dissociation of the complex during SEC. This may result in an apparent mass that is affected by the mixture of monomers and complexes. SEC-MALS may not be an appropriate technique for the determination of the true stoichiometry of the complex, because of the low affinity interactions may not occur consistently.

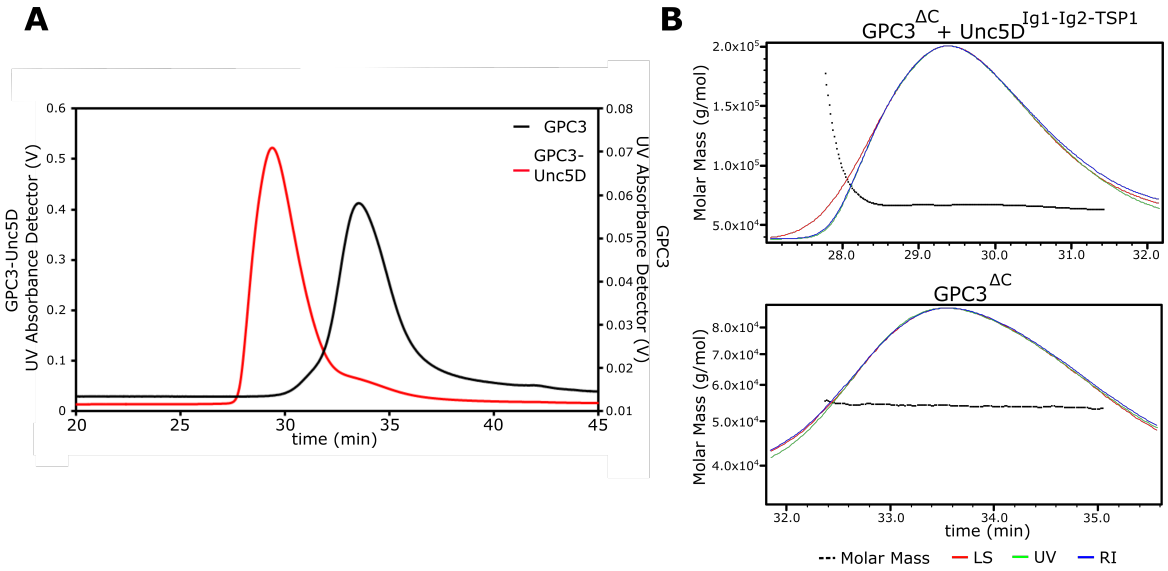


Figure 5.5: SEC-MALS analysis of *mm*GPC3$^{\Delta C}$ in complex with *rn*Unc5D$^{\text{Ig1-Ig2-TSP1}}$. **A)** SEC UV profile of *mm*GPC3$^{\Delta C}$ (Black; $\sim$ 56 kDa) and *mm*GPC3$^{\Delta C}$ mixed with *rn*Unc5D$^{\text{Ig1-Ig2-TSP1}}$ (Red; $\sim$ 90 kDa). Addition of *rn*Unc5D$^{\text{Ig1-Ig2-TSP1}}$ results in a shift in elution time, suggesting the formation of a complex. **B)** Calculated molar mass of the main peak of *mm*GPC3ΔC (bottom) and 5 mg/ml mixture of *mm*GPC3$^{\Delta C}$ and *rn*Unc5D$^{\text{Ig1-Ig2-TSP1}}$ (Top). Each table shows the aligned peaks of the HELEOS-II 8-angle light detector (red), SPD20A UV/vis detector (green), and rEX refractive index monitor (blue). The molar mass is plotted as a black dashed line. Data was processed and prepared using ASTRA.

Table 5.2: Apparent Mass of *m*GPC3$^{\Delta C}$ and *mm*GPC3$^{\Delta C}$ in complex with *rn*Unc5D$^{\text{Ig1-Ig2-TSP1}}$

Construct	Expected Mw (kDa)	Apparent Mw (kDa)	polydispersity (mw/mn)
*mm*GPC3$^{\Delta C}$	56.7	54.0 ± 1.12%	1.00± 1.18%
*mm*GPC3$^{\Delta C}$ *rn*Unc5D$^{\text{Ig1-Ig2-TSP1}}$	89.4	67.6 ± 0.83%	1.01 ± 1.18%

5.2.4 Native MS of the protein complex

A well-established method for identifying the mass of transient complexes is by native MS. This technique has been successfully employed in the lab with the FLRT/Lphn/Unc5D supercomplex to determine its octameric stoichiometry [69]. For Native MS the protein must be in a volatile buffer, such as ammonium acetate, which replaces any other salts.

Table 5.3: Native MS assigned molecular masses. The predicted molecular weight was determined by Expasy ProtParam [340], of which 1.2 kDa was added per N-glycosylation site [267]. *rn*Unc5D$^{\text{Ig1-Ig2-TSP1}}$ and *hs*GPC3$^{\Delta\text{C R355R358AA}}$ were predicted to be 34.37 and 56.75 kDa respectively. The expected masses of the different stoichiometries complexes were calculated to be 91.12, 182.24 and 364.48 kDa for a 1:1, 2:2 and 4:4 respectively.

Peak	Assigned molecular weight (kDa)	Deviation from predicted molecular weight
*rn*Unc5D$^{\text{Ig1-Ig2-TSP1}}$	35.66	3.75%
*hs*GPC3$^{\Delta\text{C R355R358AA}}$	56.78	0.05%
1:1 Complex	92.66	1.69%
2:2 Complex	185.4	1.88%
4:4 Complex	370.1	1.54%

Initial attempts used the constructs *mm*GPC3$^{\Delta\text{C}}$ and *rn*Unc5D$^{\text{Ig1-Ig2-TSP1}}$ to determine the stoichiometry. When injected alone both *mm*GPC3$^{\Delta\text{C}}$ and *rn*Unc5D$^{\text{Ig1-Ig2-TSP1}}$ revealed molecular weights that were similar to the predicted masses. Interestingly, the spectra of *mm*GPC3$^{\Delta\text{C}}$ contained two distinct species which differed in mass by 1.9 kDa (appendix D.1). The difference in mass could be a consequence of the double cleavage sites, as observed in previous data (figure 3.4). Spectra of the complex, however, were difficult to assign the molecular weight of higher oligomers (2:2 and higher). Heterogeneity within the sample may have complicated the detection and assignment of these higher oligomer peaks. Therefore, to minimize heterogeneity caused by the two species identified in the wildtype GPC3 the construct *mm*GPC3$^{\Delta\text{C R355R358AA}}$ was used to determine the stoichiometry of the complex by native MS. The best spectra obtained of *mm*GPC3$^{\Delta\text{C R355R358AA}}$ in complex with *rn*Unc5D$^{\text{Ig1-Ig2-TSP1}}$ was at 1.0 *mg/ml* in 0.2 *M* ammonium acetate which revealed peaks corresponding to a 1:1, 2:2 and 4:4 stoichiometry (figure 5.6). The assigned masses of each peak are shown in table 5.3. To further validate the content of each peaks, tandem MS (MS/MS) was performed for peaks corresponding to a 1:1, 2:2 and 4:4 stoichiometry. The MS/MS spectra validated that each complex consisted of a *mm*GPC3$^{\Delta\text{C R355R358AA}}$. *rn*Unc5D$^{\text{Ig1-Ig2-TSP1}}$ could be annotated in the MS/MS of the 1:1 complex peak, but not in the higher oligomers. Nonetheless, the size of 2:2 and 4:4 complex coincide as multiples of the 1:1 complex.

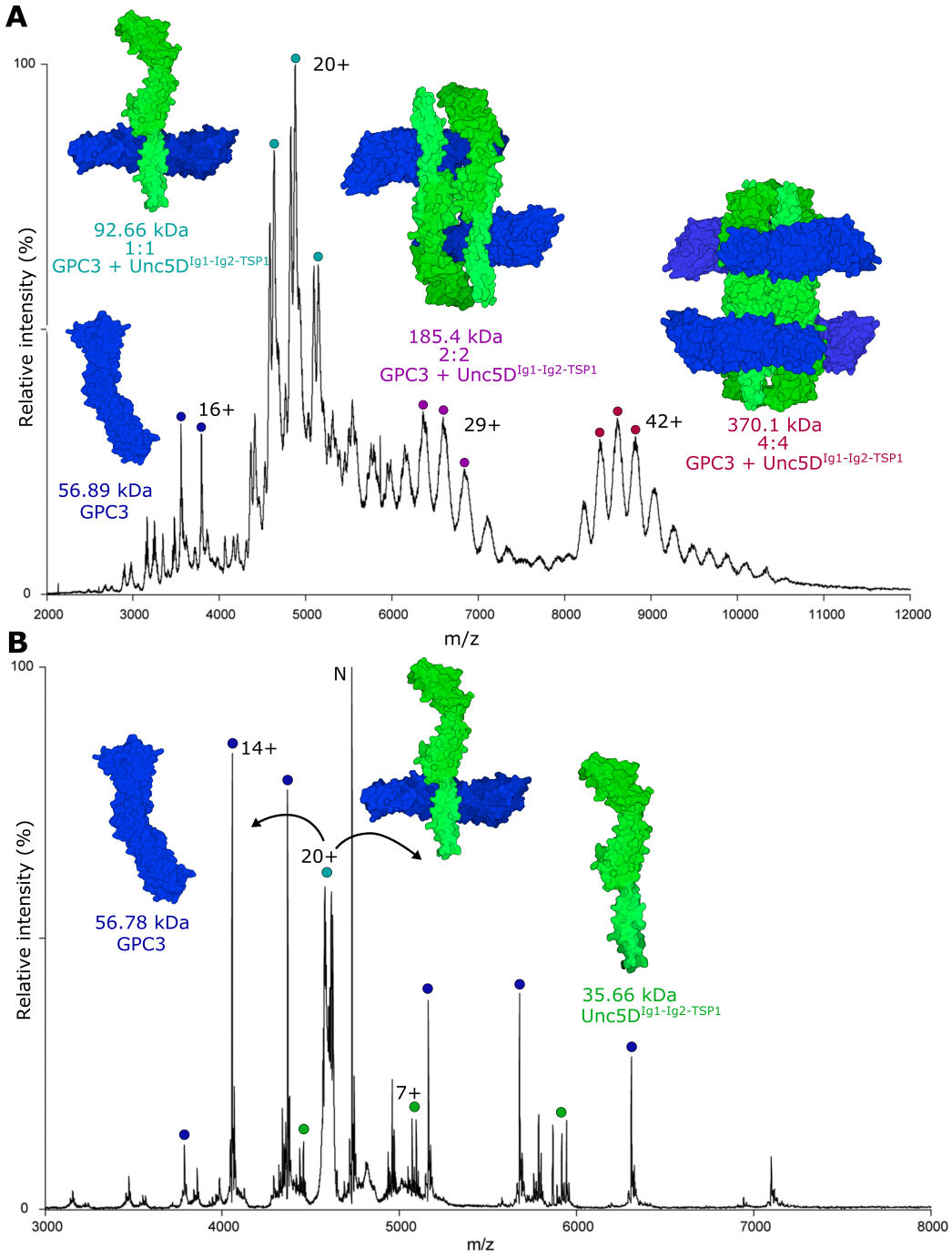


Figure 5.6: Native-MS of GPC3/Unc5D complex and MS/MS of the 1:1 peak. **A)** Native MS of the GPC3/Unc5D complex at 1.0 *mg/ml* in 0.2 *M* ammonium acetate, in which four species were annotated, *hs*GPC3$^{\Delta C\ R355R358AA}$ (blue), 1:1 complex (cyan), 2:2 complex (purple) and 4:4 complex (red). The molecular weight was determined as 56.89, 92.66, 185.4 and 370.1 kDa respectively. **B)** MS/MS was performed on the 1:1 complex (cyan) peak, in which peaks for *rn*Unc5D$^{Ig1\text{-}Ig2\text{-}TSP1}$ (green) and *hs*GPC3$^{\Delta C\ R355R358AA}$ (blue) corresponding to a size of 35.66 and 56.78 kDa could be annotated. Peaks were annotated by Dr. Ritu Raj. GPC3 (blue) and Unc5 (green) are shown as surfaces and were prepared in Chimera [68].

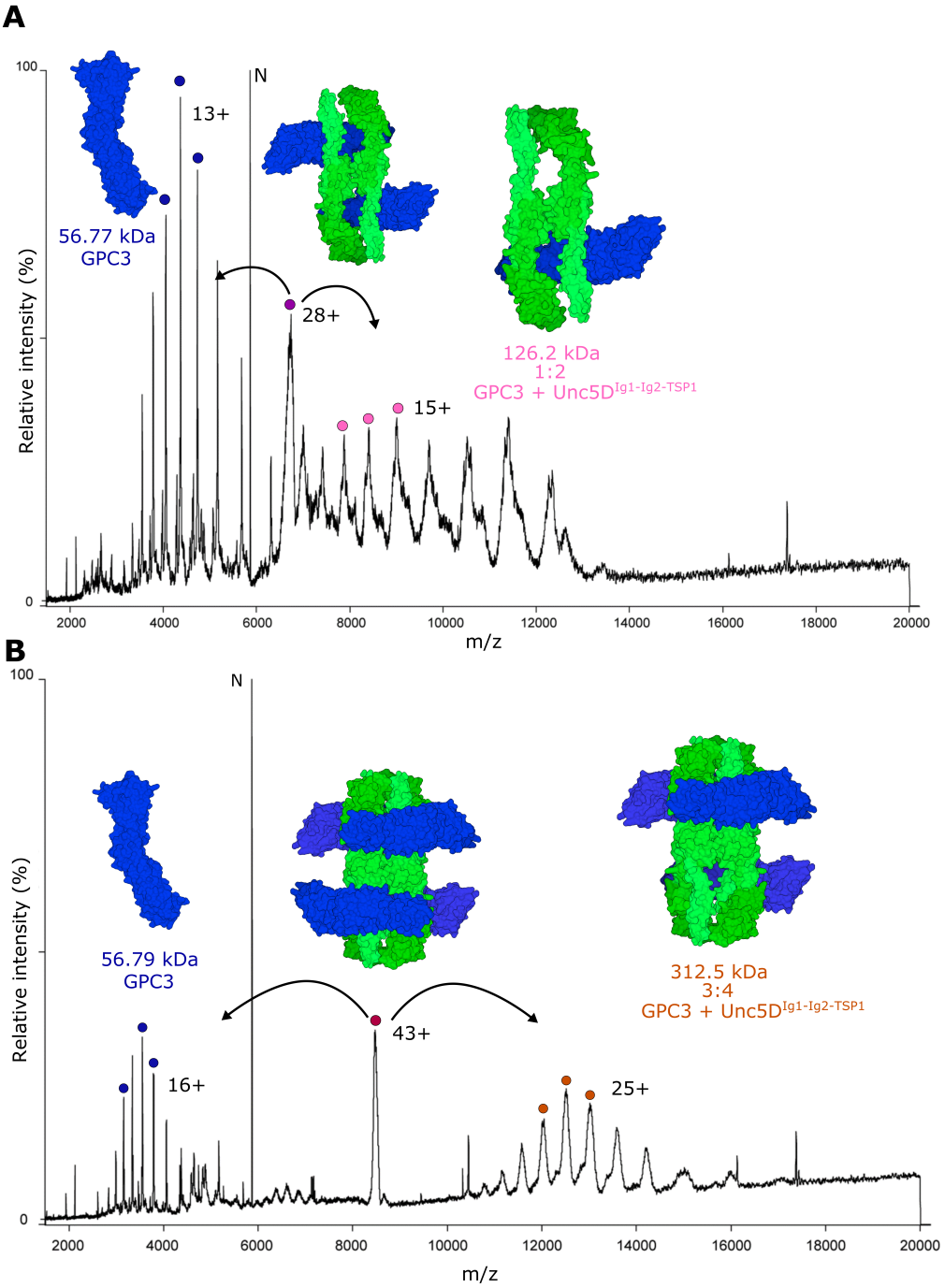


Figure 5.7: MS/MS analysis of the larger oligomer GPC3/Unc5D complexes. **A)** MS/MS of peak corresponding to a 2:2 (purple) was performed. Peaks for *hs*GPC3$^{\Delta C\ R355R358AA}$ (blue) and a 1:2 *hs*GPC3$^{\Delta C\ R355R358AA}$/*rn*Unc5D$^{Ig1\text{-}Ig2\text{-}TSP1}$ complex (pink) corresponding to a size of 56.77 and 126.2 kDa could be annotated. **B)** MS/MS of peak corresponding to a 4:4 (red) was performed. Peaks for *hs*GPC3$^{\Delta C\ R355R358AA}$ (blue) and a 3:4 *hs*GPC3$^{\Delta C\ R355R358AA}$/*rn*Unc5D$^{Ig1\text{-}Ig2\text{-}TSP1}$ complex (orange) corresponding to a size of 56.79 and 312.5 kDa could be annotated. Peaks were annotated by Dr. Ritu Raj. GPC3 (blue) and Unc5 (green) are shown as surfaces and were prepared in Chimera [68].

6

Discussion and Future Work

6.1 Organization of the GPC3/Unc5 Signalling Complex

Receptor oligomerization often leads to the formation of signalling hubs that amplify ligand sensitivity [40, 341], and/or modulate downstream signalling. These signalling hubs have been reported in morphogen [342–345] and cellular guidance receptors [346–350]. Heterotypic interactions with HSPG regulate the spatial organization of many of these receptors and ligands to the discrete cellular regions and could facilitate the formation of tertiary complexes [143, 351]. The results of my study suggest the formation of such a signalling hub. It is possible that upon GPC3 binding multiple Unc5 repulsive guidance receptors are brought together.

The multitude of signals required to inform the many different cell population makes it necessary to modulate the signalling capacity of a limited number of receptors. This attenuation of signalling is possible in the FLRT/Unc5/Lphn interaction which can adopt several different stoichiometries. Similarly, the GPC3/Unc5 interaction may also form a 1:1, 2:2 and 4:4 complex, observed in native MS. Similar to the FLRT/Unc5/Lphn interaction, the different stoichiometries could be homologue dependent. The formation of a different stoichiometry may already be reflected in the difference in affinity for Unc5B and D to GPC3, even though the Unc5's interfaces for the GPC3 interaction is conserved across all four family members. Native MS using each Unc5 family member in complex with GPC3 could be used to further investigate the extend of multimerization of the Unc5 receptor.

How the receptors would be organized on the cell membrane remains unclear. It is conceivable that the complex could adopt a 2:2 or 4:4 stoichiometry in a *cis* or *trans* orientation (figure 6.2). These different orientations and possible stoichiometries could have varying signalling effects in respect to the cytoplasmic domains of Unc5. With advances in cryo-EM the GPC3/Unc5 protein complex to be studied with all its ectodomains or as a full-length protein, revealing its stoichiometry, orientation and cytoplasmic domain architecture. Extracellular vesicles have been

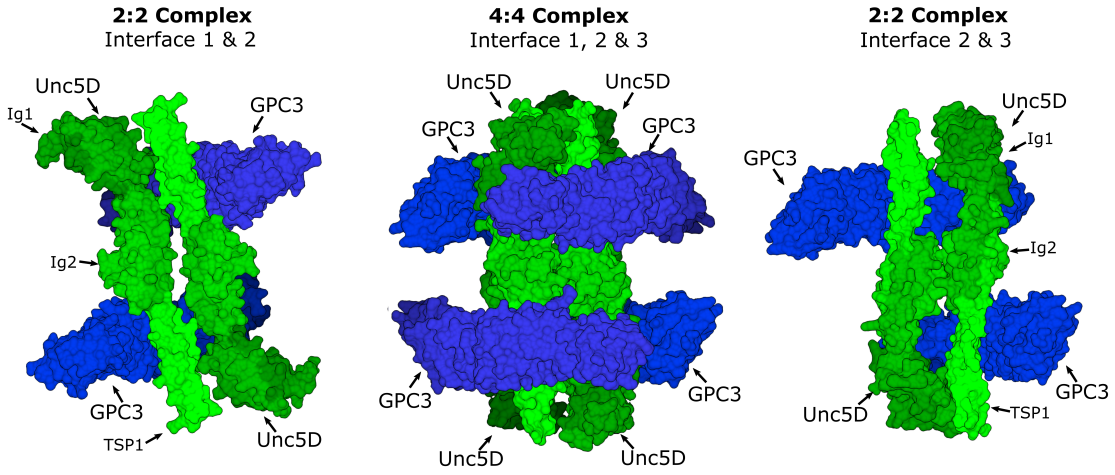


Figure 6.1: The three possible higher order complexes derived from the GPC3/Unc5 crystal structure. Unc5D (green) and GPC3 (blue) are depicted as surfaces. Two possible 2:2 configurations are shown, in which interface 1 and 2 (left panel), or interface 2 and 3 (right panel) are used. The full 4:4 assembly is shown in the middle panel. The images were prepared in Chimera.

used to study transmembrane proteins in their native lipid membrane [352]. The weak interactions that maintain the GPC3/Unc5 may not result in the complex dissociating during sample preparation. Fixation of the complex using gradient fixation could stabilize the complex [353].

It has been proposed that Unc5 requires homo- and/or heterodimerization to inhibit its apoptotic signalling as a dependency receptor, such homodimerization is observed in a 4:4 *trans* interaction. A *trans* interaction would orient the complex in such a manner that the crystallized portion of the complex would span 130 Å. Such a *trans* interaction would be sufficient to span a tight junction or synapse, accounting for the addition of two TSP2 domains at either end. In such a scenario, the GPC3 C-termini face inwards, suggesting that it acts as a soluble ligand; however, the stalk region of glypicans have not yet been characterized and so the relative orientation cannot be predicted. To ascertain a *trans* interaction, cell aggregation assays have been implemented between homo- and heteromeric receptors [54, 354, 355]. Suspension cells (such as K562) expressing Unc5 tagged with a fluorescent protein could be mixed or co-expressed with GPC3 to determine if they aggregate. If such a *trans* interaction occurs, then it is conceivable that cells which express Unc5 must

remain together to cluster these receptors for signal transduction. Detachment from other cells could induce apoptosis, also known as anoikis [356].

Interestingly, a *cis* interaction has striking similarities in its Unc5 arrangement as the octameric supercomplex of FLRT2/Unc5D/Lphn3, which contains two Unc5D receptors in an antiparallel configuration [69]. In such an interaction, the orientation of GPC3 would suggest that it could still be membrane tethered. Single particle tracking could identify if a cell expressing both GPC3 and Unc5 on its cells colocalize. Furthermore, if the Unc5 receptors come from the same cell, binding to GPC3 in such a manner would separate their cytoplasmic domains (in a 2:2 interaction). It has been demonstrated using FRET that upon ligand binding, integrins separate their cytoplasmic domains [357, 358]. Similarly, cells expressing two different Unc5s with a FRET pair could probe the separation of the domains upon GPC3 addition of GPC3. The biological significance of Unc5s cytoplasmic domain separation is not yet understood.

6.2 Biological Significance of the GPC3/Unc5 Interaction

6.2.1 GPC3 extends the neuronal context

Unc5 is important in all stages of neuronal development [56, 359]. For migration, Unc5 is found throughout the developing brain; for example, its interaction with FLRT delays migration of neurons from the subventricular zone to the cortical plate [104]. For synapse development and maintenance, both netrin1/DCC and FLRT/Lphn have been shown to play a role in the formation of synapses, possibly in conjunction with Unc5 [359–361]; however, the mechanism by which Unc5 regulates synaptogenesis is not fully understood.

GPC3, on the other hand, has no known function in the developing nervous system, which is in contrasts with the other glypican members. For example, GPC1

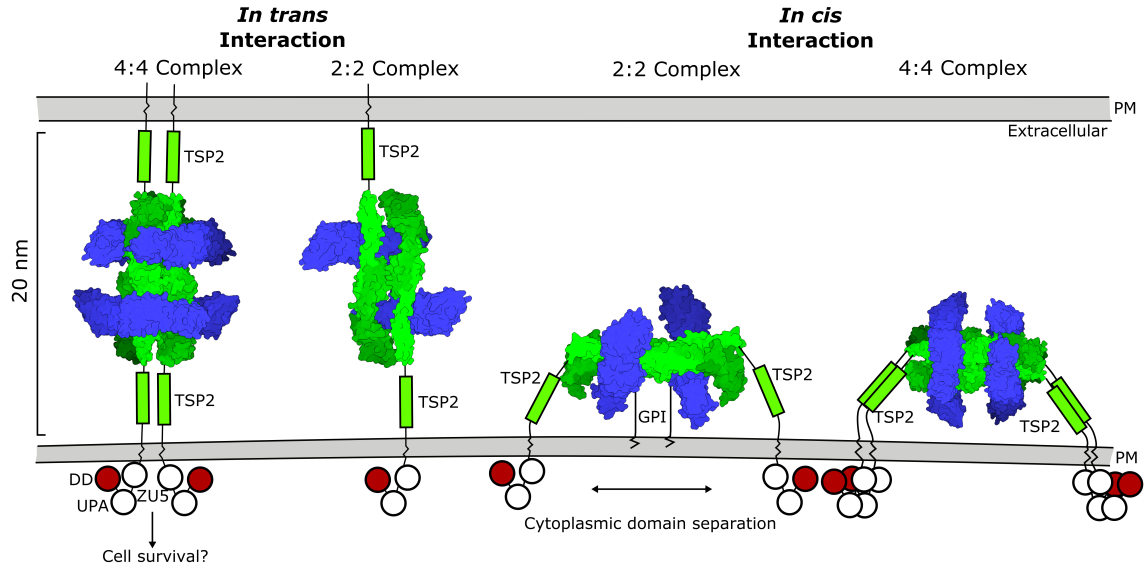


Figure 6.2: Possible orientations of the GPC3/Unc5D interactions. Unc5Ds extracellular domains are shown as surfaces (green), in which the green box represents the TSP2 domain not present in the crystal structure. The crystallized portion of GPC3 is shown as a surface (blue), in which the C-terminal portion is not shown. The *trans* interaction can possibly span across synaptic clefts or tight junctions (20 *nm*) (left panel). The *cis* interaction may be oriented the Unc5 parallel to the surface, in which the C-terminus of GPC3 faces to the membrane in a 2:2 stoichiometry (right panel). The structure was prepared in Chimera.

regulates brain size [170]; GPC2 modulates neural differentiation [128]; GPC4 and GPC6 promote the formation of excitatory synapses [182, 362]; and GPC5 stabilizes excitatory synapses through its interaction with LRRTM4 [184]. Indeed, GPC3 expression was only identified in motoneurons and dorsal root ganglia, in which its function is not yet understood [196]. Nonetheless, in recent years advances in single-cell transcriptomic analysis have revealed subpopulations of neurons that are characterized by their expression of GPC3 [363–365]. These neuronal populations may reveal that the specific interaction of GPC3 to Unc5 has a unique biological role.

One such neuronal subpopulation was identified in the adult mouse visual cortex. Vasoactive intestinal peptide (VIP)-positive GABAergic interneuron population were characterized by their GPC3 expression [363, 364]. Unlike other VIP-positive cell types, which are enriched in the upper cortical layers, GPC3 expressing VIP-positive cells were found in cortical layers 5 and 6. The use of single-cell transcriptomics

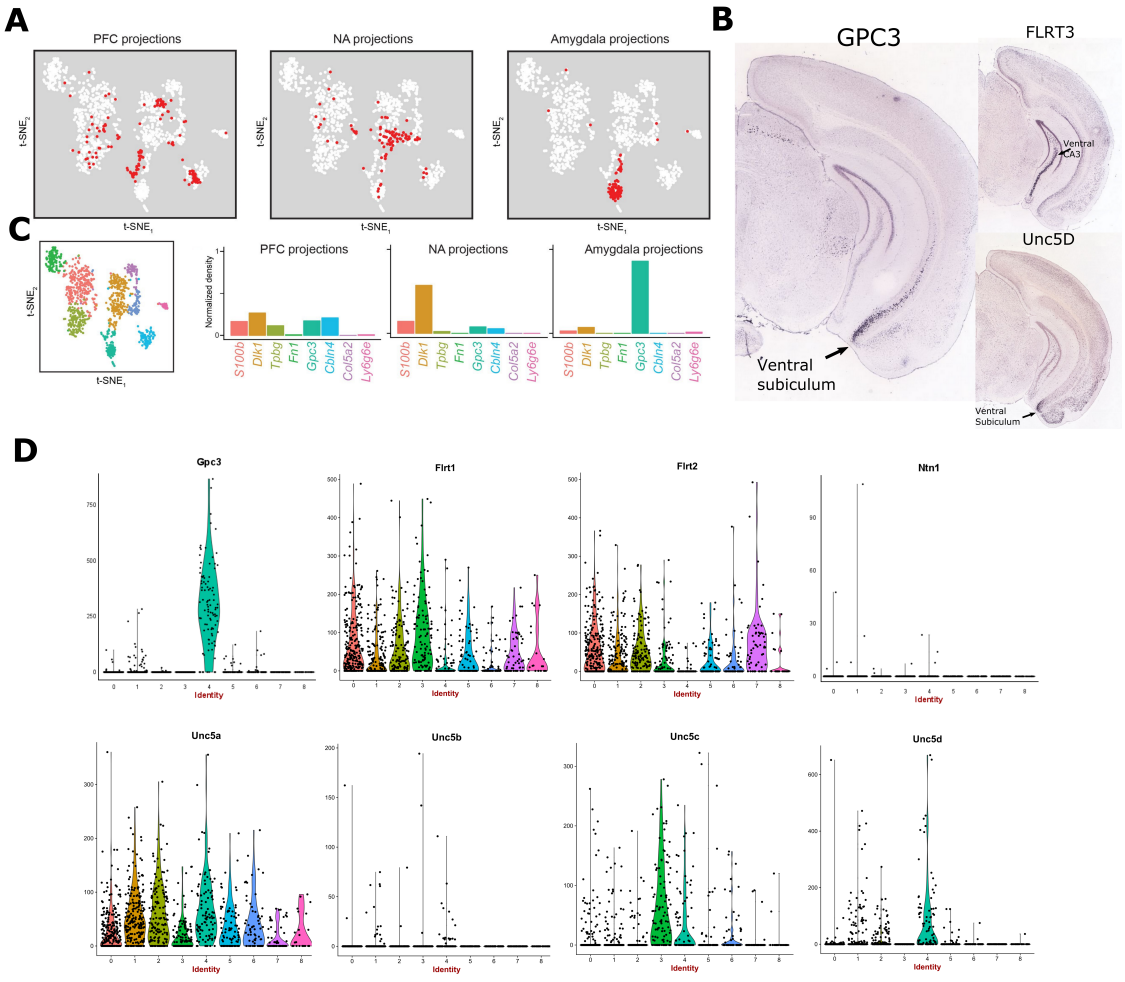


Figure 6.3: Expression profile of the hippocampus and subiculum neurons. **A/C)** Sequencing profile of three different neuronal populations, in which amygdala projections have high levels of GPC3. The figure was taken from Cembrowski et al. (2018) [365]. **B)** Allen brain atlas coronal section of the mouse brain (P56) showing expression of GPC3, Unc5D and FLRT3 [199]. **D)** RNAseq of Unc5A-D and FLRT1/2 and the corresponding graphs were obtained from the Cembrowski et al. (2018) database. High levels of Unc5, especially Unc5D, are found in identity four neurons, which correspond to GPC3 expressing amygdala projecting neurons. FLRT1/2 is found in several identities, in which little expression is in identity four. Single-cell RNA-seq was obtained from mature (P56) male C57BL/6 mice.

has been effectively used to understand how different neuronal cell classes confer an unique identity. If GPC3 acts through Unc5 in these neuronal population has yet to be explored. Identification of neuronal populations that present both Unc5 and GPC3 using single-cell transcriptomics or immunofluorescence colocalization may reveal possible targets for further study.

Another recently identified neuronal subpopulation, characterized by its specific GPC3 expression, is present in the subiculum and projects to the amygdala (>P56 male C57BL/6 mice) (figure 6.5A/C) [365]. The expression of GPC3 in these neurons implies that they have a specific cellular context involved in postnatal amygdala development (figure 6.3C). Using the same database, HippoSeq, we find that these subpopulation of neurons also express Unc5A, Unc5C and Unc5D. Conversely, these neurons do not express FLRT1, FLRT2 and netrin1 (FLRT3 and DCC data was not available; figure 6.3D). It is interesting that these neurons form connections with the amygdala because the dorsal and ventral part of the hippocampus are considered functional and physiologically distinct [366]. The dorsal hippocampus connects to the cortical areas, involved in spatial learning [367, 368], while the ventral hippocampus is connected to the amygdala and hypothalamic-pituitary-adrenal axis, involved in emotional processing and anxiety [367–369]. The distinction between the ventral and dorsal hippocampus also can be registered in the expression of FLRT found in the dorsal CA1, for FLRT2, and the CA3, for FLRT3 (P56; figure 6.3B) [199]. In contrast, GPC3 is predominantly in the ventral part of the hippocampus, CA1 [199]. Targeted knockout/down of GPC3 and/or Unc5D in these neuronal populations could alter the number of functional neural connections, which could be visualized using histological or electrophysiological methods [370].

The distinct expression patterns found in the dorsal and ventral hippocampus for FLRT and GPC3 is especially interesting as both proteins have been found secreted from the membrane [104]. A dorsal to ventral gradient between FLRT and GPC3 could compete for Unc5 binding. Indeed, the crystal structure presented in this thesis suggests that GPC3s interaction with Unc5 would be incompatible

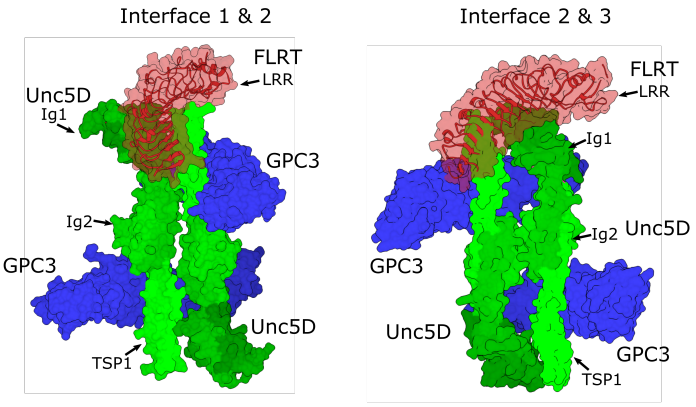


Figure 6.4: Superposed FLRT^{LRR} domain interaction on both GPC3/Unc5D 2:2 stoichiometry. Unc5D (green) and GPC3 (blue) are depicted as surfaces. FLRT^{LRR} is shown as a transparent surface with its cartoon representation for clarity (red). The FLRT^{LRR}/Unc5D^{Ig1} structure (PDB 4VC2) was used to superpose the Ig1 domains onto each other. The two possible 2:2 configurations are shown, in which interface 1 and 2 (left panel), or interface 2 and 3 (right panel) are used. Both indicate that FLRT^{LRR} would clash with the GPC3/Unc5D interaction.

with the other structurally characterized FLRT/Lphn interaction. In figure 6.6, assuming a minimal 2:2 binding of GPC3 with Unc5D, both possible arrangements would sterically hinder FLRT^{LRR} interaction with Unc5 through the antiparallel Unc5^{TSP1}. Similarly, both FLRT and GPC3 have similar affinities around 300-500 *nM*. The possible competitive interaction could be biologically relevant as both GPC3 and FLRT can be shed from the membrane and interact with similar affinity to Unc5D in a gradient. In regard to the FLRT/Unc5/Lphn supercomplex, which utilizes the same conserved interfaces of Unc5 as GPC3; however, in such a case, the high affinity of the supercomplex (94 *nM* [69]) may outcompete GPC3 binding.

6.2.2 Modulating migration

Netrin1 interaction with DCC is well understood as an attractive guidance cue for commissural neurons. The presence of Unc5 on the cell surface results in the switching from attractive to repulsive guidance through DCC-dependent or -independent pathways [96]. Finci and colleagues proposed a model in which specific

HS chains may promote the formation of a netrin1/DCC homodimer complex or a netrin1/Unc5/DCC heterodimer complex. This modulation between DCC and Unc5 through HS was shown in C. *elegans*, in which the glypican, LON-2, modulates netrin1/DCC attractive and repulsive signalling [371]. As is characteristic of the glypican family, GPC3 may stabilize the formation of a tertiary complex through its interaction with Unc5, while the HS-GAGs may interact with netrin1/DCC. Colocalization of Unc5, DCC and netrin1 by GPC3 core and HS chains could form such a signalling hub. Conversely, GPC3 may sequester Unc5 from the netrin1/DCC signalling and so switching repulsion to attraction. Unc5 has been shown to selectively undergo endocytosis of protein kinase C [372]. It is conceivable that GPC3 may cluster Unc5 for endocytosis, similar to GPC3 induced endocytosis of Wnt [158], and Shh [219].

Netrin1 has been shown to act as a survival factor in commissural neurons [373]; however, Unc5A-induced apoptosis in motoneurons was shown to be independent of netrin1 (E12 and E16) [374]. This suggest to a yet unknown mechanism by which Unc5 regulates the numbers of motoneuron in the spinal cord. GPC3 expression has been reported in the motoneurons of the spinal cord and dorsal root ganglia in fetal periods 2 and 3 (9 to 19 weeks) [196];however, the Unc5A-induced apoptosis study (in mice) and the expression of GPC3 (in human) do not occur in the same Carnegie stages. Nonetheless, patients with SGBS present hypotonia, which could be a consequence of improper innervation of the muscles by motoneurons [187]. Of particular interest, Manitt and colleagues found that during the early stages of development in the spinal cord (E14), the rat expresses a shorter splice variant of Unc5A, which lacks the TSP1 domain, whilst in the adult spinal cord the full length and isoform were detected [333]. Considering netrin1 does not act through TSP1 [51, 101], and GPC3 only interacts when TSP1 is present it presents an interesting avenue for further investigation. Identifying the expression of GPC3 and the Unc5 isoforms during the development of the spinal cord motoneurons may reveal an overlap that could be further explored for biological significance.

Migration can also be regulated by GPC3 in the vascular system, in which Unc5B is ubiquitously expressed. FLRT has been shown to inhibit angiogenesis and HUVEC cell migration [54, 61], while GPC3 has been associated with vascular invasion of tumours [233] and inhibiting the accumulation of coronary arteries [177]. Like FLRT, GPC3 affinity to Unc5B is significantly lower compared to Unc5D, with Unc5B having an K_D of $\sim 2\ \mu M$ for $GPC3^{\Delta C}$ and 21 μM for $FLRT2^{LRR}$ [54]. Importantly, this affinity was shown to be higher in cell binding assays, where $FLRT3^{LRR}$ has an K_D of 66 nM [53]. Nonetheless, it is conceivable that secreted FLRT and GPC3 could compete for Unc5B on endothelial cells to regulate angiogenesis. This mechanism could be probed by using a stripe assay, in which stripes either contain FLRT or GPC3, in which HUVEC cells are allowed to migrate to or away from attractive and repulsive signalling. The ability for GPC3 to regulate angiogenesis through Unc5B could be further investigated by incubating live retinal explants with GPC3 and mutants that are unable to bind Unc5.

6.3 GPC3s Role in Cancer

Unc5 and GPC3 have both been implicated in promoting proliferation (by inhibiting apoptosis) and modulating migration in cancer cells. Therefore, they have proven attractive targets for the development of drugs for the treatment of specific cancers. Netrin1 is overexpressed by many different cancer cells, and through Unc5 or DCC inhibits apoptosis and promotes Yes-associated protein (YAP) that induce proliferation and migration [112, 116]. Overexpression of GPC3 promotes proliferation and migration in cancer cells, such as HCC [234–236, 241]. Conversely, downregulation of GPC3 in breast cancer promotes invasiveness [219, 260, 261]. The suggested mechanisms by which GPC3 promotes proliferation and migration is through the Wnt and Hh pathways [219, 236]. Characterization of the GPC3/Unc5 interaction may elucidate alternative regulatory pathways in these cancer cells that have not yet been explored. Identifying cancer cell lines that express both

Unc5 and GPC3 could act as good model cells to test if GPC3/Unc5 interactions has any pathological significance.

The generation of therapeutic drugs that target not properly regulated pathways that promote cancer proliferation, migration, or inhibit apoptosis are especially attractive targets. Netrin1 antibodies have been generated that disrupt the specific interaction of netrin1 to Unc5, triggering apoptosis in several cancer cells [75, 76, 79, 84, 375, 376]. A GPC3 single domain antibody (HN3) targeting GPC3 has shown to inhibit HCC proliferation through Wnt/β-catenin and YAP signalling [239, 258, 259]. The structure of both GPC3 and GPC3/Unc5 provide important structural knowledge that can guide the development of small drugs or therapeutic antibodies to disrupts such binding.

6.4 One Receptor and its Several Functions

Unc5 was thought to interact with only netrin1/DCC for many years. As such, knockout models of Unc5 attributed the physiological consequences to netrin1 [102]. The characterization of the FLRT/Unc5 interaction revealed how Unc5 acts independently from netrin1 in migration and neuronal guidance [53, 54]. This study presents the first structural characterization of the novel GPC3/Unc5 interaction. The GPC3/Unc5 crystal structure reveals a compact multimeric protein assembly that adds to the functional repertoire of Unc5s previously known only to interact with netrin1/DCC/DSCAM or FLRT/Lphn (figure 6.6). Although the biological role of this interaction is not yet understood, further investigation will likely reveal roles in migration or cell proliferation/apoptosis. GPC3 has been attributed to the regulation of several signalling pathways, such as Wnt and Hh, by localizing stable signalling platforms, sequester ligands, or endocytose ligands and receptors [157, 163]. These findings might provide further evidence of the extensive crosstalk between signalling pathways. Indeed, it has been proposed that HS play a role in switching the interaction of netrin1/DCC to recruit Unc5. GPC3 as a HSPG

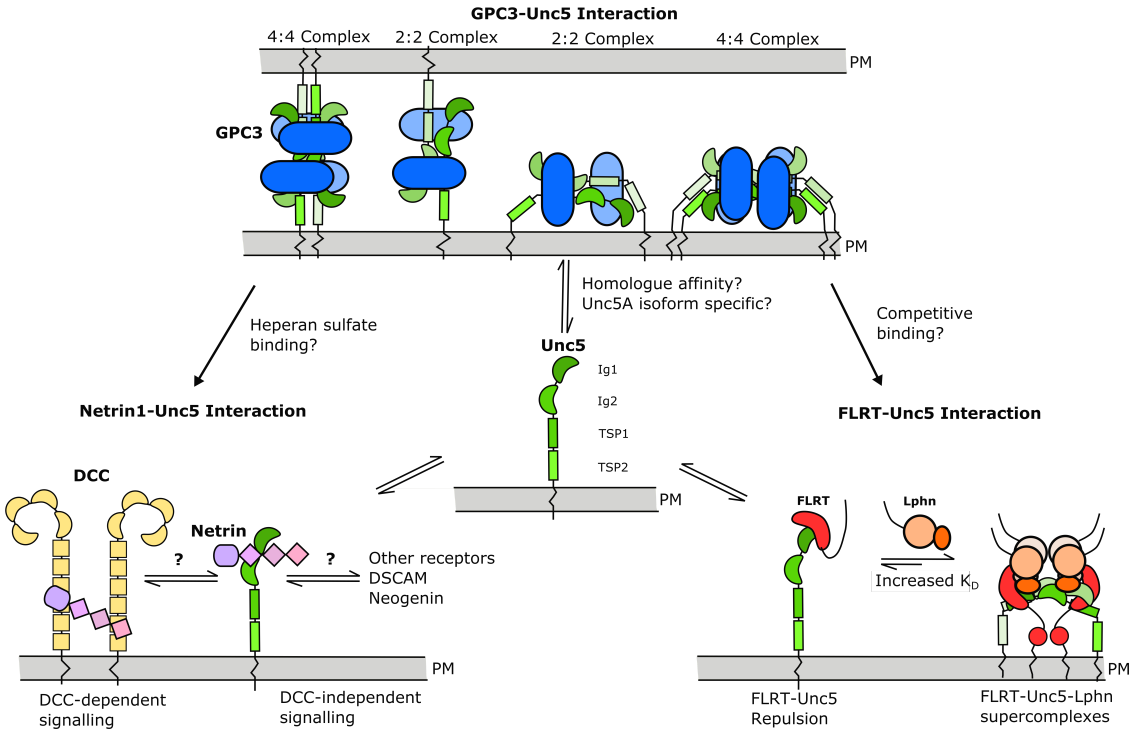


Figure 6.5: The known extracellular interactions of Unc5s. The netrin1/Unc5 interaction occurs through Unc5s Ig domains. It has been proposed that netrin1 (pink) incorporates Unc5 into DCC (yellow); however, the hetero oligomerization of Unc5 with DCC/neogenin/DSCAM is not yet known. The FLRT/Unc5 primary interaction occurs with the LRR domain of FLRT (red) with the Ig1 domain of Unc5. In the presence of Lphn (orange), multimeric complex form with a 1:1:2 or 2:2:4 stoichiometry, FLRT/Unc5/Lphn. The GPC3/Unc5 interaction has four proposed assemblies of which its orientation on the plasma membrane (annotated PM) is not yet known. The GPC3/Unc5 interaction may be involved in the netrin1/Unc5 interaction through GPC3 HS-GAGs or compete with FLRT for Unc5 binding. Figure was prepared in Inkscape.

could play a role this switching [98]. Conversely, GPC3 may compete with FLRT for Unc5 binding in the vascular and/or nervous system. The newly identified interaction between GPC3/Unc5 demonstrates how a single receptor can interact with several ligands and may shed light on how cells acquire cellular context, through the crosstalk between multiple pathways.

Appendices

A

Appendix: Previous Constructs and Primers

Table A.1: Previously cloned constructs used in this thesis. Constructs that were subcloned before the start of this thesis. The pHlSec vector containing either a C-terminal (C) hexahistidine-tag (His6), Avitag (Avi), or Green fluorescent protein (mVenus). The pHlSec vector could also contain the N-terminal (N) Human influenza hemagglutinin epitode tag (HA). The amino acid boundaries a.a_N-a.a_C subcloned into the pHlSec vector.

Construct	Mutation	Vector	Cloning Sites	Tags	a.a_N-a.a_C
*hs*Unc5A^{ecto}		pHlSec	EcoRI/KpnI	His6(C)	1-300
*hs*Unc5B^{ecto}		pHlSec	EcoRI/KpnI	His6(C)	1-355
*hs*Unc5B^{ecto}		pHlSec	EcoRI/KpnI	Avi(C) His6(C)	1-355
*rn*Unc5D^{Ig1}		pHlSec	EcoRI/KpnI	His6(C)	1-161
*rn*Unc5D$^{Ig1\text{-}Ig2}$		pHlSec	EcoRI/KpnI	His6(C)	1-244
*rn*Unc5D$^{Ig1\text{-}Ig2\text{-}TSP}$		pHlSec	EcoRI/KpnI	His6(C)	1-307
*rn*Unc5D^{ecto}		pHlSec	EcoRI/KpnI	His6(C)	1-382
*rn*Unc5D^{ecto}	Y154N R156T	pHlSec	EcoRI/KpnI	His6(C)	1-382
*rn*Unc5D^{ecto}		pHlSec-mVenus	Age1/KpnI	His6(C)	1-382
*rn*Unc5D^{ecto}	Y154N R156T	pHlSec-mVenus	Age1/KpnI	HA(N) His6(C)	1-382
*mm*GPC3$^{\Delta C}$		pHlSec	Age1/KpnI	His6(C)	31-482
*mm*GPC3$^{\Delta C}$		pHlSec	Age1/KpnI	Avi(C) His6(C)	31-482
*mm*GPC3$^{e\Delta C}$		pHlSec	Age1/KpnI	His6(C)	31-488
*mm*FLRT^{LRR}		pHlSec	Age1/KpnI	His6(C)	35-362

Table A.2: Primers of the constructs used in this thesis. The direction (Dir.) of the primers, forward (Fwd.) and reverse (Rev.).

Construct	Cloning Sites	Dir.	Primers
*hs*Unc5B^{ecto}-Avi	AgeI/KpnI	Fwd	GTAGCTGAAACCGGTGGCACTGATTCTGGCAGCGAGGTGC
		Rev	GGAACCTCCGGTACCCGCCGCATCCCCTGAGGCCTCCAGC
*hs*Unc5B$^{Y150N\ R152T}$-Avi		Fwd	TACGTCCGCATCGCCAACCTGACGAAGAACTTCGATCAGGAGCCTCTGG
		Rev	GGCGATGCGGACGTAGGCTCGGCGAC
*hs*Unc5B$^{A279N\ L281T}$-Avi		Fwd	ACCTGCACCAACCCCAATCCAACTAACGGAGGGGCCTTCTGCGAG
		Rev	GGGGTTGGTGCAGGTCCGGGTGCGC
*mm*GPC3$^{\Delta C}$	AgeI/KpnI	Fwd	GTAGCTGAAACCGGTGACGCCACCTGTCACCAGGTCCGTTC
		Rev	GTGATGGTGGTGCTTGGTACCTTTACCCTTGGGCACAGACATGGTTC
*mm*GPC3$^{AQYA\ \Delta C}$		Fwd	GCCCATTCTCAACAAGCCCAATATGCATTTGCTTATTATCCTGAAGATCTC
		Rev	TTGTTGAGAATGGGCACATAACTTGC
*mm*GPC3$^{\Delta 8\ \Delta C}$		Fwd	GGCAAGTTATGTGCCTTTGCTTATTATCCTGAAGATCTCTTTATTGAC
*mm*GPC3$^{\Delta 9\ \Delta C}$		Fwd	GGCAAGTTATGTGCCGCTTATTATCCTGAAGATCTCTTTATTGAC
*mm*GPC3$^{\Delta 10\ \Delta C}$		Fwd	GGCAAGTTATGTGCCTATTATCCTGAAGATCTCTTTATTGAC
*mm*GPC3$^{\Delta 11\ \Delta C}$		Fwd	GGCAAGTTATGTGCCTATCCTGAAGATCTCTTTATTGACAAG
*mm*GPC3$^{\Delta 12\ \Delta C}$		Fwd	GGGCAAGTTATGTGCCCCTGAAGATCTCTTTATTGACAAGAAAG
*mm*GPC3$^{\Delta 13\ \Delta C}$		Fwd	GGCAAGTTATGTGCCGAAGATCTCTTTATTGACAAGAAAGTATTAAAAGTTGC
*mm*GPC3$^{\Delta 23\ \Delta C}$		Fwd	TGGCAAGTTATGTGCCACCTTATCCAGCCGAAGAAGGGAAC
		Rev	GGCACATAACTTGCCAATAGTGGTGGTCAGCTTTCCTGC
*hs*GPC3$^{\Delta C}$	AgeI/KpnI	Fwd	GTAGCTGAAACCGGTGACGCCACCTGTCACCAAGTC
		Rev	GTGGTGCTTGGTACCAACTCTACCTTTGGGCATAGACATGG
*hs*GPC3$^{\Delta C}$-avi		Rev	GGAACCTCCGGTACCAACTCTACCTTTGGGCATAGAC
*hs*GPC3^{L156N}-avi		Fwd	GTGTCTCTCTACATCAACGGTTCTGACATCAATGTAGATGACATGG
		Rev	GATGTAGAGAGACACATCTGTGAAAAATTCACC
*hs*GPC3$^{S158N\ I160T}$-avi		Fwd	CTCTACATCTTGGGTAACGACACTAATGTAGATGACATGGTCAATGAATTG
		Rev	ACCCAAGATGTAGAGAGACACATCTG
*hs*GPC3^{D150N}-avi		Fwd	GGTGAATTTTTCACAAATGTGTCTCTCTACATCTTGGGTTCTG
		Rev	TGTGAAAAATTCACCCACAAACTC
*hs*GPC3^{E147R}-avi		Fwd	TTTGAGTTTGTGGGTCGATTTTTCACAGATGTGTCTCTCTACATCTTGGGTTCTG
*hs*GPC3^{D150R}-avi		Fwd	TTTGAGTTTGTGGGTGAATTTTTCACACGAGTGTCTCTCTACATCTTGGGTTCTG
*hs*GPC3$^{E147R\ D150R}$-avi		Fwd	TTTGAGTTTGTGGGTCGATTTTTCACACGAGTGTCTCTCTACATCTTGGGTTCTG
		Rev	ACCCACAAACTCAAAAGCTTGTGG
*hs*GPC3^{D165R}-avi		Fwd	GACATCAATGTAGATCGAATGGTCAATGAATTGTTTGACAGCCTGTTTCCAGTC
*hs*GPC3^{E169R}-avi		Fwd	GACATCAATGTAGATGACATGGTCAATCGATTGTTTGACAGCCTGTTTCCAGTC
*hs*GPC3$^{D165\ E169R}$-avi		Fwd	GACATCAATGTAGATCGAATGGTCAATCGATTGTTTGACAGCCTGTTTCCAGTC
		Rev	ATCTACATTGATGTCAGAACCCAAGATG

B

Appendix: Anisotropy Data Statistics

Table B.1: Anisotropy correction before and after anisotropic cut-off for each resolution shell for *hs*GPC3$^{\Delta C}$ (#3).

Resolution shell	Observed reflectons		Completeness (%)		I/σ	
	Before	After	Before	After	Before	After
10.6	762	762	100	100	20.24	20.24
8.47	764	764	100	100	19.42	19.42
7.38	764	764	100	100	14.05	14.05
6.71	766	767	99.9	99.9	10.57	10.57
6.23	767	767	100	100	7.81	7.81
5.87	767	767	100	100	7.02	7.02
5.56	765	765	99.7	99.7	6.21	6.21
5.31	768	768	98.5	98.5	5.89	5.89
5.10	768	768	96.6	96.6	5.77	5.77
4.93	768	768	96.6	96.6	5.40	5.40
4.76	766	766	95.5	95.5	5.38	5.38
4.61	830	830	97.1	89.5	5.04	5.39
4.45	1076	1076	97.0	69.5	4.37	5.75
4.28	1279	1083	97.8	58.5	3.32	5.11
4.10	1499	940	98.0	50.1	2.44	4.35
3.92	1952	916	96.8	37.9	1.52	3.42
3.71	2621	932	97.5	28.6	1.09	3.22
3.50	3426	931	98.7	22.0	0.80	3.40
4.27	4908	917	99.8	15.5	0.48	2.90
3.01	7560	840	99.9	10.6	0.20	2.24
Total	33576	16890	98.8	45.2	3.33	7.17

Table B.2: Anisotropy correction before and after anisotropic cut-off for each resolution shell for *mm*GPC3$^{\Delta}$ & *rn*Unc5D$^{\text{Ig1-Ig2-TSP1}}$ (#7).

Resolution shell	Observed reflectons		Completeness (%)		I/σ	
	Before	After	Before	After	Before	After
11.9	790	790	99.5	99.5	47.9	47.9
9.38	789	789	100	100	47.6	47.6
8.14	791	791	100	100	37.7	37.7
7.37	788	790	99.9	99.9	26.0	26.0
6.83	791	788	100	100	17.5	17.5
6.31	790	791	100	100	13.5	13.5
6.07	790	790	100	100	10.2	10.2
5.80	789	789	100	100	8.50	8.50
5.57	790	790	100	100	7.65	7.65
5.37	790	790	100	100	7.27	7.27
5.20	790	790	100	100	6.61	6.61
5.05	789	789	100	100	6.05	6.05
4.91	790	790	100	100	5.58	5.58
4.79	789	789	100	100	4.91	4.91
4.67	842	842	100	93.7	3.62	3.82
4.53	1061	1061	100	74.5	3.46	4.38
4.38	1335	1056	100	59.2	2.37	3.51
4.21	1761	941	100	44.9	1.64	2.98
4.02	2393	867	100	33.0	1.01	2.29
3.80	3297	722	99.9	23.9	0.47	1.43
Total	21745	16545	100	72.6	9.74	13.4

Table B.3: Anisotropy correction before and after anisotropic cut-off for each resolution shell for *hs*GPC3$^{\Delta}$ & *rn*Unc5D$^{\text{Ig1-Ig2-TSP1}}$ (#9).

Resolution shell	Observed reflectons		Completeness (%)		I/σ	
	Before	After	Before	After	Before	After
13.5	901	901	99.9	99.9	6.49	6.49
10.7	901	901	99.7	99.7	6.79	6.79
9.30	902	902	100	100	6.02	6.02
8.44	901	901	99.9	99.9	5.89	5.89
7.83	901	901	99.9	99.9	5.71	5.71
7.37	901	901	99.9	99.9	4.95	4.95
7.00	901	901	100	100	4.05	4.05
6.69	902	902	100	100	3.24	3.24
6.43	901	901	100	100	2.85	2.85
6.20	901	901	99.9	99.9	2.45	2.45
6.01	901	901	100	100	2.18	2.18
5.83	901	901	100	100	2.04	2.04
5.68	924	924	100	97.6	1.94	1.97
5.53	950	950	100	94.8	1.73	1.78
5.38	1054	1001	100	85.5	1.68	1.82
5.22	1277	1116	100	70.6	1.56	1.80
5.05	1561	1188	99.9	57.7	1.43	1.84
4.84	2227	1396	99.8	40.4	1.28	1.88
4.55	3847	1456	99.9	23.4	0.90	1.73
4.10	8226	1115	100	10.9	0.48	1.59
Total	30880	119977	99.9	58.3	2.17	3.39

C

Appendix: Conservational Analysis

Table C.1: Conservational analysis of GPC3. The sequences used for conservational analysis were obtained from Uniprot.

GPC3	Species	Uniprot entry
	Homo sapiens (Human)	P51654
	Pan troglodytes (Chimpanzee)	A5A6P7
	Pongo abelii (Sumatran orangutan)	H2PWT4
	Nomascus leucogenys (Northern white-cheeked gibbon)	G1QMX0
	Macaca mulatta (Rhesus macaque)	A0A1D5QAU1
	Mus musculus (Mouse)	Q8CFZ4
	Rattus norvegicus (Rat)	P13265
	Oryctolagus cuniculus (Rabbit)	G1SG22
	Ictidomys tridecemlineatus (squirrel)	I3MES6
	Canis familiaris (Dog)	F1PM34
	Felis catus (Cat)	A0A337S4V2
	Mustela furo (European domestic ferret)	M3YMU2
	Monodelphis domestica (Gray short-tailed opossum)	F6TML0
	Anas platyrhynchos (Northern mallard)	U3J5H7
	Bos taurus (Bovine)	Q3ZBZ6
	Equus caballus (Horse)	F7B944
	Sus scrofa (Pig)	K7GQ93
	Ailuropoda melanoleuca (Giant panda)	G1L3N6
	Ornithorhynchus anatinus (Duckbill platypus)	F7AT46
	Gallus gallus (chicken)	A0A1D5NTH6
	Taeniopygia guttata (Zebra finch)	H0YXP1

Table C.2: Conservational analysis of GPC1. The sequences used for conservational analysis were obtained from Uniprot.

GPC1	Species	Uniprot entry
	Homo sapiens (Human)	P35052
	Pan troglodytes (Chimpanzee)	K7BMY8
	Callithrix jacchus (White-tufted-ear marmoset)	F7HWX6
	Mus musculus (Mouse)	Q9QZF2
	Rattus norvegicus (Rat)	P35053
	*Canis*familiaris (Dog)	F1PPA1
	Anas platyrhynchos (Northern mallard)	U3IFC4
	Bos taurus (Bovine)	G3X745
	Equus caballus (Horse)	F7DRG2
	Ornithorhynchus anatinus (Duckbill platypus)	U3IFC4
	Gallus gallus (chicken)	P50593
	Meleagris gallopavo (Wild turkey)	Q6QA54
	Xenopus tropicalis (Western clawed frog)	Q0V9W0

Table C.3: Conservational analysis of Unc5. The sequences used for conservational analysis were obtained from Uniprot.

Unc5	Species	Uniprot entry
Unc5B	*Homo* sapiens (Human)	Q8IZJ1
Unc5C	*Homo* sapiens (Human)	O95185
Unc5D	*Homo* sapiens (Human)	Q6UXZ4
Unc5A	*Pan* troglodytes (Chimpanzee)	A0A2I3SB57
Unc5B	*Pan* troglodytes (Chimpanzee)	K7BVI5
Unc5C-2	*Pan* troglodytes (Chimpanzee)	H2QPW9
Unc5D	*Pan* paniscus (Bonobo)	F7HWX6
Unc5A	*Mus* musculus (Mouse)	Q8K1S4
Unc5B	*Mus* musculus (Mouse)	Q8K1S3
Unc5C	*Mus* musculus (Mouse)	O08747
Unc5D	*Mus* musculus (Mouse)	Q8K1S2
Unc5A	*Rattus* norvegicus (Rat)	O08721
Unc5B	*Rattus* norvegicus (Rat)	O08722
Unc5C	*Rattus* norvegicus (Rat)	Q761X5
Unc5D	*Rattus* norvegicus (Rat)	F1LW30
Unc5B	*Gallus* gallus (chicken)	E1C228
Unc5C	*Gallus* gallus (chicken)	Q7T2Z5
Unc5D	*Gallus* gallus (chicken)	A0A1D5PNP5
Unc5b-b	*Xenopus* tropicalis (Western clawed frog)	C5IAW9

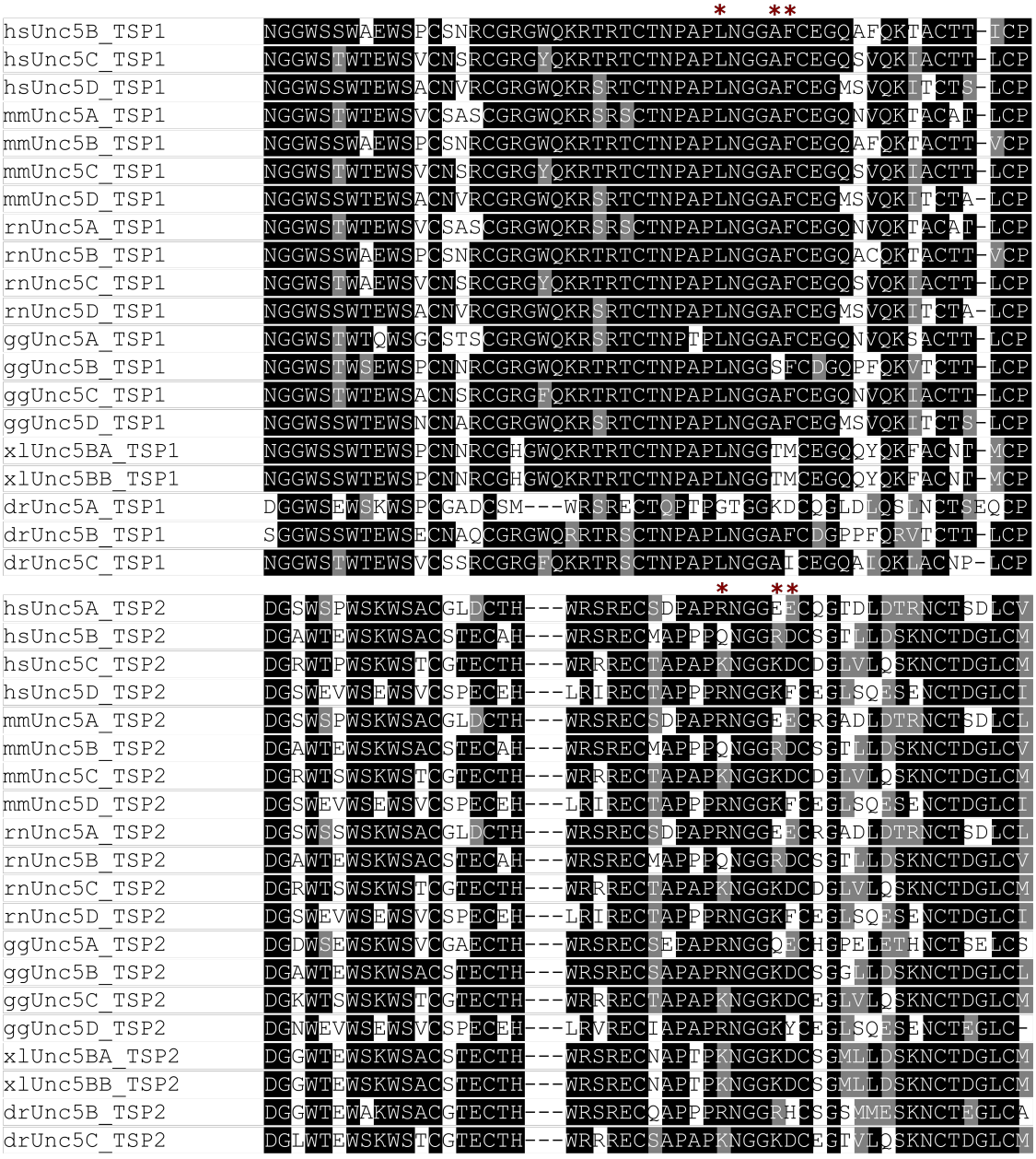


Figure C.4: Sequence alignment of TSP1 and TSP2. The sequences of TSP1 and TSP2 were aligned using TCOFFEE and prepared with Boxshade. The key residues in TSP1, L283, A287 and F288 are annotated with an asterisk.

D

Appendix: Native MS of GPC3

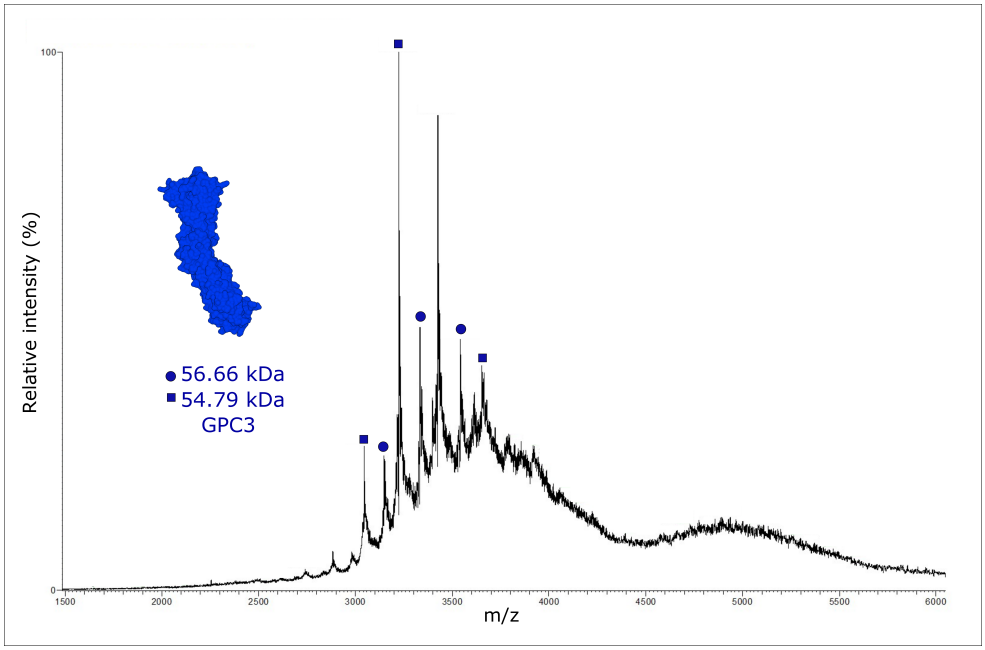


Figure D.1: Native MS of *mm*GPC3$^{\Delta C}$. Native MS was performed on 10 μM of *hs*GPC3$^{\Delta C}$ in 1.0 M of ammonium acetate. Two peaks that correspond to 56.66 (blue circle) and 54.79 kDa (blue square) could be identified. The expected mass of *mm*GPC3$^{\Delta C}$ is 56.86 kDa, determined by ExPaSy ProtParam [340] and with the addition of 3 N-glycosylation sugars of 1.2 kDa. Data collected and analysed by Dr. Ritu Raj.

References

[1] Samantha Fox, Paul Southam, Florent Pantin, Richard Kennaway, Sarah Robinson, Giulia Castorina, Yara E. Sánchez-Corrales, Robert Sablowski, Jordi Chan, Verônica Grieneisen, Athanasius F. M. Marée, J. Andrew Bangham, and Enrico Coen. "Spatiotemporal coordination of cell division and growth during organ morphogenesis". en. In: *PLOS Biology* 16.11 (Nov. 2018), e2005952.

[2] M. Suzanne and H. Steller. "Shaping organisms with apoptosis". en. In: *Cell Death and Differentiation* 20.5 (May 2013), pp. 669–675.

[3] J. F. R. Kerr, A. H. Wyllie, and A. R. Currie. "Apoptosis: A Basic Biological Phenomenon with Wide-ranging Implications in Tissue Kinetics". In: *British Journal of Cancer* 26.4 (Aug. 1972), pp. 239–257.

[4] Aravind Sivakumar and Natasza A. Kurpios. "Transcriptional regulation of cell shape during organ morphogenesis". en. In: *The Journal of Cell Biology* 217.9 (Sept. 2018), pp. 2987–3005.

[5] C. A. Erickson, K. W. Tosney, and J. A. Weston. "Analysis of migratory behavior of neural crest and fibroblastic cells in embryonic tissues". In: *Developmental Biology* 77.1 (June 1980), pp. 142–156.

[6] Andy Aman and Tatjana Piotrowski. "Cell migration during morphogenesis". eng. In: *Developmental Biology* 341.1 (May 2010), pp. 20–33.

[7] Verena Ruprecht, Pascale Monzo, Andrea Ravasio, Zhang Yue, Ekta Makhija, Pierre Olivier Strale, Nils Gauthier, G. V. Shivashankar, Vincent Studer, Corinne Albiges-Rizo, and Virgile Viasnoff. "How cells respond to environmental cues – insights from bio-functionalized substrates". en. In: *Journal of Cell Science* 130.1 (Jan. 2017), pp. 51–61.

[8] Norbert Perrimon, Chrysoula Pitsouli, and Ben-Zion Shilo. "Signaling mechanisms controlling cell fate and embryonic patterning". In: *Cold Spring Harbor perspectives in biology* 4.8 (2012), a005975.

[9] Anastacia Berzat and Alan Hall. "Cellular responses to extracellular guidance cues". In: *The EMBO journal* 29.16 (2010), pp. 2734–2745.

[10] Michael A. Rowland, Joseph M. Greenbaum, and Eric J. Deeds. "Crosstalk and the evolvability of intracellular communication". eng. In: *Nature Communications* 8 (2017), p. 16009.

[11] Irene Delgado and Miguel Torres. "Coordination of limb development by crosstalk among axial patterning pathways". eng. In: *Developmental Biology* 429.2 (2017), pp. 382–386.

[12] Daniel Morales and Artur Kania. “Cooperation and crosstalk in axon guidance cue integration: Additivity, synergy, and fine-tuning in combinatorial signaling”. eng. In: *Developmental Neurobiology* 77.7 (2017), pp. 891–904.

[13] Daniel Morales and Artur Kania. “Cooperation and crosstalk in axon guidance cue integration: Additivity, synergy, and fine-tuning in combinatorial signaling”. en. In: *Developmental Neurobiology* 77.7 (2017), pp. 891–904.

[14] Nobue Itasaki and Stefan Hoppler. “Crosstalk between Wnt and bone morphogenic protein signaling: A turbulent relationship”. en. In: *Developmental Dynamics* 239.1 (2010), pp. 16–33.

[15] Emma R. Andersson, Rickard Sandberg, and Urban Lendahl. “Notch signaling: simplicity in design, versatility in function”. en. In: *Development* 138.17 (Sept. 2011), pp. 3593–3612.

[16] Naomi Levy-Strumpf and Joseph G. Culotti. “Netrins and Wnts Function Redundantly to Regulate Antero-Posterior and Dorso-Ventral Guidance in C. elegans”. In: *PLoS Genetics* 10.6 (June 2014).

[17] Douglas A Lauffenburger and Alan F Horwitz. “Cell migration: a physically integrated molecular process”. In: *Cell* 84.3 (1996), pp. 359–369.

[18] Fei Xue, Deanna M Janzen, and David A Knecht. “Contribution of filopodia to cell migration: a mechanical link between protrusion and contraction”. In: *International journal of cell biology* 2010 (2010).

[19] Roberto Mayor and Sandrine Etienne-Manneville. “The front and rear of collective cell migration”. In: *Nature reviews Molecular cell biology* 17.2 (2016), p. 97.

[20] R. W. Sperry. “Chemoaffinity In The Orderly Growth of Nerve Fiber Patterns and Connections*”. In: *Proceedings of the National Academy of Sciences of the United States of America* 50.4 (Oct. 1963), pp. 703–710.

[21] Marc Tessier-Lavigne and Corey S. Goodman. “The Molecular Biology of Axon Guidance”. en. In: *Science* 274.5290 (Nov. 1996), pp. 1123–1133.

[22] Raghu Kalluri and Robert A Weinberg. “The basics of epithelial-mesenchymal transition”. In: *The Journal of clinical investigation* 119.6 (2009), pp. 1420–1428.

[23] Elizabeth D Hay. “An overview of epithelio-mesenchymal transformation”. In: *Cells Tissues Organs* 154.1 (1995), pp. 8–20.

[24] Kyra Campbell and Jordi Casanova. “A common framework for EMT and collective cell migration”. In: *Development* 143.23 (2016), pp. 4291–4300.

[25] Bryan L. Krock, Nicolas Skuli, and M. Celeste Simon. “Hypoxia-Induced Angiogenesis”. In: *Genes & Cancer* 2.12 (Dec. 2011), pp. 1117–1133.

[26] Charles Betz, Anna Lenard, Heinz-Georg Belting, and Markus Affolter. “Cell behaviors and dynamics during angiogenesis”. en. In: *Development* 143.13 (July 2016), pp. 2249–2260.

[27] Martin J. Siemerink, Ingeborg Klaassen, Cornelis J.F. Van Noorden, and Reinier O. Schlingemann. “Endothelial Tip Cells in Ocular Angiogenesis”. In: *Journal of Histochemistry and Cytochemistry* 61.2 (Feb. 2013), pp. 101–115.

[28] Raquel Blanco and Holger Gerhardt. “VEGF and Notch in Tip and Stalk Cell Selection”. In: *Cold Spring Harbor Perspectives in Medicine* 3.1 (Jan. 2013).

[29] Holger Gerhardt, Matthew Golding, Marcus Fruttiger, Christiana Ruhrberg, Andrea Lundkvist, Alexandra Abramsson, Michael Jeltsch, Christopher Mitchell, Kari Alitalo, David Shima, and Christer Betsholtz. "VEGF guides angiogenic sprouting utilizing endothelial tip cell filopodia". eng. In: *The Journal of Cell Biology* 161.6 (June 2003), pp. 1163–1177.

[30] Kerri-Ann Norton and Aleksander S Popel. "Effects of endothelial cell proliferation and migration rates in a computational model of sprouting angiogenesis". In: *Scientific reports* 6 (2016), p. 36992.

[31] Yimin Zou and Anna I. Lyuksyutova. "Morphogens as conserved axon guidance cues". eng. In: *Current Opinion in Neurobiology* 17.1 (Feb. 2007), pp. 22–28.

[32] Frank Schnorrer and Barry J. Dickson. "Axon guidance: morphogens show the way". eng. In: *Current biology: CB* 14.1 (Jan. 2004), R19–21.

[33] Anna I. Lyuksyutova, Chin-Chun Lu, Nancy Milanesio, Leslie A. King, Nini Guo, Yanshu Wang, Jeremy Nathans, Marc Tessier-Lavigne, and Yimin Zou. "Anterior-Posterior Guidance of Commissural Axons by Wnt-Frizzled Signaling". en. In: *Science* 302.5652 (Dec. 2003), pp. 1984–1988.

[34] Frédéric Charron, Elke Stein, Juhee Jeong, Andrew P McMahon, and Marc Tessier-Lavigne. "The Morphogen Sonic Hedgehog Is an Axonal Chemoattractant that Collaborates with Netrin-1 in Midline Axon Guidance". In: *Cell* 113.1 (Apr. 2003), pp. 11–23.

[35] Laura Anne Lowery and David Van Vactor. "The trip of the tip: understanding the growth cone machinery". In: *Nature reviews. Molecular cell biology* 10.5 (May 2009), pp. 332–343.

[36] Laura Anne Lowery and David Van Vactor. "The trip of the tip: understanding the growth cone machinery". In: *Nature reviews Molecular cell biology* 10.5 (2009), p. 332.

[37] Clarence E Chan and David J Odde. "Traction dynamics of filopodia on compliant substrates". In: *Science* 322.5908 (2008), pp. 1687–1691.

[38] Aih Cheun Lee and Daniel M Suter. "Quantitative analysis of microtubule dynamics during adhesion-mediated growth cone guidance". In: *Developmental neurobiology* 68.12 (2008), pp. 1363–1377.

[39] Steven M Shamah, Michael Z Lin, Jeffrey L Goldberg, Soline Estrach, Mustafa Sahin, Linda Hu, Mihaela Bazalakova, Rachel L Neve, Gabriel Corfas, Anne Debant, et al. "EphA receptors regulate growth cone dynamics through the novel guanine nucleotide exchange factor ephexin". In: *Cell* 105.2 (2001), pp. 233–244.

[40] Irina Dudanova and Rüdiger Klein. "Integration of guidance cues: parallel signaling and crosstalk". In: *Trends in neurosciences* 36.5 (2013), pp. 295–304.

[41] Sinem Ozgul, Sventja von Daake, Sumie Kakehi, Davide Sereni, Natalia Denissova, Carlie Hanlon, Yuanpeng Janet Huang, John K Everett, Cuifeng Yin, Gaetano T Montelione, et al. "An ELISA-Based Screening Platform for Ligand–Receptor Discovery". In: *Methods in enzymology*. Academic Press Inc., 2019, pp. 453–475.

[42] Fanomezana M Ranaivoson, Liam S Turk, Sinem Ozgul, Sumie Kakehi, Sventja von Daake, Nicole Lopez, Laura Trobiani, Antonella De Jaco, Natalia Denissova, Borries Demeler, et al. "A Proteomic Screen of Neuronal Cell-Surface Molecules Reveals IgLONs as Structurally Conserved Interaction Modules at the Synapse". In: *Structure* 27.6 (2019), pp. 893–906.

[43] Jorge Filmus, Mariana Capurro, and Jonathan Rast. "Glypicans". In: *Genome Biology* 9.5 (2008), p. 224.

[44] E David Leonardo, Lindsay Hinck, Masayuki Masu, Kazuko Keino-Masu, Susan L Ackerman, and Marc Tessier-Lavigne. "Vertebrate homologues of C. elegans UNC-5 are candidate netrin receptors". In: *Nature* 386.6627 (1997), p. 833.

[45] Chungyee Leung-Hagesteijn, Andrew M. Spence, Brian D. Stern, Youwen Zhou, Ming-Wan Su, Edward M. Hedgecock, and Joseph G. Culotti. "UNC-5, a transmembrane protein with immunoglobulin and thrombospondin type 1 domains, guides cell and pioneer axon migrations in C. elegans". In: *Cell* 71.2 (Oct. 1992), pp. 289–299.

[46] E. David Leonardo, Lindsay Hinck, Masayuki Masu, Kazuko Keino-Masu, Susan L. Ackerman, and Marc Tessier-Lavigne. "Vertebrate homologues of C. elegans UNC-5 are candidate netrin receptors". En. In: *Nature* 386.6627 (Apr. 1997), p. 833.

[47] Dieter Engelkamp. "Cloning of three mouse Unc5 genes and their expression patterns at mid-gestation". In: *Mechanisms of Development* 118.1 (Oct. 2002), pp. 191–197.

[48] K. Keleman and B. J. Dickson. "Short- and long-range repulsion by the Drosophila Unc5 netrin receptor". eng. In: *Neuron* 32.4 (Nov. 2001), pp. 605–617.

[49] Edward M Hedgecock, Joseph G Culotti, and David H Hall. "The unc-5, unc-6, and unc-40 genes guide circumferential migrations of pioneer axons and mesodermal cells on the epidermis in C. elegans". In: *Neuron* 4.1 (1990), pp. 61–85.

[50] Brian V. Geisbrecht, Kimberly A. Dowd, Ronald W. Barfield, Patti A. Longo, and Daniel J. Leahy. "Netrin Binds Discrete Subdomains of DCC and UNC5 and Mediates Interactions between DCC and Heparin". en. In: *Journal of Biological Chemistry* 278.35 (Aug. 2003), pp. 32561–32568.

[51] Mélodie Grandin, Markus Meier, Jean Guy Delcros, Denise Nikodemus, Raphael Reuten, Trushar R. Patel, David Goldschneider, George Orriss, Natalie Krahn, Amina Boussouar, Riad Abes, Yann Dean, David Neves, Agnes Bernet, Stephane Depil, Fiona Schneiders, Kate Poole, Robert Dante, Manuel Koch, Patrick Mehlen, and Jörg Stetefeld. "Structural Decoding of the Netrin-1/UNC5 Interaction and its Therapeutical Implications in Cancers". In: *Cancer Cell* 29.2 (Feb. 2016), pp. 173–185.

[52] Emil Karaulanov, Ralph T Böttcher, Peter Stannek, Wei Wu, Marlene Rau, Souichi Ogata, Ken WY Cho, and Christof Niehrs. "Unc5B interacts with FLRT3 and Rnd1 to modulate cell adhesion in Xenopus embryos". In: *PloS one* 4.5 (2009), e5742.

[53] Satoru Yamagishi, Falko Hampel, Katsuhiko Hata, Daniel Del Toro, Manuela Schwark, Elena Kvachnina, Martin Bastmeyer, Toshihide Yamashita, Victor Tarabykin, Rüdiger Klein, et al. "FLRT2 and FLRT3 act as repulsive guidance cues for Unc5-positive neurons". In: *The EMBO journal* 30.14 (2011), pp. 2920–2933.

[54] Elena Seiradake, Daniel del Toro, Daniel Nagel, Florian Cop, Ricarda Härtl, Tobias Ruff, Gönül Seyit-Bremer, Karl Harlos, Ellen Clare Border, Amparo Acker-Palmer, E. Yvonne Jones, and Rüdiger Klein. "FLRT structure: balancing repulsion and cell adhesion in cortical and vascular development". eng. In: *Neuron* 84.2 (Oct. 2014), pp. 370–385.

[55] Susan L. Ackerman, Leslie P. Kozak, Stefan A. Przyborski, Laurie A. Rund, Bert B. Boyer, and Barbara B. Knowles. "The mouse rostral cerebellar malformation gene encodes an UNC-5-like protein". En. In: *Nature* 386.6627 (Apr. 1997), p. 838.

[56] S. A. Przyborski, B. B. Knowles, and S. L. Ackerman. "Embryonic phenotype of Unc5h3 mutant mice suggests chemorepulsion during the formation of the rostral cerebellar boundary". en. In: *Development* 125.1 (Jan. 1998), pp. 41–50.

[57] Anish A. Purohit, Weiquan Li, Chao Qu, Trisha Dwyer, Qiangqiang Shao, Kun-Liang Guan, and Guofa Liu. "Down Syndrome Cell Adhesion Molecule (DSCAM) Associates with Uncoordinated-5C (UNC5C) in Netrin-1-mediated Growth Cone Collapse". In: *The Journal of Biological Chemistry* 287.32 (Aug. 2012), pp. 27126–27138.

[58] S Alcantara, M Ruiz, F De Castro, E Soriano, and C Sotelo. "Netrin 1 acts as an attractive or as a repulsive cue for distinct migrating neurons during the development of the cerebellar system". In: *Development* 127.7 (2000), pp. 1359–1372.

[59] Xiaowei Lu, Ferdinand le Noble, Li Yuan, Quingjan Jiang, Benjamin de Lafarge, Daisuke Sugiyama, Christiane Bréant, Filip Claes, Frederik De Smet, Jean-Léon Thomas, Monica Autiero, Peter Carmeliet, Marc Tessier-Lavigne, and Anne Eichmann. "The netrin receptor UNC5B mediates guidance events controlling morphogenesis of the vascular system". En. In: *Nature* 432.7014 (Nov. 2004), p. 179.

[60] Bruno Larrivée, Catarina Freitas, Marc Trombe, Xiang Lv, Benjamin Delafarge, Li Yuan, Karine Bouvrée, Christiane Bréant, Raquel Del Toro, Nicolas Bréchot, Stéphane Germain, Françoise Bono, Frédérique Dol, Filip Claes, Christian Fischer, Monica Autiero, Jean-Léon Thomas, Peter Carmeliet, Marc Tessier-Lavigne, and Anne Eichmann. "Activation of the UNC5B receptor by Netrin-1 inhibits sprouting angiogenesis". eng. In: *Genes & Development* 21.19 (Oct. 2007), pp. 2433–2447.

[61] Ikue Tai-Nagara, Yusuke Yoshikawa, Naoko Numata, Tomofumi Ando, Keisuke Okabe, Yuki Sugiura, Masaki Ieda, Nobuyuki Takakura, Osamu Nakagawa, Bin Zhou, Koji Okabayashi, Makoto Suematsu, Yuko Kitagawa, Martin Bastmeyer, Kohji Sato, Rüdiger Klein, Sutip Navankasattusas, Dean Y. Li, Satoru Yamagishi, and Yoshiaki Kubota. "Placental labyrinth formation in mice requires endothelial FLRT2/UNC5B signaling". eng. In: *Development (Cambridge, England)* 144.13 (2017), pp. 2392–2401.

[62] Sutip Navankasattusas, Kevin J. Whitehead, Arminda Suli, Lise K. Sorensen, Amy H. Lim, Jia Zhao, Kye Won Park, Joshua D. Wythe, Kirk R. Thomas, Chi-Bin Chien, and Dean Y. Li. "The netrin receptor UNC5B promotes angiogenesis in specific vascular beds". In: *Development (Cambridge, England)* 135.4 (Feb. 2008), pp. 659–667.

[63] Kye Won Park, Dana Crouse, Mark Lee, Satyajit K. Karnik, Lise K. Sorensen, Kelly J. Murphy, Calvin J. Kuo, and Dean Y. Li. "The axonal attractant Netrin-1 is an angiogenic factor". eng. In: *Proceedings of the National Academy of Sciences of the United States of America* 101.46 (Nov. 2004), pp. 16210–16215.

[64] Brent D. Wilson, Masaaki Ii, Kye Won Park, Arminda Suli, Lise K. Sorensen, Fréderic Larrieu-Lahargue, Lisa D. Urness, Wonhee Suh, Jun Asai, Gerhardus A. H. Kock, Tina Thorne, Marcy Silver, Kirk R. Thomas, Chi-Bin Chien, Douglas W. Losordo, and Dean Y. Li. "Netrins promote developmental and therapeutic angiogenesis". eng. In: *Science (New York, N.Y.)* 313.5787 (Aug. 2006), pp. 640–644.

[65] Marie Castets, Marie-May Coissieux, Céline Delloye-Bourgeois, Laure Bernard, Jean-Guy Delcros, Agnès Bernet, Vincent Laudet, and Patrick Mehlen. "Inhibition of endothelial cell apoptosis by netrin-1 during angiogenesis". eng. In: *Developmental Cell* 16.4 (Apr. 2009), pp. 614–620.

[66] Frederic Larrieu-Lahargue, Kirk R Thomas, and Dean Y Li. "Netrin ligands and receptors: lessons from neurons to the endothelium". In: *Trends in cardiovascular medicine* 22.2 (2012), pp. 44–47.

[67] Yun Yang, Li Zou, Yong Wan, Ke-Shu Xu, Jin-Xiang Zhang, and Jing-Hui Zhang. "Axon guidance cue Netrin-1 has dual function in angiogenesis". In: *Cancer biology & therapy* 6.5 (2007), pp. 743–748.

[68] Eric F Pettersen, Thomas D Goddard, Conrad C Huang, Gregory S Couch, Daniel M Greenblatt, Elaine C Meng, and Thomas E Ferrin. "UCSF Chimera—a visualization system for exploratory research and analysis". In: *Journal of computational chemistry* 25.13 (2004), pp. 1605–1612.

[69] Verity A. Jackson, Shahid Mehmood, Matthieu Chavent, Pietro Roversi, Maria Carrasquero, Daniel Del Toro, Goenuel Seyit-Bremer, Fanomezana M. Ranaivoson, Davide Comoletti, Mark S. P. Sansom, Carol V. Robinson, Rüdiger Klein, and Elena Seiradake. "Super-complexes of adhesion GPCRs and neural guidance receptors". eng. In: *Nature Communications* 7 (Apr. 2016), p. 11184.

[70] Kemin Tan, Mark Duquette, Jin-huan Liu, Yicheng Dong, Rongguang Zhang, Andrzej Joachimiak, Jack Lawler, and Jia-huai Wang. "Crystal structure of the TSP-1 type 1 repeats: a novel layered fold and its biological implication". eng. In: *The Journal of Cell Biology* 159.2 (Oct. 2002), pp. 373–382.

[71] Philip A. Klenotic, Richard C. Page, Saurav Misra, and Roy L. Silverstein. "Expression, purification and structural characterization of functionally replete thrombospondin-1 type 1 repeats in a bacterial expression system". eng. In: *Protein Expression and Purification* 80.2 (Dec. 2011), pp. 253–259.

[72] Rui Wang, Zhiyi Wei, Hao Jin, Hao Wu, Cong Yu, Wenyu Wen, Ling-Nga Chan, Zilong Wen, and Mingjie Zhang. "Autoinhibition of UNC5b revealed by the cytoplasmic domain structure of the receptor". eng. In: *Molecular Cell* 33.6 (Mar. 2009), pp. 692–703.

[73] Vann Bennett and Jane Healy. "Organizing the fluid membrane bilayer: diseases linked to spectrin and ankyrin". eng. In: *Trends in Molecular Medicine* 14.1 (Jan. 2008), pp. 28–36.

[74] Patrick Mehlen and Servane Tauszig-Delamasure. "Dependence receptors and colorectal cancer". In: *Gut* 63.11 (2014), pp. 1821–1829.

[75] Benjamin Gibert and Patrick Mehlen. "Dependence Receptors and Cancer: Addiction to Trophic Ligands". eng. In: *Cancer Research* 75.24 (Dec. 2015), pp. 5171–5175.

[76] D. Goldschneider and P. Mehlen. "Dependence receptors: a new paradigm in cell signaling and cancer therapy". eng. In: *Oncogene* 29.13 (Apr. 2010), pp. 1865–1882.

[77] S. Rabizadeh, J. Oh, L. T. Zhong, J. Yang, C. M. Bitler, L. L. Butcher, and D. E. Bredesen. "Induction of apoptosis by the low-affinity NGF receptor". eng. In: *Science (New York, N.Y.)* 261.5119 (July 1993), pp. 345–348.

[78] Zhi Lin, Jason Y. Tann, Eddy T. H. Goh, Claire Kelly, Kim Buay Lim, Jian Fang Gao, and Carlos F. Ibanez. "Structural basis of death domain signaling in the p75 neurotrophin receptor". eng. In: *eLife* 4 (Dec. 2015), e11692.

[79] Hyun Ho Park, Yu-Chih Lo, Su-Chang Lin, Liwei Wang, Jin Kuk Yang, and Hao Wu. "The Death Domain Superfamily in Intracellular Signaling of Apoptosis and Inflammation". In: *Annual review of immunology* 25 (2007), pp. 561–586.

[80] Peter D Mace and Stefan J Riedl. "Molecular cell death platforms and assemblies". In: *Current opinion in cell biology* 22.6 (2010), pp. 828–836.

[81] S. Cuenin, A. Tinel, S. Janssens, and J. Tschopp. "p53-induced protein with a death domain (PIDD) isoforms differentially activate nuclear factor-kappaB and caspase-2 in response to genotoxic stress". eng. In: *Oncogene* 27.3 (Jan. 2008), pp. 387–396.

[82] Hyun Ho Park, Emmanuelle Logette, Stefan Raunser, Solange Cuenin, Thomas Walz, Jurg Tschopp, and Hao Wu. "Death domain assembly mechanism revealed by crystal structure of the oligomeric PIDDosome core complex". eng. In: *Cell* 128.3 (Feb. 2007), pp. 533–546.

[83] Noriko Handa, Mutsuko Kukimoto-Niino, Ryogo Akasaka, Kazutaka Murayama, Takaho Terada, Makoto Inoue, Takashi Yabuki, Masaaki Aoki, Eiko Seki, Takayoshi Matsuda, et al. "Structure of the UNC5H2 death domain". In: *Acta Crystallographica Section D: Biological Crystallography* 62.12 (2006), pp. 1502–1509.

[84] Fabien Llambi, Frédéric Causeret, Evelyne Bloch-Gallego, and Patrick Mehlen. "Netrin-1 acts as a survival factor via its receptors UNC5H and DCC". In: *The EMBO Journal* 20.11 (June 2001), pp. 2715–2722.

[85] Hong Wang, Toshinori Ozaki, M Shamim Hossain, Yohko Nakamura, Takehiko Kamijo, Xindong Xue, and Akira Nakagawara. "A newly identified dependence receptor UNC5H4 is induced during DNA damage-mediated apoptosis and transcriptional target of tumor suppressor p53". In: *Biochemical and biophysical research communications* 370.4 (2008), pp. 594–598.

[86] Céline Guenebeaud, David Goldschneider, Marie Castets, Catherine Guix, Guillaume Chazot, Céline Delloye-Bourgeois, Avital Eisenberg-Lerner, Galit Shohat, Mingjie Zhang, Vincent Laudet, et al. "The dependence receptor UNC5H2/B triggers apoptosis via PP2A-mediated dephosphorylation of DAP kinase". In: *Molecular cell* 40.6 (2010), pp. 863–876.

[87] Melissa R Junttila, Pietri Puustinen, Minna Niemelä, Raija Ahola, Hugh Arnold, Trine Böttzauw, Risto Ala-aho, Christina Nielsen, Johanna Ivaska, Yoichi Taya, et al. "CIP2A inhibits PP2A in human malignancies". In: *Cell* 130.1 (2007), pp. 51–62.

[88] Yuyan Zhu, Yuanyuan Li, Seiki Haraguchi, Meng Yu, Miki Ohira, Toshinori Ozaki, Atsuko Nakagawa, Toshikazu Ushijima, Eriko Isogai, Haruhiko Koseki, et al. "Dependence receptor UNC5D mediates nerve growth factor depletion–induced neuroblastoma regression". In: *The Journal of clinical investigation* 123.7 (2013), pp. 2935–2947.

[89] K. Hong, L. Hinck, M. Nishiyama, M. M. Poo, M. Tessier-Lavigne, and E. Stein. "A ligand-gated association between cytoplasmic domains of UNC5 and DCC family receptors converts netrin-induced growth cone attraction to repulsion". eng. In: *Cell* 97.7 (June 1999), pp. 927–941.

[90] Alexandra Neuhaus-Follini and Greg J Bashaw. "Crossing the embryonic midline: molecular mechanisms regulating axon responsiveness at an intermediate target". In: *Wiley Interdisciplinary Reviews: Developmental Biology* 4.4 (2015), pp. 377–389.

[91] Amin Fazeli, Stephanie L Dickinson, Michelle L Hermiston, Robert V Tighe, Robert G Steen, Clayton G Small, Esther T Stoeckli, Kazuko Keino-Masu, Masayuki Masu, Helen Rayburn, et al. "Phenotype of mice lacking functional deleted in colorectal cancer (Dec) gene". In: *Nature* 386.6627 (1997), p. 796.

[92] Kai Xu, Zhuhao Wu, Nicolas Renier, Alexander Antipenko, Dorothea Tzvetkova-Robev, Yan Xu, Maria Minchenko, Vincenzo Nardi-Dei, Kanagalaghatta R. Rajashankar, Juha Himanen, Marc Tessier-Lavigne, and Dimitar B. Nikolov. "Structures of Netrin-1 Bound to two Receptors Provide Insight into its Axon Guidance Mechanism". In: *Science (New York, N.Y.)* 344.6189 (June 2014), pp. 1275–1279.

[93] Supraja G. Varadarajan, Jennifer H. Kong, Keith D. Phan, Tzu-Jen Kao, S. Carmen Panaitof, Julie Cardin, Holger Eltzschig, Artur Kania, Bennett G. Novitch, and Samantha J. Butler. "Netrin1 Produced by Neural Progenitors, Not Floor Plate Cells, Is Required for Axon Guidance in the Spinal Cord". In: *Neuron* 94.4 (May 2017), 790–799.e3.

[94] Chloé Dominici, Juan Antonio Moreno-Bravo, Sergi Roig Puiggros, Quentin Rappeneau, Nicolas Rama, Pauline Vieugue, Agns Bernet, Patrick Mehlen, and Alain Chédotal. "Floor-plate-derived netrin-1 is dispensable for commissural axon guidance". en. In: *Nature* 545.7654 (May 2017), pp. 350–354.

[95] Daniel Morales. "A new model for netrin1 in commissural axon guidance". In: *Journal of neuroscience research* 96.2 (2018), pp. 247–252.

[96] K. Keleman and B. J. Dickson. "Short- and long-range repulsion by the Drosophila Unc5 netrin receptor". eng. In: *Neuron* 32.4 (Nov. 2001), pp. 605–617.

[97] Esma Lejmi, Laurence Leconte, Sandrine Pédron-Mazoyer, Stanislas Ropert, William Raoul, Sophie Lavalette, Ilyes Bouras, Jean-Guillaume Feron, Martine Maitre-Boube, Franck Assayag, et al. "Netrin-4 inhibits angiogenesis via binding to neogenin and recruitment of Unc5B". In: *Proceedings of the National Academy of Sciences* 105.34 (2008), pp. 12491–12496.

[98] Lorenzo I. Finci, Nina Krüger, Xiaqin Sun, Jie Zhang, Magda Chegkazi, Yu Wu, Gundolf Schenk, Haydyn D. T. Mertens, Dmitri I. Svergun, Yan Zhang, Jia-huai Wang, and Rob Meijers. "The crystal structure of netrin-1 in complex with DCC reveals the bi-functionality of netrin-1 as a guidance cue". In: *Neuron* 83.4 (Aug. 2014), pp. 839–849.

[99] Ying Liu, Tuhin Bhowmick, Yiqiong Liu, Xuefan Gao, Haydyn D.T. Mertens, Dmitri I. Svergun, Junyu Xiao, Yan Zhang, Jia-huai Wang, and Rob Meijers. "Structural Basis for Draxin-Modulated Axon Guidance and Fasciculation by Netrin-1 through DCC". In: *Neuron* 97.6 (Mar. 2018), 1261–1267.e4.

[100] K. L. Bennett, J. Bradshaw, T. Youngman, J. Rodgers, B. Greenfield, A. Aruffo, and P. S. Linsley. "Deleted in colorectal carcinoma (DCC) binds heparin via its fifth fibronectin type III domain". eng. In: *The Journal of Biological Chemistry* 272.43 (Oct. 1997), pp. 26940–26946.

[101] Robert P. Kruger, Jeeyong Lee, Weiquan Li, and Kun-Liang Guan. "Mapping netrin receptor binding reveals domains of Unc5 regulating its tyrosine phosphorylation". eng. In: *The Journal of Neuroscience: The Official Journal of the Society for Neuroscience* 24.48 (Dec. 2004), pp. 10826–10834.

[102] Robert W Burgess, Thomas J Jucius, and Susan L Ackerman. "Motor axon guidance of the mammalian trochlear and phrenic nerves: dependence on the netrin receptor Unc5c and modifier loci". In: *Journal of Neuroscience* 26.21 (2006), pp. 5756–5766.

[103] Christian Söllner and Gavin J Wright. "A cell surface interaction network of neural leucine-rich repeat receptors". In: *Genome biology* 10.9 (2009), R99.

[104] Satoru Yamagishi, Falko Hampel, Katsuhiko Hata, Daniel Del Toro, Manuela Schwark, Elena Kvachnina, Martin Bastmeyer, Toshihide Yamashita, Victor Tarabykin, Rüdiger Klein, and Joaquim Egea. "FLRT2 and FLRT3 act as repulsive guidance cues for Unc5-positive neurons". eng. In: *The EMBO journal* 30.14 (June 2011), pp. 2920–2933.

[105] Monica K. Wetzel-Smith, Julie Hunkapiller, Tushar R. Bhangale, Karpagam Srinivasan, Janice A. Maloney, Jasvinder K. Atwal, Susan M. Sa, Murat B. Yaylaoglu, Oded Foreman, Ward Ortmann, Nisha Rathore, David V. Hansen, Marc Tessier-Lavigne, Alzheimer's Disease Genetics Consortium, Richard Mayeux, Margaret Pericak-Vance, Jonathan Haines, Lindsay A. Farrer, Gerard D. Schellenberg, Alison Goate, Timothy W. Behrens, Carlos Cruchaga, Ryan J. Watts, and Robert R. Graham. "A rare mutation in

UNC5C predisposes to late-onset Alzheimer's disease and increases neuronal cell death". eng. In: *Nature Medicine* 20.12 (Dec. 2014), pp. 1452–1457.

[106] Bin Jiao, Xiaoyan Liu, Beisha Tang, Lihua Hou, Lin Zhou, Fufeng Zhang, Yafang Zhou, Jifeng Guo, Xinxiang Yan, and Lu Shen. "Investigation of TREM2, PLD3, and UNC5C variants in patients with Alzheimer's disease from mainland China". eng. In: *Neurobiology of Aging* 35.10 (Oct. 2014), 2422.e9–2422.e11.

[107] Francesca Mangialasche, Alina Solomon, Bengt Winblad, Patrizia Mecocci, and Miia Kivipelto. "Alzheimer's disease: clinical trials and drug development". eng. In: *The Lancet. Neurology* 9.7 (July 2010), pp. 702–716.

[108] Jun Wang, Ben J. Gu, Colin L. Masters, and Yan-Jiang Wang. "A systemic view of Alzheimer disease — insights from amyloid- metabolism beyond the brain". en. In: *Nature Reviews Neurology* 13.10 (Oct. 2017), pp. 612–623.

[109] W. Vallen Graham, Alessandra Bonito-Oliva, and Thomas P. Sakmar. "Update on Alzheimer's Disease Therapy and Prevention Strategies". In: *Annual Review of Medicine* 68.1 (2017), pp. 413–430.

[110] Karine Thiebault, Laetitia Mazelin, Laurent Pays, Fabien Llambi, Marie-Odile Joly, Jean-Yves Scoazec, Jean-Christophe Saurin, Giovanni Romeo, and Patrick Mehlen. "The netrin-1 receptors UNC5H are putative tumor suppressors controlling cell death commitment". eng. In: *Proceedings of the National Academy of Sciences of the United States of America* 100.7 (Apr. 2003), pp. 4173–4178.

[111] Irene Ylivinkka, Jorma Keski-Oja, and Marko Hyytiäinen. "Netrin-1: A regulator of cancer cell motility?" In: *European Journal of Cell Biology.* Integrated mechano-chemical signals in invasion 95.11 (Nov. 2016), pp. 513–520.

[112] Qi Qi, Dean Y. Li, Hongbo R. Luo, Kun-Liang Guan, and Keqiang Ye. "Netrin-1 exerts oncogenic activities through enhancing Yes-associated protein stability". en. In: *Proceedings of the National Academy of Sciences* 112.23 (June 2015), pp. 7255–7260.

[113] Ping Han, Yu Fu, Jingmei Liu, Yunwu Wang, Jiayi He, Jin Gong, Mengke Li, Qinghai Tan, Dongxiao Li, Yixing Luo, Jian Han, Jiqiao Liu, Wei Tu, Ying Wang, Dean Tian, and Wei Yan. "Netrin-1 promotes cell migration and invasion by down-regulation of BVES expression in human hepatocellular carcinoma". In: *American Journal of Cancer Research* 5.4 (Mar. 2015), pp. 1396–1409.

[114] Wei Yan, Ping Han, Zhenzhen Zhou, Wei Tu, Jiazhi Liao, Peiyuan Li, Mei Liu, Dean Tian, and Yu Fu. "Netrin-1 Induces Epithelial–Mesenchymal Transition and Promotes Hepatocellular Carcinoma Invasiveness". en. In: *Digestive Diseases and Sciences* 59.6 (June 2014), pp. 1213–1221.

[115] Patrick N. Harter, Jenny Zinke, Alexander Scholz, Julia Tichy, Cornelia Zachskorn, Hans M. Kvasnicka, Benjamin Goeppert, Céline Delloye-Bourgeois, Elke Hattingen, Christian Senft, Joachim P. Steinbach, Karl H. Plate, Patrick Mehlen, Dorothea Schulte, and Michel Mittelbronn. "Netrin-1 Expression Is an Independent Prognostic Factor for Poor Patient Survival in Brain Metastases". en. In: *PLOS ONE* 9.3 (Mar. 2014), e92311.

[116] Kai Yin, Shengchun Dang, Lei Cui, Xin Fan, Linjun Wang, Rong Xie, Jianguo Qu, Mengyuan Shang, Jixiang Chen, and Zekuan Xu. "Netrin-1 promotes metastasis of gastric cancer by regulating YAP activity". eng. In: *Biochemical and Biophysical Research Communications* 496.1 (2018), pp. 76–82.

[117] Kai Yin, Linjun Wang, Xuan Zhang, Zhongyuan He, Yiwen Xia, Jianghao Xu, Song Wei, Bowen Li, Zheng Li, Guangli Sun, Qing Li, Hao Xu, and Zekuan Xu. "Netrin-1 promotes gastric cancer cell proliferation and invasion via the receptor neogenin through PI3K/AKT signaling pathway". eng. In: *Oncotarget* 8.31 (Aug. 2017), pp. 51177–51189.

[118] Ping Han, Yu Fu, Jingmei Liu, Yunwu Wang, Jiayi He, Jin Gong, Mengke Li, Qinghai Tan, Dongxiao Li, Yixing Luo, Jian Han, Jiqiao Liu, Wei Tu, Ying Wang, Dean Tian, and Wei Yan. "Netrin-1 promotes cell migration and invasion by down-regulation of BVES expression in human hepatocellular carcinoma". eng. In: *American Journal of Cancer Research* 5.4 (2015), pp. 1396–1409.

[119] Thomas Lahlali, Marie-Laure Plissonnier, Cristina Romero-López, Maud Michelet, Benjamin Ducarouge, Alfredo Berzal-Herranz, Fabien Zoulim, Patrick Mehlen, and Romain Parent. "Netrin-1 protects hepatocytes against cell death through sustained translation during the unfolded protein response". In: *Cellular and molecular gastroenterology and hepatology* 2.3 (2016), pp. 281–301.

[120] *First in Human Evaluation of Safety, Pharmacokinetics, and Clinical Activity of a Monoclonal Antibody Targeting Netrin 1 in Patients With Advanced/Metastatic Solid Tumors - Full Text View - ClinicalTrials.gov*. en.

[121] Mary C. Farach-Carson, Curtis R. Warren, Daniel A. Harrington, and Daniel D. Carson. "Border Patrol: Insights into the Unique Role of Perlecan/Heparan Sulfate Proteoglycan2 at Cell and Tissue Borders". In: *Matrix biology : journal of the International Society for Matrix Biology* 34 (Feb. 2014), pp. 64–79.

[122] A. J. Groffen, M. A. Ruegg, H. Dijkman, T. J. van de Velden, C. A. Buskens, J. van den Born, K. J. Assmann, L. A. Monnens, J. H. Veerkamp, and L. P. van den Heuvel. "Agrin is a major heparan sulfate proteoglycan in the human glomerular basement membrane". eng. In: *The Journal of Histochemistry and Cytochemistry: Official Journal of the Histochemistry Society* 46.1 (Jan. 1998), pp. 19–27.

[123] John R Couchman, Sandeep Gopal, Hooi Ching Lim, Steffen Nørgaard, and Hinke AB Multhaupt. "Syndecans: from peripheral coreceptors to mainstream regulators of cell behaviour". In: *International Journal of Experimental Pathology* 96.1 (Feb. 2015), pp. 1–10.

[124] Hiroshi Nakato, Tracy A Futch, and Scott B Selleck. "The division abnormally delayed (dally) gene: a putative integral membrane proteoglycan required for cell division patterning during postembryonic development of the nervous system in Drosophila". en. In: (), p. 16.

[125] N. Khare and S. Baumgartner. "Dally-like protein, a new Drosophila glypican with expression overlapping with wingless". eng. In: *Mechanisms of Development* 99.1-2 (Dec. 2000), pp. 199–202.

[126] Mansi Gupta and Michael Brand. “Identification and Expression Analysis of Zebrafish Glypicans during Embryonic Development”. en. In: *PLOS ONE* 8.11 (Nov. 2013), e80824.

[127] G. David, V. Lories, B. Decock, P. Marynen, J. J. Cassiman, and H. Van den Berghe. “Molecular cloning of a phosphatidylinositol-anchored membrane heparan sulfate proteoglycan from human lung fibroblasts”. eng. In: *The Journal of Cell Biology* 111.6 Pt 2 (Dec. 1990), pp. 3165–3176.

[128] C. S. Stipp, E. D. Litwack, and A. D. Lander. “Cerebroglycan: an integral membrane heparan sulfate proteoglycan that is unique to the developing nervous system and expressed specifically during neuronal differentiation”. en. In: *The Journal of Cell Biology* 124.1 (Jan. 1994), pp. 149–160.

[129] J Filmus, J G Church, and R N Buick. “Isolation of a cDNA corresponding to a developmentally regulated transcript in rat intestine.” In: *Molecular and Cellular Biology* 8.10 (Oct. 1988), pp. 4243–4249.

[130] K. Watanabe, H. Yamada, and Y. Yamaguchi. “K-glypican: a novel GPI-anchored heparan sulfate proteoglycan that is highly expressed in developing brain and kidney.” en. In: *The Journal of Cell Biology* 130.5 (Sept. 1995), pp. 1207–1218.

[131] Mark Veugelers, Joris Vermeesch, Gunter Reekmans, Robert Steinfeld, Peter Marynen, and Guido David. “Characterization of Glypican-5 and Chromosomal Localization of HumanGPC5,a New Member of the Glypican Gene Family”. In: *Genomics* 40.1 (Feb. 1997), pp. 24–30.

[132] Stephenie Paine-Saunders, Beth L. Viviano, and Scott Saunders. “GPC6, a Novel Member of the Glypican Gene Family, Encodes a Product Structurally Related to GPC4 and Is Colocalized withGPC5on Human Chromosome 13”. In: *Genomics* 57.3 (May 1999), pp. 455–458.

[133] Jonathan J Ward, Liam J McGuffin, Kevin Bryson, Bernard F Buxton, and David T Jones. “The DISOPRED server for the prediction of protein disorder”. In: *Bioinformatics* 20.13 (2004), pp. 2138–2139.

[134] Wael Awad, Barbara Adamczyk, Jessica Örnros, Niclas G. Karlsson, Katrin Mani, and Derek T. Logan. “Structural Aspects of N-Glycosylations and the C-terminal Region in Human Glypican-1”. en. In: *Journal of Biological Chemistry* 290.38 (Sept. 2015), pp. 22991–23008.

[135] Gabriel Svensson, Wael Awad, Maria Håkansson, Katrin Mani, and Derek T. Logan. “Crystal Structure of N-Glycosylated Human Glypican-1 Core Protein Structure of two Loops Evolutionarily Conserved in Vertebrate Glypican-1”. en. In: *Journal of Biological Chemistry* 287.17 (Apr. 2012), pp. 14040–14051.

[136] Min-Sung Kim, Adam M. Saunders, Brent Y. Hamaoka, Philip A. Beachy, and Daniel J. Leahy. “Structure of the protein core of the glypican Dally-like and localization of a region important for hedgehog signaling”. eng. In: *Proceedings of the National Academy of Sciences of the United States of America* 108.32 (Aug. 2011), pp. 13112–13117.

[137] Stuart McNicholas and Jon Agirre. “Glycoblocks: a schematic three-dimensional representation for glycans and their interactions”. In: *Acta Crystallographica Section D: Structural Biology* 73.2 (2017), pp. 187–194.

[138] Ryan J Weiss, Jeffrey D Esko, and Yitzhak Tor. "Targeting heparin and heparan sulfate protein interactions". In: *Organic & biomolecular chemistry* 15.27 (2017), pp. 5656–5668.

[139] Bart De Cat, Sin-Ya Muyldermans, Christien Coomans, Gisèle Degeest, Bernadette Vanderschueren, John Creemers, Frédéric Biemar, Bernard Peers, and Guido David. "Processing by proprotein convertases is required for glypican-3 modulation of cell survival, Wnt signaling, and gastrulation movements". In: *The Journal of Cell Biology* 163.3 (Nov. 2003), pp. 625–635.

[140] Howard H Song and Jorge Filmus. "The role of glypicans in mammalian development". In: *Biochimica et Biophysica Acta (BBA) - General Subjects*. Developmental Glycobiology 1573.3 (Dec. 2002), pp. 241–246.

[141] *ProP 1.0 Server*.

[142] Lijuan Zhang, Guido David, and Jeffrey D Esko. "Repetitive Ser-Gly sequences enhance heparan sulfate assembly in proteoglycans". In: *Journal of Biological Chemistry* 270.45 (1995), pp. 27127–27135.

[143] Yusuke Mii, Takayoshi Yamamoto, Ritsuko Takada, Shuji Mizumoto, Makoto Matsuyama, Shuhei Yamada, Shinji Takada, and Masanori Taira. "Roles of two types of heparan sulfate clusters in Wnt distribution and signaling in Xenopus". En. In: *Nature Communications* 8.1 (Dec. 2017), p. 1973.

[144] Isao Matsuo and Chiharu Kimura-Yoshida. "Extracellular distribution of diffusible growth factors controlled by heparan sulfate proteoglycans during mammalian embryogenesis". In: *Philosophical Transactions of the Royal Society B: Biological Sciences* 369.1657 (2014), p. 20130545.

[145] Yung-Heng Chang and Yi Henry Sun. "Carrier of Wingless (Cow), a secreted heparan sulfate proteoglycan, promotes extracellular transport of Wingless". eng. In: *PloS One* 9.10 (2014), e111573.

[146] Rogier M Reijmers, Richard WJ Groen, Annemieke Kuil, Kees Weijer, Fiona C Kimberley, Jan Paul Medema, Toin H van Kuppevelt, Jin-Ping Li, Marcel Spaargaren, and Steven T Pals. "Disruption of heparan sulfate proteoglycan conformation perturbs B-cell maturation and APRIL-mediated plasma cell survival". In: *Blood* 117.23 (2011), pp. 6162–6171.

[147] Fabienne E. Poulain and H. Joseph Yost. "Heparan sulfate proteoglycans: a sugar code for vertebrate development?" en. In: *Development* 142.20 (Oct. 2015), pp. 3456–3467.

[148] Jeffrey D. Esko and Scott B. Selleck. "Order out of chaos: assembly of ligand binding sites in heparan sulfate". eng. In: *Annual Review of Biochemistry* 71 (2002), pp. 435–471.

[149] Stephan Gysi, Christa Rhiner, Stephane Flibotte, Donald G. Moerman, and Michael O. Hengartner. "A network of HSPG core proteins and HS modifying enzymes regulates netrin-dependent guidance of D-type motor neurons in Caenorhabditis elegans". eng. In: *PloS One* 8.9 (2013), e74908.

[150] Hannes E Bülow and Oliver Hobert. "Differential Sulfations and Epimerization Define Heparan Sulfate Specificity in Nervous System Development". In: *Neuron* 41.5 (Mar. 2004), pp. 723–736.

[151] S. Saunders, S. Paine-Saunders, and A. D. Lander. "Expression of the cell surface proteoglycan glypican-5 is developmentally regulated in kidney, limb, and brain". eng. In: *Developmental Biology* 190.1 (Oct. 1997), pp. 78–93.

[152] Robert L. Chen and Arthur D. Lander. "Mechanisms Underlying Preferential Assembly of Heparan Sulfate on Glypican-1". en. In: *Journal of Biological Chemistry* 276.10 (Sept. 2001), pp. 7507–7517.

[153] Mariana Capurro, Wen Shi, Tomomi Izumikawa, Hiroshi Kitagawa, and Jorge Filmus. "Processing by Convertases Is Required for Glypican-3-induced Inhibition of Hedgehog Signaling". In: *The Journal of Biological Chemistry* 290.12 (Mar. 2015), pp. 7576–7585.

[154] Susan Pang, Paula Urquhart, and Nigel M Hooper. "N-glycans, not the GPI anchor, mediate the apical targeting of a naturally glycosylated, GPI-anchored protein in polarised epithelial cells". In: *Journal of Cell Science* 117.21 (2004), pp. 5079–5086.

[155] Gabriel Svensson, Axel Hyrenius Wittsten, Sara Linse, and Katrin Mani. "The structural role of N-linked glycans on human glypican-1". In: *Biochemistry* 50.43 (2011), pp. 9377–9387.

[156] Y Song, KE Nestor, DC McFarland, and Sandra Gayle Velleman. "Effect of glypican-1 covalently attached chains on turkey myogenic satellite cell proliferation, differentiation, and fibroblast growth factor 2 responsiveness". In: *Poultry science* 89.1 (2010), pp. 123–134.

[157] Na Li, Liwen Wei, Xiaoyu Liu, Hongjun Bai, Yvonne Ye, Dan Li, Nan Li, Ulrich Baxa, Qun Wang, Ling Lv, Yun Chen, Mingqian Feng, Byungkook Lee, Wei Gao, and Mitchell Ho. "A Frizzled-Like Cysteine-Rich Domain in Glypican-3 Mediates Wnt Binding and Regulates Hepatocellular Carcinoma Tumor Growth in Mice". eng. In: *Hepatology (Baltimore, Md.)* (Apr. 2019).

[158] Mariana Capurro, Tonya Martin, Wen Shi, and Jorge Filmus. "Glypican-3 binds to Frizzled and plays a direct role in the stimulation of canonical Wnt signaling". en. In: *Journal of Cell Science* 127.7 (Apr. 2014), pp. 1565–1575.

[159] Celia E. Shiau, Na Hu, and Marianne Bronner-Fraser. "Altering Glypican-1 levels modulates canonical Wnt signaling during trigeminal placode development". In: *Developmental biology* 348.1 (Dec. 2010), pp. 107–118.

[160] Hiroshi Sakane, Hideki Yamamoto, Shinji Matsumoto, Akira Sato, and Akira Kikuchi. "Localization of glypican-4 in different membrane microdomains is involved in the regulation of Wnt signaling". en. In: *Journal of Cell Science* 125.2 (Jan. 2012), pp. 449–460.

[161] Satoshi Kakugawa, Paul F. Langton, Matthias Zebisch, Steve Howell, Tao-Hsin Chang, Yan Liu, Ten Feizi, Ganka Bineva, Nicola O'Reilly, Ambrosius P. Snijders, E. Yvonne Jones, and Jean-Paul Vincent. "Notum deacylates Wnt proteins to suppress signalling activity". eng. In: *Nature* 519.7542 (Mar. 2015), pp. 187–192.

[162] Min-Sung Kim, Adam M. Saunders, Brent Y. Hamaoka, Philip A. Beachy, and Daniel J. Leahy. "Structure of the protein core of the glypican Dally-like and localization of a region important for hedgehog signaling". eng. In: *Proceedings of the National Academy of Sciences of the United States of America* 108.32 (Aug. 2011), pp. 13112–13117.

[163] Mariana I. Capurro, Ping Xu, Wen Shi, Fuchuan Li, Angela Jia, and Jorge Filmus. "Glypican-3 inhibits Hedgehog signaling during development by with patched for Hedgehog binding". eng. In: *Developmental Cell* 14.5 (May 2008), pp. 700–711.

[164] Nicole H. Wilson and Esther T. Stoeckli. "Sonic hedgehog regulates its own receptor on postcrossing commissural axons in a glypican1-dependent manner". eng. In: *Neuron* 79.3 (Aug. 2013), pp. 478–491.

[165] Sabrina C. Desbordes and Bénédicte Sanson. "The glypican Dally-like is required for Hedgehog signalling in the embryonic epidermis of Drosophila". eng. In: *Development (Cambridge, England)* 130.25 (Dec. 2003), pp. 6245–6255.

[166] Tatyana Y. Belenkaya, Chun Han, Dong Yan, Robert J. Opoka, Marat Khodoun, Hongzhu Liu, and Xinhua Lin. "Drosophila Dpp Morphogen Movement Is Independent of Dynamin-Mediated Endocytosis but Regulated by the Glypican Members of Heparan Sulfate Proteoglycans". In: *Cell* 119.2 (Oct. 2004), pp. 231–244.

[167] Katsufumi Dejima, Makoto I. Kanai, Takuya Akiyama, Daniel C. Levings, and Hiroshi Nakato. "Novel Contact-dependent Bone Morphogenetic Protein (BMP) Signaling Mediated by Heparan Sulfate Proteoglycans". en. In: *Journal of Biological Chemistry* 286.19 (May 2011), pp. 17103–17111.

[168] Prem P. Dwivedi, Randall H. Grose, Jorge Filmus, Charles S. T. Hii, Cory J. Xian, Peter J. Anderson, and Barry C. Powell. "Regulation of bone morphogenetic protein signalling and cranial osteogenesis by Gpc1 and Gpc3". In: *Bone* 55.2 (Aug. 2013), pp. 367–376.

[169] Suparna Taneja-Bageshwar and Tina L. Gumienny. "Regulation of TGF superfamily signaling by two separable domains of glypican LON-2 in C. elegans". eng. In: *Worm* 2.3 (July 2013), e23843.

[170] Yi-Huei Linda Jen, Michele Musacchio, and Arthur D. Lander. "Glypican-1 controls brain size through regulation of fibroblast growth factor signaling in early neurogenesis". eng. In: *Neural Development* 4 (Sept. 2009), p. 33.

[171] Jaime Gutiérrez and Enrique Brandan. "A Novel Mechanism of Sequestering Fibroblast Growth Factor 2 by Glypican in Lipid Rafts, Allowing Skeletal Muscle Differentiation". In: *Molecular and Cellular Biology* 30.7 (Apr. 2010), pp. 1634–1649.

[172] Jin-Ping Lai, Dalbir S. Sandhu, Chunrong Yu, Tao Han, Catherine D. Moser, Kenard K. Jackson, Ruben Bonilla Guerrero, Ileana Aderca, Hajime Isomoto, Megan M. Garrity-Park, Hongzhi Zou, Abdirashid M. Shire, David M. Nagorney, Schuyler O. Sanderson, Alex A. Adjei, Ju-Seog Lee, Snorri S. Thorgeirsson, and Lewis R. Roberts. "Sulfatase 2 up-regulates glypican 3, promotes fibroblast growth factor signaling, and decreases survival in hepatocellular carcinoma". eng. In: *Hepatology (Baltimore, Md.)* 47.4 (Apr. 2008), pp. 1211–1222.

[173] Howard H. Song, Wen Shi, and Jorge Filmus. "OCI-5/Rat Glypican-3 Binds to Fibroblast Growth Factor-2 but Not to Insulin-like Growth Factor-2". en. In: *Journal of Biological Chemistry* 272.12 (Mar. 1997), pp. 7574–7577.

[174] Dong Yan and Xinhua Lin. "Drosophila glypican Dally-like acts in FGF-receiving cells to modulate FGF signaling during tracheal morphogenesis". eng. In: *Developmental Biology* 312.1 (Dec. 2007), pp. 203–216.

[175] Jonathan K. Ivins, E. David Litwack, Asli Kumbasar, Christopher S. Stipp, and Arthur D. Lander. "Cerebroglycan, a Developmentally Regulated Cell-Surface Heparan Sulfate Proteoglycan, Is Expressed on Developing Axons and Growth Cones". In: *Developmental Biology* 184.2 (Apr. 1997), pp. 320–332.

[176] S. Lugert, T. Kremer, R. Jagasia, A. Herrmann, S. Aigner, C. Giachino, I. Mendez-David, A. M. Gardier, J. P. Carralot, H. Meistermann, A. Augustin, M. D. Saxe, J. Lamerz, G. Duran-Pacheco, A. Ducret, V. Taylor, D. J. David, and C. Czech. "Glypican-2 levels in cerebrospinal fluid predict the status of adult hippocampal neurogenesis". en. In: *Scientific Reports* 7 (Apr. 2017), p. 46543.

[177] Ann Ng, Michelle Wong, Beth Viviano, Jonathan M Erlich, George Alba, Camila Pflederer, Patrick Y Jay, and Scott Saunders. "Loss of glypican-3 function causes growth factor-dependent defects in cardiac and coronary vascular development". In: *Developmental biology* 335.1 (2009), pp. 208–215.

[178] Silviu Grisaru, Danielle Cano-Gauci, James Tee, Jorge Filmus, and Norman D Rosenblum. "Glypican-3 modulates BMP-and FGF-mediated effects during renal branching morphogenesis". In: *Developmental biology* 231.1 (2001), pp. 31–46.

[179] Beth L Viviano, Laura Silverstein, Camila Pflederer, Stephenie Paine-Saunders, Kathy Mills, and Scott Saunders. "Altered hematopoiesis in glypican-3-deficient mice results in decreased osteoclast differentiation and a delay in endochondral ossification". In: *Developmental biology* 282.1 (2005), pp. 152–162.

[180] Mariana I Capurro, Fuchuan Li, and Jorge Filmus. "Overgrowth of a mouse model of Simpson–Golabi–Behmel syndrome is partly mediated by Indian Hedgehog". In: *EMBO reports* 10.8 (2009), pp. 901–907.

[181] K. Hagihara, K. Watanabe, J. Chun, and Y. Yamaguchi. "Glypican-4 is an FGF2-binding heparan sulfate proteoglycan expressed in neural precursor cells". eng. In: *Developmental Dynamics: An Official Publication of the American Association of Anatomists* 219.3 (Nov. 2000), pp. 353–367.

[182] Isabella Farhy-Tselnicker, Adriana C. M. van Casteren, Aletheia Lee, Veronica T. Chang, A. Radu Aricescu, and Nicola J. Allen. "Astrocyte-Secreted Glypican 4 Regulates Release of Neuronal Pentraxin 1 from Axons to Induce Functional Synapse Formation". English. In: *Neuron* 96.2 (Oct. 2017), 428–445.e13.

[183] Ina Strate, Federico Tessadori, and Jeroen Bakkers. "Glypican4 promotes cardiac specification and differentiation by attenuating canonical Wnt and Bmp signaling". en. In: *Development* 142.10 (May 2015), pp. 1767–1776.

[184] Katelyn Kenny, Leandro Royer, Anna R Moore, Xiao Chen, Michael T Marr II, and Suzanne Paradis. "Rem2 signaling affects neuronal structure and function in part by regulation of gene expression". In: *Molecular and Cellular Neuroscience* 85 (2017), pp. 190–201.

[185] Mariana Capurro, Tomomi Izumikawa, Philippe Suarez, Wen Shi, Marzena Cydzik, Tomoyuki Kaneiwa, Jean Gariepy, Luisa Bonafe, and Jorge Filmus. "Glypican-6 promotes the growth of developing long bones by stimulating Hedgehog signaling". en. In: *The Journal of Cell Biology* 216.9 (Sept. 2017), pp. 2911–2926.

[186] Giuseppe Pilia, Rhiannon M. Hughes-Benzie, Alex MacKenzie, Primo Baybayan, Ellson Y. Chen, Reid Huber, Giovanni Neri, Antonio Cao, Antonino Forabosco, and David Schlessinger. "Mutations in GPC3 , a glypican gene, cause the Simpson-Golabi-Behmel overgrowth syndrome". En. In: *Nature Genetics* 12.3 (Mar. 1996), p. 241.

[187] Brian J. Sajorda, Christina X. Gonzalez-Gandolfi, Evan R. Hathaway, and Jennifer M. Kalish. "Simpson-Golabi-Behmel Syndrome Type 1". eng. In: *GeneReviews®*. Ed. by Margaret P. Adam, Holly H. Ardinger, Roberta A. Pagon, Stephanie E. Wallace, Lora JH Bean, Karen Stephens, and Anne Amemiya. Seattle (WA): University of Washington, Seattle, 1993.

[188] Jair Tenorio, Pedro Arias, Víctor Martínez-Glez, Fernando Santos, Sixto García-Miñaur, Julián Nevado, and Pablo Lapunzina. "Simpson-Golabi-Behmel syndrome types I and II". eng. In: *Orphanet Journal of Rare Diseases* 9 (Sept. 2014), p. 138.

[189] Michael R. DeBaun, Jennifer Ess, and Scott Saunders. "Simpson Golabi Behmel Syndrome: Progress toward Understanding the Molecular Basis for Overgrowth, Malformation, and Cancer Predisposition". In: *Molecular Genetics and Metabolism* 72.4 (Apr. 2001), pp. 279–286.

[190] Marie-Laure Vuillaume, Marie-Pierre Moizard, Sylvie Rossignol, Edouard Cottereau, Sandrine Vonwill, Jean-Luc Alessandri, Tiffany Busa, Estelle Colin, Marion Gérard, Fabienne Giuliano, Laetitia Lambert, Mathilde Lefevre, Udhaya Kotecha, Sheela Nampoothiri, Irène Netchine, Martine Raynaud, Frédéric Brioude, and Annick Toutain. "Mutation update for the GPC3 gene involved in Simpson–Golabi–Behmel syndrome and review of the literature". en. In: *Human Mutation* 39.12 (2018), pp. 2110–2112.

[191] M. Veugelers, B. D. Cat, S. Y. Muyldermans, G. Reekmans, N. Delande, S. Frints, E. Legius, J. P. Fryns, C. Schrander-Stumpel, B. Weidle, N. Magdalena, and G. David. "Mutational analysis of the GPC3/GPC4 glypican gene cluster on Xq26 in patients with Simpson-Golabi-Behmel syndrome: identification of loss-of-function mutations in the GPC3 gene". eng. In: *Human Molecular Genetics* 9.9 (May 2000), pp. 1321–1328.

[192] Wen Shi and Jorge Filmus. "A patient with the Simpson-Golabi-Behmel syndrome displays a loss-of-function point mutation in GPC3 that inhibits the attachment of this proteoglycan to the cell surface". eng. In: *American Journal of Medical Genetics. Part A* 149A.3 (Mar. 2009), pp. 552–554.

[193] Eric Chiao, Peter Fisher, Laura Crisponi, Manila Deiana, Ioannis Dragatsis, David Schlessinger, Giuseppe Pilia, and Argiris Efstratiadis. "Overgrowth of a Mouse Model of the Simpson–Golabi–Behmel Syndrome Is Independent of IGF Signaling". In: *Developmental Biology* 243.1 (Mar. 2002), pp. 185–206.

[194] Danielle F. Cano-Gauci, Howard H. Song, Huiling Yang, Colin McKerlie, Barbara Choo, Wen Shi, Rose Pullano, Tino D. Piscione, Silviu Grisaru, Shawn Soon, Larisa Sedlackova, A. Keith Tanswell, Tak W. Mak, Herman Yeger, Gina A. Lockwood, Norman D. Rosenblum, and Jorge Filmus. "Glypican-3–Deficient Mice Exhibit Developmental Overgrowth and Some of the Abnormalities Typical of Simpson-Golabi-Behmel Syndrome". en. In: *The Journal of Cell Biology* 146.1 (July 1999), pp. 255–264.

[195] Massimo Pellegrini, Giuseppe Pilia, Serafino Pantano, Franco Lucchini, Manuela Uda, Mariapaola Fumi, Antonio Cao, David Schlessinger, and Antonino Forabosco. "Gpc3 expression correlates with the phenotype of the Simpson-Golabi-Behmel syndrome". fr. In: *Developmental Dynamics* 213.4 (1998), pp. 431–439.

[196] Bibiana V Iglesias, Gloria Centeno, Hector Pascuccelli, Flavia Ward, María Giselle Peters, Jorge Filmus, and Lydia Puricelli. "Expression pattern of glypican-3 (GPC3) during human embryonic and fetal development". en. In: (), p. 8.

[197] Jennifer M. Kalish, Leslie Doros, Lee J. Helman, Raoul C. Hennekam, Roland P. Kuiper, Saskia M. Maas, Eamonn R. Maher, Kim E. Nichols, Sharon E. Plon, Christopher C. Porter, Surya Rednam, Kris Ann P. Schultz, Lisa J. States, Gail E. Tomlinson, Kristin Zelley, and Todd E. Druley. "Surveillance Recommendations for Children with Overgrowth Syndromes and Predisposition to Wilms Tumors and Hepatoblastoma". en. In: *Clinical Cancer Research* 23.13 (July 2017), e115–e122.

[198] R. M. Hughes-Benzie, A. G. Hunter, J. E. Allanson, and A. E. Mackenzie. "Simpson-Golabi-Behmel syndrome associated with renal dysplasia and embryonal tumor: localization of the gene to Xqcen-q21". eng. In: *American Journal of Medical Genetics* 43.1-2 (May 1992), pp. 428–435.

[199] Elaine H. Shen, Caroline C. Overly, and Allan R. Jones. "The Allen Human Brain Atlas: Comprehensive gene expression mapping of the human brain". In: *Trends in Neurosciences* 35.12 (Dec. 2012), pp. 711–714.

[200] Hans Clevers. "Wnt/beta-catenin signaling in development and disease". eng. In: *Cell* 127.3 (Nov. 2006), pp. 469–480.

[201] Zachary Steinhart and Stephane Angers. "Wnt signaling in development and tissue homeostasis". en. In: *Development* 145.11 (June 2018), dev146589.

[202] Raymond Teck Ho Lee, Zhonghua Zhao, and Philip W. Ingham. "Hedgehog signalling". en. In: *Development* 143.3 (Feb. 2016), pp. 367–372.

[203] James Briscoe and Pascal P. Thérond. "The mechanisms of Hedgehog signalling and its roles in development and disease". en. In: *Nature Reviews Molecular Cell Biology* 14.7 (July 2013), pp. 416–429.

[204] Christof Niehrs. "The complex world of WNT receptor signalling". eng. In: *Nature Reviews. Molecular Cell Biology* 13.12 (Dec. 2012), pp. 767–779.

[205] Kyungwon Lee, Younghwa Shin, Rui Cheng, Kyoungmin Park, Yang Hu, Jeffrey McBride, Xuemin He, Yusuke Takahashi, and Jian-Xing Ma. "Receptor heterodimerization as a novel mechanism for the regulation of Wnt/-catenin signaling". eng. In: *Journal of Cell Science* 127.Pt 22 (Nov. 2014), pp. 4857–4869.

[206] Angela M Arensdorf, Suresh Marada, and Stacey K Ogden. "Smoothened regulation: a tale of two signals". In: *Trends in pharmacological sciences* 37.1 (2016), pp. 62–72.

[207] Mariana I. Capurro, Yun-Yan Xiang, Corrinne Lobe, and Jorge Filmus. "Glypican-3 Promotes the Growth of Hepatocellular Carcinoma by Stimulating Canonical Wnt Signaling". en. In: *Cancer Research* 65.14 (July 2005), pp. 6245–6254.

[208] Na Li, Liwen Wei, Xiaoyu Liu, Hongjun Bai, Yvonne Ye, Dan Li, Nan Li, Ulrich Baxa, Qun Wang, Ling Lv, Yun Chen, Mingqian Feng, Byungkook Lee, Wei Gao, and Mitchell Ho. "A Frizzled-Like Cysteine-Rich Domain in Glypican-3 Mediates Wnt Binding and Regulates Hepatocellular Carcinoma Tumor Growth in Mice". eng. In: *Hepatology (Baltimore, Md.)* (Apr. 2019).

[209] Lucy Brunt and Steffen Scholpp. "The function of endocytosis in Wnt signaling". eng. In: *Cellular and molecular life sciences: CMLS* 75.5 (2018), pp. 785–795.

[210] Jeremy T. Blitzer and Roel Nusse. "A critical role for endocytosis in Wnt signaling". eng. In: *BMC cell biology* 7 (July 2006), p. 28.

[211] Ingyu Kim, Weijun Pan, Sara A. Jones, Youxin Zhang, Xiaowei Zhuang, and Dianqing Wu. "Clathrin and AP2 are required for PtdIns(4,5)P2-mediated formation of LRP6 signalosomes". eng. In: *The Journal of Cell Biology* 200.4 (Feb. 2013), pp. 419–428.

[212] Anja I. H. Hagemann, Jennifer Kurz, Silke Kauffeld, Qing Chen, Patrick M. Reeves, Sabrina Weber, Simone Schindler, Gary Davidson, Tomas Kirchhausen, and Steffen Scholpp. "In vivo analysis of formation and endocytosis of the Wnt/-catenin signaling complex in zebrafish embryos". eng. In: *Journal of Cell Science* 127.Pt 18 (Sept. 2014), pp. 3970–3982.

[213] Alexandra Traister, Wen Shi, and Jorge Filmus. "Mammalian Notum induces the release of glypicans and other GPI-anchored proteins from the cell surface". eng. In: *The Biochemical Journal* 410.3 (Mar. 2008), pp. 503–511.

[214] Johan Kreuger, Lidia Perez, Antonio J. Giraldez, and Stephen M. Cohen. "Opposing activities of Dally-like glypican at high and low levels of Wingless morphogen activity". eng. In: *Developmental Cell* 7.4 (Oct. 2004), pp. 503–512.

[215] Katie L. Ayers, Armel Gallet, Laurence Staccini-Lavenant, and Pascal P. Thérond. "The long-range activity of Hedgehog is regulated in the apical extracellular space by the glypican Dally and the hydrolase Notum". eng. In: *Developmental Cell* 18.4 (Apr. 2010), pp. 605–620.

[216] S. G. Velleman, Y. Song, J. Shin, and D. C. McFarland. "Modulation of turkey myogenic satellite cell differentiation through the shedding of glypican-1". In: *Comparative Biochemistry and Physiology Part A: Molecular & Integrative Physiology* 164.1 (Jan. 2013), pp. 36–43.

[217] Claudia Y. Janda, Deepa Waghray, Aron M. Levin, Christoph Thomas, and K. Christopher Garcia. "Structural basis of Wnt recognition by Frizzled". eng. In: *Science (New York, N.Y.)* 337.6090 (July 2012), pp. 59–64.

[218] Fuchuan Li, Wen Shi, Mariana Capurro, and Jorge Filmus. "Glypican-5 stimulates rhabdomyosarcoma cell proliferation by activating Hedgehog signaling". en. In: *The Journal of Cell Biology* 192.4 (Feb. 2011), pp. 691–704.

[219] Mariana I. Capurro, Wen Shi, and Jorge Filmus. "LRP1 mediates Hedgehog-induced endocytosis of the GPC3–Hedgehog complex". en. In: *Journal of Cell Science* 125.14 (July 2012), pp. 3380–3389.

[220] Jeffery A Porter, Stephen C Ekker, Woo-Jin Park, Doris P von Kessler, Keith E Young, Chien-Huan Chen, Yong Ma, Amina S Woods, Robert J Cotter, Eugene V Koonin, and Philip A Beachy. "Hedgehog Patterning Activity: Role of a Lipophilic Modification Mediated by the Carboxy-Terminal Autoprocessing Domain". In: *Cell* 86.1 (July 1996), pp. 21–34.

[221] R. Blake Pepinsky, Chenhui Zeng, Dingyi Wen, Paul Rayhorn, Darren P. Baker, Kevin P. Williams, Sarah A. Bixler, Christine M. Ambrose, Ellen A. Garber, Konrad Miatkowski, Frederick R. Taylor, Elizabeth A. Wang, and Alphonse Galdes. "Identification of a Palmitic Acid-modified Form of Human Sonic hedgehog". en. In: *Journal of Biological Chemistry* 273.22 (May 1998), pp. 14037–14045.

[222] F. R. Taylor, D. Wen, E. A. Garber, A. N. Carmillo, D. P. Baker, R. M. Arduini, K. P. Williams, P. H. Weinreb, P. Rayhorn, X. Hronowski, A. Whitty, E. S. Day, A. Boriack-Sjodin, R. I. Shapiro, A. Galdes, and R. B. Pepinsky. "Enhanced potency of human Sonic hedgehog by hydrophobic modification". eng. In: *Biochemistry* 40.14 (Apr. 2001), pp. 4359–4371.

[223] R. B. Pepinsky, C. Zeng, D. Wen, P. Rayhorn, D. P. Baker, K. P. Williams, S. A. Bixler, C. M. Ambrose, E. A. Garber, K. Miatkowski, F. R. Taylor, E. A. Wang, and A. Galdes. "Identification of a palmitic acid-modified form of human Sonic hedgehog". eng. In: *The Journal of Biological Chemistry* 273.22 (May 1998), pp. 14037–14045.

[224] Yina Li, Huimin Zhang, Ying Litingtung, and Chin Chiang. "Cholesterol modification restricts the spread of Shh gradient in the limb bud". en. In: *Proceedings of the National Academy of Sciences* 103.17 (Apr. 2006), pp. 6548–6553.

[225] Carsten Peters, Alexander Wolf, Melanie Wagner, Jürgen Kuhlmann, and Herbert Waldmann. "The cholesterol membrane anchor of the Hedgehog protein confers stable membrane association to lipid-modified proteins". eng. In: *Proceedings of the National Academy of Sciences of the United States of America* 101.23 (June 2004), pp. 8531–8536.

[226] Paula M. Lewis, Matthew P. Dunn, Jill A. McMahon, Malcolm Logan, James F. Martin, Benoit St-Jacques, and Andrew P. McMahon. "Cholesterol Modification of Sonic Hedgehog Is Required for Long-Range Signaling Activity and Effective Modulation of Signaling by Ptc1". In: *Cell* 105.5 (June 2001), pp. 599–612.

[227] Hanna Tukachinsky, Ryan P. Kuzmickas, Cindy Y. Jao, Jing Liu, and Adrian Salic. "Dispatched and scube mediate the efficient secretion of the cholesterol-modified hedgehog ligand". eng. In: *Cell Reports* 2.2 (Aug. 2012), pp. 308–320.

[228] Adrian Creanga, Thomas D. Glenn, Randall K. Mann, Adam M. Saunders, William S. Talbot, and Philip A. Beachy. "Scube/You activity mediates release of dually lipid-modified Hedgehog signal in soluble form". eng. In: *Genes & Development* 26.12 (June 2012), pp. 1312–1325.

[229] Neha Vyas, Debanjan Goswami, A. Manonmani, Pranav Sharma, H. A. Ranganath, K. VijayRaghavan, L. S. Shashidhara, R. Sowdhamini, and Satyajit Mayor. "Nanoscale Organization of Hedgehog Is Essential for Long-Range Signaling". In: *Cell* 133.7 (June 2008), pp. 1214–1227.

[230] Corinna Ortmann, Ute Pickhinke, Sebastian Exner, Stefanie Ohlig, Roger Lawrence, Hamodah Jboor, Rita Dreier, and Kay Grobe. "Sonic hedgehog processing and release are regulated by glypican heparan sulfate proteoglycans". en. In: *Journal of Cell Science* 128.12 (June 2015), pp. 2374–2385.

[231] Chun Han, Tatyana Y. Belenkaya, Bei Wang, and Xinhua Lin. "Drosophila glypicans control the cell-to-cell movement of Hedgehog by a dynamin-independent process". eng. In: *Development (Cambridge, England)* 131.3 (Feb. 2004), pp. 601–611.

[232] Y. Bellaiche, I. The, and N. Perrimon. "Tout-velu is a Drosophila homologue of the putative tumour suppressor EXT-1 and is needed for Hh diffusion". eng. In: *Nature* 394.6688 (July 1998), pp. 85–88.

[233] Hong Liu, Chunmei Yang, Wenzhu Lu, and Yong Zeng. "Prognostic significance of glypican-3 expression in hepatocellular carcinoma: A meta-analysis". eng. In: *Medicine* 97.4 (Jan. 2018), e9702.

[234] Yutaka Midorikawa, Shumpei Ishikawa, Hiroko Iwanari, Takeshi Imamura, Hirohiko Sakamoto, Kohei Miyazono, Tatsuhiko Kodama, Masatoshi Makuuchi, and Hiroyuki Aburatani. "Glypican-3, overexpressed in hepatocellular carcinoma, modulates FGF2 and BMP-7 signaling". eng. In: *International Journal of Cancer* 103.4 (Feb. 2003), pp. 455–465.

[235] Masahiro Suzuki, Kazushi Sugimoto, Junichiro Tanaka, Masahiko Tameda, Yuji Inagaki, Satoko Kusagawa, Keiichiro Nojiri, Tetsuya Beppu, Kentaro Yoneda, Norihiko Yamamoto, Masaaki Ito, Misao Yoneda, Kazuhiko Uchida, Koujiro Takase, and Katsuya Shiraki. "Up-regulation of Glypican-3 in Human Hepatocellular Carcinoma". en. In: *Anticancer Research* 30.12 (Jan. 2010), pp. 5055–5061.

[236] Pei Hu, Bin Cheng, Yulin He, Zhiqiang Wei, Dongfang Wu, and Zhongji Meng. "Autophagy suppresses proliferation of HepG2 cells via inhibiting glypican-3/wnt/-catenin signaling". eng. In: *OncoTargets and Therapy* 11 (2018), pp. 193–200.

[237] Wei Gao, Heungnam Kim, Mingqian Feng, Yen Phung, Charles P. Xavier, Jeffrey S. Rubin, and Mitchell Ho. "Inactivation of Wnt signaling by a human antibody that recognizes the heparan sulfate chains of glypican-3 for liver cancer therapy". eng. In: *Hepatology (Baltimore, Md.)* 60.2 (Aug. 2014), pp. 576–587.

[238] Wei Gao, Heungnam Kim, and Mitchell Ho. "Human Monoclonal Antibody Targeting the Heparan Sulfate Chains of Glypican-3 Inhibits HGF-Mediated Migration and Motility of Hepatocellular Carcinoma Cells". eng. In: *PloS One* 10.9 (2015), e0137664.

[239] Mingqian Feng, Wei Gao, Ruoqi Wang, Weizao Chen, Yan-Gao Man, William Douglas Figg, Xin Wei Wang, Dimiter S. Dimitrov, and Mitchell Ho. "Therapeutically targeting glypican-3 via a conformation-specific single-domain antibody in hepatocellular carcinoma". eng. In: *Proceedings of the National Academy of Sciences of the United States of America* 110.12 (Mar. 2013), E1083–1091.

[240] Wei Gao and Mitchell Ho. "The role of glypican-3 in regulating Wnt in hepatocellular carcinomas". In: *Cancer reports* 1.1 (2011), pp. 14–19.

[241] Chris K. Sun, Mei-Sze Chua, Jing He, and Samuel K. So. "Suppression of glypican 3 inhibits growth of hepatocellular carcinoma cells through up-regulation of TGF-2". eng. In: *Neoplasia (New York, N.Y.)* 13.8 (Aug. 2011), pp. 735–747.

[242] Freddie Bray, Jacques Ferlay, Isabelle Soerjomataram, Rebecca L. Siegel, Lindsey A. Torre, and Ahmedin Jemal. "Global cancer statistics 2018: GLOBOCAN estimates of incidence and mortality worldwide for 36 cancers in 185 countries". en. In: *CA: A Cancer Journal for Clinicians* 68.6 (2018), pp. 394–424.

[243] W. Thomas London, Jessica L. Petrick, and Katherine A. McGlynn. *Liver Cancer*. en_US. Oxford University Press, Nov. 2017.

[244] Arjun Gupta, Avash Das, Kaustav Majumder, Nivedita Arora, Helen G. Mayo, Preet P. Singh, Muhammad S. Beg, and Siddharth Singh. "Obesity is Independently Associated With Increased Risk of Hepatocellular Cancer-related Mortality: A Systematic Review and Meta-Analysis". eng. In: *American Journal of Clinical Oncology* 41.9 (2018), pp. 874–881.

[245] Andrea Marengo, Chiara Rosso, and Elisabetta Bugianesi. "Liver Cancer: Connections with Obesity, Fatty Liver, and Cirrhosis". eng. In: *Annual Review of Medicine* 67 (2016), pp. 103–117.

[246] Amit G. Singal, Anjana Pillai, and Jasmin Tiro. "Early Detection, Curative Treatment, and Survival Rates for Hepatocellular Carcinoma Surveillance in Patients with Cirrhosis: A Meta-analysis". In: *PLoS Medicine* 11.4 (Apr. 2014).

[247] Omair Atiq, Jasmin Tiro, Adam C. Yopp, Adam Muffler, Jorge A. Marrero, Neehar D. Parikh, Caitlin Murphy, Katharine McCallister, and Amit G. Singal. "An assessment of benefits and harms of hepatocellular carcinoma surveillance in patients with cirrhosis". en. In: *Hepatology* 65.4 (2017), pp. 1196–1205.

[248] Amit G. Singal, Hari S. Conjeevaram, Michael L. Volk, Sherry Fu, Robert J. Fontana, Fred Askari, Grace L. Su, Anna S. Lok, and Jorge A. Marrero. "Effectiveness of hepatocellular carcinoma surveillance in patients with cirrhosis". eng. In: *Cancer Epidemiology, Biomarkers & Prevention: A Publication of the American Association for Cancer Research, Cosponsored by the American Society of Preventive Oncology* 21.5 (May 2012), pp. 793–799.

[249] Kristina Tzartzeva, Joseph Obi, Nicole E. Rich, Neehar D. Parikh, Jorge A. Marrero, Adam Yopp, Akbar K. Waljee, and Amit G. Singal. "Surveillance Imaging and Alpha Fetoprotein for Early Detection of Hepatocellular Carcinoma in Patients With Cirrhosis: A Meta-analysis". en. In: *Gastroenterology* 154.6 (May 2018), 1706–1718.e1.

[250] Mariana Capurro, Ian R. Wanless, Morris Sherman, Gerrit Deboer, Wen Shi, Eiji Miyoshi, and Jorge Filmus. "Glypican-3: a novel serum and histochemical marker for hepatocellular carcinoma". eng. In: *Gastroenterology* 125.1 (July 2003), pp. 89–97.

[251] B Li, H Liu, HW Shang, P Li, N Li, and HG Ding. "Diagnostic value of glypican-3 in alpha fetoprotein negative hepatocellular carcinoma patients". In: *African Health Sciences* 13.3 (Sept. 2013), pp. 703–709.

[252] Mingqian Feng Ho Mitchell. "Glypican-3 antibodies: a new therapeutic target for liver cancer". In: *FEBS letters* 588.2 (Jan. 2014), pp. 377–382.

[253] Kiyotaka Nakano, Tetsuro Orita, Junichi Nezu, Takeshi Yoshino, Iwao Ohizumi, Masamichi Sugimoto, Koh Furugaki, Yasuko Kinoshita, Takahiro Ishiguro, Takao Hamakubo, Tatsuhiko Kodama, Hiroyuki Aburatani, Hisafumi Yamada-Okabe, and Masayuki Tsuchiya. "Anti-glypican 3 antibodies cause ADCC against human hepatocellular carcinoma cells". eng. In: *Biochemical and Biophysical Research Communications* 378.2 (Jan. 2009), pp. 279–284.

[254] Takahiro Ishiguro, Masamichi Sugimoto, Yasuko Kinoshita, Yoko Miyazaki, Kiyotaka Nakano, Hiroyuki Tsunoda, Izumi Sugo, Iwao Ohizumi, Hiroyuki Aburatani, Takao Hamakubo, Tatsuhiko Kodama, Masayuki Tsuchiya, and Hisafumi Yamada-Okabe. "Anti-glypican 3 antibody as a potential antitumor agent for human liver cancer". eng. In: *Cancer Research* 68.23 (Dec. 2008), pp. 9832–9838.

[255] Kiyotaka Nakano, Takahiro Ishiguro, Hiroko Konishi, Megumi Tanaka, Masamichi Sugimoto, Izumi Sugo, Tomoyuki Igawa, Hiroyuki Tsunoda, Yasuko Kinoshita, Kiyoshi Habu, Tetsuro Orita, Masayuki Tsuchiya, Kunihiro Hattori, and Hisafumi Yamada-Okabe. "Generation of a humanized anti-glypican 3 antibody by CDR grafting and stability optimization". eng. In: *Anti-Cancer Drugs* 21.10 (Nov. 2010), pp. 907–916.

[256] Yen Phung, Wei Gao, Yan-Gao Man, Satoshi Nagata, and Mitchell Ho. "High-affinity monoclonal antibodies to cell surface tumor antigen glypican-3 generated through a combination of peptide immunization and flow cytometry screening". eng. In: *mAbs* 4.5 (Oct. 2012), pp. 592–599.

[257] Yi-Fan Zhang and Mitchell Ho. "Humanization of high-affinity antibodies targeting glypican-3 in hepatocellular carcinoma". en. In: *Scientific Reports* 6 (Sept. 2016), p. 33878.

[258] Mingqian Feng, Wei Gao, Ruoqi Wang, Weizao Chen, Yan-Gao Man, William Douglas Figg, Xin Wei Wang, Dimiter S. Dimitrov, and Mitchell Ho. "Therapeutically targeting glypican-3 via a conformation-specific single-domain antibody in hepatocellular carcinoma". In: *Proceedings of the National Academy of Sciences of the United States of America* 110.12 (Mar. 2013), E1083–E1091.

[259] Wei Gao, Zhewei Tang, Yi-Fan Zhang, Mingqian Feng, Min Qian, Dimiter S. Dimitrov, and Mitchell Ho. "Immunotoxin targeting glypican-3 regresses liver cancer via dual inhibition of Wnt signalling and protein synthesis". en. In: *Nature Communications* 6 (Mar. 2015), p. 6536.

[260] Yun-Yan Xiang, Virginia Ladeda, and Jorge Filmus. "Glypican-3 expression is silenced in human breast cancer". En. In: *Oncogene* 20.50 (Nov. 2001), p. 7408.

[261] Lilian Fedra Castillo, Rocío Tascón, María Amparo Lago Huvelle, Gisela Novack, María Candelaria Llorens, Ancely Ferreira dos Santos, Jorge Shortrede, Ana María Cabanillas, Elisa Bal de Kier Joffé, Leticia Labriola, and María Giselle Peters. "Glypican-3 induces a mesenchymal to epithelial transition in human breast cancer cells". In: *Oncotarget* 7.37 (Aug. 2016), pp. 60133–60154.

[262] Gary Temple, Daniela S Gerhard, Rebekah Rasooly, Elise A Feingold, Peter J Good, Cristen Robinson, Allison Mandich, Jeffrey G Derge, Jeanne Lewis, Debonny Shoaf, et al. "The completion of the mammalian gene collection (MGC)". In: *Genome research* 19.12 (2009), pp. 2324–2333.

[263] A Radu Aricescu, Weixian Lu, and E Yvonne Jones. "A time-and cost-efficient system for high-level protein production in mammalian cells". In: *Acta Crystallographica Section D: Biological Crystallography* 62.10 (2006), pp. 1243–1250.

[264] Gert-Jan Kremers, Joachim Goedhart, Erik B van Munster, and Theodorus WJ Gadella. "Cyan and yellow super fluorescent proteins with improved brightness, protein folding, and FRET Förster radius". In: *Biochemistry* 45.21 (2006), pp. 6570–6580.

[265] Chad R Irwin, Andrew Farmer, David O Willer, and David H Evans. "In-fusion® cloning with vaccinia virus DNA polymerase". In: *Vaccinia Virus and Poxvirology*. Springer, 2012, pp. 23–35.

[266] Baogong Zhu, Guifang Cai, Emily O Hall, and Gordon J Freeman. "In-Fusion™ assembly: seamless engineering of multidomain fusion proteins, modular vectors, and mutations". In: *Biotechniques* 43.3 (2007), pp. 354–359.

[267] Veronica T Chang, Max Crispin, A Radu Aricescu, David J Harvey, Joanne E Nettleship, Janet A Fennelly, Chao Yu, Kent S Boles, Edward J Evans, David I Stuart, et al. "Glycoprotein structural genomics: solving the glycosylation problem". In: *Structure* 15.3 (2007), pp. 267–273.

[268] Alan D Elbein, Joseph E Tropea, Mike Mitchell, and Gur P Kaushal. "Kifunensine, a potent inhibitor of the glycoprotein processing mannosidase I." In: *Journal of Biological Chemistry* 265.26 (1990), pp. 15599–15605.

[269] Philip J Reeves, Nico Callewaert, Roland Contreras, and H Gobind Khorana. "Structure and function in rhodopsin: high-level expression of rhodopsin with restricted and homogeneous N-glycosylation by a tetracycline-inducible N-acetylglucosaminyltransferase I-negative HEK293S stable mammalian cell line". In: *Proceedings of the National Academy of Sciences* 99.21 (2002), pp. 13419–13424.

[270] Michael Fairhead and Mark Howarth. "Site-specific biotinylation of purified proteins using BirA". In: (2015), pp. 171–184.

[271] Patrick Englebienne, Anne Van Hoonacker, and Michel Verhas. "Surface plasmon resonance: principles, methods and applications in biomedical sciences". In: *Journal of Spectroscopy* 17.2-3 (2003), pp. 255–273.

[272] Marco Faini, Florian Stengel, and Ruedi Aebersold. "The evolving contribution of mass spectrometry to integrative structural biology". In: *Journal of the American Society for Mass Spectrometry* 27.6 (2016), pp. 966–974.

[273] Helena Hernández and Carol V Robinson. "Determining the stoichiometry and interactions of macromolecular assemblies from mass spectrometry". In: *Nature protocols* 2.3 (2007), p. 715.

[274] Fabrice Gorrec. "The MORPHEUS protein crystallization screen". In: *Journal of applied crystallography* 42.6 (2009), pp. 1035–1042.

[275] Fabrice Gorrec. "The MORPHEUS II protein crystallization screen". In: *Acta Crystallographica Section F: Structural Biology Communications* 71.7 (2015), pp. 831–837.

[276] Rebecca Page and Raymond C Stevens. "Crystallization data mining in structural genomics: using positive and negative results to optimize protein crystallization screens". In: *Methods* 34.3 (2004), pp. 373–389.

[277] Janet Newman, David Egan, Thomas S Walter, Ran Meged, Ian Berry, Marouane Ben Jelloul, Joel L Sussman, David I Stuart, and Anastassis Perrakis. "Towards rationalization of crystallization screening for small-to medium-sized academic laboratories: the PACT/JCSG+ strategy". In: *Acta Crystallographica Section D: Biological Crystallography* 61.10 (2005), pp. 1426–1431.

[278] T-C Hu, Justyna Korczyńska, David K Smith, and Andrzej Marek Brzozowski. "High-molecular-weight polymers for protein crystallization: poly-γ-glutamic acid-based precipitants". In: *Acta Crystallographica Section D: Biological Crystallography* 64.9 (2008), pp. 957–963.

[279] Sergei Radaev and Peter D Sun. "Crystallization of protein–protein complexes". In: *Journal of applied crystallography* 35.6 (2002), pp. 674–676.

[280] Clemens Grimm, Ashwin Chari, Klaus Reuter, and Utz Fischer. "A crystallization screen based on alternative polymeric precipitants". In: *Acta Crystallographica Section D: Biological Crystallography* 66.6 (2010), pp. 685–697.

[281] Elspeth F Garman and Thomas R Schneider. "Macromolecular cryocrystallography". In: *Journal of Applied Crystallography* 30.3 (1997), pp. 211–237.

[282] Alexander McPherson and Bob Cudney. "Optimization of crystallization conditions for biological macromolecules". In: *Acta Crystallographica Section F: Structural Biology Communications* 70.11 (2014), pp. 1445–1467.

[283] Alexander McPherson and Bob Cudney. "Optimization of crystallization conditions for biological macromolecules". In: *Acta Crystallographica Section F: Structural Biology Communications* 70.11 (2014), pp. 1445–1467.

[284] Joseph R Luft, Jennifer R Wolfley, Meriem I Said, Raymond M Nagel, Angela M Lauricella, Jennifer L Smith, Max H Thayer, Christina K Veatch, Edward H Snell, Michael G Malkowski, et al. "Efficient optimization of crystallization conditions by manipulation of drop volume ratio and temperature". In: *Protein science* 16.4 (2007), pp. 715–722.

[285] Alexander McPherson and Bob Cudney. "Searching for silver bullets: an alternative strategy for crystallizing macromolecules". In: *Journal of structural biology* 156.3 (2006), pp. 387–406.

[286] R Cudney, Sam Patel, Karl Weisgraber, YVONNE Newhouse, and Alexander McPherson. "Screening and optimization strategies for macromolecular crystal growth". In: *Acta Crystallographica Section D: Biological Crystallography* 50.4 (1994), pp. 414–423.

[287] Joseph R Luft and George T DeTitta. "A method to produce microseed stock for use in the crystallization of biological macromolecules". In: *Acta Crystallographica Section D: Biological Crystallography* 55.5 (1999), pp. 988–993.

[288] Areej Abuhammad, Michael A McDonough, Jurgen Brem, Anne Makena, Steven Johnson, Christopher J Schofield, and Elspeth F Garman. ""To cross-seed or not to cross-seed": a pilot study using metallo-β-lactamases". In: *Crystal Growth & Design* 17.2 (2017), pp. 913–924.

[289] Elspeth F Garman and Martin Weik. "X-ray radiation damage to biological macromolecules: further insights". In: (2017).

[290] G Winter. "xia2: an expert system for macromolecular crystallography data reduction". In: *Journal of applied crystallography* 43.1 (2010), pp. 186–190.

[291] Graeme Winter, David G Waterman, James M Parkhurst, Aaron S Brewster, Richard J Gildea, Markus Gerstel, Luis Fuentes-Montero, Melanie Vollmar, Tara Michels-Clark, Iris D Young, et al. "DIALS: implementation and evaluation of a new integration package". In: *Acta Crystallographica Section D* 74.2 (2018), pp. 85–97.

[292] Graeme Winter, David G Waterman, James M Parkhurst, Aaron S Brewster, Richard J Gildea, Markus Gerstel, Luis Fuentes-Montero, Melanie Vollmar, Tara Michels-Clark, Iris D Young, et al. "DIALS: implementation and evaluation of a new integration package". In: *Acta Crystallographica Section D* 74.2 (2018), pp. 85–97.

[293] Philip R Evans and Garib N Murshudov. "How good are my data and what is the resolution?" In: *Acta Crystallographica Section D: Biological Crystallography* 69.7 (2013), pp. 1204–1214.

[294] Michael R Sawaya. "Methods to refine macromolecular structures in cases of severe diffraction anisotropy". In: *Structural Genomics*. Springer, 2014, pp. 205–214.

[295] IJ Tickle, C Flensburg, P Keller, W Paciorek, A Sharff, C Vonrhein, and G Bricogne. "Staraniso". In: *Global Phasing Ltd., Cambridge, United Kingdom* (2018).

[296] P Andrew Karplus and Kay Diederichs. "Assessing and maximizing data quality in macromolecular crystallography". In: *Current opinion in structural biology* 34 (2015), pp. 60–68.

[297] Kay Diederichs and P Andrew Karplus. "Improved R-factors for diffraction data analysis in macromolecular crystallography". In: *Nature structural biology* 4.4 (1997), p. 269.

[298] Airlie J McCoy, Ralf W Grosse-Kunstleve, Paul D Adams, Martyn D Winn, Laurent C Storoni, and Randy J Read. "Phaser crystallographic software". In: *Journal of applied crystallography* 40.4 (2007), pp. 658–674.

[299] Wolfgang Kabsch. "Xds". In: *Acta Crystallographica Section D: Biological Crystallography* 66.2 (2010), pp. 125–132.

[300] Thomas C Terwilliger, Paul D Adams, Randy J Read, Airlie J McCoy, Nigel W Moriarty, Ralf W Grosse-Kunstleve, Pavel V Afonine, Peter H Zwart, and L-W Hung. "Decision-making in structure solution using Bayesian estimates of map quality: the PHENIX AutoSol wizard". In: *Acta Crystallographica Section D: Biological Crystallography* 65.6 (2009), pp. 582–601.

[301] Paul D Adams, Pavel V Afonine, Gábor Bunkóczi, Vincent B Chen, Ian W Davis, Nathaniel Echols, Jeffrey J Headd, L-W Hung, Gary J Kapral, Ralf W Grosse-Kunstleve, et al. "PHENIX: a comprehensive Python-based system for macromolecular structure solution". In: *Acta Crystallographica Section D: Biological Crystallography* 66.2 (2010), pp. 213–221.

[302] Thomas C Terwilliger. "SOLVE and RESOLVE: automated structure solution and density modification". In: *Methods in enzymology*. Vol. 374. Elsevier, 2003, pp. 22–37.

[303] Thomas C Terwilliger, Ralf W Grosse-Kunstleve, Pavel V Afonine, Nigel W Moriarty, Peter H Zwart, L-W Hung, Randy J Read, and Paul D Adams. "Iterative model building, structure refinement and density modification with the PHENIX AutoBuild wizard". In: *Acta Crystallographica Section D: Biological Crystallography* 64.1 (2008), pp. 61–69.

[304] Paul Emsley and Kevin Cowtan. "Coot: model-building tools for molecular graphics". In: *Acta Crystallographica Section D: Biological Crystallography* 60.12 (2004), pp. 2126–2132.

[305] Weikai Li and Fang Li. "Cross-crystal averaging with search models to improve molecular replacement phases". In: *Structure* 19.2 (2011), pp. 155–161.

[306] MD Winn, MN Isupov, and Garib N Murshudov. "Use of TLS parameters to model anisotropic displacements in macromolecular refinement". In: *Acta Crystallographica Section D: Biological Crystallography* 57.1 (2001), pp. 122–133.

[307] Jeffrey J Headd, Nathaniel Echols, Pavel V Afonine, Ralf W Grosse-Kunstleve, Vincent B Chen, Nigel W Moriarty, David C Richardson, Jane S Richardson, and Paul D Adams. "Use of knowledge-based restraints in phenix. refine to improve macromolecular refinement at low resolution". In: *Acta Crystallographica Section D: Biological Crystallography* 68.4 (2012), pp. 381–390.

[308] Byron DeLaBarre and Axel T Brunger. "Considerations for the refinement of low-resolution crystal structures". In: *Acta Crystallographica Section D: Biological Crystallography* 62.8 (2006), pp. 923–932.

[309] Vincent B Chen, W Bryan Arendall, Jeffrey J Headd, Daniel A Keedy, Robert M Immormino, Gary J Kapral, Laura W Murray, Jane S Richardson, and David C Richardson. "MolProbity: all-atom structure validation for macromolecular crystallography". In: *Acta Crystallographica Section D: Biological Crystallography* 66.1 (2010), pp. 12–21.

[310] Christopher J Williams, Jeffrey J Headd, Nigel W Moriarty, Michael G Prisant, Lizbeth L Videau, Lindsay N Deis, Vishal Verma, Daniel A Keedy, Bradley J Hintze, Vincent B Chen, et al. "MolProbity: More and better reference data for improved all-atom structure validation". In: *Protein Science* 27.1 (2018), pp. 293–315.

[311] Jon Agirre, Javier Iglesias-Fernández, Carme Rovira, Gideon J Davies, Keith S Wilson, and Kevin D Cowtan. "Privateer: software for the conformational validation of carbohydrate structures". In: *Nature structural & molecular biology* 22.11 (2015), p. 833.

[312] R Gupta, E Jung, and S Brunak. "Prediction of N-glycosylation sites in human proteins". In: (2004).

[313] Ahmad Saad, Benjamin Liet, Gilles Joucla, Xavier Santarelli, Justine Charpentier, Stephane Claverol, Christophe F Grosset, and Veronique Trezeguet. "Role of Glycanation and Convertase Maturation of Soluble Glypican-3 in Inhibiting Proliferation of Hepatocellular Carcinoma Cells". In: *Biochemistry* 57.7 (2018), pp. 1201–1211.

[314] Mariana I. Capurro, Wen Shi, Shaifali Sandal, and Jorge Filmus. "Processing by Convertases Is Not Required for Glypican-3-induced Stimulation of Hepatocellular Carcinoma Growth". en. In: *Journal of Biological Chemistry* 280.50 (Dec. 2005), pp. 41201–41206.

[315] Laurent Vuillard, Bassem Baalbaki, Mogens Lehmann, Sofie Nørager, Pierre Legrand, and Michel Roth. "Protein crystallography with non-detergent sulfobetaines". In: *Journal of crystal growth* 168.1-4 (1996), pp. 150–154.

[316] Tony Collins, Salvino D'Amico, Daphné Georlette, Jean Claude Marx, Adrienne L Huston, and Georges Feller. "A nondetergent sulfobetaine prevents protein aggregation in microcalorimetric studies". In: *Analytical biochemistry* 352.2 (2006), pp. 299–301.

[317] Benjamin T Porebski, Bosco K Ho, and Ashley M Buckle. "Interactive visualization tools for the structural biologist". In: *Journal of applied crystallography* 46.5 (2013), pp. 1518–1520.

[318] Max TB Clabbers, Tim Gruene, James M Parkhurst, Jan Pieter Abrahams, and David G Waterman. "Electron diffraction data processing with DIALS". In: *Acta Crystallographica Section D: Structural Biology* 74.6 (2018).

[319] Philip Evans. "Scaling and assessment of data quality". In: *Acta Crystallographica Section D: Biological Crystallography* 62.1 (2006), pp. 72–82.

[320] Petrus H Zwart, Ralf W Grosse-Kunstleve, and Paul D Adams. "Xtriage and Fest: automatic assessment of X-ray data and substructure structure factor estimation". In: *CCP4 Newsl* 43 (2005), pp. 27–35.

[321] Katherine A Kantardjieff and Bernhard Rupp. "Matthews coefficient probabilities: improved estimates for unit cell contents of proteins, DNA, and protein–nucleic acid complex crystals". In: *Protein Science* 12.9 (2003), pp. 1865–1871.

[322] Marco Biasini, Stefan Bienert, Andrew Waterhouse, Konstantin Arnold, Gabriel Studer, Tobias Schmidt, Florian Kiefer, Tiziano Gallo Cassarino, Martino Bertoni, Lorenza Bordoli, et al. "SWISS-MODEL: modelling protein tertiary and quaternary structure using evolutionary information". In: *Nucleic acids research* 42.W1 (2014), W252–W258.

[323] Pavel V Afonine, Ralf W Grosse-Kunstleve, Nathaniel Echols, Jeffrey J Headd, Nigel W Moriarty, Marat Mustyakimov, Thomas C Terwilliger, Alexandre Urzhumtsev, Peter H Zwart, and Paul D Adams. "Towards automated crystallographic structure refinement with phenix. refine". In: *Acta Crystallographica Section D: Biological Crystallography* 68.4 (2012), pp. 352–367.

[324] Oleg V Sobolev, Pavel V Afonine, Paul D Adams, and Alexandre Urzhumtsev. "Programming new geometry restraints: parallelity of atomic groups". In: *Journal of applied crystallography* 48.4 (2015), pp. 1130–1141.

[325] Computational Project Collaborative et al. "The CCP4 suite: programs for protein crystallography." In: *Acta crystallographica. Section D, Biological crystallography* 50.Pt 5 (1994), p. 760.

[326] C Thaller, LH Weaver, G Eichele, E Wilson, R Karlsson, and JN Jansonius. "Repeated seeding technique for growing large single crystals of proteins". In: *Journal of molecular biology* 147.3 (1981), pp. 465–469.

[327] Richard D Bunker, James MJ Dickson, Tom T Caradoc-Davies, Kerry M Loomes, and Edward N Baker. "Use of a repetitive seeding protocol to obtain diffraction-quality crystals of a putative human d-xylulokinase". In: *Acta Crystallographica Section F: Structural Biology and Crystallization Communications* 68.10 (2012), pp. 1259–1262.

[328] Veronica Kane Dickson. "Phasing and structure of bestrophin-1: a case study in the use of heavy-atom cluster compounds with multi-subunit transmembrane proteins". In: *Acta Crystallographica Section D: Structural Biology* 72.3 (2016), pp. 319–325.

[329] F Xavier Gomis-RuÈth and Miquel Coll. "Solving a 300 kDa multimeric protein by low-resolution MAD phasing and averaging/phase extension". In: *Acta Crystallographica Section D: Biological Crystallography* 57.6 (2001), pp. 800–805.

[330] E Krissinel and K Henrick. "Protein interfaces, surfaces and assemblies service PISA at European Bioinformatics Institute". In: *J Mol Biol* 372 (2007), pp. 774–797.

[331] Kemin Tan, Mark Duquette, Jin-huan Liu, Yicheng Dong, Rongguang Zhang, Andrzej Joachimiak, Jack Lawler, and Jia-huai Wang. "Crystal structure of the TSP-1 type 1 repeats: a novel layered fold and its biological implication". In: *The Journal of cell biology* 159.2 (2002), pp. 373–382.

[332] Haim Ashkenazy, Elana Erez, Eric Martz, Tal Pupko, and Nir Ben-Tal. "ConSurf 2010: calculating evolutionary conservation in sequence and structure of proteins and nucleic acids". In: *Nucleic acids research* 38.suppl_2 (2010), W529–W533.

[333] Colleen Manitt, Katherine M Thompson, and Timothy E Kennedy. "Developmental shift in expression of netrin receptors in the rat spinal cord: Predominance of UNC-5 homologues in adulthood". In: *Journal of neuroscience research* 77.5 (2004), pp. 690–700.

[334] Cédric Notredame, Desmond G Higgins, and Jaap Heringa. "T-Coffee: A novel method for fast and accurate multiple sequence alignment". In: *Journal of molecular biology* 302.1 (2000), pp. 205–217.

[335] Eric Beitz. "TeXshade: shading and labeling of multiple sequence alignments using LaTeX2e". In: *Bioinformatics* 16.2 (2000), pp. 135–139.

[336] Zheng Wang, Lara M Linden, Kaleb M Naegeli, Joshua W Ziel, Qiuyi Chi, Elliott J Hagedorn, Natasha S Savage, and David R Sherwood. "UNC-6 (netrin) stabilizes oscillatory clustering of the UNC-40 (DCC) receptor to orient polarity". In: *J Cell Biol* 206.5 (2014), pp. 619–633.

[337] B Imperiali, KL Shannon, M Unno, and KW Rickert. "Mechanistic proposal for asparagine-linked glycosylation". In: *Journal of the American Chemical Society* 114.20 (1992), pp. 7944–7945.

[338] Flavio Schwarz and Markus Aebi. "Mechanisms and principles of N-linked protein glycosylation". In: *Current opinion in structural biology* 21.5 (2011), pp. 576–582.

[339] Eric D Merkley, Steven Rysavy, Abdullah Kahraman, Ryan P Hafen, Valerie Daggett, and Joshua N Adkins. "Distance restraints from crosslinking mass spectrometry: mining a molecular dynamics simulation database to evaluate lysine–lysine distances". In: *Protein science* 23.6 (2014), pp. 747–759.

[340] Elisabeth Gasteiger, Christine Hoogland, Alexandre Gattiker, Marc R Wilkins, Ron D Appel, Amos Bairoch, et al. "Protein identification and analysis tools on the ExPASy server". In: *The proteomics protocols handbook*. Springer, 2005, pp. 571–607.

[341] Manoj Gopalakrishnan, Kimberly Forsten-Williams, Matthew A Nugent, and Uwe C Täuber. "Effects of receptor clustering on ligand dissociation kinetics: theory and simulations". In: *Biophysical journal* 89.6 (2005), pp. 3686–3700.

[342] Gabriel Waksman and Andrew B Herr. "New insights into heparin-induced FGF oligomerization". In: *Nature Structural & Molecular Biology* 5.7 (1998), p. 527.

[343] Dawei Shi, Xiangdong Lv, Zhao Zhang, Xiaofeng Yang, Zhaocai Zhou, Lei Zhang, and Yun Zhao. "Smoothened oligomerization/higher order clustering in lipid rafts is essential for high Hedgehog activity transduction". In: *Journal of Biological Chemistry* 288.18 (2013), pp. 12605–12614.

[344] Yue Hua, Yilin Yang, Qian Li, Xinyu He, Wei Zhu, Jiyong Wang, and Xiaoqing Gan. "Oligomerization of Frizzled and low-density lipoprotein receptor-related protein 5/6 initiates intracellular signaling for the canonical WNT/β-catenin pathway". In: *Journal of Biological Chemistry* (2018), jbc–RA118.

[345] Takahito Higashi, Shinji Tanaka, Tadatsune Iida, and Shigeo Okabe. "Synapse elimination triggered by BMP4 exocytosis and presynaptic BMP receptor activation". In: *Cell reports* 22.4 (2018), pp. 919–929.

[346] Mara E Pitulescu and Ralf H Adams. "Eph/ephrin molecules—a hub for signaling and endocytosis". In: *Genes & development* 24.22 (2010), pp. 2480–2492.

[347] Samuel Ojosnegros, Francesco Cutrale, Daniel Rodríguez, Jason J Otterstrom, Chi Li Chiu, Verónica Hortigüela, Carolina Tarantino, Anna Seriola, Stephen Mieruszynski, Elena Martínez, et al. "Eph-ephrin signaling modulated by polymerization and condensation of receptors". In: *Proceedings of the National Academy of Sciences* 114.50 (2017), pp. 13188–13193.

[348] Bert JC Janssen, Tomas Malinauskas, Greg A Weir, M Zameel Cader, Christian Siebold, and E Yvonne Jones. "Neuropilins lock secreted semaphorins onto plexins in a ternary signaling complex". In: *Nature structural & molecular biology* 19.12 (2012), p. 1293.

[349] Angelica A Gopal, Benjamin Rappaz, Vincent Rouger, Iain B Martyn, Peter D Dahlberg, Rachel J Meland, Ian V Beamish, Timothy E Kennedy, and Paul W Wiseman. "Netrin-1-regulated distribution of UNC5B and DCC in live cells revealed by TICCS". In: *Biophysical journal* 110.3 (2016), pp. 623–634.

[350] Zheng Wang, Lara M Linden, Kaleb M Naegeli, Joshua W Ziel, Qiuyi Chi, Elliott J Hagedorn, Natasha S Savage, and David R Sherwood. "UNC-6 (netrin) stabilizes oscillatory clustering of the UNC-40 (DCC) receptor to orient polarity". In: *J Cell Biol* 206.5 (2014), pp. 619–633.

[351] RG Martinho, S Castel, J Urena, M Fernandez-Borja, Ricardo Makiya, Gunilla Olivecrona, M Reina, Ana Alonso, and Senén Vilaró. "Ligand binding to heparan sulfate proteoglycans induces their aggregation and distribution along actin cytoskeleton." In: *Molecular biology of the cell* 7.11 (1996), pp. 1771–1788.

[352] Tzviya Zeev-Ben-Mordehai, Daven Vasishtan, C Alistair Siebert, Cathy Whittle, and Kay Grünewald. "Extracellular vesicles: a platform for the structure determination of membrane proteins by cryo-EM". In: *Structure* 22.11 (2014), pp. 1687–1692.

[353] Holger Stark. "GraFix: stabilization of fragile macromolecular complexes for single particle cryo-EM". In: *Methods in enzymology*. Vol. 481. Elsevier, 2010, pp. 109–126.

[354] Ashutosh Pandey and Hamed Jafar-Nejad. "Cell aggregation assays to evaluate the binding of the Drosophila notch with trans-ligands and its inhibition by cis-ligands". In: *JoVE (Journal of Visualized Experiments)* 131 (2018), e56919.

[355] Yue C Lu, Olha V Nazarko, Richard Sando III, Gabriel S Salzman, Nan-Sheng Li, Thomas C Südhof, and Demet Araç. "Structural basis of latrophilin-FLRT-UNC5 interaction in cell adhesion". In: *Structure* 23.9 (2015), pp. 1678–1691.

[356] AP Gilmore. *Anoikis*. 2005.

[357] Minsoo Kim, Christopher V Carman, and Timothy A Springer. "Bidirectional transmembrane signaling by cytoplasmic domain separation in integrins". In: *Science* 301.5640 (2003), pp. 1720–1725.

[358] Kate L Wegener and Iain D Campbell. "Transmembrane and cytoplasmic domains in integrin activation and protein-protein interactions". In: *Molecular membrane biology* 25.5 (2008), pp. 376–387.

[359] Vivian Y Poon, Matthew P Klassen, and Kang Shen. "UNC-6/netrin and its receptor UNC-5 locally exclude presynaptic components from dendrites". In: *Nature* 455.7213 (2008), p. 669.

[360] Jennifer S Goldman, Mohammed A Ashour, Margaret H Magdesian, Nicolas X Tritsch, Stephanie N Harris, Nicolas Christofi, Raja Chemali, Yaakov E Stern, Greta Thompson-Steckel, Pavel Gris, et al. "Netrin-1 promotes excitatory synaptogenesis between cortical neurons by initiating synapse assembly". In: *Journal of Neuroscience* 33.44 (2013), pp. 17278–17289.

[361] Matthew L O'Sullivan, Joris de Wit, Jeffrey N Savas, Davide Comoletti, Stefanie Otto-Hitt, John R Yates III, and Anirvan Ghosh. "Postsynaptic FLRT proteins are endogenous ligands for the black widow spider venom receptor Latrophilin and regulate excitatory synapse development". In: *Neuron* 73.5 (2012), p. 903.

[362] Joris de Wit, Matthew L O'Sullivan, Jeffrey N Savas, Giuseppe Condomitti, Max C Caccese, Kristel M Vennekens, John R Yates III, and Anirvan Ghosh. "Unbiased discovery of glypican as a receptor for LRRTM4 in regulating excitatory synapse development". In: *Neuron* 79.4 (2013), pp. 696–711.

[363] Bosiljka Tasic, Vilas Menon, Thuc Nghi Nguyen, Tae Kyung Kim, Tim Jarsky, Zizhen Yao, Boaz Levi, Lucas T Gray, Staci A Sorensen, Tim Dolbeare, et al. "Adult mouse cortical cell taxonomy revealed by single cell transcriptomics". In: *Nature neuroscience* 19.2 (2016), p. 335.

[364] Rebecca D Hodge, Trygve E Bakken, Jeremy A Miller, Kimberly A Smith, Eliza R Barkan, Lucas T Graybuck, Jennie L Close, Brian Long, Nelson Johansen, Osnat Penn, et al. "Conserved cell types with divergent features in human versus mouse cortex". In: *Nature* (2019), pp. 1–8.

[365] Mark S Cembrowski, Lihua Wang, Andrew L Lemire, Monique Copeland, Salvatore F DiLisio, Jody Clements, and Nelson Spruston. "The subiculum is a patchwork of discrete subregions". In: *Elife* 7 (2018), e37701.

[366] A-Ram Lee, Jong-Hwan Kim, Eunsil Cho, Mirang Kim, and Mikyoung Park. "Dorsal and ventral hippocampus differentiate in functional pathways and differentially associate with neurological disease-related genes during postnatal development". In: *Frontiers in molecular neuroscience* 10 (2017), p. 331.

[367] David M Bannerman, Rolf Sprengel, David J Sanderson, Stephen B McHugh, J Nicholas P Rawlins, Hannah Monyer, and Peter H Seeburg. "Hippocampal synaptic plasticity, spatial memory and anxiety". In: *Nature reviews neuroscience* 15.3 (2014), p. 181.

[368] Stephen B McHugh, Marianne Fillenz, John P Lowry, J Nicolas P Rawlins, and David M Bannerman. "Brain tissue oxygen amperometry in behaving rats demonstrates functional dissociation of dorsal and ventral hippocampus during spatial processing and anxiety". In: *European Journal of Neuroscience* 33.2 (2011), pp. 322–337.

[369] DM Bannerman, JNP Rawlins, SB McHugh, RMJ Deacon, BK Yee, T Bast, W-N Zhang, HHJ Pothuizen, and J Feldon. "Regional dissociations within the hippocampus—memory and anxiety". In: *Neuroscience & biobehavioral reviews* 28.3 (2004), pp. 273–283.

[370] Alexander Z Harris, Danielle Golder, and Ekaterina Likhtik. "Multisite Electrophysiology Recordings in Mice to Study Cross-Regional Communication During Anxiety". In: *Current protocols in neuroscience* 80.1 (2017), pp. 8–40.

[371] Cassandra R. Blanchette, Paola N. Perrat, Andrea Thackeray, and Claire Y. Bénard. "Glypican Is a Modulator of Netrin-Mediated Axon Guidance". eng. In: *PLoS biology* 13.7 (July 2015), e1002183.

[372] Megan E Williams, Sareina C-Y Wu, William L McKenna, and Lindsay Hinck. "Surface expression of the netrin receptor UNC5H1 is regulated through a protein kinase C-interacting protein/protein kinase-dependent mechanism". In: *Journal of Neuroscience* 23.36 (2003), pp. 11279–11288.

[373] Céline Furne, Nicolas Rama, Véronique Corset, Alain Chédotal, and Patrick Mehlen. "Netrin-1 is a survival factor during commissural neuron navigation". In: *Proceedings of the National Academy of Sciences* 105.38 (2008), pp. 14465–14470.

[374] Megan E Williams, Xiaowei Lu, William L McKenna, Raesha Washington, Adam Boyette, Phyllis Strickland, Allison Dillon, Zaven Kaprielian, Marc Tessier-Lavigne, and Lindsay Hinck. "UNC5A promotes neuronal apoptosis during spinal cord development independent of netrin-1". In: *Nature neuroscience* 9.8 (2006), p. 996.

[375] Megan E. Williams, Phyllis Strickland, Ken Watanabe, and Lindsay Hinck. "UNC5H1 Induces Apoptosis via Its Juxtamembrane Region through an Interaction with NRAGE". en. In: *Journal of Biological Chemistry* 278.19 (Sept. 2003), pp. 17483–17490.

[376] Fabien Llambi, Filipe Calheiros Lourenço, Devrim Gozuacik, Catherine Guix, Laurent Pays, Gabriel Del Rio, Adi Kimchi, and Patrick Mehlen. "The dependence receptor UNC5H2 mediates apoptosis through DAP-kinase". eng. In: *The EMBO journal* 24.6 (Mar. 2005), pp. 1192–1201.